Magnetism and quantum criticality in intermetallic compounds $RNiSi_3$ based on rare earths: experiments and simulations

Doctoral thesis

by

Deisy Viviana Aristizábal Giraldo

Advisor: Prof. Dr. Jorge Mario Osorio Guillén
Co-advisor: Prof. Dr. Marcos de Abreu Avila

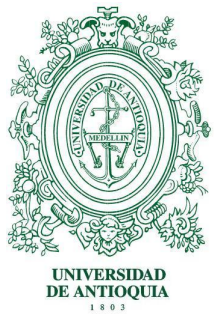

University of Antioquia
Faculty of Exact and Natural Sciences
Institute of Physics

Medellín, 2021

Prof. Dr. Jorge Mario Osorio Guillén, Institute of Physics, University of Antioquia, Medellín - Colombia

Prof. Dr. Marcos de Abreu Avila, Center of Natural and Human Sciences, Federal University of ABC, Santo André -Brazil

Preface

This work is a direct continuation of my experimental master's dissertation research *"Growth and characterization of single crystals of $RNiSi_3$ series (R =rare earth)"* [1] which was developed during the years 2013-2015 in the Grupo de Materiais Quânticos (GMQ) at the Federal University of ABC (Santo André-São Paulo, Brazil) under supervision by Prof. Dr. Marcos de Abreu Avila. Here, we studied the optimal growth conditions for these single crystals using the flux method in relation to the initial proportion of the elements and the temperature ramp. As a result, we successfully achieved to be the first to grow them and to perform the first structural and magnetic characterization at low temperatures.

This was the starting point for new research and collaborations whose primary goal was to give continuity to the characterization of single crystals already obtained for heavy rare earths (R=Y, Gd, Tb, Dy, Ho, Er, Tm, Yb, Lu), by means of specific heat and resistivity measurements as a function of temperature and magnetic field. This allowed us to report the physical properties of the intermetallic series $RNiSi_3$ in Physical Review Materials in 2018 [2]. Because of its relevance, we will refer to it frequently during the development of this thesis.

Our next step was to investigate $YNiSi_3$ and $LuNiSi_3$ at low temperatures as an attempt to find superconductivity. Also, to expand the research to pseudo-ternary systems such as $Gd_{1-x}Y_xNiSi_3$ and $Tb_{1-x}Y_xNiSi_3$ in order to systematically study the changes presented in their physical properties. Likewise, we consider the intermetallic compounds belonging to $YbNiSi_{3-x}Ge_x$ due to their potential to exhibit quantum critical phenomena. Simultaneously, we start to use electronic structure calculations using density functional theory in order to improve our understanding of such systems.

This thesis was submitted to the Postgraduate Program in Physics Institute of the University of Antioquia (UdeA), as a partial fulfillment of the requirements for the degree of Philosophiae Doctor (PhD) in Physics. This work was carried out during the years 2017-2021 thanks to Colciencias scholarship - convocatoria No. 757 de 2016.

Acknowledgments

I would like to take this opportunity to thank God, life, financial institutions and all those people who have contributed academically, socially and emotionally to the development of this doctoral thesis. My deepest gratitude and admiration to my advisor Prof. Dr. Jorge Mario Osorio Guillén and my co-advisor Prof. Dr. Marcos de Abreu Avila for all the supervision, their immeasurable patience, brilliant suggestions, understanding, help and enormous support in following my own ideas. Thanks a lot to GMQ group: Prof. Dr. Carlos Rettori and Prof. Dr. Leticie Mendoça-Ferreira for assistance, fruitful discussions, patient explanations, to both of you also my deepest admiration and respect. Dr. Fabiana Arantes, Dr. Michael Cabrera, Dr. Julián Munevar, Dr. Shiva Singh, César Sônego, Gustavo Vasques, Kariny Ferreira, Rodrigo Paulino and Vitor Vital for the physical and experimental discussions, the machine times in PPMS and SQUID, and all the work that we have performed together as a team. I also thank to Colciencias for believing in my research abilities, for having financed all my doctoral studies, as well as my travels and stays in Brazil during this investigation. Also, for buying the workstation and the VASP license, to perform my computational calculations. I thank the multiuser center of the UFABC and the Laboratory of Crystallography and Structural Characterization of Materials (LCCEM) of UFABC for the availability of the equipment to carry out the structural, magnetic and transport measurements of my samples. With all my heart I would like to thank to my small brazilian family the Marlinhos (João Miranda, Danilo Lopes, Maria Luiza Carvalho, Alexandre Lemes and Andryos Carvalho), Vitor's family, Angel Masa and to all those people who despite the distance they always made me feel like I was at home. Finally but not least important, I thank to Prof. Nelson Gil, Prof. Marta Rivera, my husband Faber Franco, my parents, brothers and friends for being there in the most difficult moments during my doctorate, supporting me unconditionally.

Deisy Aristizábal

Medellín, Colombia, September 2021

Abstract

$RNiSi_3$ (R=Gd-Yb) series have exhibited a wide variety of physical phenomena including antiferromagnetism, magnetic hysteresis accompanied by metamagnetic transitions, complex magnetic phase diagrams, coexistence of RKKY interaction and Kondo effect, among others. The combined effect between some of them constitutes a great challenge to comprehend their fundamental interactions. This thesis is the result of trying to understand such interactions in $YNiSi_3$, $LuNiSi_3$, $Gd_{1-x}Y_xNiSi_3$, $Tb_{1-x}Y_xNiSi_3$ and $YbNiSi_{3-x}Ge_x$ from two different approaches: electronic structure calculations where we employ first-principles DFT, and an experimental focus where we grow single crystals via Sn-flux method and characterize them from X-ray diffraction, magnetization, specific heat and resistivity measurements. As a result of this investigation, we observe that $YNiSi_3$ and $LuNiSi_3$ are non-conventional type-I superconductors at $T_c = 1.36(3)$ and 1.61(2) K, respectively, categorized as anisotropic three-dimensional metals with multiband superconducting ground states in the weak-coupling regime. Moreover, their Cooper pairs are formed by the coupling of Y(Lu), Ni d with Si p electrons. On the other hand, Y-dilute antiferromagnetic systems in which a reduction of the RKKY interaction is expected, lead to other physical manifestations such as the emergence of Ni magnetic moment. This causes competition between ferromagnetic and antiferromagnetic interactions that are evidenced as anomalies above T_N in $Tb_{0.5}Y_{0.5}NiSi_3$, or they generate the exchange bias effect in $Gd_{0.50}Y_{0.50}NiSi_3$ and $Gd_{0.35}Y_{0.65}NiSi_3$. Finally, initial studies on quantum criticality in $YbNiSi_{3-x}Ge_x$ antiferromagnetic-Kondo lattice indicate that the strong competition between the RKKY and Kondo interactions allow only a weak change of the ground state of the systems toward fluctuating valence systems.

Key words: Magnetism, superconductivity, quantum critical point, density functional theory.

List of papers

1. FR Arantes, D Aristizábal, SH Masunaga, FN Costa, FF Ferreira, T Takabatake, L Mendonça, RA Ribeiro, and MA Avila. *Structure, magnetism, and transport of single-crystalline $RNiSi_3$ (R= Y, Gd-Tm, Lu).* Physical Review Materials (**2018**), vol. 2, no. 4, p. 044402.

2. FR Arantes, D Aristizábal, DA Mayoh, Y Yamane, C Yang, MR Lees, JM Osorio, T Takabatake, and MA Avila. *Superconductivity in monocrystalline $YNiSi_3$ and $LuNiSi_3$*. Physical Review B (**2019**), vol. 99, no. 22, p. 224505.

Acronyms

AC	alternating current
AE	all electron
AFM	antiferromagnetic
AM	amplitude modulated
AMF	around mean field
ANI	anisotropic
APW	augmented-plane wave
APW+lo	augmented-plane wave with local orbital
BCS	Bardeen, Cooper and Schrieffer
BZ	Brillouin zone
CA	Ceperley-Alder
CEF	crystalline electric field
CW	Curie-Weiss
DC	direct current
dc	double-counting
DFT	density functional theory
DFT+U	density functional theory plus Hubbard parameter U
dG	de Gennes factor
DG	double gap
DOS	density of states
EB	exchange bias
EDS	energy-dispersive X-ray spectroscopy
ELF	electron localization function
EM	equal magnetic moment structure
EOS	equation of state
FBZ	first Brillouin zone
FC	field cooling
FLL	fully localized limit
FM	ferromagnetic
FP	full potential
GGA	generalized gradient approximation

HAXPES	hard X-ray photoemission spectroscopy
HK	Hohenberg-Kohn
IR	interstitial region
KS	Kohn-Sham
LDA	local density approximation
MF	muffin-tin
MPMS	magnetic property measurement system
NFL	non-Fermi liquid
PAW	projector augmented-wave
PBE	Perdew-Burke-Ernzerhof
PBEsol	Perdew-Burke-Ernzerhof revised for solids
PDOS	projected density of states
PFY	partial fluorescence yield mode
PPMS	physical property measurement system
PS	pseudo
PZ	Perdew and Zunger
QCP	quantum critical point
RKKY	Rudernam, Kittel, Kasuya and Yoshida
RRR	residual resistivity ratio
RXES	resonant X-ray emission spectroscopy
SG	single gap
SGNF	single gap with nonsuperconducting contribution fraction
SOC	spin-orbit coupling
SQUID	superconducting quantum interference device
XAS	X-ray absorption spectroscopy
XRD	X ray diffraction
ZFC	zero field cooling

Contents

1

Introduction

Technological advances that have been achieved throughout human history are due to a deep understanding of the physical properties of materials. This is the case of rare earths, which have abundant magnetic, luminescent, electrochemical and thermal properties that have made possible the manufacture of permanent magnets for electrical generators, glass-polishing powders, energy-saving lamps, light-emitting diodes, wind turbines and more. They even have high-tech applications such as hard-disk drives, smart phones, flat-screen televisions and monitors, rechargeable batteries (household and automotive), electric cars, medical imaging and tiny earphones.

Rare earth elements have an outer shell atomic configuration of the form $4f^{n+1}5s^25p^6$, where the partially filled $4f$ shell lies close to the core and inside the $5s$ and $5p$ shell, which determine the size of the lanthanoids ions. As a consequence, the electrons in the f shell exhibit strong correlations where the motion of each electron causes an inertial reaction on the surrounding electrons. Moreover, since there is not perfect shielding of the nuclear charge, as the atomic number increases from lanthanum to lutetium, there is a progressive decrease in their ionic radius. On the other hand, yttrium has an ionic radius and chemical behavior similar to Gd and Tb. Therefore, it is considered as another heavy rare earth element (Gd-Lu) despite having a different atomic structure $4d^15s^2$.

Intermetallic compounds based on rare earths and $3d$ transition elements exhibit a rich variety of physical phenomena including complex magnetic structures with metamagnetic transition [3, 4], crystalline field effects, magentoresistivity, Kondo effect [5], valence fluctuation phenomena, non-Fermi liquid behavior [6], heavy fermion behavior, quantum criticality [7, 8] or even unconventional superconductivity.

Several of these phenomena have been observed in compounds belonging to the $RNiSi_3$ (R=Y, Gd-Yb, Lu) series. These crystallize in the orthorhombic $Cmmm$

space group and exhibit, except for $YNiSi_3$ and $LuNiSi_3$, anisotropic antiferromagnetic ground states with Néel temperature T_N between 2.6 ($TmNiSi_3$) up to 33.2 K ($TbNiSi_3$). Additionally, $DyNiSi_3$ and $HoNiSi_3$ present a second anomaly below T_N indicating a magnetic transition induced by temperature [1,9]. Moreover, they all show external magnetic field-induced metamagnetic transitions, which for $TbNiSi_3$, $DyNiSi_3$ and $HoNiSi_3$ are accompanied by hysteresis. Also, $YbNiSi_3$ is a Kondo lattice that shows moderately heavy fermion behavior which makes it an good candidate to present quantum criticality [10].

The aim of this thesis is to investigate the physical properties of $YNiSi_3$ and $LuNiSi_3$ at low temperature from an experimental and computational approach. Also, to study the effect of non-magnetic ions (Y and Ge) on the magnetic properties of $GdNiSi_3$, $TbNiSi_3$ and $YbNiSi_3$ compounds.

This thesis is organized in three parts: The first part is a background of $RNiSi_3$ family, which include theoretical framework, methodology and bibliographic searches. In chapter 2 we refer to the key concepts that will allow us to understand the structural, magnetic, electronic, elastic and transport properties of these compounds. So, it will involve a brief introduction to the density functional theory. Next, in chapter 3 we indicate the experimental and computational methodology used throughout these investigation. Finally, in chapter 4 we detail all the physical properties reported in the literature about these series and the isovalent $YbNiGe_3$ compound. The second part presents our research contributions to these compounds. Here we report the superconductor properties of $YNiSi_3$ and $LuNiSi_3$ in chapter 5 and the physical properties of doped systems as $Gd_{1-x}Y_xNiSi_3$ in chapter 6 and $Tb_{1-x}Y_xNiSi_3$ in chapter 7. Finally, the third part deals with the work that is in progress. These will be outlined in chapter 8, where we will give the first hints on the study of quantum criticality in the pseudo-quaternary system $YbNiSi_{3-x}Ge_x$.

Part I

Background

2

Theoretical background

In this section we will briefly consider several fundamental solid-state topics such as density functional theory, band theory, magnetism, elasticity, specific heat, resistivity, superconductivity and quantum criticality, which will allow us to understand the physics involved in the $RNiSi_3$ series and their Y/Ge-doped systems such as $Gd_{1-x}Y_xNiSi_3$, $Tb_{1-x}Y_xNiSi_3$ and $YbNiSi_{3-x}Ge_x$.

2.1 DFT

A solid is a system of many interacting particles: electrons and nuclei. The Hamiltonian that describes it considers the kinetic energy of the electrons and the kinetic energy of the nuclei, Coulomb interaction between nuclei, electrons and nuclei-electrons. However, since the nucleus is more massive than the electrons it is possible to assume *the Born–Oppenheimer approximation* where the nuclei are frozen instantaneously, while the electrons move in the field produced by the presence of the fixed nuclei, defining *the external potential*. Thus, it is only necessary to consider the electronic system whose energy is determined by: (i) the kinetic energy of the electrons, (ii) the electrostatic external potential and (iii) the electronic interaction. The latter includes classical effects described by the *the Hartree energy*:

$$E_{Hartree} = \frac{e^2}{2} \int d^3r d^3r' \frac{n(\mathbf{r})n(\mathbf{r'})}{|\mathbf{r} - \mathbf{r'}|}, \tag{2.1}$$

which is associated with the self-interaction energy of the electronic charge density $n(\mathbf{r})$. This satisfies the Poisson equation $\nabla^2 v_H(\mathbf{r}) = -4\pi n(\mathbf{r})$, for a Coulomb potential v_H at point $\mathbf{r}$ generated by a charge $-n(\mathbf{r'})d^3r'$. Additionally, the electronic interaction includes quantum effects involving exchange and correlation effects.

2.1.1 Hohenberg-Kohn (HK) theorems

The total energy associated with this system can be determined through the charge density of the system according to the following theorems:

Theorem 2.1.1 *For any system of interacting particles moving in an external potential v_{ext} and a static magnetic field B_{ext}, the set (V_{ext}, B_{ext}) will uniquely determine the ground state charge density given by the set ($n_0(\boldsymbol{r})$, $n_0^\sigma(\boldsymbol{r})$), and reverse. Here $n(\boldsymbol{r})$ is the electronic charge density and $n^\sigma(\boldsymbol{r})$ is the magnetic charge density with σ-spin-polarization [11, 12].*

Theorem 2.1.2 *For any external potential V_{ext} and static magnetic field B_{ext}, it is possible to define the energy functional in terms of the electronic $n(\boldsymbol{r})$ and magnetic $n^\sigma(\boldsymbol{r})$ density as:*

$$E_{HK}[n(\boldsymbol{r}), n^\sigma(\boldsymbol{r})] = T[n, n^\sigma] + E_{int}[n, n^\sigma] + \int d^3r\{v_{ext}(\boldsymbol{r})n(\boldsymbol{r}) + \boldsymbol{B}_{ext}(\boldsymbol{r}) \cdot \hat{n}^\sigma(\boldsymbol{r})\}, \tag{2.2}$$

where $T[n, n^\sigma]$ and $E_{int}[n, n^\sigma]$ are functionals associated with the kinetic and potential energy of the interacting system. The density that minimizes the energy functional is the ground state density and the minimum of that functional corresponds to the ground state energy [11, 12].

Although these theorems give us an idea over how to determine the ground state energy of a many-body system, they tell us nothing about how we can compute these functionals.

2.1.2 Kohn-Sham (KS) scheme

Walter Kohn and Lu Jeu Sham (1965) demonstrated that by considering the (HK) theorems the interacting electronic system can be mapped onto a non-interacting electronic system (or *auxiliary system*) with a specific external potential, such that both have the same ground state density. For the latter, the Hamiltonian is the sum of σ-spin-polarized individual Hamiltonians called

the Kohn-Sham (KS) equation, which alludes to a particle moving in an effective KS potential v_s [13]:

$$\left[-\frac{\hbar^2\nabla^2}{2m} + v_s^\sigma(\mathbf{r})\right]\phi_{i,\sigma}(\mathbf{r}) = \varepsilon_{i,\sigma}\phi_{i,\sigma}(\mathbf{r}), \tag{2.3}$$

where

$$v_s^\sigma(\mathbf{r}) = v_{Hartree}[n](\mathbf{r}) + v_{xc}[n, n^\sigma](\mathbf{r}) + v_{ext}(\mathbf{r}). \tag{2.4}$$

$\phi_{i,\sigma}(\mathbf{r})$ are the KS orbitals and $\varepsilon_{i,\sigma}$ are the KS eigenvalues. This equation must be solved in a self-consistent way, so in section 3 we will detail how to do this computationally. On the other hand, in the interacting system the energy functional of Eq. 2.2 can be rewritten as:

$$E_{KS}[n, n^\sigma] = T_{nonint}[n, n^\sigma] + E_{Hartree}[n, n^\sigma] + E_{xc}[n, n^\sigma] + E_{ext}[n, n^\sigma], \tag{2.5}$$

where $T_{nonint}[n, n^\sigma] = -\frac{1}{2}\sum_i^N |\nabla\phi_{i,\sigma}|^2$ is the kinetic energy of particles in the non-interacting system and $E_{ext}[n, n^\sigma]$ is the external functional that depends on the configuration of the nuclei and the external fields.

All quantum exchange and correlation (xc) effects that are present in both the kinetic energy functional and internal energy functional in the interacting system are included in $E_{xc}[n, n^\sigma]$ energy functional. It does not have an exact form, but there are simple approximations that allow one to calculate its ground state properties. Among the most common are the local spin density approximation (LSDA) and the generalized gradient approximation (GGA). They differ in the dependence on the electronic charge density. For example, LDA assumes that the electronic system behaves like an interacting homogeneous gas, where the spin density varies slowly over the space. Thus, E_{xc} is a local functional that depends only the charge density and it can be parametrized according to Ceperley-Alder (CA) [14] and Perdew and Zunger (PZ) [15]. Systematic errors encountered when using LDA are (1) overestimating the bonding, (2) underestimating lattice parameters and (3) giving large bulk moduli [16]. These can disappear with GGA due to its consideration of the electronic system as uniform gas with small local perturbations. Hence, E_{xc} is a semilocal functional that depends on the charge density and its first-order gradient at each point in space. In this case, the most commonly used parametrizations are the Perdew-Burke-Ernzerhof (PBE) [17] and Perdew-Burke-Ernzerhof revised for solids (PBEsol) [18,19]. The latter occupies a midpoint between LDA and PBE producing better energies and lattice parameters values in periodic systems. For example, while LSDA underestimates the lattice parameters of solids with respect to experimental value, PBE overestimates them. In contrast, PBESol values are lower than PBE by 1-2%, which improves the bulk modulus of the system.

KS scheme is a purely mathematical tool that only helps us to find the ground density of the system, without indicating the formal ground state of the interacting system, so the KS-orbital and KS-eigenvalues in general have no physical meaning. However, they are of qualitative use in understanding the structural, electronic, magnetic and phononic properties of solids.

2.1.3 DFT+U

Consider that each atomic orbital is an atomic site that can be doubly occupied by electrons with spin-up $\sigma =\uparrow$ and spin-down $\sigma =\downarrow$ to satisfy the Pauli exclusion principle. The movement of electrons through the crystal can be described by "hopping" from one atomic site to its neighbors whether it is empty or single occupied by an electron with opposite spin. When two antiparallel spin electrons are at the same site they will experience a Coulomb interaction U. The Hamiltonian that describes this system is called *Hubbard Hamiltonian*:

$$H = \sum_{i,j} t_{ij} \hat{c}_i^{\dagger} \hat{c}_j + U \sum_i \hat{n}_{i,\uparrow} \hat{n}_{i,\downarrow},$$

where t_{ij} is the hopping amplitude, i and j denotes nearest-neighbor atomic sites, $\hat{n}_{i,\sigma}$ is the number operator for σ spin-polarized electrons on i-site, $\hat{c}_i^{\dagger}$ and $\hat{c}_j$ are the creator and annihilation operators, respectively, which indicate the creation of an electron at i site and annihilation at j site. The competition between U and t controls the behavior of the solid and the character of its electronic ground state. If $t >> U$, the electrons are delocalized and their wave functions are Bloch states. This behavior is typical of metallic systems which are well described by DFT. In contrast, when $t << U$, short-range Coulomb interactions occur as in strongly correlated electronic states. In this case DFT does not correctly describe the ground state of the system. However, it can be improved by adding the U Hubbard parameter (DFT+U).

The goal of DFT+U is to separate the system into two subsystems: those behaving as delocalized s and p electrons which could be treated by DFT and others as highly localized d and f electrons for which the Coulomb interaction is considered. The generalized DFT+U functional can be written as:

$$E^{DFT+U}[n(\mathbf{r})] = E^{DFT}[n(\mathbf{r})] + E^{U}[\hat{n}_{i,\sigma}] - E_{dc}[\hat{n}_{i,\sigma}], \tag{2.6}$$

where E^{DFT} consider the standard DFT functional in some xc approximation, E^{U} is the term containing the electron-electron interaction as modeled in the Hubbard Hamiltonian. Note that in both terms we consider the interaction

energy, to avoid double-counting (dc) we subtract it in the E^{dc} term.

For double-counting we can consider two possibilities depending on whether the system is strongly or weakly correlated. In the first case it is common to use the fully localized limit (FLL) approach [20], while in the other the around mean field (AMF) approximation [21]. Systems that do not lie in these limits are treated as a linear interpolation of both

$$E_{dc}^{INT} = \alpha E_{dc}^{FLL} + (1-\alpha) E_{dc}^{AMF}, \tag{2.7}$$

for some α parameter. The dc prescriptions allow us to rewrite E^{dc} functional in terms of U and J which are the screened Coulomb and exchange parameters, respectively. Also, in terms of effective Slater integrals F^k which are the radial part of the k on-site Coulomb interaction between two electrons. They are given by [22]:

$$F^k = \int dr_1 r_1^2 R_l^2(r_1) g_k(r_1, r_2) R_l^2(r_2) r_2^2 dr_2.$$

where

$$g(r_1, r_2) = e^{-\frac{\lambda r_{12}}{r_{12}}}, \tag{2.8}$$

is the Yukawa potential and λ is the Yukawa screening length parameter [22]. For d electrons F^0, F^2 and F^4 are required while for f electrons F^6 is also necessary, which determines $U = F^0$, $J = (F^2 + F^4)/14$ while $A_1 = F^4/F^2$ and $A_2 = F^6/F^2$ are constant.

2.2 Structural Properties

2.2.1 Symmetries of Crystals

As mentioned above, a solid is a system of many interacting particles: electrons and nuclei. The way in which the nuclei are arranged determines its crystalline structure. From a crystallographic point of view, this can be described by: (i) Bravais lattice, (ii) space group and (iii) atomic basis. In this thesis we will consider orthorhombic cells ($a_1 \neq a_2 \neq a_3$ and $\alpha = \beta = \gamma = 90°$) and tetragonal cells ($a_1 = a_2 \neq a_3$ and $\alpha = \beta = \gamma = 90°$) with space group $Cmmm$,

$I4/mmm$ and $I4_1amd$. These groups are denoted by an uppercase letters describing the lattice type: C (base-centered) and I (body-centered), and the point group identifier mmm, $4/mmm$ and 4_1amd, which can be rewritten as $2/m\ 2/m\ 2/m$, $4/m\ 2/m\ 2/m$ and $4_1/a\ 2/m\ 2/d$, respectively. We label them as $i\ j\ k$ indicating the i-symmetry along x-axis, j-symmetry along the y-axis and k-symmetry along z-axis. n/m with n=2, 4 means that the plane perpendicular to the n-fold rotation (360°/n) is a mirror plane. a and d are reflection in a plane followed by a translation parallel with that plane, but the latter is along the space diagonal of the unit cell. Finally, 4_1 corresponds with rotations by 90° followed by a translation of 1/4 of the lattice vector.

2.2.2 Equation of State (EOS)

The ground state energy of a system in equilibrium is determined by macroscopic variables such as temperature (T), pressure (P) and volume (V). The variation of some of them describes its thermodynamic evolution through an EOS. As example, at $T = 0$ the volume dependent energy Birch-Murnaghan equation (3rd order) is described by [23]:

$$E(V) = E_0 + \frac{9}{2}V_0B_0f^2[1 + (B_0' - 4)f], \tag{2.9}$$

and the pressure dependent energy is given by [23]:

$$P(V) = \tfrac{3}{2}B_0f(2f+1)^{5/2}[2 + 3(B_0' - 4)f] \quad \text{with} \quad f = \tfrac{1}{2}\left[\left(\tfrac{V_r}{V}^{2/3} - 1\right)\right], \tag{2.10}$$

or equivalently for diluted systems as [24]

$$P = B_0\frac{V_0 - V(x)}{V(0)}, \tag{2.11}$$

where E_0, V_0 and B_0 correspond to energy, volume and bulk modulus at zero pressure, respectively. V_r is a reference volume, B_0' is the pressure derivative of the bulk modulus at reference pressure and x is the concentration level. This approach will be used to calculate the ground state properties (E_0, V_0, B_0 and lattice parameters) at $P = 0$ GPa and $T = 0$ K of $YNiSi_3$, $LuNiSi_3$ and $GdNiSi_3$ compounds.

2.3 Electronic properties

2.3.1 Electronic band structure

The complete set of KS eigenvalues for each **k**-point in the Brillouin zone forms the *energy band structure* $E(\mathbf{k})$ of the crystal, where a pair of antiparallel spin electrons can be accommodated on each of these bands. This filling takes place from the lowest energy band to the highest energy band. The energy level of the highest occupied level at $T = 0$, which separates the occupied states from unoccupied states is called the *Fermi level* E_F. The bands below E_F are *valence bands*, while above it they are *conduction bands*. As the temperature increases the valence electrons that are in k_BT energy range near the Fermi level are thermally excited to conduction bands leaving a vacancy or hole in the valence band.

Both electrons and holes contribute to electrical conductivity in the solid. In presence of an electrical and magnetic field, the electron acts as a negative charge and the hole as a positive charges. In a crystal, due to the presence of electron-electron and electron-phonon interactions, they are endowed with an effective mass m^* which may be greater or less than the free electron mass. For example, moderate heavy fermions have $m^* \sim 100m_e$ while for heavy fermions $m^* \sim 1000m_e$ [25]. We can determine the effect of the crystal lattice on the electron motion from the dispersion relation, because the effective electron mass is inversely proportional to the curvature of the energy band $\partial^2\varepsilon/\partial k^2$. Thus, a band with upward curvature is associated with positive effective mass, and it is called *electron-like band*, while downward curvature is linked to the negative effective mass and it is known as the *hole-like band*.

2.3.2 Fermi surface

In metallic compounds, one or more bands cross the Fermi level indicating that it is partially filled. Each of them determines a sheet of the *Fermi surface*. The connection of all of them forms a constant energy surface E_F in **k**-space, which indicates which wave vectors **k** in the Brillouin zone correspond to occupied states and which wave vectors correspond to unoccupied states. The

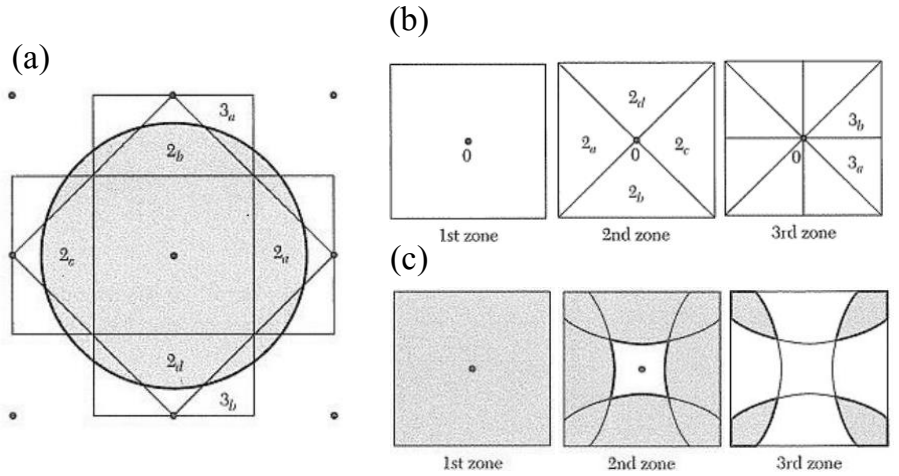

Figure 2.1: (a) Brillouin zones for a two dimensional square lattice. Gray circle is the Fermi surface for free electron gas. (b) First, second and third Brillouin zone moved to first Brillouin zone through appropriate reciprocal lattice. (c) Mapping the FS of (a) in the reduced zone scheme. This Figure is taken from Ref [25].

physical properties of a metal are greatly affected by connectivity of the Fermi surface [26].

According to Dirichlet's construction, the Brillouin zone is built by bisecting with perpendicular planes nearest neighbors reciprocal lattice vectors, which divide this space into fragments. The central cell is called the first Brillouin zone (FBZ) and it is characterized by being the polyhedron with the smallest volume in the reciprocal space. The shape of the Fermi surface in the Brillouin zone depends on the electron-electron interaction strength and the electron concentration. For example, for a free electron gas (where the electron-electron interaction is neglected) the Fermi surface is spherical whose center coincides with the origin of reciprocal space [Fig. 2.1(a)]. In this case, if the electron concentration is low the entire FS lies within the FBZ, determining a single sheet. Conversely, as the electron concentration increases the FS extends to higher orders of the BZ. In this case, since any **k**-vector can be brought into the FBZ through the reciprocal vector, we can place all the fragments of the FS in the FBZ [Fig. 2.1(b) and (c)]. The appropriate attachment of fragments per zone will determine a sheet of the complete FS. On the other hand, when the electron-electron interaction is considered, the spherical FS becomes distorted and its structure in the FBZ can become quite complicated [25].

2.3.3 Electronic density of states

The electronic density of states (DOS) of a system describes the number of states allowed at energy level ε to be occupied by electrons. They can be calculated from KS eigenvalues as

$$D(\varepsilon) = \frac{1}{N_{\mathbf{k}}} \sum_{n,\mathbf{k}} \delta(\varepsilon_{n,\mathbf{k}} - \varepsilon),$$

where $N_{\mathbf{k}}$ is the total number of $\mathbf{k}$-vectors considered in the Brillouin zone and n is the n-KS eigenvalue. The number of occupied states at Fermi level is exactly equal to the total number of conduction electrons in the metal [27]. If these states are counted as a contribution from a specific atom or orbital μ, it is called *the projected density of states (PDOS)* $D_\mu(\varepsilon)$, such that $D(\varepsilon) = \sum_\mu D_\mu(\varepsilon)$.

2.3.4 Electron localization function

The electron localization function (ELF) is an electronic spatial distribution function that allows us to determine where the electrons tend to be located. Its topology reveals the location of core and all the chemical bonding details of the system [28]. It is defined as [29]

$$ELF = \frac{1}{1+\left(\frac{D}{D_h}\right)^2} \quad \text{with} \quad D = \frac{1}{2}\sum_i |\nabla\phi_i|^2 - \frac{1}{8}\frac{|\nabla n|^2}{n}, \quad D_h = \frac{3}{10}(3\pi^2)^{5/3} n^{5/3}, \tag{2.12}$$

ϕ_i are the KS orbitals and $n = \sum_i |\phi_i|^2$ is the electronic charge density. ELF is a dimensionless localization index defined between zero and one, whose calibration is with respect to the uniform density electron gas which has a value of 1/2. Thus, ELF=0 and 1 correspond to perfect delocalization and localization, respectively.

In general, solids are formed by ionic, covalent and/or metallic bonds. Ionic bonds are formed by electrostatic interaction between positive and negative ions, whose charge distribution has an approximately spherical symmetry. In this case, the electrons are highly localized close to nuclei, so that the ELF exhibits high values around the nuclei and low values (almost 0) in the interstitial region. In contrast, covalent bonding is a shared-electron interaction where the electrons tend to be partially localized, with opposite spins, on the line connecting those atoms. Here, the ELF shows a local maximum, between

0.6 and 1.0, which depends on the bond strength. Finally, metallic bond is compared to a free electron gas, in which the electrons move freely through the crystal reaching ELF values close to 1/2.

2.4 Phononic properties

2.4.1 Phononic band structure

At temperatures above $T = 0$, the atoms are displaced by thermal motion from their equilibrium positions ($\mathbf{R}$) performing small-amplitude oscillations around it with instantaneous displacement ($\mathbf{u}$(t)). In the harmonic approximation, the potential U felt by the ions is

$$U(\mathbf{r}) = \frac{1}{2} \sum_{\kappa,\alpha} \sum_{\kappa',\beta} \left(\frac{\partial^2 U}{\partial u_{\kappa,\alpha} \partial u_{\kappa',\beta}} \right) u_{\kappa\alpha} u_{\kappa'\beta}.$$

The classical equation of motion for the κ-ion is

$$F_\kappa = M_\kappa \frac{\partial^2 u_{k,\alpha}}{\partial t^2} = -\nabla U = \sum_{\kappa',\beta} \left(\frac{\partial^2 U}{\partial u_{\kappa\alpha} \partial u_{\kappa'\beta}} \right) u_{\kappa'\beta}, \tag{2.13}$$

where for each κ-ion there are three equations of motion (one for each Cartesian direction). Being coupled to other atomic displacements, their solution involves displacements that have a temporal dependency as a plane wave with respect to cell coordinates: $u_{\kappa\alpha}(t) = \frac{1}{\sqrt{M_\kappa}} \eta(\kappa\alpha) e^{i\mathbf{q} \cdot \mathbf{R}} e^{-i\omega_\mathbf{q} t}$. Then, this equation can be rewritten as

$$\omega_\mathbf{q}^2 \eta(\kappa\alpha) = \sum_{\kappa',\beta} D_{\kappa\alpha,\kappa'\beta}(\mathbf{q}) \eta(\kappa'\beta), \tag{2.14}$$

where

$$D_{\kappa\alpha,\kappa'\beta} = \frac{C_{\kappa\alpha,\kappa'\beta}(\mathbf{q})}{\sqrt{M_\kappa M_{\kappa'}}} \quad \text{where} \quad C_{\kappa\alpha,\kappa'\beta} = \left(\frac{\partial^2 U}{\partial u_{\kappa\alpha} \partial u_{\kappa'\beta}} \right) e^{i\mathbf{q} \cdot \mathbf{R}}. \tag{2.15}$$

$D_{\kappa\alpha,\kappa'\beta}$ is called *dynamical matrix* and $C_{\kappa\alpha,\kappa'\beta}(\mathbf{q})$ is the *force constant*. The system of Eq. 2.14 has nontrivial solutions when $det(D_{\kappa\alpha,\kappa'\beta}(\mathbf{q}) - \omega^2 \delta_{\alpha\beta} \delta_{\kappa\kappa'}) = 0$ and the complete set of eigenvalues ω for each $\mathbf{q}$-point in the Brillouin zone forms the phononic band structure $\omega(\mathbf{q})$ of the crystal. If a $\omega < 0$ appears for any wave vector, it indicates that the structure is dynamically unstable.

A system of N atoms has $3N$ vibrational frequencies for each vector $\mathbf{q}$: 3 branches correspond to acoustic vibrations, while the other $3N-3$ branches to optical ones, each associated with three polarization modes: one longitudinal polarization and two transverse polarizations [25]. Acoustic modes start from $\omega = 0$ at $\mathbf{q}$=0 up to finite frequency value. In this regime the atoms oscillate in phase with equal vibrational amplitude, so that the atomic displacement is in the direction of propagation of the vibration. This behavior is similar to that of a sound wave in air (hence the name acoustic). In contrast, optical modes proceed from a finite frequency value. Here, the atoms move in opposite directions such that the center of mass remains stationary, similar to motion of atoms during excitation by an electric field of a light wave. For this reason they are called optical modes.

2.4.2 Phonon density of states

Similar to electronic density of states mentioned above in subsection 2.3.3, the phonon density of states $F(\omega)$ describes the number of phonon modes of a specific frequency ω in a given frequency interval $(\omega - 1/2\Delta\omega, \omega + 1/2\Delta\omega)$. On the other hand, the partial phonon density of states $F_\lambda(\omega)$ includes information about the vibrational behavior of each atom and it is such that

$$F(\omega) = \sum_\lambda F_\lambda(\omega) = \sum_\lambda \int \frac{d\mathbf{q}}{(2\pi)^3} \delta(\omega - \omega_\lambda(\mathbf{q})).$$

which is directly related to the lattice specific heat [sec. 2.6.1], the electron-phonon coupling constant and, therefore, the phase transition temperature of bulk superconductors [sec. 2.8.3].

2.5 Magnetic properties

The spin polarized electrons considered above determine the magnetic charge density $n_\uparrow$ and $n_\downarrow$ and therefore the magnetization ($m = n^\uparrow - n^\downarrow$). This affects directly the electronic properties of materials, so they must be treated for each spin orientation. In the following we will establish how the magnetization characterizes the magnetic properties of solids.

2.5.1 Spin-orbit coupling

Atomic magnetism is due to electrons in partially filled shells moving around the nucleus. It can be determined according to Russel-Saunder scheme (called *spin-orbit coupling*) where the total magnetic moment $\mathbf{J} = \mathbf{L} + \mathbf{S}$ is obtained by coupling the total angular moment $\mathbf{L} = \sum_i \mathbf{l}_i$ with the spin angular momentum $\mathbf{S} = \sum_i \mathbf{s}_i$. Here $\mathbf{l}_i$ and $\mathbf{s}_i$ are the orbital angular moment and the intrinsic spin angular moment for each electron, respectively. Since this coupling increases with atomic number, it is expected that for rare earths this interaction is important. Now, all possible J values that minimize the atomic energy are determined by *Hund's rules*: (i) maximize S and (ii) maximize L, to reduce Coulomb repulsion. (ii) $J = |L - S|$ for shells occupied less than half full and $J = |L + S|$ for more half full, to diminish the spin-orbit energy. Thus, after calculating J, the total magnetic moment μ_J and saturation magnetic moment μ_{J_z} are given by:

$$\begin{aligned} &\mu_J = g_J\sqrt{J(J+1)}\mu_B, \quad \text{with} \quad g_J = \tfrac{3}{2} + \tfrac{S(S+1)-L(L+1)}{2J(J+1)}, \\ &\mu_{J_z} = g_J J \mu_B, \end{aligned} \tag{2.16}$$

where g_J is the Landé g-factor and μ_B is the Bohr magneton. In Table 2.1 we summarize the above mentioned quantities for rare earths.

Table 2.1: Magnetic ground states for heavy rare eath ions using Hund's rules: total orbital angular moment (L), total spin angular moment (S), total angular moment (J), Landé g-factor (g_J) and de Gennes factor ($dG = (g_J - 1)^2 J(J+1)$). For each atoms, the expected magnetic moment (μ_J) and saturation magnetic moment (μ_{J_z}) are given according to Eq. 2.16. This Table is taken from Ref. [30]

ion	shell	S	L	J	g_J	dG	μ_J (μ_B)	μ_{J_z} (μ_B)
Ce^{3+}	$4f^1$	1/2	3	5/2	6/7	0.18	2.57	2.15
Pr^{3+}	$4f^2$	1	5	4	4/5	0.80	3.58	3.20
Nd^{3+}	$4f^3$	3/2	6	9/2	72/99	1.84	3.62	3.28
Pm^{3+}	$4f^4$	2	6	4	3/5	3.20	2.68	2.4
Sm^{3+}	$4f^5$	5/2	5	5/2	2/7	4.46	0.85	0.72
Eu^{3+}	$4f^6$	3	3	0	-	-	0.0	-
Gd^{3+}	$4f^7$	7/2	0	7/2	2	15.75	7.94	7
Tb^{3+}	$4f^8$	3	3	6	3/2	10.50	9.72	9
Dy^{3+}	$4f^9$	5/2	5	15/2	4/3	7.08	10.63	10
Ho^{3+}	$4f^{10}$	2	6	8	5/4	4.50	10.60	10
Er^{3+}	$4f^{11}$	3/2	6	15/2	6/5	2.55	9.59	9
Tm^{3+}	$4f^{12}$	1	5	6	7/6	1.17	7.57	7
Yb^{3+}	$4f^{13}$	1/2	3	7/2	8/7	0.32	4.53	4

A general feature of spin-orbit coupling is the shift of atomic energy levels or energy bands. In atoms, it is due to the electromagnetic interaction between the electron spin and electric field produced by the nucleus. In a solid, the conduction electrons move in the potential of the crystalline lattice. When the spin of these electron and the lattice potential are coupled, there is an alteration in the motion of electrons and thus a spin-splitting in some energy bands [subsec. 2.3.1].

2.5.2 RKKY interaction

In a metal, coupling between magnetic ions is mediated by conduction electrons. A localized magnetic moment produces an oscillatory magnetization on the electron gas which polarizes their spin. Then, they interact and couple with a neighboring localized magnetic moment at a distance r. This interaction is known as the RKKY Interaction (Rudernam, Kittel, Kasuya and Yoshida) and the coupling takes the form:

$$J_{RKKY}(r) \propto \frac{\cos(2k_F r)}{r^3}.$$

Notice that the polarization of the conduction electrons decreases as the distance from the magnetic ion increases in a damped oscillatory fashion. So, the interaction is long range and its oscillatory dependence determines whether the interaction between magnetic moments is ferromagnetic or antiferromagnetic. On the other hand, the strength of RKKY interaction is represented by *de Gennes factor* defined as $dG = (g_J - 1)^2 J(J+1)$ [31]. For systems in which the R-R interactions are dominant dG values are summarized in Table 2.1.

2.5.3 Magnetic materials

Paramagnetic, antiferromagnetic and ferromagnetic materials contain atoms with unpaired electrons and therefore they exhibit a permanent magnetic moment. In the first one the interaction between neighboring magnetic moment is very weak, so they are considered independent. In absence of external magnetic fields these are randomly oriented leading to null magnetization $\mathbf{M}$ (magnetic moment per unit volume). In the presence of a weak field, they will tend to align in the field direction. In contrast, in the latter two material types the moments act cooperatively. The structure is divided into *magnetic*

domains where in each of them the magnetic moments are aligned parallel with $\mathbf{M}\neq 0$ or antiparallel with $\mathbf{M}=0$ for ferromagnetic and antiferromagntic materials, respectively. In absence of fields each domain is randomly oriented, and in presence of this they are oriented in the field direction, including some moment overcoming the antiferromagnetic interaction. We will come back to this point later. When the field is removed, the domains do not return to their original orientation and the materials exhibit a spontaneous magnetization. The magnetic field necessary to reduce the magnetization to zero is called *coercive field* H_{coe}. This magnetic history can be described in a M vs H plot, where a *hysteresis loop* is drawn as shown in Figure 2.3 (a).

These magnetic solids have well-defined magnetic structures. If this is such that their periodicity is a rational multiple of the crystallographic lattice, both structures are *commensurate*, otherwise they are *incommensurate*. On the other hand, if the size of ordered magnetic moments are equal along the lattice they define an *equal magnetic (EM) moment structure*, while if they change from one site to another they form an *amplitude modulated (AM) structure*. For any case, the Hamiltonian that describes the interaction between magnetic moments on neighboring atoms is given by:

$$H = \sum_{ij} \mathcal{J}_{ij}(g_J - 1)^2 \mathbf{J}_i \cdot \mathbf{J}_j,$$

where $\mathcal{J}_{ij}$ is the *exchange constant* between sites i and j. In the *mean-field theory* this interaction can be reduced to a magnetic moment that is in presence of an effective molecular field produced by the neighboring magnetic ions. This disappears progressively with the thermal fluctuations up to the critical temperature, where a magnetic phase transition occurs. The system changes from the magnetically ordered phase to a paramagnetic (disordered) phase. For antiferromagnetic transitions, this temperature is called the *Néel temperature* T_N, while for ferromagnetic transitions it is known as *Curie temperature* T_C. Above it, the molecular field is completely destroyed and the susceptibility has a *Curie-Weiss*-type behavior [30, 32]:

$$\chi = \frac{M}{H} = \chi_0 + \frac{C}{T-\theta_{cw}} \quad \text{with} \quad C = \frac{\mu_0 N_A \mu_{eff}^2 \mu_B^2}{3k_B}, \tag{2.17}$$

where χ_0 is the *Pauli paramagnetic susceptibility*, C is the *Curie constant*, N_A is the Avogadro number, μ_{eff} is the *effective magnetic moment* and θ_{cw} is the *Curie-Weiss temperature* which is a measure of the interaction of an ion with its surroundings. So, the effective molecular field is directly related to the size of the exchange interaction between magnetic ions. If this is via the RKKY mechanism T_N and θ_{cw} can be written as [33, 34]:

$$T_N, \theta_{cw} \propto \mathcal{J}^2 D(E_F)(g_J - 1)^2 J(J+1). \tag{2.18}$$

Notice that as the de Gennes factor is largest for Gd, Table 2.1, it is expected that in a rare-earth series the Gd-based compound displays the highest ordering temperature. Also, the sign of the exchange constant determines the type of magnetic material. $\mathcal{J}_{ij}$, $\theta_{cw} = 0$ for non-interacting magnetic systems as the paramagnet, $\mathcal{J}_{ij}$, $\theta_{cw} > 0$ for ferromagnetics and $\mathcal{J}_{ij}$, $\theta_{cw} < 0$ for antiferromagnetics. For the latter it is expected that $|\theta_{cw}|/T_N = 1$, however this does not occur in many compounds because the effective molecular field generated by the nearest neighbor moments is not sufficient to describe the magnetic behavior of the system and it is necessary to consider the next-nearest neighbor interactions. These behaviors are shown in Figure 2.2(a) and (b) for χ vs T and $1/\chi$ vs T, respectively. On the other hand, in diluted systems these temperatures are proportional to the magnetic moment concentration.

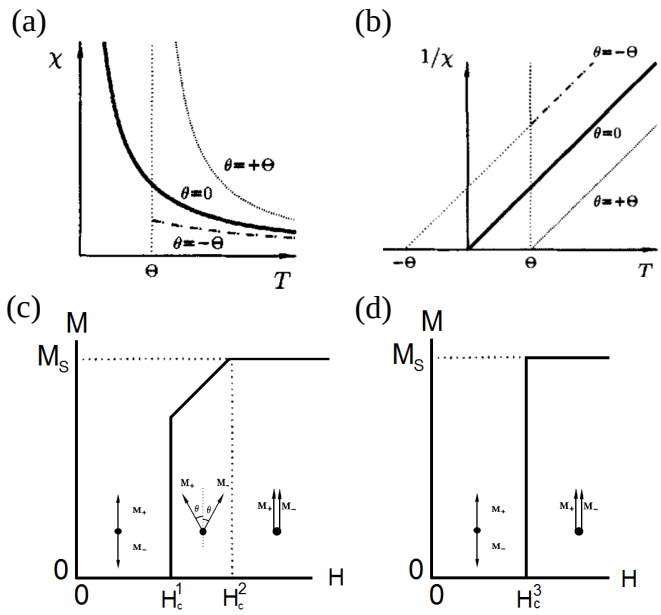

Figure 2.2: Temperature dependent (a) susceptibility and (b) inverse susceptibility of Curie-Weiss law [Eq. 2.17] for paramagnets $\theta_{cw} = 0$, ferromagnetics $\theta_{cw} = \Theta > 0$ and antiferromagnetics $\theta_{cw} = -\Theta < 0$. Magnetization as a function of magnetic field for (c) spin-flop and (d) spin-flip transition.

Temperature independent Pauli paramagnetic susceptibility occurs in metals due to the response of conduction electrons to the external magnetic field. In absence of this, each state is doubly occupied by spin-up and spin-down electrons and the density of state curve is the same for both polarizations. In

presence of an applied field, the energy of electrons with spin antiparallel to field is raised, while the parallel is reduced. In order to minimize the total energy of the system ($E = -\sum_i \mu_B \mathbf{s}_i \cdot \mathbf{H}$) the electrons with spin antiparallel that are close to the Fermi level reverses to parallel spin. As a consequence the density of states shows a field-proportional splitting [30, 32].

Experimentally, the effective magnetic moment is obtained from χ vs T (χ is in emu/mol) to fit Eq. 2.17, subtracting χ_0 and fitting $(\chi - \chi_0)^{-1} = aT + b$ where $a = \frac{1}{C}$ and $b = -\frac{\theta_{cw}}{C}$. Thus,

$$\mu_{eff} = \sqrt{8C} = 2.827\sqrt{\chi T}. \tag{2.19}$$

For dilute systems, it is common to determine the magnetic moment from the ratio of Curie constants respect to the pure compound. For this, it is important to plot $(\chi - \chi_0) * (T - \theta_{cw})$ vs T and check the constant C behavior at high temperatures.

While rising temperature tends to disorder the magnetic moments, increasing the field aims to align them. In antiferromagnets these can be forced towards the ferromagnetic configuration by the presence of a high intensity field. However, how this occurs depends greatly on the applied field direction with respect to the initial moment orientations. Antiferromagnetic materials can be considered as two equivalent interpenetrating sublattices, one with the moments pointing upwards and another with them pointing downwards. If the applied field is perpendicular to the sublattice, as the field rises the component of these on the field increase and therefore so does the magnetization until they become completely aligned and the system reaches *magnetic saturation*. On the other hand, when a weak magnetic field is applied parallel to sublattice [Fig. 2.2 (c) and (d)] they remain in their original positions until a *critical field* H_c^1, where the antiparallel moments rotate to the field direction so there are two equivalent magnetic moment components. As in the previous case, the induced ferromagnetic state is gradually reached by increasing the field strength to H_c^2. This process is called *spin-flop transition*. On the other hand, if the anisotropic effect is very strong to increase the field to H_c^3 the magnetization of one sublattice is suddenly reversed, and therefore the systems moves immediately in a single step to the ferromagnetic state indicating a *spin-flip transition*. The critical field can be determined as the position of the peaks in dM/dH. Finally, the evolution of magnetic transitions with respect to magnetic field and temperature allows the construction of magnetic phase diagrams H vs T, which give a schematic representation of phases adopted by a material and the conditions at which its phase transitions occur.

2.5.4 Crystalline electric field (CEF)

In a crystal the ions experience an electrostatic interaction called *crystal electric field* (CEF), due to neighboring ions and outer valence electrons. As this depends on the symmetry of the local environment, in some cases overlapping orbitals can occur, which raises the orbital energy.

$3d$ transition metals have their orbitals far away from the nucleus, so the crystal electric field interaction is much stronger than the spin-orbit interaction. As a consequence they present a ground state such that $L = 0$ called *orbital quenching* and therefore a total magnetic moment $\mu_{eff} = 2\sqrt{S(S+1)}\mu_B$ [Eq. 2.16]. For example, Ni^{2+} is a $3d^8$ shell, with $S = 1$ and $\mu_{eff} = 2.83\ \mu_B$. In contrast, in rare earths such effect is much smaller than the spin-orbit coupling. However, due to lanthanide contraction the crystalline lattice is weakly contracted which can generate a virtual indirect overlap between orbitals of different ions [35] making the CEF important for them.

2.5.5 Anisotropy

In solids, the spatial arrangement of electron orbitals is strongly related to the crystallographic structure. The spin-orbit coupling interaction forces the magnetic moment to align along well-defined crystallographic axis, giving rise to *magnetocrystalline anisotropy*. As a consequence they show a magnetic response that depends on the direction in which it is measured allowing to differentiate between *easy magnetic axis* where the crystal is rapidly magnetized in presence of a weak magnetic field and *hard axis* where they need more energy to magnetize.

In materials with low symmetry and high magnetocrystalline anisotropy it is common to perform magnetic susceptibility measurements in several directions and then consider the physical behavior from the estimated *polycrystalline average curve*. Without loss of generality, if measured along a, b and c crystallographic directions the average curve is computed as the arithmetic mean of these at each temperature:

$$\chi_{avg} = \frac{\chi_a + \chi_b + \chi_c}{3}. \tag{2.20}$$

On the other hand, ferromagnetic/antiferromagnetic multilayer systems present unidirectional anisotropy called *exchange anisotropy* that has its origin in the magnetic coupling interaction between their interfaces. This can be understood by considering that T_C for ferromagnetics is higher than T_N for antiferromagnetics. So, upon cooling this system in presence of an external magnetic field such that $T_C > T > T_N$, M vs H curve exhibit a symmetric hysteresis loop as shown in Figure 2.3(a). However, as the temperature is reduced to $T_N > T$, the antiferromagnetic material causes a shift of the loop by a *exchange bias field* H_{EB}, Figure 2.3(b). This occurs because it is energetically more favorable for the ferromagnetic material to be magnetized in the direction in which it was cooled [30].

This system shows a magnetic history dependent on the field cooling process. At high temperature thermal fluctuations dominate and the moments are randomly oriented. Upon cooling the material in absence of field called *zero-field cooling* (ZFC) processes, the moments are immobilized with this randomness. So, the application of an external field will evidence the anisotropy present in the compound. On the contrary, when cooling the material in presence of a magnetic field called *field cooling* (FC) processes, the moments freeze in the orientation defined by the field direction, altering the anisotropy of compound. The difference between these allow us to define the conditions for exchange bias as:

- Shift of the hysteresis loop along the magnetic field axis by magnetic field cooling.
- An enhancement of the coercive field in FC-hysteresis compared to the ZFC case. Coercive field is calculated as $H_{coe} = (H_+ - H_-)/2$, while exchange bias field as $H_{EB} = (H_+ + H_-)/2$ where $H\pm$ are the positive and negative intercepts of the magnetization curve with the field axis. Additionally, we will consider the vertical displacement of hysteresis loop as $M_{EB} = (M_+ + M_-)/2$ where $M\pm$ are the positive and negative intercepts of the magnetization curve with the magnetization axis.

2.6 Thermal properties: specific heat

The specific heat is a thermal property of solids that gives the quantity of heat required to raise a unit mass of the system by one degree in temperature. In this section we will study how this is influenced by electronic, magnetic and vibrational properties.

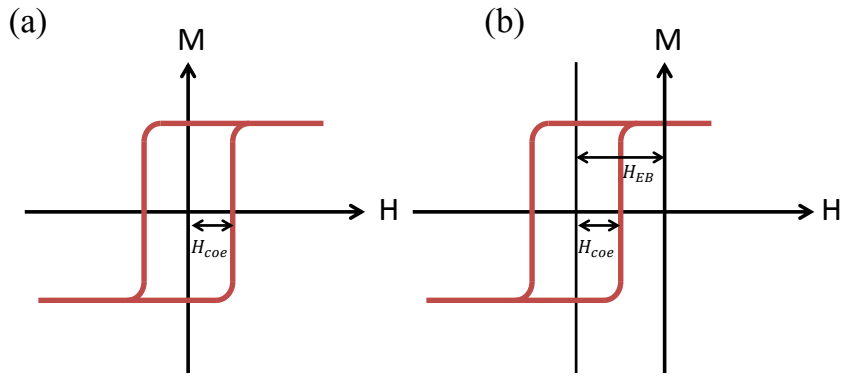

Figure 2.3: Hysteresis loop (a) centered at zero magnetic field and (b) shifted by exchange bias field H_{EB} due to exchange anisotropy.

2.6.1 Phononic contribution

In a solid, each lattice vibration mode ω is associated with a harmonic oscillator, called *phonon*, with energy $\varepsilon = \left(n + \frac{1}{2}\right)\hbar\omega$ where n is a quantum number. Considering a phonon gas in thermal equilibrium, the number of phonons which are in the quantum state n is determined by the Planck distribution $\langle n(\omega)\rangle = \{exp(\hbar\omega/k_BT) - 1\}^{-1}$. The energy of a collection of oscillators is

$$U = \int F(\omega)\,\langle n(\omega)\rangle\; d\omega, \tag{2.21}$$

where $F(\omega)$ is the phononic density of states [subsec. 2.4.2]. In three dimensions it is given by

$$F(\omega) = \frac{dN^{'}}{d\omega} = \frac{d[(L/2\pi)^3(4\pi k^3/3)]}{d\omega} = \left(\frac{VK^2}{2\pi}\right)\left(\frac{dk}{d\omega}\right) = \frac{3V\omega^2}{2\pi^2 v^3}, \tag{2.22}$$

where $N^{'}$ is the number of modes with wavevector less than k. So, substituting Eq. 2.22 into Eq. 2.21 and deriving with respect to temperature, we find the heat capacity of lattice at constant volume

$$C_{latt} = 9NK_B\left(\frac{T}{\Theta_D}\right)^3 \int_0^{x_D} \frac{x^4 e^x}{(e^x - 1)^2} dx, \tag{2.23}$$

where $x = \frac{\hbar\omega}{k_B T}$ and therefore $x_D = \frac{\hbar\omega_D}{k_B T} = \frac{\Theta_D}{T}$ with

$$\omega_D = \left(\frac{6\pi^2 v^3 N}{V}\right)^{1/3} \quad \text{and} \quad \Theta_D = \frac{\hbar v}{k_B}\left(\frac{6\pi^2 N}{V}\right)^{1/3}. \tag{2.24}$$

Here, ω_D is known as the *Debye frequency* and it determines the maximum frequency allowed for phonons, which occurs at the *Debye temperature* Θ_D. At $T >> \Theta_D$ the specific heat approaches the classical value of $3Nk_B$. At low temperature $T << \Theta_D$

$$C_{latt} = \beta T^3 \quad \text{where} \quad \beta = \frac{12\pi^4}{5} N K_B \left(\frac{T}{\Theta_D}\right)^3 \text{ J/mol K}^4. \tag{2.25}$$

This behavior occurs only when long-wavelength acoustic modes are thermally excited. For bulk it is reasonable to consider temperatures below $T = \frac{\Theta_D}{50}$.

2.6.2 Electronic contribution

At low temperatures, lattices vibrations are small and the phononic contributions to the specific heat are neglected with respect to electronic contributions. The latter can be determined by considering an ideal electrons gas. The probability that an orbital at energy ε becoming occupied is defined by the Fermi-Dirac distribution $f(\varepsilon) = \{exp[(\varepsilon - \mu)/k_B T] + 1\}^{-1}$ where μ is the chemical potential of the system. At absolute zero temperature, μ is equal to Fermi energy, however for $T \neq 0$, it is temperature dependent $\mu(T) = E_F[1 - (\pi^2/12)(k_B T/E_F)^2 + (\pi^4/80)(k_B T/E_F)^4 + ...]$. For temperatures below the Debye temperature and Fermi temperature ($T_F = E_F/k_B$), the internal energy increase for system of N electrons when it is heated from 0 to T

$$\Delta U = U(T) - U(0) = \int_0^\infty \varepsilon D(\varepsilon) f(\varepsilon) d\varepsilon - \int_0^{E_F} \varepsilon D(\varepsilon) d\varepsilon, \tag{2.26}$$

where electronic density of states is given by

$$D(\varepsilon) = \frac{dN'}{d\varepsilon} = \frac{d[2(L/2\pi)^3(4\pi k^3/3)]}{d\varepsilon} = \frac{V}{2\pi^2}\left(\frac{2m}{\hbar^2}\right)^{3/2} \varepsilon^{1/2}, \tag{2.27}$$

for a spherical Fermi surface $\varepsilon = \hbar^2 k^2/2m$ in the three dimensional **k**-space. Substituting Eq. 2.27 into Eq. 2.26 and differentiating with respect to tempera-

ture, we find the heat capacity of an electron gas is

$$C_{elec} = k_B^2 T D(E_F) \int_{-E_F/k_B T}^{\infty} x^2 \frac{e^x}{(e^x+1)^2} = \gamma T \quad \text{where} \quad \gamma = \frac{1}{3}\pi^2 k_B^2 D(E_F), \tag{2.28}$$

is called *the Sommerfeld coefficient*. This is an experimental measure of the effective mass (m^*) of the electrons inside the metal, previously calculated by the curvature of the band in subsection 2.3.1. So, they are related by

$$m^* = \frac{\hbar^2 k_F^2 \gamma}{\pi^2 n k_B^2}, \tag{2.29}$$

where $k_F = (3n\pi^2)^{1/3}$ for spherical surface and n the electronic density. Neglecting the electron-electron interaction, the difference between effective mass and electron mass must occur by electron-phonon interaction. If this is represented in terms of the coupling constant λ_{e-ph}, the enhancement in the experimentally observed value γ_{exp} respect to calculated for free electrons γ_{bare} can be expressed as

$$\frac{\gamma_{exp}}{\gamma_{bare}} = (1 + \lambda_{e-ph}). \tag{2.30}$$

On the other hand, according to Eq. 2.25 and 2.28 the electronic and phononic contribution to specific heat is given by

$$C_{elec-phon} = C_{elec} + C_{latt} = \gamma T + \beta T^3. \tag{2.31}$$

So, the linear extrapolation on $C_p/T \times T^2$ curve lead to γ as intercept and β the slope of this curve.

2.6.3 Magnetic contribution

In antiferromagnetic systems, both temperature-dependent magnetic specific heat and lattice specific heat are proportional to T^3. Therefore, it is impossible to separate these contributions. However, a reasonable estimate can be determined by subtracting the specific heat of a non-magnetic isomorphous compound that has similar electronic and phononic contribution $C_{elec-phon}$

$$C_m = C_p - C_{elec-phon} \approx C_p - C_{nm}. \tag{2.32}$$

For $RNiSi_3$ series, the nonmagnetic compounds are $YNiSi_3$ and $LuNiSi_3$. Therefore, the magnetic contribution can be determined according to the Debye

expansion [36, 37]:

$$C_{nm}^{R} = C_{p}^{Lu}(T) - [C_{p}^{Lu}(T) - C_{p}^{Y}(T)] \left[\frac{M_{Lu}^{3/2} - M_{R}^{3/2}}{M_{Lu}^{3/2} - M_{Y}^{3/2}} \right], \tag{2.33}$$

where $C_{nm}^{R}(T)$ is the non-magnetic specific heat of $RNiSi_3$, $C_{p}^{Lu}(T)$ and $C_{p}^{Y}(T)$ are the specific heats of $YNiSi_3$ and $LuNiSi_3$, respectively, and M_X is the molar mass of each atom. However, for compounds doped with non-magnetic ions such as $Gd_{1-x}Y_xNiSi_3$ it is common to consider the electron-phonon contribution only from $YNiSi_3$ and make a renormalization in the temperature values on C versus T curve to accounts for the amount of doping and the difference in molar masses between Gd and Y. This is calculated according to the expression [37]

$$\rho_{norm} = \left[\frac{M_{Y}^{3/2} + M_{Ni}^{3/2} + 3M_{Si}^{3/2}}{(1-x)M_{Gd}^{3/2} + xM_{Y}^{3/2} + M_{Ni}^{3/2} + 3M_{Si}^{3/2}} \right]^{1/3}, \tag{2.34}$$

where M_Z is the atomic mass of Z=Gd, Y, Ni and Si, and relates the Debye temperature through

$$\Theta_D(Gd_{1-x}Y_xNiSi_3) = \rho_{norm}\Theta_D(YNiSi_3). \tag{2.35}$$

Mean-field theory predicts that the magnetic specific heat rises monotonically up to a maximum value at T_N and then it drops to zero suddenly and discontinuously. Furthermore, it is related to the total angular moment by [38]:

$$\Delta C_{m}^{MF}(T_N) = 5R\frac{J(J+1)}{[(J+1)^2 + J^2]}, \tag{2.36}$$

whose values for rare earth ions are indicated in Table 2.2. However, real systems do not exhibit this discontinuity and at $T > T_N$ display a tail indicating short-range magnetic order.

On the other hand, the numerical integration of C_m/T curve determines the molar magnetic entropy S_m of the system, which relates the changes in the ordered magnetic state and reflects the disorder of the magnetic moments. It increases with rising temperature and reaches a maximum value at S_m^{max}. For systems whose magnetism comes only from the $4f$ ions, Table 2.2 the maximum magnetic entropy without taking into account the splitting of energy levels due to CEF effects is given by:

$$S_{m}^{max} = R\ln(2J+1), \tag{2.37}$$

at high temperatures when all $2J+1$ levels are populated and R is the gas constant (R=8.314 Jmol^{-1}).

Table 2.2: Theoretical variation of specific heat ΔC_m^{MF} and maximum entropy S_m^{max} expected from Eq. 2.36 and 2.37, respectively, for rare earth ions.

	Gd	Tb	Dy	Ho	Er	Tm	Yb
ΔC_m^{MF}	20.15	20.54	20.62	20.64	20.62	20.54	20.15
S_m^{max}	17.3	21.3	23.1	23.6	23.1	21.3	17.3

2.6.4 Other contributions

An ion with magnetic moment **J** has $(2J+1)$-fold degenerate discrete energy level to be populated by electrons. In a solid, the crystalline field lifts this degeneracy from the ground state [subsec. 2.5.4]. When the temperature is comparable to the splitting between levels Δ, there is a transition probability between them and as a consequence the specific heat shows an anomaly in the form of a broad peak, known as *the Schottky effect*. In contrast, this effect is not observed at either low and high temperature because the transitions are negligible. In the first region $C_{sch} \propto e^{(-\Delta/T)}$ so there is not enough energy to excite the transitions from the ground state, while in the second $C_{sch} \propto T^{-2}$ and therefore all states are equally occupied [30, 38].

In the lanthanide series, the $4f$ electrons orbital motion produces a very large effective field that interacts with the nuclear magnetic moment of the nucleus **I** which removes the $(2I+1)$-fold degenerate levels. This effect is commonly called *the nuclear Schottky effect* and originates from the Zeeman interaction with the effective magnetic field [38].

2.7 Elastic properties

Elastic solids have the property of returning to their original shape and size after the forces that cause small deformations on them have been removed. Thus, they satisfy Hooke's law where the force applied on solids (called *the stress* and denoted by X) is proportional to deformation of this (known as *the strain* and labeled as x) $x = SX$ or $X = Cx$, where S is the elastic compliance coefficient and C is the stiffness coefficient such that $C = S^{-1}$. Work-energy theorem permits to write the stored mechanical energy density as $dW =$

$X_i dx_i = C_{ij} x_j dx_i$ for i and j direction of X and x, and $C_{ij} = \partial^2 W / \partial x_i \partial x_j$. For orthorhombic structure C matrix can be written as [39, 40]

$$\begin{bmatrix} C_{11} & C_{12} & C_{13} & 0 & 0 & 0 \\ C_{12} & C_{22} & C_{23} & 0 & 0 & 0 \\ C_{13} & C_{23} & C_{33} & 0 & 0 & 0 \\ 0 & 0 & 0 & C_{44} & 0 & 0 \\ 0 & 0 & 0 & 0 & C_{55} & 0 \\ 0 & 0 & 0 & 0 & 0 & C_{66} \end{bmatrix} \tag{2.38}$$

whose structure is mechanically stable under the following conditions

$$C_{11} > 0, C_{22} > 0, C_{33} > 0, C_{44} > 0, C_{55} > 0, C_{66} > 0,$$

$$C_{11} + C_{22} + C_{33} + 2(C_{12} + C_{13} + C_{23}) > 0,$$

$$C_{11} + C_{22} - 2C_{12} > 0, C_{11} + C_{33} - 2C_{13} > 0, C_{22} + C_{33} - 2C_{23} > 0.$$

From the calculated elastic constants the bulk modulus (B) and shear modulus (G) can be deduced according to Voigt [41] (labed as $_V$) and Reuss and Angew [42] (label as $_R$):

$$\begin{gathered} 9B_V = (C_{11} + C_{22} + C_{33}) + 2(C_{12} + C_{23} + C_{13}), \\ \tfrac{1}{B_R} = (S_{11} + S_{12} + S_{33}) + 2(S_{12} + S_{23} + S_{13}), \\ 15G_V = (C_{11} + C_{22} + C_{33}) - (C_{12} + C_{23} + C_{13}) + 3(C_{44} + C_{55} + C_{66}), \\ \tfrac{15}{G_R} = 4(S_{11} + S_{22} + S_{33}) - 4(S_{12} + S_{23} + S_{13}) + 3(S_{44} + S_{55} + S_{66}). \end{gathered} \tag{2.39}$$

where S_{ij} are defined by

$$S_{11} = (C_{22}C_{33}4 - C_{23}^2)/\Delta, S_{22} = (C_{11}C_{33} - C_{13}^2)/\Delta, S_{ii} = \tfrac{1}{C_{ii}} (i = 4, 5, 6),$$

$$S_{33} = (C_{11}C_{22} - C_{12}^2)/\Delta, S_{12} = (C_{13}C_{23} - C_{12}C_{23})/\Delta,$$

$$S_{13} = (C_{12}C_{23} - C_{13}C_{22})/\Delta, S_{23} = (C_{12}C_{13} - C_{11}C_{23})/\Delta,$$

with

$$\Delta = C_{13}(C_{12}C_{23} - C_{13}C_{22}) + C_{23}(C_{12}C_{13} - C_{23}C_{11}) + C_{33}(C_{11}C_{22} - C_{12}^2).$$

Thus, the bulk modulus (B) and shear modulus (G) are determined using the arithmetic average of Voigt and Reuss approximations:

$$B = \frac{B_V + B_R}{2} \quad \text{and} \quad G = \frac{G_V + G_R}{2} \tag{2.40}$$

which determine the longitudinal (v_l), transversal (v_s) and average (v_m) sound velocity

$$v_l = [(B + 4/3G)/\rho]^{1/2}, \quad v_s = (G/\rho)^{1/2}, \quad 3/v_m^3 = 1/v_l^3 + 2/v_s^3. \tag{2.41}$$

At low temperature Debye temperature Θ_D is proportional to the sound velocity through

$$\Theta_D = \frac{\hbar}{k_B} \sqrt[3]{\frac{3nN_A\rho}{4\pi M}} v_m, \tag{2.42}$$

where $\hbar$ is Planck's constant, k_B is Boltzmann's constant, n is the number of atoms per formula unit, M is the molecular weight, N_A is Avogadro's number and ρ is the density of compound. Thus, Θ_D can be determined from specific heat measurements according to Eq. 2.25 or from elastic constant through bulk and shear modulus with Eq. 2.42.

2.8 Electrical properties: resistivity

2.8.1 Resistivity in metals

Electrical resistance (R) is a measure how strongly the material resists electric current under the influence of a voltage. This is associated with an intrinsic property of solids called *resistivity*

$$\rho = \frac{RA}{L}, \tag{2.43}$$

which depends only on the dimension of the element, A is the area and L is the length, through which the current flows. Both depend on the electronic scattering processes that occur in the material due to impurities and lattice imperfections, lattice vibrations, localized magnetic moment and other electrons. Near to T=0 the scattering processes are due to impurity atoms and lattice imperfections, thus generating a *residual resistivity* (ρ^0) that is approximately

independent of temperature. The residual resistivity ratio (RRR) defined as

$$RRR = \frac{\rho(300K)}{\rho(2K)}. \tag{2.44}$$

can be used to characterize the purity and overall quality of the sample. By increasing the temperature many different behaviors can be observed. In the low temperature region, the electron-electron scattering is dominant and the Fermi liquid theory predicts that $\rho(T) \sim T^2$ [43]. Next, together with these the scattering of electrons by acoustic phonons begins and as consequence $\rho(T) \sim T^5$. At high temperatures ($T > \Theta_D$), the latter is dominant and a T-linear behavior is observed

$$\rho_{ph}(T) \sim \rho(300K) \left[\frac{T}{300}\right]. \tag{2.45}$$

On the other hand, free electron model predicts that the mean free path of electrons between successive collisions is given by

$$l = \frac{\hbar k_F}{ne^2\rho_0}. \tag{2.46}$$

However, in presence of an external magnetic field it can change altering the resistivity of the material. This phenomenon is called *magnetoresistance* and it is expressed as

$$\frac{\Delta\rho}{\rho} = \frac{R(H) - R(0)}{R(0)}.$$

If the magnetoresistance is positive, the field forces the electrons to take a path that leads to more scattering causing the resistivity to increase with the field. In contrast, negative magnetoresistance occurs because the application of a small magnetic field decreases the resistance due to the reduction in the number of electrons scattering. In these cases the electrons behave as if they were weakly localized.

2.8.2 Magnetic contribution

In general, magnetic materials exhibit an anomaly in the resistivity curve at T_N. This may be in the form of a sharp peak or only show a change in slope which generates a peak in the differential resistivity $d\rho/dT$. However, in many cases this transition is very smooth, so it is much easier to fit a function composed

of two contiguous segments to the points near the transition:

$$\rho(T) = \begin{cases} a + bT, & \text{for } T \leq T_N \\ a + bT + c(T - T_N), & \text{for } T > T_N \end{cases} \tag{2.47}$$

where a, b, c and T_N are free parameters. In the paramagnetic region the resistivity has a behavior described by Eq. 2.45, while at $T < T_N$ the localized moments condense into an antiferromagnetic ordered array, so that the elastic scattering of itinerant spins by located magnetic moments is determined by

$$\rho(T) = \rho^0 + AT^n \tag{2.48}$$

for $n = 2$ where A is a temperature-independent coefficient related with the effective mass of the compound through the universal relation $A/\gamma^2 \sim 1.0 \times 10^{-5}$ $\mu\Omega$cm(molK/mJ)^2 for heavy-fermion compounds [44].

On the other hand, in some materials the electronic scattering process is inelastic, i.e. the electron spin state changes by so-called *spin-flip scattering*. Furthermore, if these hybridize with the magnetic moment so that the electrons form a cloud of opposite spin-polarization (exchange constant $\mathcal{I}$<0) that screening the moment of magnetic ions, the phenomenon known as the *Kondo effect* occurs. The temperature at which it begins to be observed is the *Kondo temperature* defined as

$$T_K \propto e^{\left(-\frac{1}{\mathcal{J}}\right)}. \tag{2.49}$$

Above T_K, the resistivity exhibits a logarithmic dependence of form

$$\rho = a - b\log(T) \tag{2.50}$$

with $b = |\mathcal{I}|$, and goes through a minimum at T_{min} that is proportional to $x^{1/5}$, where $x = \rho(T = 0) - \rho_{min}$. Conversely, at $T < T_K$ the resistivity is enhanced reaching a maximum at a certain temperature before rapidly decreasing with cooling. This characteristic temperature is commonly referred as *coherence temperature* T_{coh} which determines the strength of the interaction between localized and conduction electrons, and therefore it is proportional to T_K. For $T > T_{coh}$ this is weak due to the electrons interact with a paramagnetic system, however at $T < T_{coh}$ this becomes strong so they begin to be entwined in a heavy-fermion fluid showing Landau–Fermi liquid behavior ($\rho(T) \sim T^2$).

2.8.3 Superconductivity

The following description is based on the microscopic theory of superconductivity proposed by Bardeen, Cooper and Schrieffer in 1957, called *BCS theory* [45].

Superconductivity is a phase-transition phenomenon from a normal electrical resistivity state to a superconducting state, which occurs at the *critical temperature* T_c. Below this, an electron induces a crystalline lattice-mediated attraction. If it exceeds the Coulomb repulsion between electrons, the lattice allows a net attraction on another electron with momentum and spin opposite to the initial one. It is as if an electron emits a phonon which is immediately absorbed by another electron. As a consequence, a weak effective attractive interaction is formed between two electrons and they become so-called *Cooper pairs* or *superelectrons*, which move through the conductor in an infinite mean free path without resistance. However, near T_c the material is in an intermediate state formed by two interpenetrating electronic fluids: normal electrons and Cooper pairs. Thus, the density of the latter gradually goes from zero in the normal region to n_s value in the superconducting region, over a distance called *BCS coherence length* ξ [46]. For a perfectly pure superconductor, it is determined by

$$\xi_0 = \frac{018\hbar^2 k_F}{k_B T_c m^*}. \tag{2.51}$$

In a superconductor with impurities whose mean free path is given by Eq. 2.46, the coherence length is reduced to $(\xi_0 l)^{1/2}$.

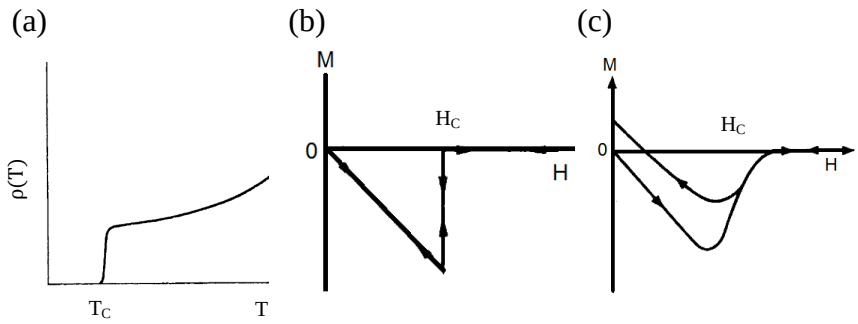

Figure 2.4: (a) Temperature dependent resistivity showing the superconductor region below T_c. Magnetic behavior of (b) ideal and (c) non-ideal type I superconductor, taken from Ref. [46].

Macroscopically, a superconductor exhibits a combined effect below T_c: (i) electrical resistivity suddenly drops to zero and (ii) perfect diamagnetism begins to emerge due to *Meissner effect*. In the latter case, Cooper pairs flowing in the material give rise to supercurrents that shield the superconductor. In presence of an external magnetic field, it induces another magnetic field that is exactly equal and opposite to the original one, canceling the field inside the conductor. The presence of supercurrents and induced fields are not generated over the entire conductor but are superficial. London determined that this field falls exponentially as the inverse of the electron charge e inside the superconductor covering a distance called *London penetration depth* λ_L which can be estimated by

$$\lambda_L = \left(\frac{m^*}{\mu_0 n_s e^2} \right)^{1/2}. \tag{2.52}$$

The ratio of the penetration depth λ and the coherence length ξ determines the *Ginzburg-Landau parameter* given by:

$$\kappa = \frac{\lambda_{GL}}{\xi_{GL}} = \frac{\lambda_L(1 + 0.75\xi_0/l)^{1/2}/\sqrt{2}}{0.74\xi_0(1 + 0.75\xi_0/l)^{-1/2}}, \tag{2.53}$$

which determines the type of superconductivity. If $\kappa < 1/\sqrt{2}$ the superconductor is of type I otherwise it is of type II. We are interested only in "ideal" type I superconductors, whose M vs H curves are completely reversible exhibiting a typical diamagnetic behavior. Here, the magnetic susceptibility χ is negative and the magnetic field induces a magnetic moment opposite to the applied magnetic field that caused it. Thus, an increasing applied magnetic field causes a linear decrease in the magnetization. This effect is observed up to the *critical magnetic field* H_c, where the superconductivity is destroyed and the magnetization suddenly drops to zero. In real type I superconductors, where the impurities or crystalline defects are present, the magnetic flux can be trapped inside them causing that when increasing the magnetic field, the magnetization follows a different path to that of the decreasing magnetic field generating a magnetic hysteresis. In this case, the superconductor is like a permanent magnet. Comparatively, in a type II superconductor the magnetization does not suddenly drop to zero as in the previous case, instead it changes gradually as the magnetic field increases. It does so up to *the second critical field* $H_c^{'}$ where the compound reaches the normal state. In the region between H_c and $H_c^{'}$ the material is in a mixed phase, i.e, the Meissner effect is only partially satisfied due to some magnetic flux lines penetrating its superconducting state [46].

On the other hand, experimentally it has been observed that the *phase diagram* H vs T, H_c associated with a type I superconductor exhibits a parabolic-like

behavior with temperature:

$$H_c(T) = H_c(0)\left[1 - \left(\frac{T}{T_c}\right)^2\right], \tag{2.54}$$

where $H_c(0)$ is the critical field at absolute zero, and H_c=0 at T_c. Notice that the superconductivity in the material depends only on the values of H and T, so the transition phase is a reversible thermodynamic process in these variables. The application of a magnetic field on the conductor in the normal state does not change the free energy, while it rises in the superconductor state due to magnetization created by the Meissner effect. This magnetic contribution is associated with the maximum magnetic field strength that can be applied on the superconductor (H_c) in the following form

$$\Delta F(T) = F_n(T) - F_s(T) = \Delta U - T\Delta S = \frac{\mu_0 V H_c^2}{2}, \tag{2.55}$$

such that

$$\Delta U = \int_T^{T_c}[C_s(T') - C_n(T')]dT' \quad \text{and} \quad \Delta S(T) = \int_T^{T_c}\frac{C_s(T')-C_n(T')}{T'}dT', \tag{2.56}$$

where F is the free energy and V is the volume of a formula unit. The n and s subscripts denote the normal and superconducting state, respectively.

Electronic specific heat is other macroscopic quantity in which the phenomenon of superconductivity is reflected. As mentioned above, at T=0 we have the maximum density of Cooper pairs, however as the temperature increases the Cooper pairs are broken. The energy required to initiate this process is called *energy gap* Δ, which is temperature dependent. Since the superconducting gap structure determines the pairing mechanism, the number of broken pairs at a temperature T is proportional to $\exp(-\Delta_0/k_BT)$ where Δ_0 denotes the energy gap at T=0. In order to correctly describe the electronic specific heat when the material is in superconductor state, several models are considered:

- For isotropic superconductor with a single gap Δ_0^{SG} is called *s-wave model*

$$C_{el}^{SG} = A_1\gamma_N T_c \exp(-\Delta_0^{SG}/k_BT). \tag{2.57}$$

  In this model the energy gap Δ_0^{SG} is isotropic, i.e, it is constant over the entire Fermi surface [47] and the term Δ_0/k_BT is an empirical measure of the coupling strength. In the weak-coupling regime, the BCS theory predicts a gap $\Delta_0^{SG} = 1.764k_BT_c$ and a specific heat jump at T_c of $\frac{\Delta C}{C_{elec}} = 1.43$ where $\Delta C = C_{el}^{SG} - C_{elec}$ with C_{elec} in the normal state given by Eq. 2.28.

- For superconductor with two isotropic gaps Δ_0^{DG1} and Δ_0^{DG2} called *double gap α model*

$$C_{el}^{DG} = A_2\gamma_N T_c(f\exp(-\Delta_0^{DG1}/k_BT) + (1-f)\exp(-\Delta_0^{DG2}/k_BT)), \tag{2.58}$$

  where $f = (1 + exp(\beta E))^{-1}$ is the superconducting fraction in each gap. They are a temperature-dependent s-wave superconducting gap. These can exist in different parts of the Fermi surface and arise due to a strong anisotropic electron-phonon interaction, such that electron coupling is stronger in certain sheets of the Fermi surface and weaker in others, as is the case of $MgBr_2$ [48].

- Single gap with a fraction in the normal state due to impurities or other inhomogeneities is called *α model with a nonsuperconducting contribution fraction*

$$C_{el}^{SGNF} = A_3\gamma_N T_c\exp(-\Delta_0^{SGNF}/k_BT) + \gamma_2 T. \tag{2.59}$$

  In this case, non-magnetic impurities do not significantly affect the superconductor. These are treated as a static external perturbation that does not produce a change in the thermodynamic properties of the superconductor. However, they generate a weakening effect on the pairs [47].

- For superconductors that exhibit strong anisotropy in its magnetic and electric properties, it is expected that the superconductor gap will be anisotropic. In this case, C_{el} is given by:

$$C_{el}^{ANI} = A_4\frac{N(E_F)}{\pi T}\int_0^{2\pi}d\phi\int_0^{\pi}d\theta\sin\theta\int_0^{\hbar\omega_D} -\frac{\partial f}{\partial E}\left(E^2 + \frac{1}{2}\beta\frac{d\Delta^2(T,\theta)}{d\beta}\right)dE, \tag{2.60}$$

  where $\Delta(T,\theta) = \Delta_0(T)(1 + \alpha'\cos 2\theta)$, α' is the anisotropy parameter, $\Delta_0(T) = \Delta_0^{ANI}\tanh[(\pi k_BT_c/\Delta_0^{ANI})\sqrt{a(T_c/T-1)}$, a is a constant that depends on the coupling strength and the geometry of the gap, $\hbar$ is the reduced Planck constant, $\beta = 1/k_BT$ and A_i's are scale factors.

On the other hand, since superconductivity does not generate changes in the lattice structure, lattice-dependent properties such as the Debye temperature and lattice contribution to the specific heat remain as in the normal state according to Eq. 2.23 and 2.24. Lattice specific heat is directly related to the electron-phonon coupling interaction. According to Junod in Ref [49, 50] $5/4R\pi^4C_{latt}T^{-3}$ take the form of convolution of the spectrum function $\omega^{-2}F(\omega)$ for $\omega = 4.928$T, which can be used as a crude alternative to the Eliashberg electron-phonon spectral function $\alpha^2F(\omega)$ associated with the *electron-phonon coupling constant*:

$$\lambda_{e-phon} = 2\int_0^{\omega}\frac{\alpha^2F(\omega)}{\omega}d\omega, \tag{2.61}$$

which determine the average strength of the electron-phonon coupling interaction. From experimental measurements it takes the form of [51]

$$\lambda_{e-ph} = \frac{1.04 + \mu^* ln(\Theta_D/1.45T_c)}{(1 - 0.62\mu^*)ln(\Theta_D/1.45T_c) - 1.04}, \tag{2.62}$$

where μ^* is the Coulomb pseudopotential usually taken between 0.1 and 0.15 for superconducting metals.

2.9 Quantum criticality

All properties we have mentioned in this chapter can be altered near absolute zero temperature, due to the existence of emergent quantum states.

At T=0 the systems are in the lowest energy state and all atomic motions cease. However, quantum mechanics predicts collective fluctuations of matter called zero-point motion, which appear due to Heinsenberg's uncertainty principle: the more certain is the particle position, the more uncertain is its velocity. Therefore, atoms and molecules cannot be at rest because their position and velocity would be fixed simultaneously, but they adopt a state of constant agitation. Like the thermal motion, the zero-point motion becomes too intense, leading in some cases to melt order [52]. Strong fluctuations drive the system to a *quantum phase transition* passing through a *quantum critical point* (QCP) and in whose vicinity emergent phases with physical properties not usually observed are stabilized. These transitions are controlled by some tuning parameter such as magnetic field, hydrostatic pressure or chemical composition.

Quantum fluctuations generate drastic changes in the physical properties of the system as we approach a QCP, among these are (i) the electronic contribution to the specific heat behaves as $C_e(T)/T = \gamma(T) \sim -ln(T)$ [54] or $C_e(T)/T = \gamma(T) \sim -\sqrt{T}$ [55] contrary to what is expected by Fermi-liquid (FL) theory, $C_{ele}/T \sim \gamma$ constant. (ii) T-linear electrical resistivity, contrary to the FL expectation $\rho(T) \sim T^2$. (iii) Magnetic susceptibility $\chi \sim T^{-1+\lambda}$ with $\lambda < 1$ [56] conversely to $\chi \sim T^{-1}$. Other behaviors could be obtained due to the quantum fluctuation characteristics. Therefore, these systems are commonly denominated as non-Fermi liquid systems (NFL) and they show an increase of the Sommerfeld coefficient near the QCP as if the electron mass on the Fermi surface becomes infinite and the electron energy vanishes [52].

QCP are commonly observed in moderate/heavy Fermion materials that exhibit both Kondo and RKKY interaction. In these cases, there is a strong competition

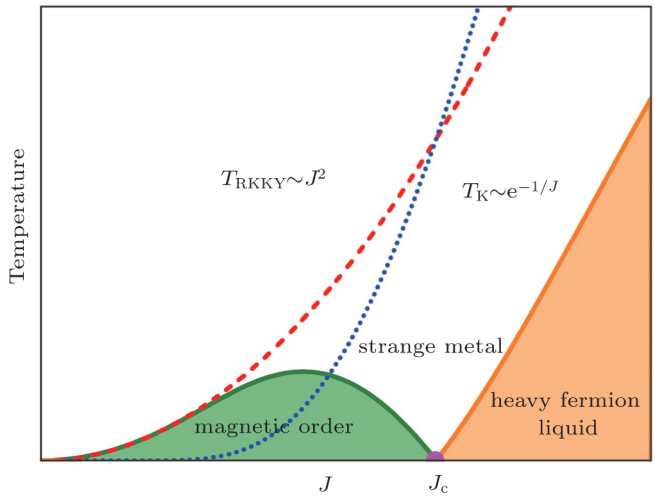

Figure 2.5: A schematic illustration of the Doniach phase diagram, taken from Ref. [53].

between the Kondo effect, which tends to demagnetize the system, and the RKKY interaction which tends to yield a magnetic ordering at low temperatures. Such competition can be described through the Doniach diagram [57] which is shown in Figure 2.5. According to Eq. 2.18 and 2.49 when $\mathcal{J}$ is small, T_N is larger than T_K. So, the system tends to become magnetically ordered, but with a reduction of the magnetic moment due to the Kondo effect, in which limiting case the material will behave as an antiferromagnetic. Conversely, when $\mathcal{J}$ is large, T_N is less than T_K and the system tends to become non-magnetically ordered, so the material will behave as paramagnetic. Therefore, as the interaction increases, T_N passes through a maximum and tends to zero at a critical value $\mathcal{J}_c$ which corresponds to QCP. From here, Kondo effect is destroyed and a coupling of the magnetic moments with both the conduction electrons and the fluctuation generated by the other local moments begins.

3

Methodology

In this chapter we will discuss the experimental and computational methology used to characterize the physical properties of $RNiSi_3$. The former includes the single crystal growth technique -flux method-, and the equipment needed to measure structural, magnetic, specific heat and resistivity properties such as: X-ray diffraction, physical property measurement system (PPMS) and magnetic property measurement system (MPMS) magnetometer. The second involves how the conduction electrons in the solid should be considered and the basis utilized to expand the Kohn-Sham orbitals: augmented-plane wave (APW), this with local orbital (APW+lo) and projector augmented-wave (PAW). Finally, we indicate how to solve computationally the Kohn-Sham equation.

3.1 Experimental methodology

3.1.1 Flux method

One of the simplest although less used techniques for the growth of well-formed and high-quality single crystals is based on molten metal fluxes, also called *the flux method*. This is a high temperature solution technique that employs an excess of a stable liquid medium (the flux) to facilitate nucleation and self-organization of atoms as the solution slowly cools [58, 59]. The idea is that the mixture goes through many metastable states, where the system at equilibrium experiences gradual changes in the external parameters such as temperature and pressure, and relaxes for a long time as the crystal formation takes place.

Knowing the desired compound for growth, we have to think about: What type of flux to use? What should be the composition of the mixture, the appropriate

recipient to keep the mixture at high temperature, the atmosphere to preserve the mixture, the temperature profile and the cooling rate throughout the growth process? How can we remove the flux from the mixture? And finally, what equipment do we need?

To grow large and high quality crystals, the ideal flux must have the following properties: high solubility with all elements that constitute the compound, not forming compounds with the solution, low melting point, easy to remove at the end of the growth process, low toxicity, available in pure form and low cost [60]. To avoid that the flux become included as an impurity in the single crystal, or form compounds with the solution, it is necessary to use a low cooling rate (approximately 5 °C/h). This promotes diffusive atomic movement to achieve a homogeneous solution. On the other hand, it reduces the crystallization temperatures required for the desired compound, since the crystal can be grown well below the melting point of the compound.

The most commonly used metal fluxes that satisfy the conditions specified above for growth of intermetallic compounds are Al, Zn, Ga, Cd, In, Sn, Sb, Hg, Pb, Bi [60]. However, the choice of any of these will depend on the type of compound we want to grow, since each crystal system is different and dictates how it should be grown. As a starting point it is advisable to review the literature and determine which flux has been used to grow similar compounds of the same structural group. In our case, to grow the series $RNiSi_3$ (R=Gd-Tm), we use the fact that $YbNiSi_3$ had already been grown by that method using Sn flux [10].

3.1.1.1 Phase diagrams

Once the flux has been chosen, we must determine the appropriate initial mixture composition, temperature profile and cooling rate of the growth. For this, we must study which phases or phase mixtures are thermodynamically stable within a range of conditions of temperature, composition, and pressure. Graphical representations of this transformation can be seen as *phase diagrams* which will allow us to plan single crystal growth in a controlled manner and mark routes to optimize the flux method.

To exemplify the use of phase diagrams, we consider the simple binary system Gd-Sn [Fig. 3.1] and study how the stability varies as a function of temperature and composition, at ambient pressure (1 atm) in an inert atmosphere.

The left axis of the diagram represents pure Gd with a melting point of 1313 °C, while the right axis represents pure Sn with a melting point of 232 °C. The

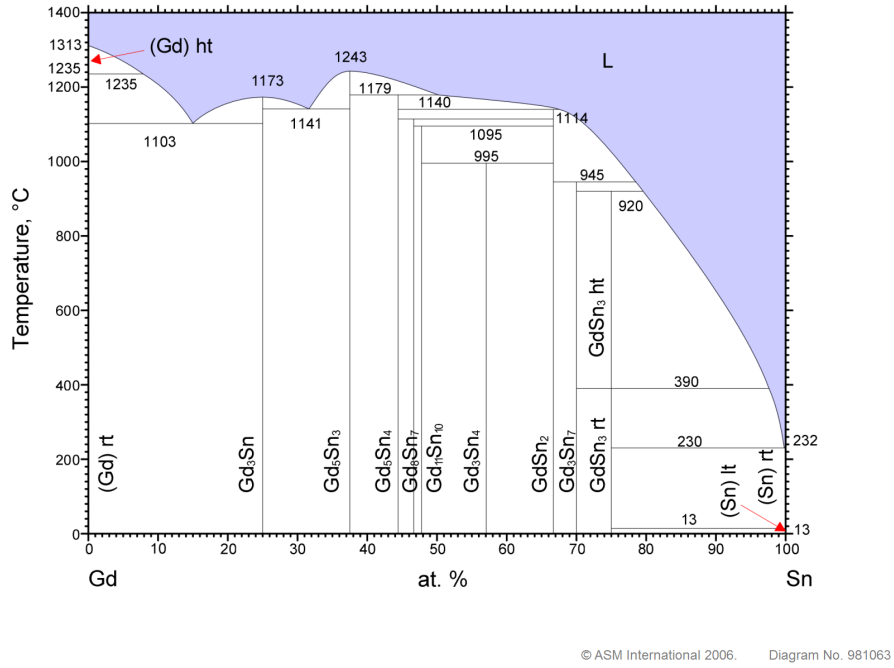

Figure 3.1: Temperature-composition phase diagram for Gd-Sn alloys obtained of ASM Alloy Phase Diagram Database

curves separating liquid region (in blue) from solid region (in white) are called *liquidus lines* and specify the maximum temperature at which crystals can coexist with the melt in thermodynamic equilibrium. Horizontal lines in the solid region are called *solidus lines* and define the lowest temperature at which liquids can exist in equilibrium over a given composition range. Therefore, at temperatures above the liquid curves, any combination of Gd and Sn is a homogeneous liquid. As the temperature of a given composition decreases below the liquidus curve, the mixture enters a metastable state. As the temperature continues to descend very slowly, small single crystals start to nucleate so that the liquid phase and solid phase coexist in equilibrium. At low temperatures, solid Gd and solid Sn coexist to form heterogeneous solid systems. These are Gd_3Sn, Gd_5Sn_3 and $GdSn_2$ associated to congruent phases, while Gd_5Sn_4, Gd_8Sn_7, $Gd_{11}Sn_{10}$, Gd_3Sn_4, Gd_3Sn_7 and $GdSn_3$ to incongruent phases. Notice that for congruent phases, when the system is heated, the crystalline phase melts into a homogeneous liquid phase of the same composition, whereas for incongruent phases a crystalline phase melts into a solid and a liquid phase of different compositions. This diagram shows nine points where the solid curve intersects the liquid curves. Two of them appear near Gd:Sn ratios of

85:15 and Gd:Sn 70:30, where the liquid locally reaches its lowest temperature, and are commonly called *eutectic points*. The other seven points are called *peritectic points* where liquid, solid Sn and the desired solid compound coexist in thermodynamic equilibrium.

To grow congruent polycrystalline phases we can use an initial composition equivalent to the stoichiometric phase. For example, Gd_3Sn can be grown using Gd:Sn in atomic proportions 75%: 25%, heating up 1200 °C to ensure that the mixture is in a homogeneous liquid state, and then we reduce the temperature below 1173 °C. It's more complicated to grow polycrystals of incongruent phases such such as Gd_3Sn_7, because it must be done by solid state reactions below the peritectic temperature of 945 °C.

Now, in order to grow single crystals of congruent or incongruent phases by the self-flux method, we must perform a stoichiometric unbalancing (excess of one of the components) so that when the mixture is heated and cooled it passes through the liquidus line of the desired phase. For example, $GdSn_2$ has a peritectic point at 945 °C. Thus, we can consider the liquidus line in the interval 67-80% Sn concentration, where there will be an Sn flux excess. Crystal yield will depend on molar ratio $\frac{x_L - x}{x_L - x_S}$ where x, x_L and x_S are the mixture, liquid and solid state compositions, respectively. When x is near x_S, the single crystal yield is large. In summary, a possible route to grow $GdSn_2$ by Sn flux method is to use Gd:Sn composition of 31%:69%, heat up to 1200 °C to obtain a homogeneous liquid state, then reduce the temperature down to 1000 °C.

Conceptually, a ternary melt can be used for crystal growth in a way similar to that described for $GdSn_2$. However, in many occasions there is insufficient information on the respective phase diagram and, therefore, we have to apply trial-and-error empirical method in order to optimize the mixture composition, temperature profile and cooling rate to obtain the desired compound. For the $RNiSi_3$ series (R=Gd-Tm) the optimization of growth conditions has been studied as part of the master's dissertation research [1]. There, we determined that by mixing R:Ni:Si:Sn in the initial proportion 1:1:3:45, heating the mixture up to 1200 °C and cooling slowly to 500 °C, it is possible to obtain single crystals on the order of several millimeters.

3.1.1.2 Other optimization parameters

After determining the flux, mixture composition and temperature profile required to grow single crystals, we must take into account other parameters that

may affect them such as the recipient, atmosphere and flux removal process. At high temperatures, intermetallic mixtures can react with oxygen and nitrogen, so it is usual to vacuum seal the material inside a quartz tube. Quartz can resist well up to 1200 °C, but above that it begins to soften. Previous studies have determined that Sn flux does not attack or crack the quartz tube, so we place all elements directly on it. To remove the flux easily, quartz wool is commonly placed on top of the reagents in the preparation process. It will be used as filter to separate single crystals from molten flux in the final centrifugation process. If the excess flux is not correctly removed, it will solidify around the crystals. Then, we have to remove the remaining flux by mechanical processes or by chemical etching [61]. The former is usually a manual and time-consuming process, whereas the latter is faster. However, we must be cautious to choose the ideal solvent so that the chemical etching dissolves the flux without attacking the crystals or, failing that, attacks the flux much faster than the crystal. For this reason, it is best to test the etchant on a small single crystal to check its reaction with the compound. Most fluxes used for growing intermetallic compounds are soluble in HCl (Al, Zn, Sn) or HNO_3 (Ga, Cd, In, Sb, Hg, Pb, Bi) [60].

3.1.2 Single crystal preparation

Typical equipment necessary to grow single crystals by the flux method is high purity elements; a quartz tube; quartz wool; alumina crucibles (Al_2O_3); acetylene-oxygen blow torch; a ventilated glass bench; a pumping station to evacuate the air from ampoule; a programmable box furnace with temperature controller that can go as high as 1200 °C and cool rather slowly (1-10 °C/h); a centrifuge with metal cups that contain a base of quartz wool to place the hot ampoule [59, 62].

To grow single crystals of $RNiSi_3$ (R=Gd-Tm) by Sn flux, we used high purity primary elements- Alfa Aesar- [Fig. 3.2] - Y, Gd, Tb, Dy, Ho, Er, Tm, Yb 99.9%; Ni 99.95%; Si, Sn 99.999%. The proportion of the elements R:Ni:Si:Sn in the initial mixture was 1:1:3:45. Since the solute does not react with silica we placed all elemental reagents directly into a quartz tube, with materials having the highest melting temperatures at the bottom. As the low-melting materials melt they flow over the higher-melting materials and begin to incorporate them into the melt. We place a quartz wool plug on top of the elements. Then, with an acetylene-oxygen blow torch we made a small neck on quartz tube of about 1 mm diameter, localized 10 cm from the bottom

Figure 3.2: Primary elements as Yb, Ni, Si, Sn, quartz tube and quartz wool to grow $YbNiSi_3$ with Sn flux.

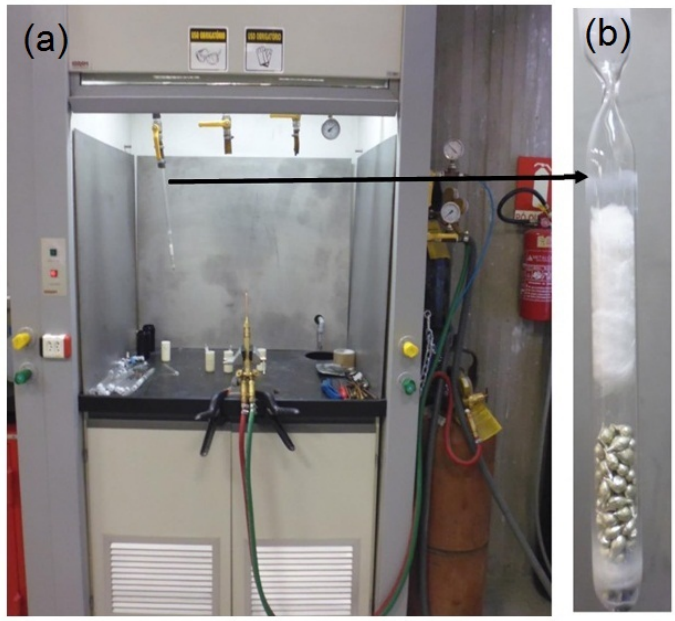

Figure 3.3: (a) Chemical fume hood adapted with blowtorch and vacuum system. (b) Quartz tube with neck keeping the reagents and quartz wool.

ampoule. Subsequently, we use a pumping station to evacuate the air from the ampoule [Fig. 3.3]. The process includes adding Ar gas, holding it for

5 minutes and evacuating for 10 minutes, repeating 3 times. Finally, the blow torch is used to finish vacuum sealing the ampoule. Vertical ampoule

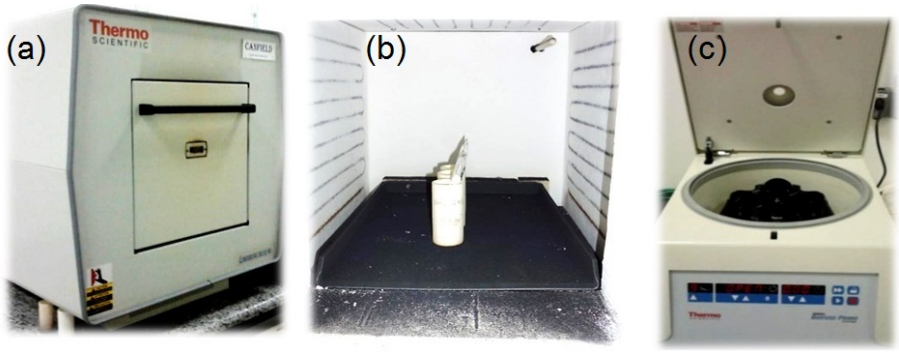

Figure 3.4: (a) External and (b) internal view of the furnaces. (c) Laboratory centrifuge.

is deposited in an alumina crucible and placed in the box furnace, in the central region where the temperature is more homogeneous. Next, we perform the programming for temperature control: the ampoule is heated from room temperature to 600 °C and maintained for 1 h to allow the flux dissolve the elements. Then, the temperature is increased to 1200 °C and held for 10 h, to obtain a homogeneously mixed liquid state of all elements. To allow time for the nucleation and growth of single crystals, the temperature is reduced to 500 °C for 150 h (cooling rate around 5 °C/h). This temperature is above the melting point of the flux and it is high enough to prevent the growth of undesired phases such as RSn_3. At 500 °C the ampoule is taken out of the furnace, inverted and placed in the centrifuge for fast-spinning at up to 1500 rpm.

After centrifugation, the ampoule is stored in a safe place to cool to room temperature. After 2 hours, we break the ampoule, being careful with glass fragments and quartz wool, as well as avoiding loss of the single crystals. Finally, we use a mechanical process to remove the residual solid flux from the single crystals. In order to completely clean their surface we etch them in HCl for 30 min.

3.1.3 Equipment

After growing single crystals, it is necessary to identify whether their crystalline structure corresponds to the desired phase. This structural characterization is done using X-Ray diffractometer. Once the phase is guaranteed, basic physical properties of the compounds are determined by magnetization, specific heat and resistivity measurements. The first is performed in a Quantum Design Magnetic Property Measurement System (MPMS) magnetometer SQUID-VSM, while the others were carried out in a Quantum Design PPMS system. In the following Subsections we will briefly mention the main features of each equipment used.

3.1.3.1 X-Ray diffractometer

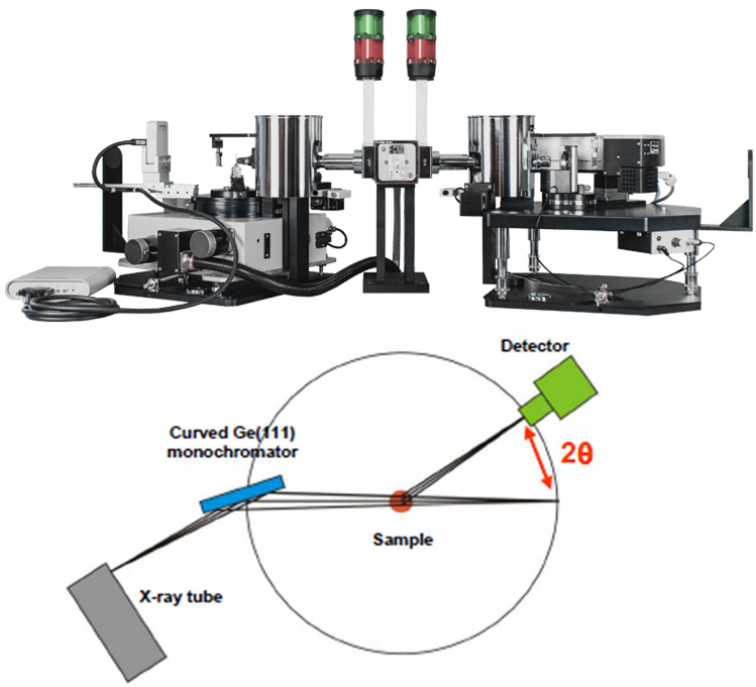

Figure 3.5: Stoe STADI-P model powder X-ray diffractometer in the Debye-Scherrer Geometry. Figure obtained from Ref. [63].

A Stoe STADI-P model powder X-ray diffractometer was used operating in transmission mode with Debye-Scherrer geometry in the configuration θ(fixed)-2θ(variable) [Fig. 3.5]. It consists of an X-ray tube, a curved Ge(111) monochromator, the powder sample and a Mythen detector.

To prepare the powdered sample, we choose a small single crystal and carefully crush it using an agate mortar and pestle until a homogeneous powder is obtained. It is deposited between two acetate-cellulose foils in the transmission sample holder.

The X-ray source consists of a low pressure vacuum tube containing a tungsten filament as a cathode and a copper metal as the anode, which allows a potential difference of 40 kV. An electric current of 40 mA passes through the filament and heats it, producing the emission of electrons. Due to the potential difference, the electrons are accelerated to collide with the anode in such a way that they eject an electron from the K-shell of a Cu atom, leading it to an excited state. Immediately, the atom returns to its ground state, when an electron in a higher energy level fills this hole, CuK_α and CuK_β radiations are emitted. X-rays are incident on a curved Ge (111) monochromator, oriented such that it diffracts only the $K_{\alpha 1}$ radiation. This reduces the background that originates from Cu K_β. Perpendicular to the diffracted beam, the polycrystalline sample is placed in a rotating goniometer to increase the number of crystal orientations. The sample diffracts the X-ray beam at Bragg angles, which are collected by a one-dimensional "silicon strip" detector, linear Mythen 1 K model. This detector is formed by 1280 independent channels for single photon counting. It collects the data at room temperature with angles between 2 ° and 124 ° and angular steps of 3.15 ° every 60 s.

The physics involved in this equipment can be explained by considering the powder sample as small crystallites. We can associate the three-dimensional crystal lattice of each of these as atomic layers. Each layer behaves as a plane that partially reflects, with equal angle, the incident X-ray light. Diffracted rays from successive planes can interfere constructively or destructively. According to *Bragg's condition*, constructive interference occurs when the optical path difference is equal to an integer number of wavelengths:

$$n\lambda = 2d_{hkl}\sin\theta \tag{3.1}$$

where λ is the wavelength, n is the order of reflection, d_{hkl} is the lattice plane spacing and θ is the angle of incidence/reflection to the plane. By varying the angle of incidence and measuring the diffraction intensity, we can generate the diffractogram for that sample. Since there is a unique diffractogram for each compound, by comparing the experimental pattern with similar ones reported

in the literature, we can determine the crystalline phase, lattice parameters, atomic positions, atomic occupations, etc. A simple way to compare is to use *the Rietveld Method* which uses a least-squares algorithm to minimize the difference between these patterns and a theoretical modelling of the structure based on the elements and their positions [64]

3.1.3.2 Physical property measurement system (PPMS)

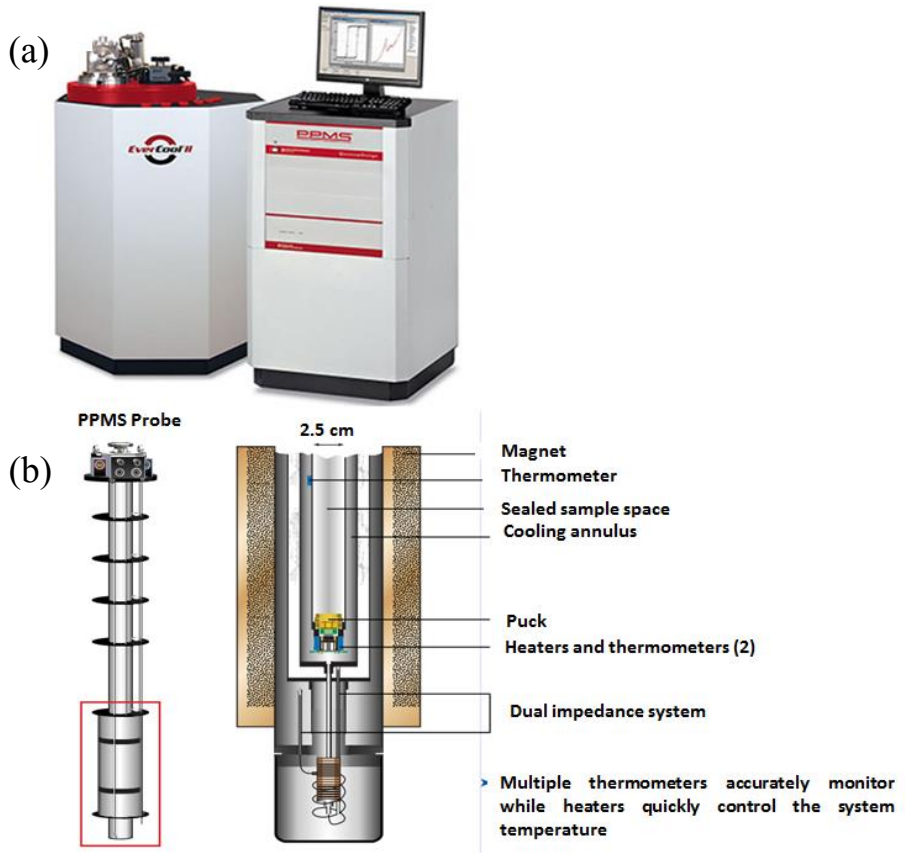

Figure 3.6: (a) Computer and PPMS controller. (b) Schematic description of the structure of the physical property measurements system (PPMS) [65]

This Quantum Design equipment allows us to measure physical properties such as AC and DC magnetic susceptibility, electrical and thermal transport properties such as resistivity, specific heat, Hall effect, Seebeck effect and

thermoelectric figure of merit. However, we only used the specific heat and resistivity options to characterize $RNiSi_3$ compounds. In addition, a ^3He system was employed for the $YNiSi_3$ and $LuNiSi_3$ superconductors because measurements below 2 K were required.

The PPMS consists of a computer and PPMS controller, cryostat, vacuum pump and an EverCool II closed-cycle helium liquifier. The computer and electronic controllers allow automatic measurements. The cryostat [Fig. 3.6] is a dewar containing high-purity helium gas (99.995 %), liquid helium reservoir, probe, pressure relief valves, superconducting magnet completely immersed in liquid helium, thermometers, a plumbing valves system (including recirculation valves, helium supply valves and manifold exhaust valve) and pressure sensors. The EverCool II option allows the PPMS to operate continuously thanks to the integrated cryocooler–Dewar system. Here, the PPMS plumbing transports helium gas to cool the sample chamber and again to the Dewar where it is directly recondensated. The scroll pump provides the vacuum for the cooling annulus and to control the temperature of the PPMS probe. The EverCool II controller turns on the scroll pump only when it is necessary to evacuate the sample chamber [66, 67]. This equipment allows to continuously vary the temperature from 1.9 to 400 K and the magnetic field from -9 to 9 T. On the other hand, the helium-3 option allows measurement at temperatures as low as 0.4 K. Its system allows helium-3 gas to be condensed in the reservoir allowing a continuous closed-loop flow and avoiding regeneration times [65]. 12-pin pucks with a diameter of about 24 mm are inserted by probes into the bottom of the cryostat to connect to the PPMS and allow data collection. Note that each measurement is associated with a different puck, as shown in Fig. 3.7.

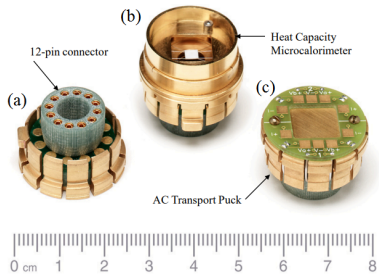

Figure 3.7: (a) 12-pin connector that is inserted into the bottom of the cryostat. (b) Heat capacity puck and (c) resistivity puck used in the PPMS [65]

For resistivity measurements, four platinum wires are connected between the sample and the puck with silver-filled epoxy adhesive (EPO-TEK® H20E), so that the two outer wires carry the currents through the sample, while the two inner wires measure the voltage drop. According to Ohm's law, the resistance

R is proportional to the voltage V and inverse to the current I, $R = \frac{V}{I}$. The device can carry currents in the range of 5 nA to 5 mA, while the voltage drop can be measured with a sensitivity of 20 nV [65]. Now, the resistance depends on the sample geometry. To avoid this dependence, it is necessary to cut the sample into an elongated bar and calculate the resistivity according to Eq. 2.43.

For specific heat measurements at constant pressure, we use a puck with a microcalorimetric platform that simultaneously controls the heat applied by the platform heater and measures the temperature read by the platform thermometer. It is suspended by eight thin wires that provide the electrical and thermal connection. The sample is adhered to the platform using a thin layer of Apiezon grease. The sample platform with grease prior to mounting a sample is called the addenda. Since the Heat Capacity software calculates the heat capacity of a sample by subtracting the addenda measurement from the total heat capacity measurement, two measurements are necessary - one with and one without sample on the sample platform. For the measurement, we must make high vacuum in the chamber with pressures below 0.01 mTorr to guarantee that all sample heat is lost to the platform and puck wires, not to the atmosphere. The measurement consists of monitoring the temperature change of the system, from the time when heat is added until it fully relaxes to the puck temperature. This process is called *a measurement cycle*. After the measurement cycle, the Heat Capacity option considers the heat capacity to be approximately constant over the temperature range and fits the entire temperature response of the sample-platform to a model that explains both the thermal relaxation of the sample-platform to the bath temperature and the relaxation between the sample-platform and the sample itself. The most commonly used model for this fit is the two-tau model [60], which assumes that the sample is not in good thermal contact with the sample platform and it is necessary to simulate the effect of heat flowing between the sample and the sample-platform, and the effect of heat flowing between the sample-platform and puck. For this process, the equipment has a resolution of 10 nJ kg^{-1} K^{-1}. [65, 68].

3.1.3.3 Magnetic Property Measurement System (MPMS) magnetometer

This equipment allows us to study the magnetic properties of small samples with a sensitivity of 10^{-8} emu over a wide range of temperatures (from 400 K down to 1.8 K) and magnetic fields (-7 T to 7 T). Its architecture is similar to the PPMS, however, it has a superconducting quantum interference device magnetometer (SQUID) and a vibrating sample magnetometer (VSM) option.

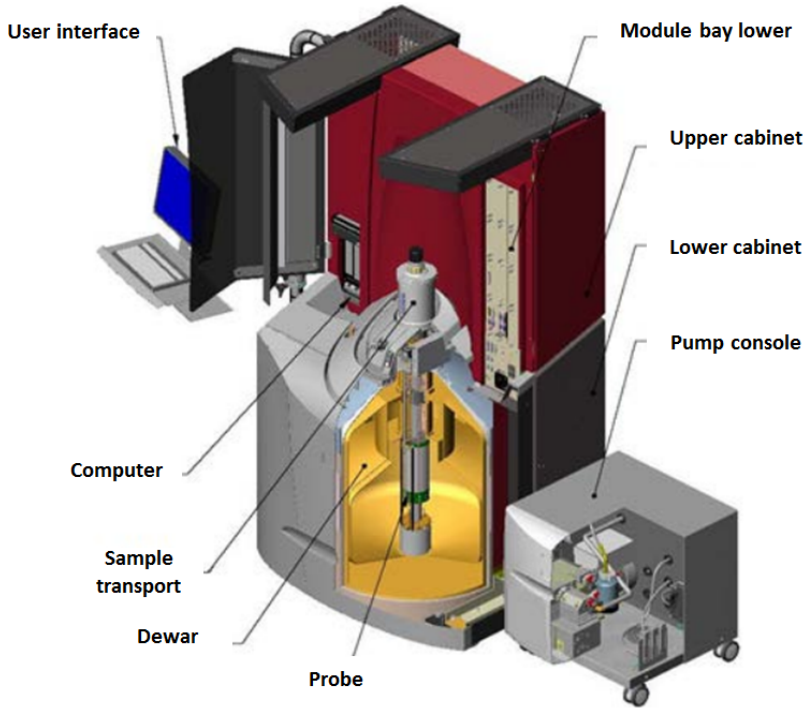

Figure 3.8: General Magnetic Property Measurement System (MPMS) magnetometer SQUID-VSM configuration [69]

Magnetic measurements are performed with superconducting pick-up coils (a superconducting solenoid wire, also called detection coils) and a Superconducting Quantum Interference Device (SQUID) magnetometer, which must be cooled in liquid helium. Direct current (DC) measurements consist of vibrating the sample sinusoidally through the superconducting pick-up coils. Here, the magnetic moment of the sample is approximated by a dipole magnetic moment, whose sign and value remain constant during the measurement. According to Faraday's law, the variable magnetic flux generates an electric current through the coils. As the sample changes position, the coil detects the change in the magnetic flux as a function of the scanning time and the amplitude of the measurement. This coil is coupled through an input transformer to DC SQUID which serves as an extremely sensitive current to voltage converter. Thus, the software adjusts the voltage as a function of position and the time, and calculates the magnetic moment for each point, based on the dipole response function.

3.2 Computational methodology

We use ELK and VASP first-principles codes to determine the electronic properties of $YNiSi_3$, $LuNiSi_3$ and $GdNiSi_3$. ELK is based on all electron full-potential augmented-plane wave method with local orbitals (FP-APW+lo). On the other hand VASP uses an all electron projector augmented wave method. In both cases, we consider the exchange correlation functional in the generalized gradient approximation (GGA) with PBEsol parametrization for $YNiSi_3$ and $LuNiSi_3$ and Perdew-Burke-Ernzerhof (PBE) parametrization for $GdNiSi_3$. The results obtained are highly reliable due to the very good agreement found in each case with the experimental measurements. The following is a brief description of the methodology used by each code.

3.2.1 Bloch's Theorem

In a perfectly crystalline solid, the atoms are arranged in periodic structures while electrons, considered independent and non-interacting, move through the periodic potential obeying the one-electron Schrödinger (or KS Eq. 2.3) equation. According to *Bloch's Theorem* [27] the electronic wave functions can be written as the product of a plane-wave $e^{i\mathbf{k}\cdot\mathbf{r}}$ modulated by a periodic function $u_{\mathbf{k}}(\mathbf{r}) = u_{\mathbf{k}}(\mathbf{r}+\mathbf{R}_L)$ with the periodicity of the crystalline lattice. Therefore,

$$\phi_{\mathbf{k}}(\mathbf{r}) = e^{i\mathbf{k}\cdot\mathbf{r}}u_{\mathbf{k}}(\mathbf{r}), \tag{3.2}$$

or equivalently,

$$\phi_{\mathbf{k}}(\mathbf{r}+\mathbf{R}_L) = e^{i\mathbf{k}\cdot\mathbf{R}_L}\phi_{\mathbf{k}}(\mathbf{r}),$$

where $\mathbf{k}$ is the wave vector within the first Brillouin zone, $\mathbf{R}_L$ is the Bravais lattice vector. The periodicity of $\phi_{\mathbf{k}}$ reduces the description of all electron motion in the solid only to the behavior in a single crystalline cell. The effective potential of Eq. 2.4 has the periodicity of the crystalline lattice. So, KS orbitals are *Bloch functions*, i.e plane-wave functions modulated by a periodic function with the same periodicity of the crystal: $\phi_k(r) = exp(i\mathbf{k}\cdot\mathbf{r})u_k(\mathbf{r})$. As a consequence, the electronic state of a solid is well described by the electrons belonging to the unit cell of the crystal. Then, solving Eq. 2.3 for each particle and for each $\mathbf{k}$-point in the irreducible Brillouin zone are obtained the KS orbitals, the ground state density $n_\sigma^{nonint}(\mathbf{r}) = \sum_i |\phi_{i,\sigma}|^2$ and finally the ground state of the interacting system according to Eq. 2.5.

3.2.2 Electron treatment

In a solid, we can distinguish three regimes for each atom according to the intensity of the electron-nucleus interaction: the core, semicore and valence. The core electrons experiment a similar potential as that of a free atom. Their wave function is highly localized and oscillating due to the strong attractive potential of the nucleus, so the eigenvalues are **k**-independent. Semicore electrons are neither sufficiently localized like core electrons nor free like the valence electrons, so their wave function overlaps both regions. Valence electrons near the semicore region experience a Coulombian screening potential, while away from it, electrons can be considered free to move throughout the lattice and actively participate in chemical bonds. Their wave function is smooth, varies slowly between atoms and depends strongly on the wave vector **k**. According to the electronic method used these regimes are treated in different ways as will be discussed in the following.

3.2.3 Augmented-plane wave (APW)

The augmented plane wave method treats the semicore electrons as if they belong to the core-nucleus, i.e., they are strongly bound to the nucleus and do not respond effectively to the movement of the valence electrons. This allows us to separate the core states from the valence states by means of spheres centered on atoms, such that the chemically active states are outside of sphere while the inert core states are inside. The spheres are called *muffin-tin spheres (MF)* with radius R_{MF}, while the space outside is called *the interstitial region(IR)*. Inside MF, the potential and charge density are spherically symmetric, while in IR the potential is constant. This way of dividing space allows us to write the KS orbitals in terms of a basis set: atomic orbitals in MF and plane waves in IR, which are continuous across the surface of a sphere. In Figure 3.9 we show a schematic representation of this basis set, where the wave functions are expanded into plane waves, each of which is augmented by atomic solutions (radial functions times spherical harmonics).

Mathematically, the i^{th} Kohn-Sham orbitals can be written as: [71]

$$\phi_{i,\mathbf{k}}(\mathbf{r}) = \sum_{\mathbf{G}} C_i^{\mathbf{G}+\mathbf{k}} \psi_{\mathbf{G}+\mathbf{k}}^{APW}(\mathbf{r}) \tag{3.3}$$

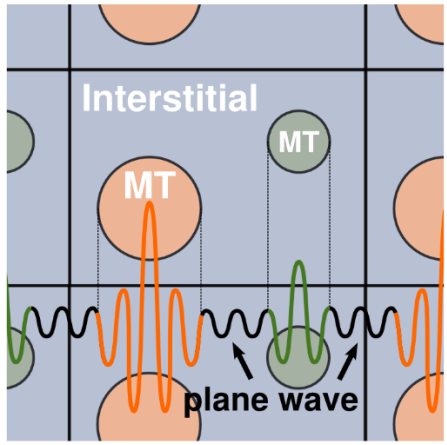

Figure 3.9: Schematic representation of the Augmented-plane wave (APW) method. Orange and green balls represent muffi-tin (MT) spheres and blue space the interstitial region (IR). Figure taken from Ref. [70].

with

$$\psi_i^{APW}(\mathbf{r},\varepsilon) = \begin{cases} \sum_{lm,\alpha} A_{lm}^{\mathbf{G}+\mathbf{k}} R_l(r_\alpha,\varepsilon) Y_{lm}(\hat{\mathbf{r}}) & \mathbf{r}_\alpha \in MT \\ \frac{1}{\sqrt{\Omega}} e^{i(\mathbf{G}+\mathbf{k})\,\cdot\,\mathbf{r}} & \mathbf{r} \in IR, \end{cases} \tag{3.4}$$

where $\mathbf{r}_\alpha$ is the atomic site, $\mathbf{k}$ is the Bloch vector, Ω is the cell volume, $\mathbf{G}$ is a reciprocal lattice vector, $Y_{lm}(\hat{\mathbf{r}})$ are spherical harmonics, $R_l(r)$ are radial functions, $A_{lm}^{\mathbf{G}+\mathbf{k}}$ are the matching coefficients that ensure the continuity of $\psi_{\mathbf{G}+\mathbf{k}}(\mathbf{r})$ at MT sphere boundary.

To completely determine the basis set $\psi_{\mathbf{G}+\mathbf{k}}$ of Eq. 3.4, we simply proceed to calculate the matching coefficients as follows:

1. Since the potential inside the MF spheres has spherical symmetry, we replace the KS effective potential $v_{KS}(\mathbf{r})$ by its spherical average $v_0(r)$.

2. We solve the radial Schrödinger equation:

$$\left[-\frac{1}{2}\frac{d^2}{dr^2} + \frac{l(l+1)}{2r^2} + v_0(r) - \varepsilon_{i\mathbf{k}}^{l,\alpha}\right](rR_{l,\alpha}(r)) = 0, \tag{3.5}$$

   where $\varepsilon_{i\mathbf{k}}^{l,\alpha}$ are the KS eigenvalue.

3. We apply the boundary conditions to the MF sphere. To do this, we

expand the plane wave as

$$\frac{1}{\sqrt{\Omega}} e^{i(\mathbf{G}+\mathbf{k})\ \cdot\ \mathbf{r}} = \frac{4\pi}{\sqrt{\Omega}} e^{i(\mathbf{G}+\mathbf{k})\ \cdot\ \mathbf{r}_\alpha} \sum_{l,m} i^l j_l(|\mathbf{G}+\mathbf{k}||\mathbf{r}|) Y^*_{l,m}(\hat{\mathbf{G}+\mathbf{k}}) Y_{l,m}(\hat{\mathbf{r}}),$$

the continuity of $\phi_{i,\mathbf{k}}(\mathbf{r})$ is reached when the coefficients $A^{\mathbf{G}+\mathbf{k}}_{lm,\alpha}$ are computed as

$$A^{\mathbf{G}+\mathbf{k}}_{lm,\alpha} = \frac{4\pi i^l e^{i(\mathbf{G}+\mathbf{k})\ \cdot\ \mathbf{r}_\alpha}}{\sqrt{\Omega} R_{l,\alpha}(\mathbf{R}_\alpha, \varepsilon)} j_l(|\mathbf{G}+\mathbf{k}|R_\alpha) Y^*_{l,m}(\hat{\mathbf{G}+\mathbf{k}})$$

where $j_l(|\mathbf{G}+\mathbf{k}|r_\alpha)$ are the spherical Bessel functions.

After choosing the basis set, we write the KS equation in matrix form as follows:

- We write the KS equation in terms of the chosen basis set:

$$H^{\mathbf{k}} C^{\mathbf{k}} = \varepsilon^{\mathbf{k}} S^{\mathbf{k}} C^{\mathbf{k}}, \tag{3.6}$$

where the Hamiltonian matrix $H^{\mathbf{k}}$ and overlap matrix $S^{\mathbf{k}}$ have elements of the form

$$H^{\mathbf{k}}_{\mathbf{G}\mathbf{G}'} = \left\langle \psi_{\mathbf{G}+\mathbf{k}} \left| -\frac{1}{2}\nabla^2 + v_{KS}(r) \right| \psi_{\mathbf{G}'+\mathbf{k}} \right\rangle, \tag{3.7}$$

and

$$S^{\mathbf{k}}_{\mathbf{G}\mathbf{G}'} = \langle \psi_{\mathbf{G}+\mathbf{k}} | \psi_{\mathbf{G}'+\mathbf{k}} \rangle, \tag{3.8}$$

respectively, while that eigenvector $C^{\mathbf{k}}$ contains as elements the coefficients $C^{\mathbf{k}}_{i,\mathbf{G}}$ of Eq. 3.3.

- We define the plane wave cutoff as $R_{MF}|\mathbf{G}+\mathbf{k}|_{max}$ in order to reduce the dimensions of the matrices $H^{\mathbf{k}}$ and $S^{\mathbf{k}}_{\mathbf{G}\mathbf{G}'}$, and therefore make the problem numerically tractable.

$R_l(r)$ are numerical solutions to the radial Schrödinger equation. This leads to some dependence between the basis set and the energy. Therefore, the eigenvalue problem is non-linear in energy and it has to be solved iteratively starting with a guessed value for ε. This process is computationally very costly.

3.2.4 Augmented plane wave and local orbital (APW+lo)

The augmented plane wave and local orbital is an extension of the APW method whose objective is to make the basis set energy independent, but keep the same basis size. The APW+lo basis is constructed with the APW basis ψ_i^{APW} augmented with local orbital functions ψ_i^{lo}:

$$\psi_i = \begin{cases} \psi_i^{APW} & i \leq N_{APW} \\ \\ \psi_i^{lo} & i > N_{APW}, \end{cases} \tag{3.9}$$

where N_{APW} is an integer that depends on the total basis set size and the number of local orbitals. Here ψ_i^{APW} are defined as per Eq. 3.4 for a set of fixed energies E_1, while ψ_i^{lo} are constructed as:

$$\psi_i^{lo} = \begin{cases} \sum_{lm}[A_{lm}^{\mathbf{G}+\mathbf{k}} R_l(r,\varepsilon_1) + B_{lm}^{\mathbf{G}+\mathbf{k}} \dot{R}_l(r,\varepsilon_1)]Y_{lm}(\hat{\mathbf{r}}) & \mathbf{r} \in MT \\ \\ 0, & \mathbf{r} \in IR \end{cases} \tag{3.10}$$

APW+lo method allows considering the semi-core states as a second set of local orbitals with a second linearization energy. In any case, the linear combination between R_l and $\dot{R}_l$ must satisfy the condition that the value of the local orbitals go to zero at the sphere boundary. In this way, APW+lo fixes the freedom of the basis and gains time in convergence, because only the continuity of the function, but not its derivatives, is required.

3.2.5 Projector augmented-wave (PAW) method

The PAW method succeeds in correctly describing the nodal behavior near the core, by considering three basic functions: all electron (AE) function $\phi(\mathbf{r})$, the pseudo (PS) functions $\tilde{\phi}(\mathbf{r})$ and the projector functions $\tilde{p}(\mathbf{r})$.

Since the AE functions are highly oscillating, according to P.E. Blōch [72], it is difficult to treat them in Hilbert space. However, we can make a linear transformation to Hilbert's pseudo space (PS) to map the AE wave function into fictitious soft nodeless PS function. Thus, the i^{th} KS orbital associated

with the eigenvalue ε_i [Eq. 2.3] can be written as

$$|\phi_i\rangle = |\tilde{\phi}_i\rangle + \sum_{aj}(|\varphi_j^a\rangle - |\tilde{\varphi}_j^a\rangle)\langle\tilde{p}_j^a|\tilde{\phi}_i\rangle, \tag{3.11}$$

where the subscript a represents the atomic site and j the atomic quantum numbers n_j, l_j and m_j. Here, the AE wave function $|\phi_i\rangle$ expands in AE partial waves $\{|\varphi_i\rangle\}$ and the PS wave function $|\tilde{\phi}_i\rangle$ expands in PS partial waves $\{|\tilde{\varphi}_j\rangle\}$ such that in both cases we have the same coefficients C_{ni}^a. The projector functions $|\tilde{p}_j\rangle$ are chosen so as to satisfy the condition $\langle\tilde{p}_i^a|\tilde{\varphi}_j\rangle = \delta_{ij}$ and therefore $\langle\tilde{p}_i^a|\tilde{\phi}_j\rangle = C_{ni}^a$. Notice that while $|\varphi_j\rangle$, $|\tilde{\varphi}_j\rangle$ and $|\tilde{p}_j\rangle$ are atom-centered localized functions, $|\tilde{\phi}_i\rangle$ belongs to the interstitial region (IR), and therefore can be expanded into plane waves.

Intuitively, Eq. 3.11 indicates that in the augmentation sphere the AE function is obtained by superposition of projector functions on the sphere such that they describe the nodal behavior of the true wave function, while on IR the AE function coincides with PS function. Graphically [Fig. 3.10], the AE function $|\phi_i\rangle$ is obtained as follows: using the PS functions $|\tilde{\phi}_i\rangle$ we describe the form of the true function away from the augmentation sphere. Next, we remove the projections on the PS-onsite functions $|\tilde{\varphi}_i^a\rangle\langle\tilde{p}_i|\tilde{\phi}_i\rangle$ and finally, we add the projections on AE-onsite functions $|\varphi_i^a\rangle\langle\tilde{p}_i|\tilde{\phi}_i\rangle$.

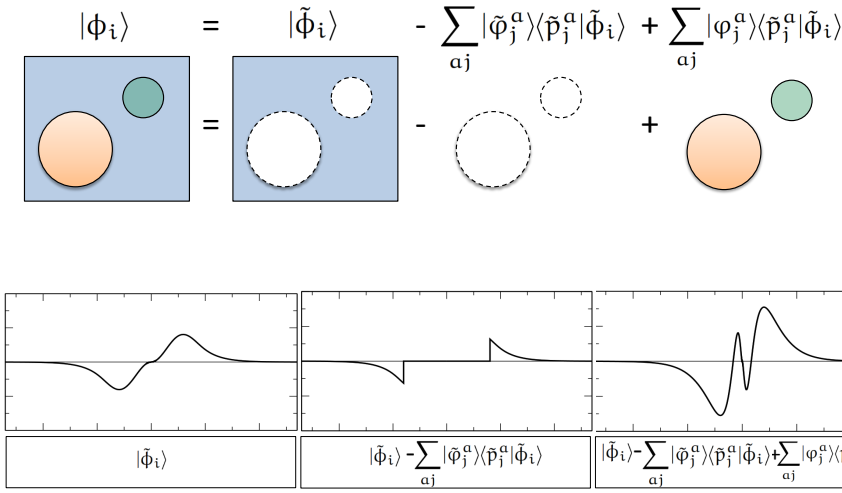

Figure 3.10: Schematic representation of the projector augmented-wave (PAW) basis and a construction of all electron (AE) function from pseudo (PS) function at atom site a according to Eq. 3.11. Figure taken from Ref [73]

To finish this Section we will show how the KS Hamiltonian is written in the PAW approach and what is the proper way to solve it.

The KS Hamiltonian [Eq. 2.3] in Hilbert space can be expressed as

$$\hat{H}|\phi_i\rangle = \varepsilon\hat{S}|\phi_i\rangle, \tag{3.12}$$

or according to Eq. 3.11 as

$$\hat{H}^{PAW}|\tilde{\phi}_i\rangle = \varepsilon\hat{O}|\tilde{\phi}_i\rangle, \tag{3.13}$$

where $\hat{H}^{PAW}$ and $\hat{O}$ operators are defined in the PS Hilbert space [74,75] by

$$\hat{H}^{PAW} = \tilde{H} + \sum_{abc} |\tilde{p}_b^a\rangle(\langle\varphi_b^a|H^a|\varphi_c^a\rangle - \langle\tilde{\varphi}_b^a|\tilde{H}^a|\tilde{\varphi}_c^a\rangle)\langle\tilde{p}_c^a| \tag{3.14}$$

and

$$\hat{O} = \hat{1} + \sum_{abc} |\tilde{p}_c^a\rangle(\langle\varphi_b^a|\varphi_c^a\rangle - \langle\tilde{\varphi}_b^a|\tilde{\varphi}_c^a\rangle)\langle\tilde{p}_c^a|. \tag{3.15}$$

To solve Eq. 3.13, we need to construct the AE and PS partial wave functions, the projectors function and the PS wave functions in the following way:

- AE partial waves $|\varphi_i\rangle$ are obtained by self-consistent procedure to solve the radial Schōdinger equation

$$\left(-\frac{\hbar^2}{2m}\nabla^2 + v_{eff}\right)|\varphi_i\rangle = \varepsilon_i|\varphi_i\rangle, \tag{3.16}$$

  where

$$v_{eff}(r) = v_{ion}(r) + e^2\int d^3r'\,\frac{n(r')}{|\mathbf{r}-\mathbf{r}'|} + \mu_{xc}[n_{core}(r) + n(r)]. \tag{3.17}$$

  Here v_{ion} is the ionic Coulomb potential

$$v_{ion}(r) = -\frac{Ze^2}{r} + e^2\int d^3r'\,\frac{n_{core}(r')}{|\mathbf{r}-\vec{r}'|}.$$

- The PS partial waves $|\tilde{\phi}\rangle$ are obtained considering the same AE eigenvalue spectrum ε_i to solve the self-consistent radial Schödinger equation for PS Hamiltonian:

$$\left(\tilde{H} + \sum_{bc}|\tilde{p}_b\rangle D_{bc}\langle\tilde{p}_c|\right)|\tilde{\varphi}_i\rangle = \varepsilon_i\left(1 + \sum_{bc}|\tilde{p}_b\rangle Q_{bc}\langle\tilde{p}_c|\right)|\tilde{\varphi}_i\rangle, \tag{3.18}$$

where

$$\tilde{H} = -\frac{\hbar^2}{2m}\nabla^2 + \tilde{v}_{eff},$$

$$\tilde{v}_{eff} = \tilde{v}_{loc}(r) + e^2 \int d^3r' \frac{\tilde{n}(r') + n(r')}{|\mathbf{r} - \mathbf{r}'|} + \mu_{xc}[\tilde{n}(r)], \tag{3.19}$$

$$Q_{bc} = \langle \phi_b | \phi_c \rangle - \langle \tilde{\phi}_b | \tilde{\phi}_c \rangle,$$

and

$$D_{bc} = \langle \phi_b | - \frac{\hbar^2}{2}\nabla^2 + v_{eff} | \phi_c \rangle - \langle \tilde{\phi}_b | - \frac{\hbar^2}{2m}\nabla^2 + \tilde{v}_{eff} | \tilde{\phi}_c \rangle.$$

- Once the PS wave functions have been obtained, we construct the projector functions according to:

$$|\tilde{p}_i\rangle = \left(-\frac{1}{2}\nabla^2 + \tilde{v}_{eff} - \varepsilon_i \right) |\varphi_i\rangle, \tag{3.20}$$

such that they are orthogonal to all PS partial waves $\langle \tilde{p}_k | \tilde{\varphi}_j \rangle = \delta_{k,j}$.

Having determined $|\varphi_i\rangle$, $|\tilde{\varphi}\rangle$ and $|\tilde{p}_i\rangle$, we solve Eq. 3.13 in order to find $|\tilde{\phi}_i\rangle$ and finally, we evaluate those functions in 3.11 to obtain the KS orbitals.

After choosing the basis set, we write the KS equation in matrix form as follows:

- We write the KS equation in terms of the set of basis found:

$$\langle \tilde{\phi}_i | \hat{H}^{PAW} | \tilde{\phi}_i \rangle = \varepsilon \langle \tilde{\phi}_i | \hat{O} | \tilde{\phi}_i \rangle, \tag{3.21}$$

whose Hamiltonian matrix $\langle \tilde{\phi}_i | \hat{H}^{PAW} | \tilde{\phi}_i \rangle$ has elements of the form

$$\langle \tilde{\phi}_i | \tilde{H}^{PAW} | \tilde{\phi}_i \rangle + \sum_{abc} \langle \tilde{\phi}_i | \tilde{p}_b^a \rangle (\langle \varphi_b^a | H^a | \varphi_c^a \rangle - \langle \tilde{\varphi}_b^a | \tilde{H}^a | \tilde{\varphi}_c^a \rangle) \langle \tilde{p}_c^a | \tilde{\phi}_i \rangle,$$

while the overlap matrix elements $\langle \tilde{\phi}_i | \hat{O} | \tilde{\phi}_i \rangle$ are:

$$\langle \tilde{\phi}_i | \hat{O} | \tilde{\phi}_i \rangle = \langle \tilde{\phi}_i | \tilde{\phi}_i \rangle + \sum_{abc} \langle \tilde{\phi}_i | \tilde{p}_c^a \rangle (\langle \varphi_b^a | \varphi_c^a \rangle - \langle \tilde{\varphi}_b^a | \tilde{\varphi}_c^a \rangle) \langle \tilde{p}_c^a | \tilde{\phi}_i \rangle.$$

- For computational reasons, only a finite number of AE and PS partial waves and projections are considered. Generally, the truncation is performed by defining cutting parameters such as the radius of the sphere and the maximum angular momentum for the plane wave. The radius

is usually about half the nearest-neighbor distance to ensure that the spheres do not overlap, the nucleus density is well contained within the sphere, and to decrease the number of plane waves in the interstitial region.

3.2.6 Solving the Kohn-Sham equation

The KS equation in matrix form must be solved in a self-consistent way:

1. We choose a trial density charge $n^0(\mathbf{r})$.
2. We calculate the Hartree-potential according to Eq. 2.1
3. We solve Poisson's equation $\nabla^2 v_{ext}(\mathbf{r}) = 4\pi n^0(\mathbf{r})$ to determine the external potential $v_{ext}(\mathbf{r})$.
4. We select the exchange correlation potential $v_{xc}[n](\mathbf{r})$ in some approximation.
5. We solve the KS equation as follows:
   - In the APW method, we introduce the $v_{Hartree}$, $v_{ext}(\mathbf{r})$ and $v_{xc}(\mathbf{r})$ in Eq. 2.4, and we use Eq. 3.7 and 3.8 to determine the matrix elements $H^{KS}_{\beta\alpha}$ and $S_{\beta\alpha}$, respectively. Next, we diagonalize the matrix equation $(\mathbf{H^{KS}} - \varepsilon_i \mathbf{S})\mathbf{c}_i = 0$, and obtain the set of eigenvalues $\{\varepsilon_i\}$ and eigenvector $\{c_{i\alpha}\}$. Finally, the KS orbitals are extracted from Eq. 3.3.
   - In the PAW method, we introduce the $v_{Hartree}$, $v_{ext}(\mathbf{r})$ and $v_{xc}(\mathbf{r})$ in 3.17 and 3.19. Using Eq. 3.16, 3.18 and 3.20 to determine the AE and PS partial waves and projectors. Replacing these in Eq. 3.13 we obtain the PS wave function. Thu, according to 3.11 we have all the functions that allow us to determine the AE wave function. Notice that the spectral eigenvalues of AE wave function are the same that PS wave function.
6. Using the KS orbital, we obtain the new charge density $n^1(\mathbf{r}) = \sum_i |\phi_i(\mathbf{r})|^2$
7. Now, we compare $n^0(\mathbf{r})$ and $n^1(\mathbf{r})$ under some convergence criterion. For example, the difference in charge density is of the order of 10^{-6}. If that criterion is satisfied, we find the ground state charge density and therefore obtain the minimum of $E_{KS}[n]$ according to Eq. 2.5. On the other hand, if the criterion is not satisfied, we choose a new charge density

$n^2 = (1-\gamma)n^0 + \gamma n^1$ with γ as a mixing parameter and the process starts again.

4

Physical Properties of $RNiSi_3$

In this chapter we detail the physical properties of $RNiSi_3$ (R=Y, Gd-Tm, Lu) whose magnetic properties were studied during my master's work. For completeness we have included $YbNiSi_3$ and its electronic isovalent $YbNiGe_3$ which have been extensively studied in the literature by other researchers .

4.1 Structural characterization

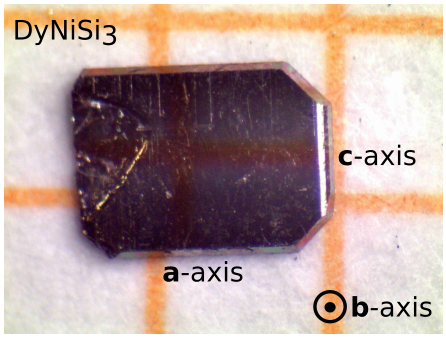

Figure 4.1: $DyNiSi_3$ single crystal on millimeter paper with defined a, b, and c-crystallographic axis [2].

The flux method described in sec. 3.1 allows the growth of single crystals of $RNiSi_3$ series in thin plate geometry with well-defined shapes and shiny surfaces as exemplified in Fig. 4.1 for $DyNiSi_3$. However, compounds such as $ErNiSi_3$, $TmNiSi_3$, and $LuNiSi_3$ grew with small crystallites of $NiSi_2$ parasitic phase on the main crystal surface which were removed by polishing before their respective characterization. Laue diffraction measurements [2] indicated that

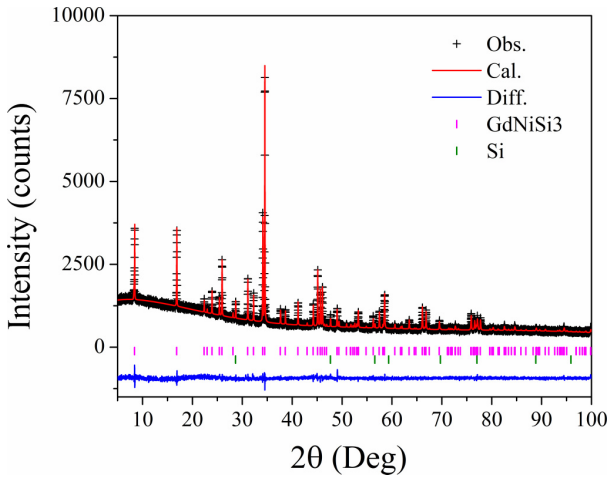

Figure 4.2: Rietveld refinement for $GdNiSi_3$. The black crosses, the red line and the blue line represent the observed data, the calculated pattern and the difference between them, respectively. The short vertical bars are associated with the expected position of the Bragg reflections of each identified phase [2].

the b-axis remains perpendicular to the plate which is plane, while a and c-axis define the plane as the longest and shortest axis, respectively.

Rietveld refinement of $RNiSi_3$ family (R=Y, Gd-Tm, Lu) was used to analyze X-ray powder diffraction patterns (example shown in Fig. 4.2 for $GdNiSi_3$) indicating that these compounds belong to the $Cmmm$ space group (No. 65) and adopt a $SmNiGe_3$-type orthorhombic structure [Fig. 4.3]. The obtained lattice parameters are listed in Table 4.1. Note that the a/c ratio [Fig. 4.4(a)] approaches unity while the a/b ratio [Fig. 4.4(b)] decreases throughout the entire series toward the heavier rare earths. As a consequence, the series becomes nearly tetragonal and the unit cell undergoes elongation along the b-axis for the heavier ions.

The crystalline structure has 20 atoms per conventional unit cell, located at the following Wyckoff positions: a single $4j$ site for rare earth, a single $4i$ site for nickel and silicon has three non-equivalent sites: Si1 at a $4j$ site, Si2 and Si3 at two different $4i$ sites. In Table 4.2 we list these positions for the $LuNiSi_3$ compound. The atoms form a set of square and rectangular pyramids, pseudo-hexagons and isosceles triangles. The square pyramids enclose a Ni atom, and they are formed by the three different Si sites: Si1 and Si2 which determine the bases and Si3 the apex. Note that Si1 atoms form Si dimers along (001) and linear chains along [100], Si2 atoms form Si dimers along (002) and linear chains along [001], and Si3 builds up zigzag chains along [100]. On the other hand, the bases of rectangular pyramids are built by Si3 atoms

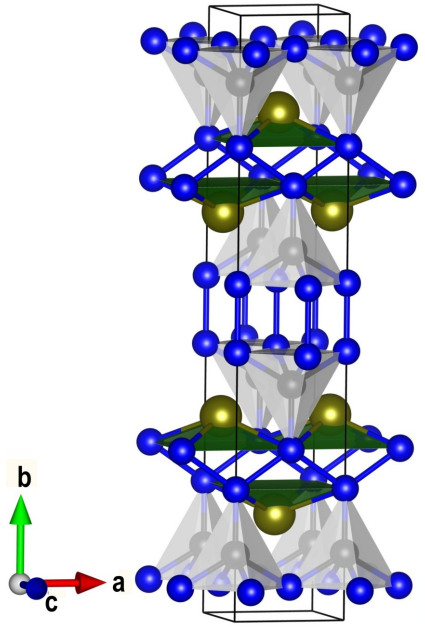

Figure 4.3: $LuNiSi_3$ crystal structure representation. Dark gold, black and blue spheres denote the Lu, the Ni and the three Si atomic positions, respectively.

Table 4.1: Lattice parameters and unit cell volumes obtained from the Rietveld refinements for each compound of the $RNiSi_3$ series [1, 2].

Compound	a (Å)	b (Å)	c (Å)	V (Å^3)
$YNiSi_3$	3.9216(1)	20.9448(6)	3.9506(1)	324.49(2)
$GdNiSi_3$	3.9402(2)	21.0224(6)	3.9730(1)	329.10(2)
$TbNiSi_3$	3.9259(1)	20.9696(5)	3.9547(1)	325.57(1)
$DyNiSi_3$	3.9167(2)	20.929(1)	3.9401(2)	322.98(3)
$HoNiSi_3$	3.9085(1)	20.9057(4)	3.92915(9)	321.05(1)
$ErNiSi_3$	3.9015(1)	20.8817(6)	3.9181(1)	319.21(2)
$TmNiSi_3$	3.8930(8)	20.8417(4)	3.90578(7)	316.90(1)
$YbNiSi_3$	3.8915(1)	20.8570(6)	3.9004(1)	316.58(3)
$LuNiSi_3$	3.8808(3)	20.792(1)	3.8868(3)	313.62(4)

with a Lu atom at the apex. The pseudo-hexagons are built up by Si2, Ni and Si3 atoms in (001) and the isosceles triangles by Lu atoms in (002). The interatomic distances of these polyhedra are indicated in Table 4.3.

Table 4.2: Atomic coordinates for $LuNiSi_3$ [76].

Site	Wyckoff position	Site symmetry	x	y	z
Lu	$4j$	$m2m$	0	0.33119(3)	1/2
Ni	$4i$	$m2m$	0	0.11183(9)	0
Si1	$4j$	$m2m$	0	0.44459(18)	0
Si2	$4i$	$m2m$	0	0.05683(18)	1/2
Si3	$4i$	$m2m$	0	0.21541(18)	0

Table 4.3: Polyhedral information (in Å) for $LuNiSi_3$ [77].

Square pyramid	
base length	2.7272
apex atom (Si)–Ni distance	2.2048
Rectangular pyramid	
base lengths	3.8558, 3.8579
apex atom Lu–Si distance	2.9078
Isosceles triangle	
leg, base	3.8725, 3.8558

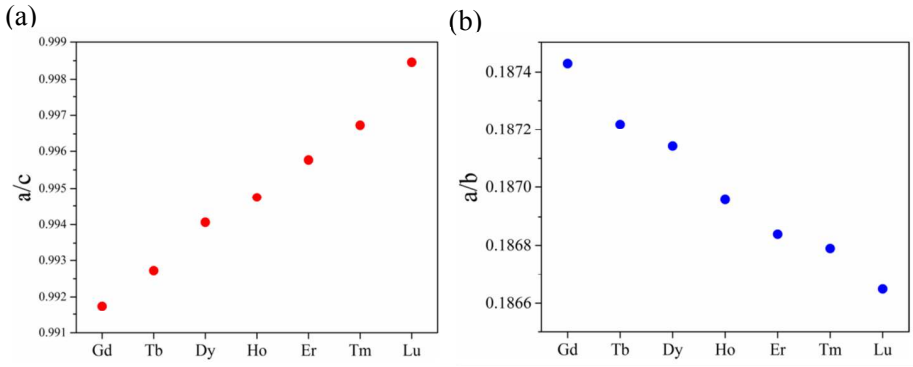

Figure 4.4: Lattice parameter ratios (a) a/c and (b) a/b along the $RNiSi_3$ series [1,2].

4.2 $RNiSi_3$ R=(Y, Gd-Tm, Lu)

To study the physical properties of $RNiSi_3$ compounds, we consider measurements on the temperature dependence of the specific heat at $H = 0$ and resistivity in the configuration $I \perp b$ at $H = 0$ and 90 kOe. Magnetization is measured as a function of temperature at $H = 1$ kOe and as a function of magnetic field at $T = 2$ K and other temperature values, both as a function of crystal orientation (a, b and c crystallographic axis and polycrystalline average according to Eq. 2.20).

4.2.1 $YNiSi_3$ and $LuNiSi_3$

Above 2 K, $YNiSi_3$ and $LuNiSi_3$ are strongly anisotropic diamagnetic compounds with metallic character. Their physical properties are summarized in Fig. 4.5. Specific heat of both compounds shows a smooth dependence on T, indicating that there is no phase transition in the measured temperature range. At low temperature, their behavior is correctly described by the Debye model [Eq. 2.25] where the linear fit on the $C_p/T \times T^2$ curve observed in the inset, predicts a Sommerfeld coefficient, phononic coefficient and Debye temperature of $\gamma = 4.1$ and 3.5 mJ mol^{-1}K^{-1}, $\beta = 0.160$ and 0.0830 mJ mol^{-1}K^{-4} and $\Theta_D = 393$ K and 489 K for $YNiSi_3$ and $LuNiSi_3$, respectively. On the other hand, the resistivity in both compounds presents metallic behavior [Eq. 2.45] with residual resistivity ratios [Eq. 2.44] of 54(5) for $YNiSi_3$ and 38(4) for $LuNiSi_3$, indicating that these are high quality single crystals. Finally, the susceptibility exhibits a marked anisotropic behavior for both compounds. Since the a and c crystallographic axis cannot be differentiated, these directions were labeled $\perp b_{(1)}$ and $\perp b_{(2)}$. The estimated average susceptibility for $YNiSi_3$ is 0.08(5)$\times 10^{-3}$ emu/mol, while for $LuNiSi_3$ is -0.07(5)$\times 10^{-3}$ emu/mol. The former has an almost constant Pauli susceptibility while the latter, at low temperatures, has a weak Curie-like susceptibility which may be associated with the presence of a small amount of paramagnetic impurities, since the elemental Lu reagent used was not as pure as Y. For both samples the susceptibility along two directions ($\parallel b$ and $\perp b_{(2)}$) are positive, while the response for $\perp b_{(1)}$ is negative. Therefore, the presence of a negative or positive susceptibility depends on the direction of the applied field [2].

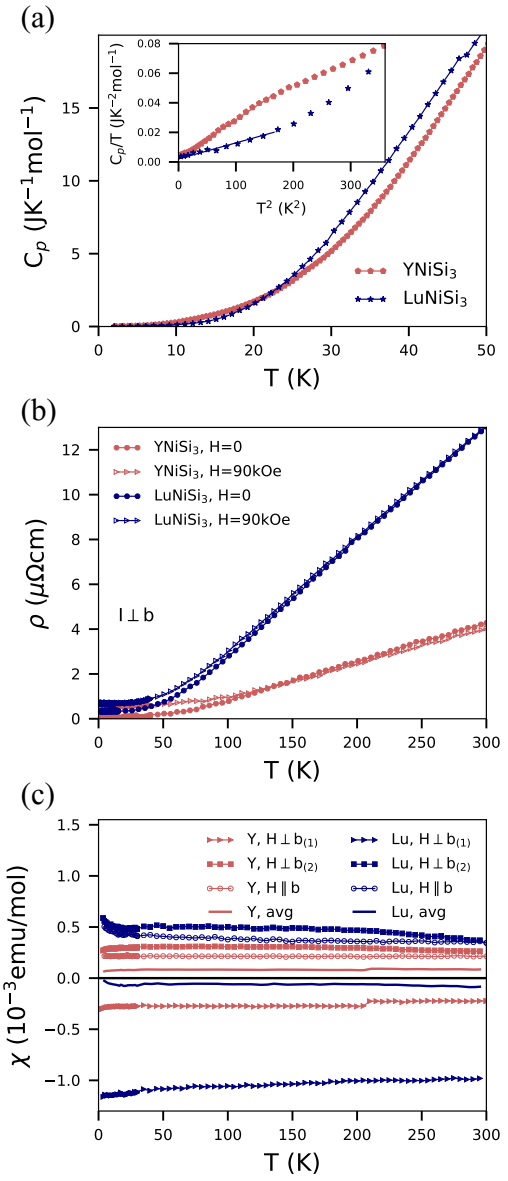

Figure 4.5: Physical properties of $YNiSi_3$ and $LuNiSi_3$. (a) Dependence of specific heat on temperature. The inset shows the Debye model fit using $C_p/T \times T^2$ curves. (b) Dependence of resistivity on temperature with no field (solid symbols) and with an applied field of 90 kOe (open symbols). (c) Susceptibility curves with an applied field of $H = 1$ kOe parallel to the three crystallographic axis. The average curve for both samples are presented as a solid line [2].

4.2.2 $RNiSi_3$ (R=Gd-Tm)

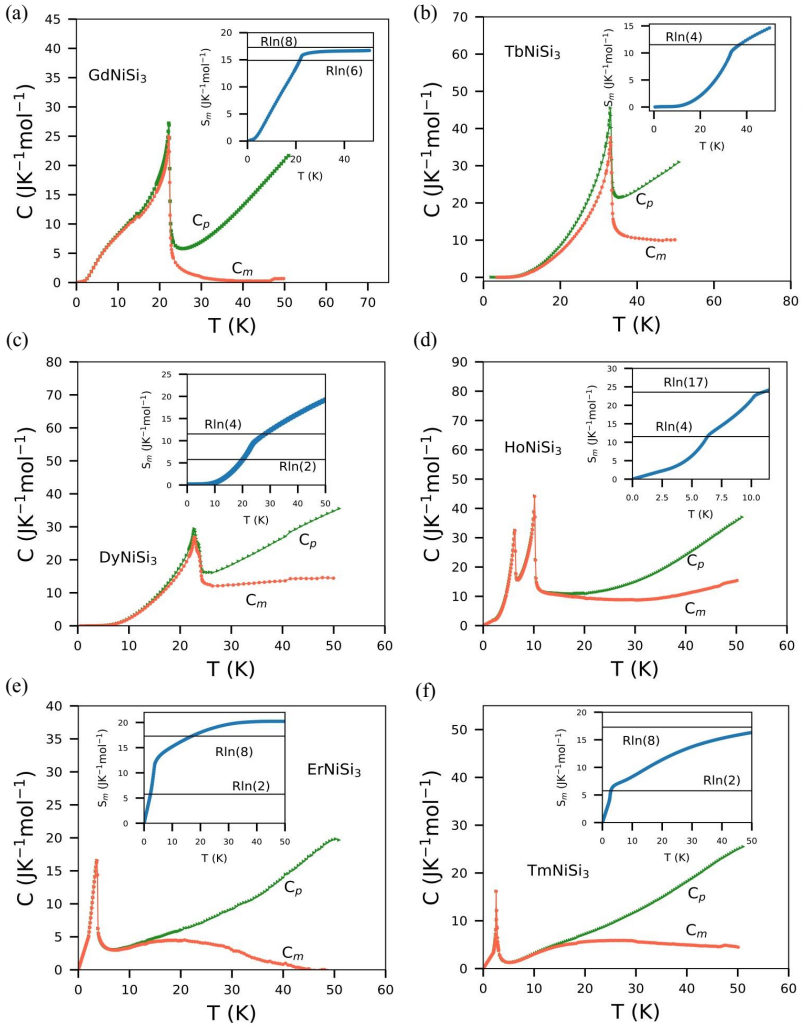

Figure 4.6: Total (C_p) and magnetic (C_m) specific heat curves for (a) $GdNiSi_3$, (b) $TbNiSi_3$, (c) $DyNiSi_3$, (d) $HoNiSi_3$ (e) $ErNiSi_3$ and (d) $TmNiSi_3$ at zero magnetic field. The inset shows the magnetic entropy for each compound. These figures were taken from Ref. [2].

The specific heat measurements and magnetic specific heat calculated according to Eq. 2.32 and 2.33 are presented in Fig. 4.6 at zero field and $2 \leq T \leq 50$ K.

Their insets correspond to the temperature dependent magnetic entropy. All samples exhibit an λ-type anomaly in both C_p and C_{mag} curves indicating a magnetic phase transition whose temperatures (T_N) are summarized in Table 4.5. $DyNiSi_3$ and $HoNiSi_3$ show a second peak at 22.8 K and 6.3 K, respectively, in response to a new temperature-induced phase transition. While at high temperature, C_{mag} continues to increase suggesting that $YNiSi_3$ and $LuNiSi_3$ cannot account for all the electronic and lattice contributions of these systems. The other compounds show a C_{mag} that persists over a wide range of temperature before reaching zero value. For its part, $GdNiSi_3$ has a broad shoulder below 10 K that is associated with Zeeman splitting due to the presence of internal fields. In contrast, $TmNiSi_3$ displays this broad shoulder above 10 K probably caused by the Schottky anomaly resulting from the splitting of the ground state by the crystalline field [subsec. 2.6.4].

Table 4.4: Experimental variation of the specific heat ΔC_m and magnetic entropy S_m cross the antiferromagnetic transition in J K^{-1} mol^{-1} units [2].

	Gd	Tb	Dy	Ho	Er	Tm
$\Delta C_m(T_N)$	20	21	13	30	12	13
$S_m(T_N)$	15.7	10.5	9.7	22.8	12.2	6.0

On the other hand, the variation of specific heat ΔC_m and magnetic entropy in the region where the magnetic transition occurs are given in Table 4.4. Comparing it with their theoretical values [Table 2.2] we find that $GdNiSi_3$ and $TbNiSi_3$ have values of $\Delta C_m(T_N)$ close to those predicted by mean-field theory, and the former almost reaches its expected value of maximum entropy $R\ln(8)$, while the latter only reaches a value close to $R\ln(4)$ above the magnetic transition, which is associated with the population of four low energy levels. On the other hand, $HoNiSi_3$ has a much larger $\Delta C_m(T_N)$ that the other compounds, although its S_m is consistent with the maximum expected value for the Ho^{3+} free-ion multiplet which is $R\ln(17)$. For the other compounds, $\Delta C_m^{exp}(T_N)$ does not exceed the theoretical value and S_m remains below even though it continues to increase above the transition temperature.

Resistivity measurements performed without and with an applied magnetic field at 90 kOe in the $2 \leq T \leq 300$ K interval are presented in Fig. 4.7. As it can be seen all compounds have a positive magnetoresistance and they exhibit a weak change on slope near to magnetic transition in both fields, except for $TmNiSi_3$, where it is not visible at 90 kOe. Moreover, the second phase transitions for $DyNiSi_3$ and $HoNiSi_3$ are not evident in this case. Néel temperatures are determined by linear regression of Eq. 2.47 whose values are given in Table 4.5. On the other hand, at high temperature the resistivity

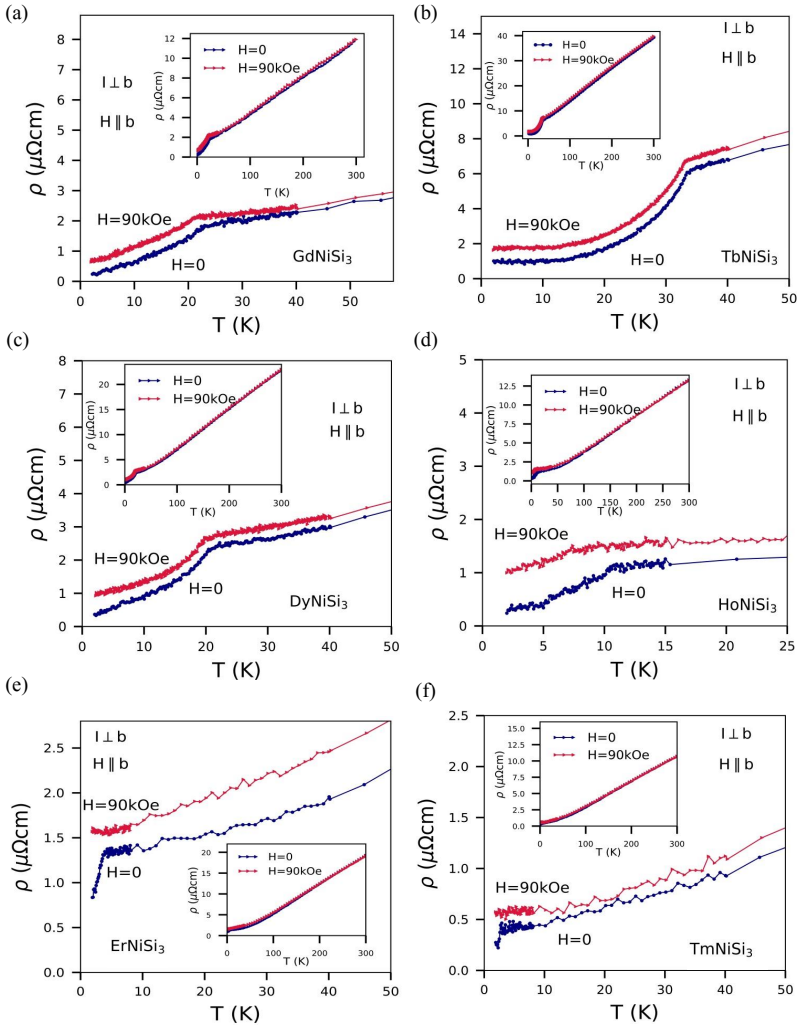

Figure 4.7: Resistivity measurements for (a) $GdNiSi_3$, (b) $TbNiSi_3$, (c) $DyNiSi_3$, (d) $HoNiSi_3$ (e) $ErNiSi_3$ and (d) $TmNiSi_3$ under zero field and 90 kOe in the temperature range where the AFM transition takes place. The inset displays the full zero-field curve to room temperature. These figures were taken from Ref. [2].

follows a T-linear behavior [Eq. 2.45] pointing to metallic transport while at low temperature there is a marked decrease in resistivity with a T^2-dependence [Eq. 2.48].

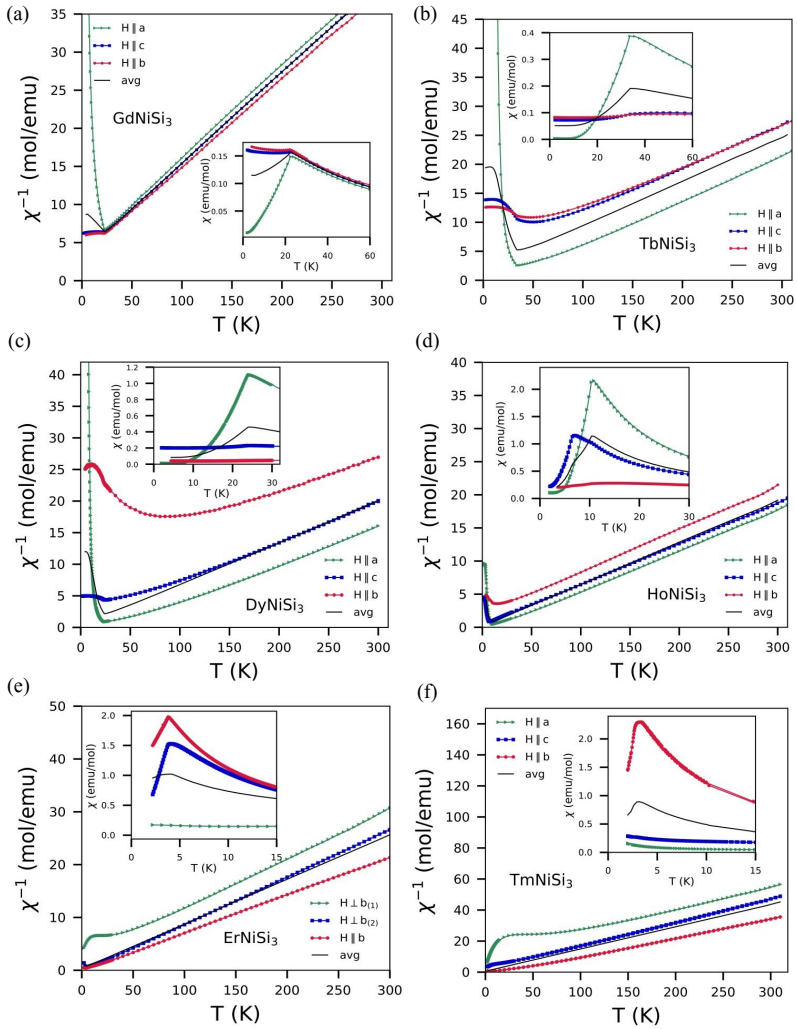

Figure 4.8: Inverse magnetic susceptibility χ^{-1} for (a) $GdNiSi_3$, (b) $TbNiSi_3$, (c) $DyNiSi_3$, (d) $HoNiSi_3$ (e) $ErNiSi_3$ and (d) $TmNiSi_3$ under $H = 1$ kOe along the a, b, and c-axis from 2 to 300 K. The inset indicates the $\chi(T)$ behavior near the magnetic transition. These figures were taken from Ref. [1, 2].

Figure 4.8 shows $\chi^{-1} \times T$ and $\chi \times T$ curves [inset] for a magnetic field of 1 kOe for three different crystallographic directions [1, 2, 9]. Moreover, since the Laue diffraction on $ErNiSi_3$ did not allow us to differentiate their planar-axis, we then label them as $\perp b_1$ and $\perp b_2$. Making a careful observation, we see that for all series the anomalies presented in the resistivity and specific heat curves are

also available in the magnetic measurements and allude to antiferromagnetic phase transition, whose T_N is shown in Table 4.5. $DyNiSi_3$ shows the two-close transition as a soft plateau in the polycrystalline average curve, while $HoNiSi_3$ has two anomalies. Additionally, we perceive that there is a shift from a to b-easy axis from R = Gd-Ho to Er-Tm, respectively. Also, R=Ho, Er and Tm have two AFM axis, a and c-axis for the former, b and $b_{(2)}$ for the second, and b and weakly a-axis for latter, respectively. For its part, $GdNiSi_3$ presents low magnetocrystalline anisotropy compared to other elements of the series due its spherical $4f$ shells ($L = 0$) which makes it insensitive to the crystalline field. Pauli susceptibility, Curie-Weiss temperature and effective magnetic moment on $H \parallel a$, b, c-axis and polycrystalline average curve [Eq. 2.20], calculated according to Eq. 2.17 and 2.19 are shown in Table 4.6 and Table 4.7. Notice that the effective magnetic moment is close to the expected value for R^{3+} free ions presented in Table 2.1, indicating that the magnetism of $RNiSi_3$ originates solely from R rare earth ions while the Ni atoms are nonmagnetic. On the other hand, the difference in the θ_{cw} values obtained suggest that all compounds in the series present a high magnetic anisotropy. Notice that the polycrystalline Curie-Weiss temperature θ^p_{cw} is negative for R=Gd-Tb evidencing AFM interaction, while for R=Dy-Ho it is positive, indicating that there are possibly some ferromagnetic correlations in these materials. Finally, for R=Er-Tm, it returns to negative values reflecting again the AFM ordering [1, 2].

Table 4.5: Néel temperatures T_N obtained from specific heat (C_p), resistivity (ρ), and magnetic susceptibility (χ) measurements and their corresponding average for each compound of the $RNiSi_3$ series [2].

R	C_p (K)	ρ (K)	χ (K)	Average (K)
Gd	22.2	22.4	21.9	22.2(2)
Tb	33.0	33.4	33.3	33.2(2)
Dy	23.6	21.8	23.6	23.6(2)
Ho	10.1	10.7	10.4	10.4(3)
Er	3.7	3.6	3.7	3.7(1)
Tm	2.6	2.7	2.6	2.6(1)

For $M \times H$ measurements at $T = 2$ K [Fig. 4.9] [1,2,9] we observed that, except for $GdNiSi_3$, all compounds present strong magnetocrystalline anisotropy in agreement with the behavior previously presented in $\chi \times T$ curves. Moreover, it is the only member of the series in which none of the magnetization axis saturate at 2 K under an applied field of 70 kOe. On the other hand, for the entire series, a shift of the magnetization easy axis is discernible when moving toward the heavier rare earths. Here, the metamagnetic transition can be seen along the a-axis for R=Gd-Dy, on both a, c-axis for $HoNiSi_3$, $H \perp b_2$,

Table 4.6: Néel temperature T_N and Curie-Weiss temperatures θ^a_{cw}, θ^b_{cw}, and θ^c_{cw} along a, b and c directions, respectively, and on polycrystalline average θ^p_{cw}. This information was extracted from [1, 2].

	AFM axis						
R	easy	other	T_N (K)	θ^p_{cw} (K)	θ^a_{cw} (K)	θ^b_{cw} (K)	θ^c_{cw} (K)
Gd	a	a	22.2(2)	-30(3)	-36	-35	-28
Tb	a	a	33.2(2)	-8.0(8)	29	-96	-60
Dy	a	a	23.6(2)	+20(2)	43	-400	-37
Ho	a	a, c	10.4(3)	+1.0(1)	23	+53	8.3
Er	b	$\perp b_2$, b	3.7(1)	-1.7(2)	-36	14	1.2(1)
Tm	b	b	2.6(1)	-12(1)	-24	17	-126

Table 4.7: Main parameters for $RNiSi_3$ series: μ_{eff} and μ_{HF} are the effective magnetic moment calculated of $\chi \times T$ at high temperatures and the moment observed at 2 K and $H = 70$ kOe in $M \times H$, respectively. χ_0 is the Pauli susceptibility and RRR is the residual resistivity ratios [1, 2].

R	μ_{eff} (μ_B)	μ_{HF} (μ_B)	χ_0 (10^{-3} emu/mol)	RRR
Y		-	0.08(5)	54(5)
Gd	8.1(2)	2.1(1)	0.40(4)	50(5)
Tb	9.6(3)	9.1(2)	3.2(3)	40(4)
Dy	9.4(3)	10.8(2)	11.7(1)	64(6)
Ho	11.0(3)	9.6(2)	2.0(2)	51(5)
Er	9.2(3)	9.5(2)	5.3(5)	23(2)
Tm	7.8(2)	6.7(2)	-3.1(3)	40(4)
Lu	-	-	-0.07(5)	38(4)

b-axis for $ErNiSi_3$ and a, b-axis for $TmNiSi_3$. $GdNiSi_3$ exhibits a plateau followed by a magnetic transition at 27 kOe. $RNiSi_3$ with R=Tb, Dy, Ho are characterized by several metamagnetic transitions accompanied by hysteresis on the easy AFM axis. For R=Tb there are four plateaus before the magnetic response saturates. Here, the hysteresis can reach a width of 4 kOe. R=Dy displays an initial plateau followed by two irreversible metamagnetic transitions before saturation at 32 kOe. The plateau inside the hysteresis achieves a magnetization of half saturation denoting the inversion of the single-spin into a four-spins AFM lattice. Similarly the latter is true for R=Ho. The main difference between these compounds is that $TbNiSi_3$ has the appearance of other magnetic structures at lower field values and the field strength required to reorient its magnetic moments is higher than for the others. On the other hand, the magnetic behavior along the a and c-axis for $HoNiSi_3$ suggests the presence of a component-separated magnetic transition [78] in which the

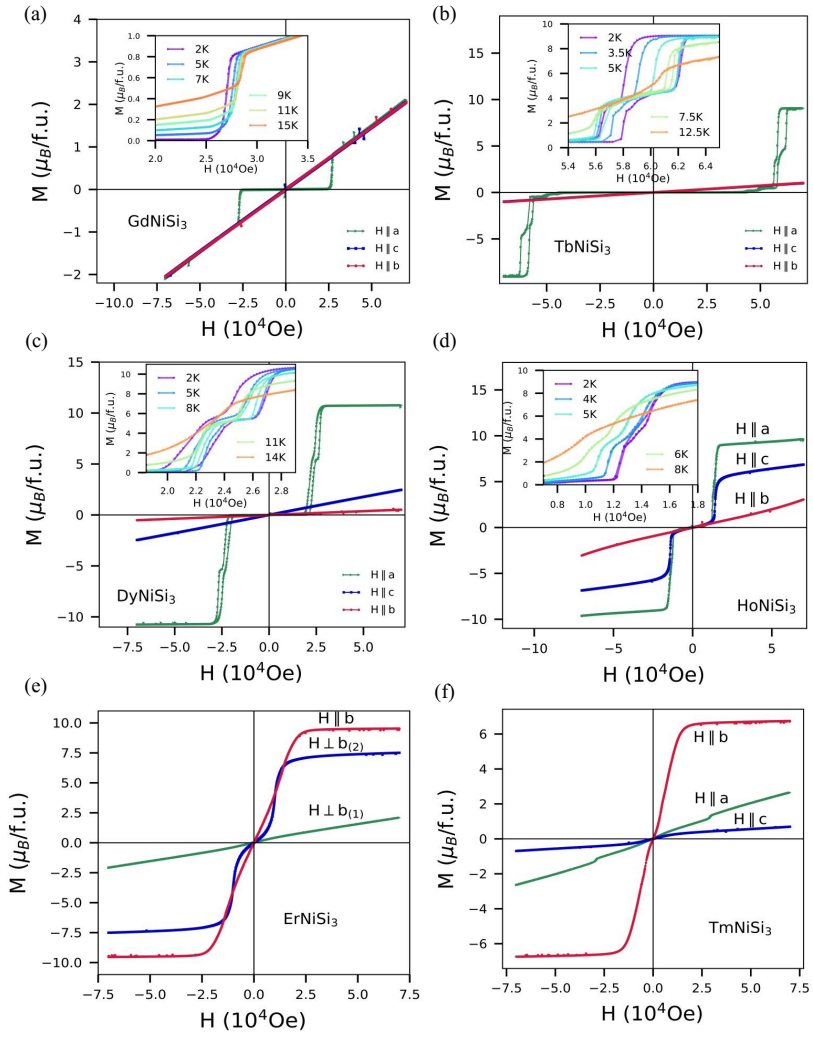

Figure 4.9: Magnetization isotherms at 2 K for (a) $GdNiSi_3$, (b) $TbNiSi_3$, (c) $DyNiSi_3$, (d) $HoNiSi_3$ (e) $ErNiSi_3$ and (d) $TmNiSi_3$ along the a, b, and c-axis. The inset shows the shift of the metamagnetic transition to higher fields with increasing temperature. These figures were taken from Ref. [1, 2].

magnetic moment components can be ordered independently in two distinct directions and with different critical temperatures. Thus, one for the AFM axis along a with $T_N^a = 10.4(3)$ K and another for the AFM axis along c with $T_N^c = 6.3(2)$ K. In the case of $ErNiSi_3$, $H \parallel b$ reaches saturation with paramagnetic-like behavior, $H \perp b_{(2)}$ curve (possibly $H \parallel c$) shows a smooth metamagnetic transition but does not saturate, while the other shows a small

magnetization along the field. In contrast, $TmNiSi_3$ has a paramagnetic-like response in $H \parallel c$, it exhibits a small step around 28 kOe on the $H \parallel a$ curve and it saturates along the b-axis.

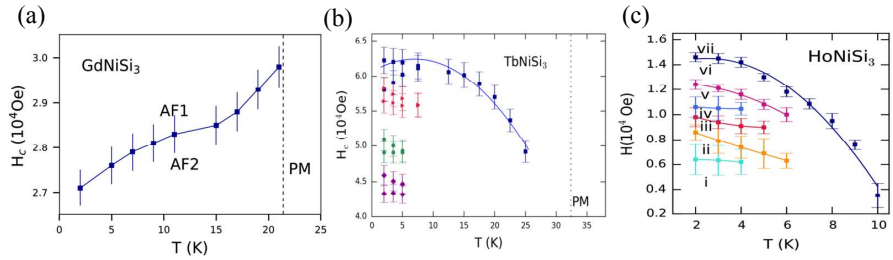

Figure 4.10: Magnetic phase diagram for $RNiSi_3$ (R=Gd, Tb and Ho) along the $H \parallel a$- magnetization easy axis [1, 2, 9].

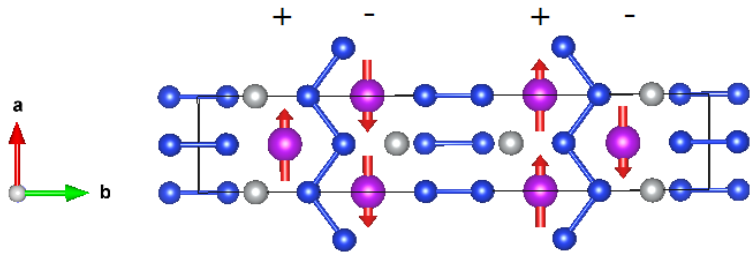

Figure 4.11: Magnetic structure of $Gd/TbNiSi_3$. Violet, blue and gray balls represent Gd/Tb, Si and Ni atoms. The red arrows indicate the direction of Gd/Tb magnetic moments.

In Fig. 4.10 [1, 2, 9] we present the most significant phase diagrams [sec. 2.5.3] of the $RNiSi_3$ series, as it is the case for R=Gd, Tb and Ho along the AFM easy axis. In $GdNiSi_3$ the critical field increases with temperature contrary to expectations for spin-flop transitions in antiferromagnets [32]. For R=Tb, since both metamagnetic transitions and hysteresis attenuate with increasing temperature, the phase diagram suggests at least four distinct ordered magnetic states. On the other hand, $HoNiSi_3$ exhibits at least six distinct magnetic transitions along the AFM easy axis. Its complex phase diagram can be related to the independent ordering of the magnetic moment components along the two axis, as discussed in the previous paragraphs.

Recently, Tartaglia *et al.* [79] studied the microscopic magnetic structures of $GdNiSi_3$ and $TbNiSi_3$, and their magnetoelastic expansion above T_N (15-36 K) by resonant X-ray magnetic diffraction experiments on single crystals at zero

field. They found that the magnetic structure is commensurate with the crystal structure and that they are the same for both compounds. Here the rare-earth magnetic moments are ferromagnetically aligned in the *ac* planes, pointing along the *a* direction, while there are antiferromagnetic alignment between the nearest-neighbor planes along the *b* axis with the + - + - pattern as shown in Fig. 4.11. On the other hand, they observed that with temperature rises there is a contraction of *a* and an expansion of *b* lattice parameters while *c* remains approximately constant. Here the magnetic configuration is maintained stable under the lattice expansion.

4.3 $YbNiSi_3$

Since 2004, several authors have succeeded in performing the full characterization of $YbNiSi_3$ in terms of its magnetic and electronic properties. Next, we will describe some of them.

As the other compounds of the series, $YbNiSi_3$ displays a very sharp λ-like peak at $T_N = 5.1$ K in specific heat measurements as shows in Fig. 4.12(a). It shifts at low temperature as the applied magnetic field increases and disappears above 80 kOe. However, above 5 K a broad what to appear on $H = 70$ kOe curve and it acquires structure and move at high temperatures as the field arises [Figs. 4.12(b) and 4.12(c)] being considered as a Schottky-type contributions [80]. At $H = 0$ kOe, γ value obtained from Eq. 2.31 is 250 mJ $mol^{-1}K^{-2}$ belonging to a moderately heavy-electron system. Also, increase the field causes that γ decreases. This tendency is generally observed in materials close to a QCP [80]. On the other hand, the magnetic entropy accumulated up to T_N is $0.6R\ln(2)$ [Fig. 4.12(d)] indicating that a ground-state doublet is responsible for the magnetic ordering, and that in this state, the Yb moments are already significantly screened when magnetic ordering occurs [10].

Electrical resistivity measurements at $H = 0$ kOe in the $I \parallel b$ and $I \perp b$ orientations for $YbNiSi_3$ show an anisotropic behavior being the first one much more resistive than the second one [Fig. 4.13(a)]. Also, both show a metallic behavior at high temperature and a change in the concavity, $d\rho/dT$, around of 5 K related to the magnetic transition. In $I \perp b$, as T is reduced from room temperature, it shows a local minimum centered in 55 K and then increases to peak at 7 K with a logarithmic behavior which is the signature of the Kondo effect [subsec. 2.8.2]. Its associated temperature was estimated through Rajan's expression $\gamma T_K = 11.2j$ as $T_K = 30$ K for $j = 1/2$ [10]. Below this temperature it decreases very sharply showing a Fermi-liquid

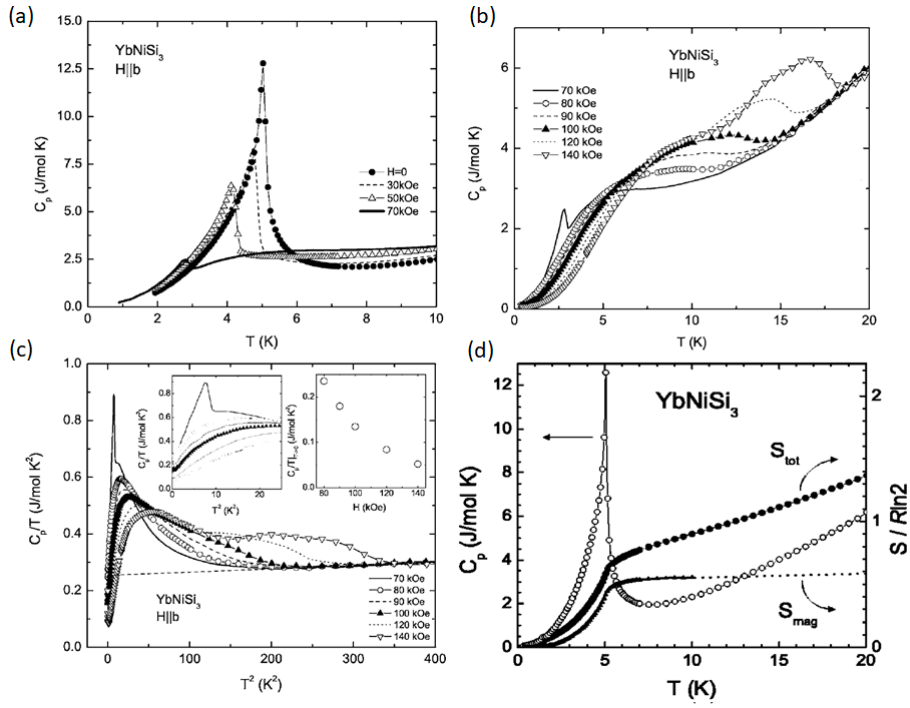

Figure 4.12: Low-temperature heat capacity C_p, measured at different applied magnetic fields (a) $H = 0$, 30, 50 and 70 kOe, and (b) $70 \leq H \leq 140$ kOe. (c) $C_p/T \times T^2$ is presented at $70 \leq H \leq 140$ kOe. Left inset is a zoom of $C_p/T \times T^2$ at low-temperature for different magnetic fields. Right inset present their corresponding estimated γ value dependent of magnetic field. (d) Total specific heat, total entropy S_{tot} and magnetic entropy S_{mag}. Figures (a)-(c) are taken from Ref. [80] and (d) from Ref. [10].

type behavior [Eq. 2.48] where $\rho_0 = 1.5$ μ Ω cm and $A = 0.36$ μ Ω cm/K^3. Thus, below 5 K $YbNiSi_3$ exhibits a combined effect of magnetic ordering with coherent scattering of the hybridized Yb moments [10]. In presence of magnetic field, ρ diminishes due to the suppression of spin fluctuations [81] [Fig. 4.13(c)], but in any case the T^2 dependence is observed. On the other hand, field-dependent resistivity isotherms [Fig. 4.13(d)], show two very pronounced step-like features associated with two critical fields. The first occurs at low field and it is T-independent, describing a first-order transition from the antiferromagnetic to spin-flop state. The second step appears at high field and decreases with the temperature arise, which may be related to the magnetic transition from spin-flop state to field-polarized paramagnet [6,80].

Due to the similarities between the a and c-crystallographic axis in $YbNiSi_3$

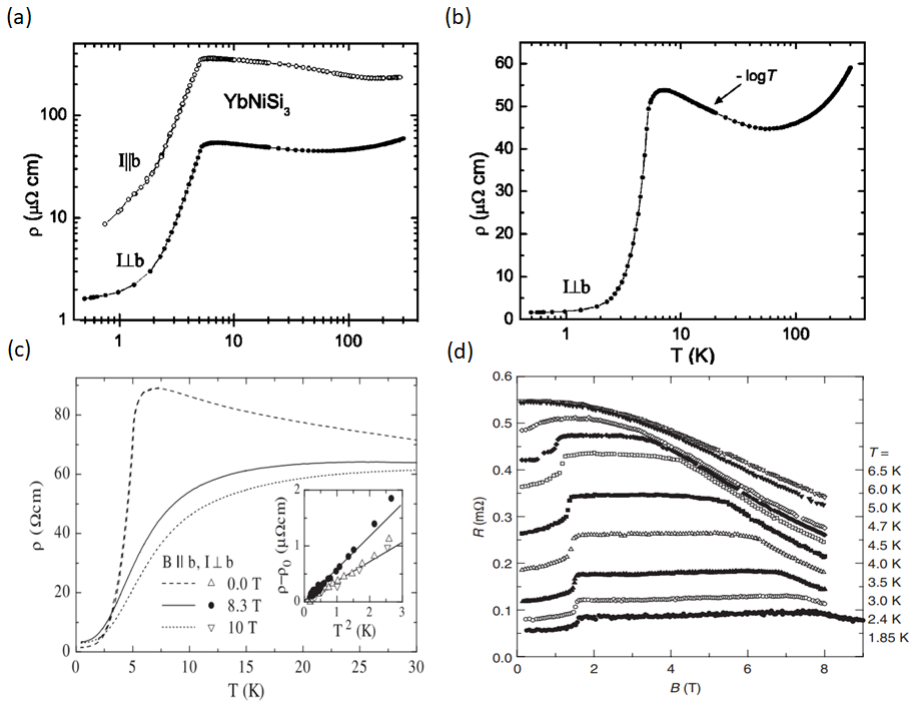

Figure 4.13: Electric resistivity $\rho(T)$ as a function of (a) temperature for two orientations $I \parallel b$ and $I \perp b$, (b) $LogT$ for $I \perp b$ at $H = 0$ and (c) T for $I \perp b$, $H \parallel b$ at $H = 0$, 8.3 and 10 T. Figures are taken from (a)-(b) Ref. [10], (c) Ref. [81] and (d) Ref. [80]

[Table 4.1], it was treated as a tetragonal structure where only the $H \parallel b$ and $H \perp b$ crystallographic orientations are considered in the magnetization measurements. So, the polycrystalline average of Eq. 2.20 is reduced to $\chi = (\chi_b + 2\chi_{ac})/3$.

Susceptibility measurements at 1 kOe [inset of Fig. 4.14(a)] show that $YbNiSi_3$ have an anisotropic antiferromagnetic ground state with b-easy AFM axis and Néel temperature $T_N = 5.1$ K, as was observed by resistivity and specific heat curves. This anisotropy is due to crystal electric field (CEF) environment at the Yb site, which splits the $4f$ multiplet into nondegenerate doublet levels [10] [subsec. 2.5.4]. Also, T_N shifts to lower temperatures as the magnetic field increasing to 55 kOe as is evidenced in $d(\chi T)/dT$ by the displacements of peak [inset of Fig. 4.14(b)]. Notice that T_N value is in general high compared to other compounds based on Yb magnetism, possibly due to the existence of a strong magnetic exchange interaction between Yb magnetic moments [82] [Eq. 2.18]. At high temperatures χ^{-1} shows typical paramagnetic behavior

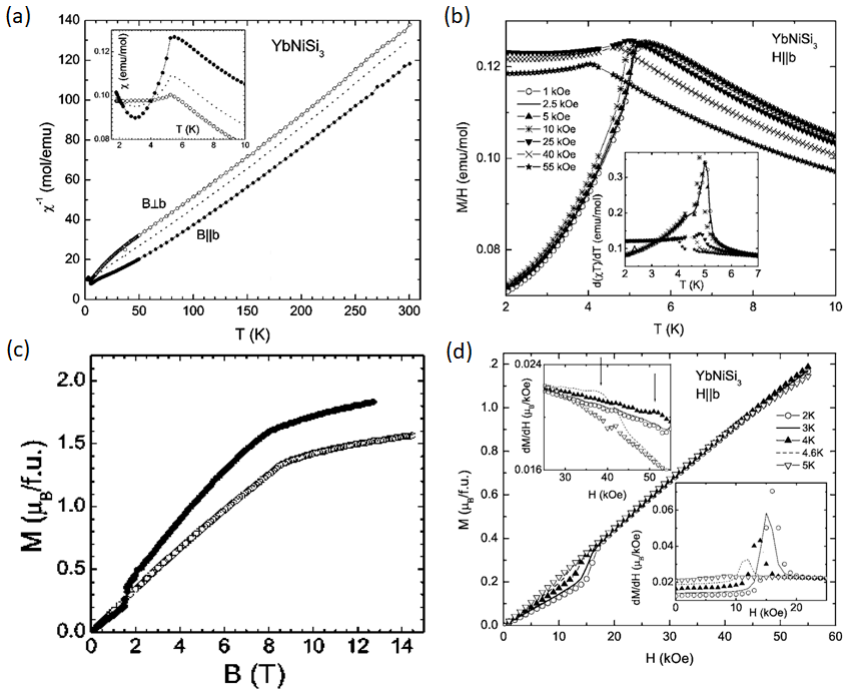

Figure 4.14: (a) Temperature dependence inverse susceptibility at $B = 0.1$ T in two crystal orientations $B \parallel b$ (solid symbols) and $B \perp b$ (open symbols), and the polycrystalline average (dotted lines). The inset shows the low temperature dependece of magnetic susceptibility detailing the antiferromagnetic transition at $T_N = 5.1$ K for two orientations mentioned before. (b) Magnetic susceptibility, $\chi = M/H$ as a function of temperature and magnetic field for $H \parallel b$. The inset displays $d(\chi T)/dT$ corresponding to the data in the main box. Magnetization isotherms are presented at (c) $T = 2$ K for two crystal orientations and (d) $2 \leq T \leq 5$ K for $H \parallel b$. The inset shows left-high temperature and right-low temperature corresponding to dM/dH curves. Figures (a) and (c) were taken from Ref. [10], while (b) and (d) from [80].

with CEF effects, where both curves are linear and parallel to each other. The Curie-Weiss law applied on the polycrystalline average yields an effective moment $\mu_{eff} = 4.45\ \mu_B$/f.u., very close to Yb^{3+} ions presented in Table 2.1. Furthermore, the paramagnetic Curie Weiss temperature is $\theta^p_{cw} = -11.6$ K, indicating an antiferromagnetic coupling between magnetic moments of Yb ions. Finally, for $M \times H$ at 2 K [Fig. 4.14(c)], the magnetic isotherms exhibit a spin-flop transition at $B = 1.7$ T on the $B \parallel b$ curve while both orientations show a change in the slope near 8 T, remaining below 2 μ_B/f.u. [10]. Also, as the temperature increases the metamagnetic transitions shift to lower fields [80] [right and left insets of Fig. 4.14(d)].

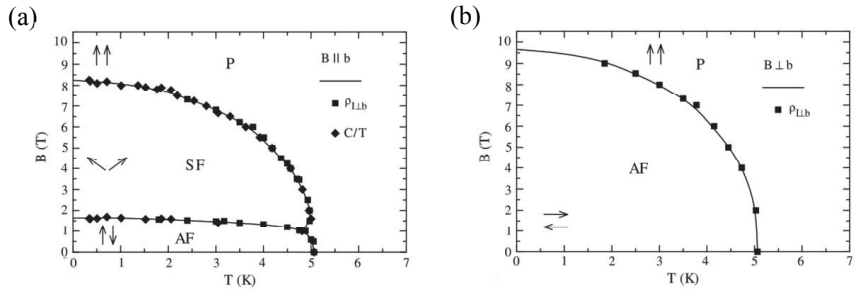

Figure 4.15: Magnetic phase diagram of $YbNiSi_3$ compound. These Figures are taken from Ref. [6].

From magnetization, resistivity or specific heat measurements it is possible to build the phase diagram of $YbNiSi_3$ for $H \parallel b$ and $H \perp b$ as shown in Fig. 4.15. As expected, for $H \parallel b$ a spin-flop transition appears at $B_{sc} = 1.7$ T where the magnetic moment changes from antiferromagnetic state (AF) to "canted" state (SF), and at the critical field $H_c = 8.3$ T the induced ferromagnetic state (P) is fully reached. On the other hand, for $H \perp b$ the magnetic moments suddenly changes from antiferromagnetic to induced ferromagnetic state with a critical field $H_c^{'} \approx 9.5$ T [80].

Kobayashi *et al.* [82] investigated the magnetic structure of the antiferromagnetic Kondo lattice $YbNiSi_3$ by neutron diffraction on a single-crystal sample. They found that it consists of Yb moments aligned ferromagnetically in the *bc* plane along the *b* direction and antiferromagnetically along the *a* axis [Fig. 4.16].

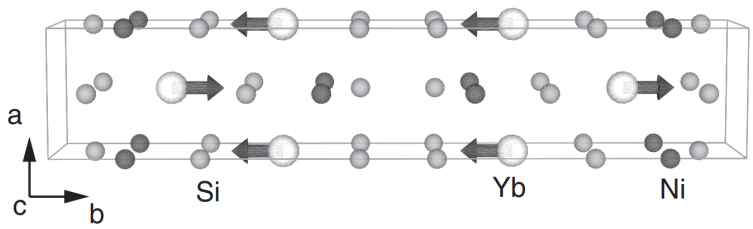

Figure 4.16: Magnetic structure representation of $YbNiSi_3$. White, gray and black balls represent Yb, Si and Ni atoms respectively. The black arrows indicate the Yb magnetic moments direction, which are aligned ferromagnetically in the *bc* plane and antiferromagnetic along the *a*-axis. Figure is taken from Ref. [82].

Comparing this magnetic structure with $Gd/TbNiSi_3$ [Fig. 4.11], Tartaglia *et al.* [79] perceived that in either case there is a planar ferromagnetic coupling

between magnetic moments, *ac* for R=Gd/Tb and *bc* for R=Yb, while there is an antiferromagnetic alignment between those nearest-neighbor planes. This indicates that the bilayers of R moments are the common magnetic units in this series. Therefore, the coupling between adjacent bilayers have the following pattern: + - + - for Gd/ $TbNiSi_3$ and + - - + in $YbNiSi_3$ along *b*-axis. So there is a change in the magnetic stacking pattern and this must be a consequence of the sign reversal of the effective Ruderman-Kittel-Kasuya-Yosida (RKKY) exchange coupling between the second-neighbor R *ac* layers when the interlayer distance decreases due to R ionic radius reduction from Gd/Tb to Yb [subsec. 2.5.2]. Thus, the magnetic properties of $RNiSi_3$ compounds between R=Gd and Yb are the result of competition between two different magnetic structures $GdNiSi_3$ and $YbNiSi_3$, and therefore there must be a certain critical value of *b* lattice parameter such that the + - + - pattern is stabilized against the competing + - - + ground state of $YbNiSi_3$ [79].

4.4 $YbNiGe_3$ an electronic isovalent

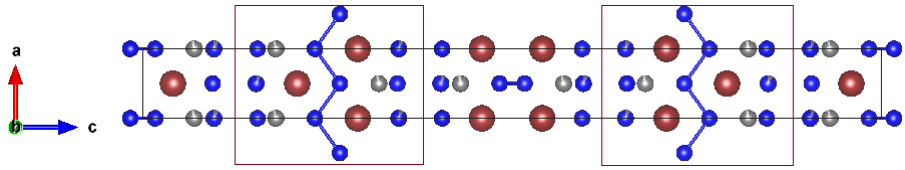

Figure 4.17: Unit cell of $YbNiGe_3$ tetragonal structure in space group $I4_1/amd$. Dark red, gray and blue spheres denote the Yb, Ni and Ge atomos, respectively.

Table 4.8: Atom coordinates for $YbNiGe_3$ compound [83].

Site	Wyckoff position	Site symmetry	x	y	z	Occ.
Yb	8*e*	2*mm*	0	0.25	0.4591(1)	1
Ni1	8*e*	2*mm*	0	0.25	0.8197(1)	0.93(1)
Ge1	8*e*	2*mm*	0	0.25	0.7669(1)	1
Ge2	8*e*	2*mm*	0	0.25	0.1553(1)	1
X(Ni/Ge)	8*e*	2*mm*	0	0.25	0.0965(1)	0.11/0.89(5)

In the literature $YbNiGe_3$ is found to crystallize in two different forms: (i) $SmNiGe_3$-type orthorhombic structure with space group *Cmm*, lattice parameters of *a*=4.044 Å, *b*=21.713 Å and *c*=4.077 Å and volume 357.99 $Å^3$ [6], and (ii)

new type of tetragonal structure with space group $I4_1/amd$ (No.141) with lattice parameters a=4.0503(0) Å and c=43.274(2) Å and volume 709.91 Å^3 [83,84], which it is presented in Fig. 4.17 and their Wyckoff Positions are included in Table 4.8. Comparison between Figs. 4.11 and 4.17 shows that although these structures have different space groups, both exhibit layered structures with one crystallographic site for Yb and one for Ni, and their unit cell differ only in the way of stacking. So $YbNiGe_3$ has the same fundamental building blocks as $SmNiGe_3$-type structure [see red squares], but the zig-zag chains of Ge atoms run along both the a and b directions [83].

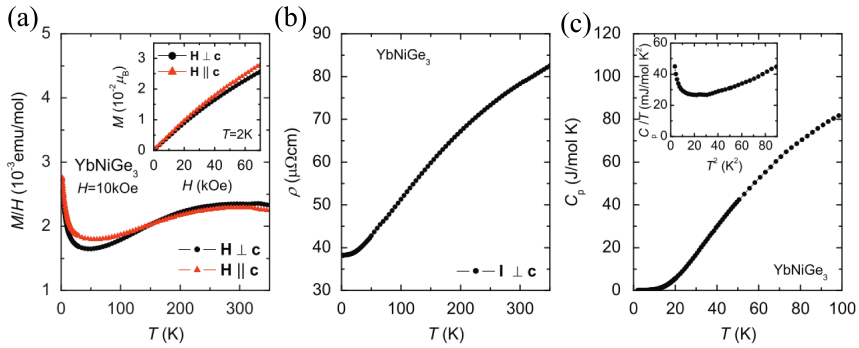

Figure 4.18: Physical properties of $YbNiGe_3$. (a) Temperature dependence magnetic susceptibility for $H \perp c$ and $H \parallel c$. Inset shows its respectively magnetization isotherm at 2 K. (b) Resistivity as a function of temperature for $I \perp c$ dependence resistivity. (c) Temperature dependence of specific heat which inset shows the $C_p/T \times T^2$ at low temperature. Figure taken from Ref. [83].

The Physical properties of $YbNiGe_3$ studied by Mun *et al.* [83] and their results are shown in Fig. 4.18. The temperature dependence susceptibility $\chi(T)$ is positive in the amount of 10^{-3} emu/mol, with an almost isotropic behavior consistent with divalent ytterbium. At low temperature the susceptibility increases due to either a small amount of Yb^{3+} ions or the presence of other paramagnetic impurities. This is followed by a minimum around of 50 K and a broad peak structure at high temperature suggests that a some small amount of Yb ions have a mixed valence. If the broad maximum is around of $T^* \approx 300$ K, this compound will have a Kondo temperature in $T_K \approx 3T^* \approx 900$ K [6, 85]. The inset show a magnetic field dependence magnetization $M(H)$ at $T = 2$ K, which it has a linear behavior up to 70 kOe with small magnetization values. The temperature dependence resistivity $\rho(T)$, in Fig. 4.18 (b), decreases to reduce the temperature from 300 to 50 K and at low temperatures shows a tendency toward saturation [Eq. 2.48]. The specific heat, Fig. 4.18(c), does not exhibit anomaly or feature that can be associated with a local magnetic

moment. The Sommerfeld coefficient calculated is $\gamma = 20$ mJ mol^{-1}K^{-2}. Thus, the physical properties of $YbNiGe_3$ indicate that it is non-magnetic metallic compound with Yb^{2+} state. This results are consistent with presented for $YbNiGe_3$ in orthorhombic structure [6].

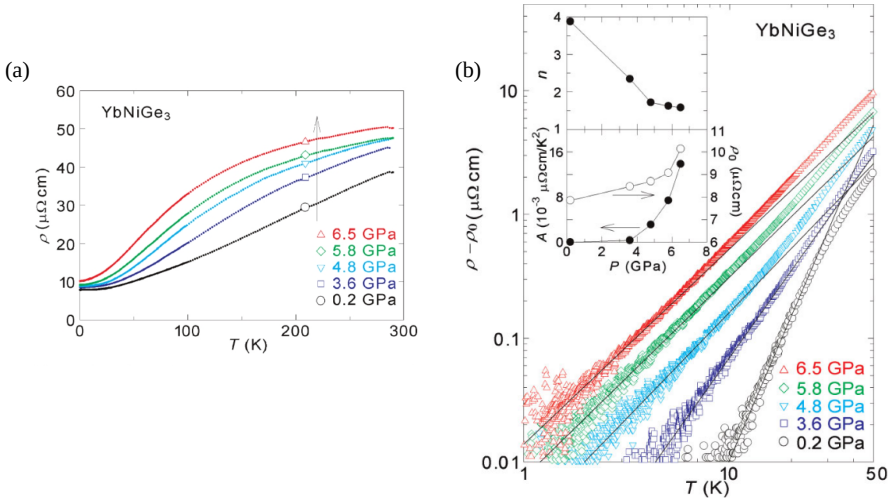

Figure 4.19: (a) Temperature dependence electrical resistivity. (b)Double logarithmic plot of the $\rho - \rho_0 \times T$ for $YbNiGe_3$ under various constant pressures. Solid lines represent the form $\rho - \rho_0 = AT^n$. The inset show a pressure dependence of n, A, and r_0. These Figures are taken from Ref. [8].

Umeo *et al.* [8] measured the electrical resistivity of a single crystal of $YbNiGe_3$ under pressures up to 6.5 GPa and at temperatures down to 0.3 K. Their results are summarized in Fig. 4.19. At $P = 0.2$ GPa, the $\rho(T)$ exhibits a normal metallic behavior without the Kondo effect. However, as the pressure increases, the value of $\rho(T)$ rises over the entire temperature range suggesting that the Kondo effect shows up with pressure. Additionally, they study the behavior of $\rho(T)$ below the 50 K according to the power form of $\rho(T) = \rho_0 + AT^n$ [Fig. 4.19]. At low pressure $n = 4$ near to 5 value which is associated with conventional electron–phonon scattering and it indicates that the electron–electron scattering is negligible. For P=3.6 GPa, $n \rightarrow 2$ expected for electron–electron scattering from Fermi-liquid theory [Eq. 2.48]. For P=6.5 GPa, $n \rightarrow 1.6$ presenting non-Fermi liquid behavior [86]. Spin-fluctuation theory for a three-dimensional antiferromagnet predicts a QCP when $n \approx 1.5$, which occurs at about 8 GPa. On the other hand, as n decreases with pressure occurs an enhancement of both A and ρ_0 [inset Fig. 4.19] which may be indicative of the valence change in the compound [8].

From here Sato *et al.* [84] began to study the Yb valence in $YbNiGe_3$ by

resonant X-ray absorption spectroscopy in Lα_1 partial fluorescence yield mode (PFY-XAS) and resonant X-ray emission spectroscopy (RXES) around the Yb L_3 absorption edge under pressures from 0 to 15.6 GPa at 300 K and to 7.7 GPa at 17 K. The results are summarized in Fig. 4.20. PFY-XAS show that at ambient pressure and room temperature there are two peaks whose intensities are comparable: one associated with the Yb^{2+} peak at $h\nu_{in} = 8938$ eV and the other with the Yb^{3+} peak at $h\nu_{in} = 8945$ eV. Thus, the Yb valence is approximately $v = 2.52$ indicating that Yb^{2+} and Yb^{3+} ions are almost equally distributed in the compound. However, when the pressure is applied the spectral weight of Yb^{2+} is continuously transferred to the Yb^{3+} peaks. The valence reaches $v = 2.87$ and thus the Yb ions approach the trivalent state. Also, the difference in valence at 300 K and 17 K is small at low pressures, where for the latter are $v = 2.45$ and $v = 2.72$ for 0 and 7.7 GPa, respectively [Fig. 4.20(c)]. Additionally, pressure derivatives of the Yb valence (dv/dP) exhibits a drops between 5 and 10 GPa, a range where a QCP is expected. On the other hand, they also measured temperature-dependent PFY-XAS and RXES spectra of $YbNiGe_3$ and $YbNiSi_3$ at ambient pressure by varying the temperature from 8 to 299 K [Fig. 4.21]. For $YbNiGe_3$ they found that the Yb valence weakly reduced with decreasing temperature [84]. In contrast, PFY-XAS spectrum for $YbNiSi_3$ exhibits a large peak associated to Yb^{3+} followed by a weak peak assigned with to a small fraction of Yb^{2+} ions, and a small peak at $h\nu_{in} = 8945$ eV attributed to the quadrupole transition. Therefore, Yb valence is close to 3 with almost no temperature dependence [Fig. 4.20 (e) and (f)].

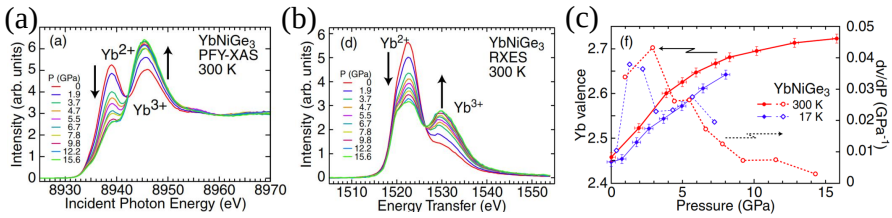

Figure 4.20: (a) Pressure dependencies of the PFY-XAS spectral and (b) RXES spectral around the Yb L_3-edge for $YbNiGe_3$ at 300 K. (c) Yb valences at 300 and 17 K as a function of pressure derived from the RXES spectral. These Figures are takes from Ref. [84].

Next, they investigate the difference in the electronic structure of $YbNiX_3$ (X=Si, Ge) by hard X-ray photoemission spectroscopy (HAXPES) on Ni $2p$ and Yb $3d$ core level, and Yb valence-band [85]. Their results are included in Fig. 4.22. Ni $2p$ core level spectrum have two peaks $2p_{3/2}$ and $2p_{1/2}$ [Fig. 4.22(a)] with a binding energy difference between the two compounds of $\Delta E_B = 0.6$ eV lower for X=Ge. Therefore, they have similar electronic conduction states. In

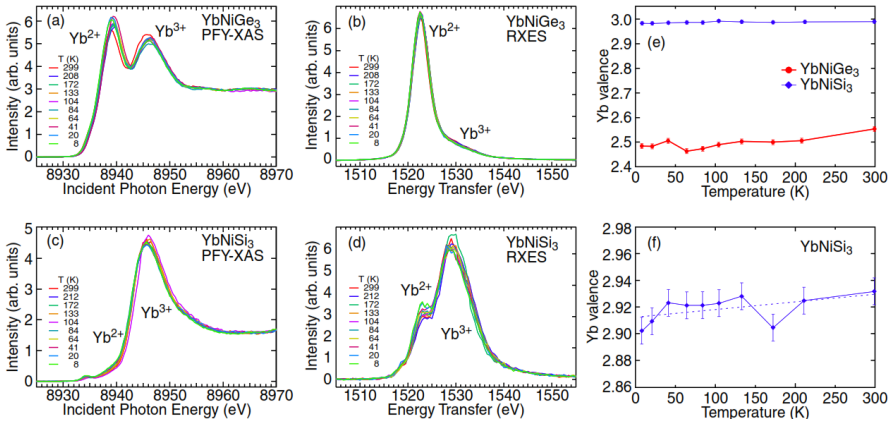

Figure 4.21: (a) Temperature dependence of the PFY-XAS spectral and (b) RXES spectral around the Yb L_3-edge for $YbNiGe_3$ at ambient pressure. (c) Temperature dependence of the PFY-XAS spectral and (d) RXES spectral around the Yb L_3-edge for $YbNiSi_3$ at ambient pressure. (e)Temperature dependencies of the Yb valences in $YbNiGe_3$ and $YbNiSi_3$ derived from PFY-XAS spectra. (f) Temperature dependence of the Yb valence in $YbNiSi_3$ derived from RXES spectra. These figures are taken from Ref. [84].

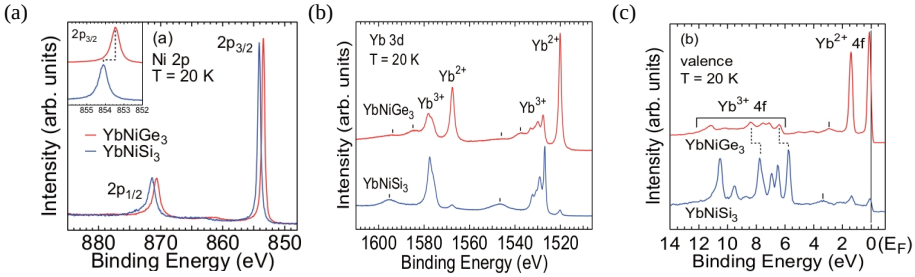

Figure 4.22: HAXPES spectral of $YbNiX_3$ (X=Si, Ge) measured at 20 K for (a) Ni $2p$, (b) Yb $3d$ and (c) Valence band. The inset in (a) show the Ni $2p_{3/2}$ region expanded. These figures are taken from Ref. [85].

contrast, Yb $3d$ core spectrum is split into $3d^{5/2}$ (1515-1560 eV) and $3d^{3/2}$ (1560-1605 eV) regions, where both Yb^{2+} and Yb^{3+} valence states are resolved [Fig. 4.22(b)]. X=Ge has comparable Yb^{2+} and Yb^{3+} peaks so Yb valence is strongly fluctuating in this compound, whereas X=Si shows weak Yb^{2+} peaks and its Yb valence is $v \sim 3$ as indicated above. The previous was corroborated in the valence-band HAXPES spectra for $YbNiGe_3$ which exhibits Yb^{3+} and Yb^{2+} $4f$-structures where the latter is formed by $4f^{7/2}$ and $4f^{5/2}$ peaks just below E_F, while $YbNiSi_3$ has only Yb^{3+} structures [Fig. 4.22(c)].

4.5 Some remarks

$RNiSi_3$ series (R = Gd-Tm) display rich magnetic properties such as anisotropic magnetization, multiple metamagnetic steps, hysteresis, double transitions and other magnetic phenomena.

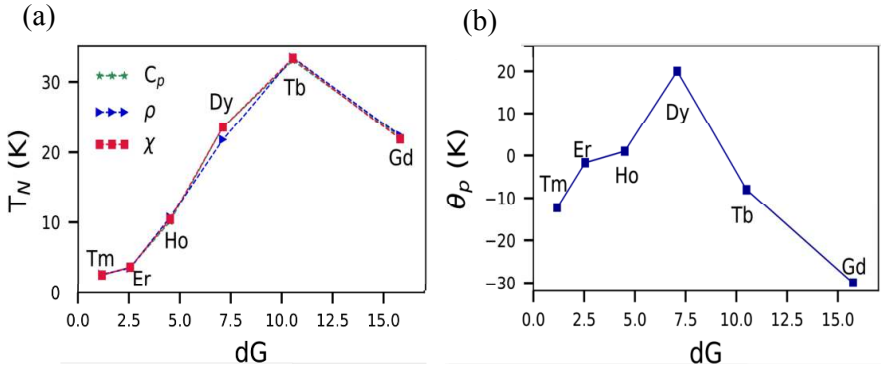

Figure 4.23: Néel temperature dependent Gennes factor $dG = (g_J - 1)^2 J(J+1)$ obtained from the experimental specific heat, resistivity, and magnetic susceptibility. (b) Dependence of the paramagnetic Curie-Weiss temperature θ^p_{cw} on dG [1,2]. De Gennes values for rare earth atoms are indicated in Table 2.1.

In systems where the magnetism originates solely from the rare earth ions,

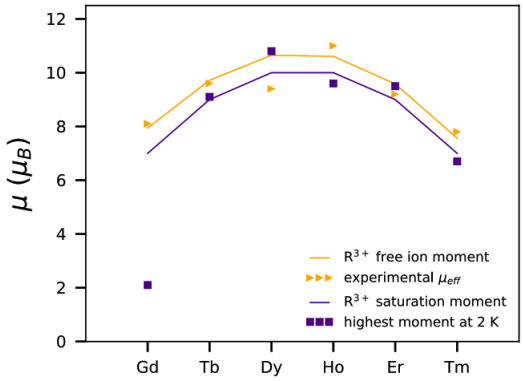

Figure 4.24: Experimental effective magnetic moment and highest observed moment at 2 K. The lines indicate the theoretical value of the free rare earth ions and their saturation moment [1,2].

that maintain the same valence throughout the series and show a J_{RKKY} constant, T_N and θ_{cw} are expected to vary linearly with the de Gennes factor [Eq. 2.18], making even Gd-based compounds show the highest temperature [Table 2.1]. However, Fig. 4.23 shows that $RNiSi_3$ series do not follow this scaling and R=Tb exhibit the maximum T_N. This behavior was verified by magnetization, resistivity and specific heat measurements. This may be due to the influence of other factors such as crystalline field effects and exchange anisotropy which change the Hamiltonian system and thus lead to deviations from the expected proportionality of the case where only RKKY is taken into account. On the other hand, $\theta_{cw}^{p} \times dG$ show positive values for $DyNiSi_3$ and $HoNiSi_3$, whose specific heat measurements reveal two magnetic transitions. These can be associated with the competition between these phases and the possible existence of ferromagnetic interaction that can cause a reduction of steps in metamagnetic transitions, the appearance of magnetic component along c-axis leading two antiferromagnetic axis and the reduction of hysteresis when going from $TbNiSi_3$ to $HoNiSi_3$. Therefore, these serve as a bridge to change in the easy axis of a to b. In view of this, it is worth noting that the magnetic properties, magnetic entropy change and magnetocaloric effect have recently been studied in the $DyNiSi_3$ compound, which appears to have potential for use in magnetic refrigerators [87].

The series under investigation have similar properties with respect to the $RNiGe_3$ family [83]. Both have an antiferromagnetic character, their effective magnetic moments are close to the theoretical values of free trivalent rare-earth ions and the Néel temperature does not scale with the de Gennes factor despite the fact that they are higher than in our case. Moreover, both Gd-compounds show similar magnetic behaviors indicating that they have the same magnetic structure. On the other hand, metamagnetism is observed only for some compounds. $NdNiGe_3$ is the only member showing two magnetic transitions. Also, $TbNiGe_3$ and $DyNiGe_3$ exhibit phase diagrams that are relatively simple. Therefore, the substitution of Ge for Si changes the crystalline field which plays a key role in understanding the complex magnetic behavior, due to the presence of multiple magnetic transitions and hysteresis observed in $RNiSi_3$ but not in $RNiGe_3$ series.

Despite the fact that $YbNiGe_3$ has a different space group and Bravais lattice with respect to $YbNiSi_3$, they are considered as electronic isostructural because both Ge and Si elements donate similar valence electrons ($4s^2 4p^2$ and $3s^2 3p^2$, respectively) to the conduction band of $YbNiX_3$ (X=Si, Ge), as verified in the HAXPES measurements mentioned above.

On the other hand, the effect of pressure on $YbNiSi_3$ suppresses its ordered state by moving to the non-magnetic state, while the application of magnetic

field causes that γ following the trend generally observed in materials close to a QCP [80] [Fig. 4.12(c)]. In contrast, for $YbNiGe_3$ the Kondo effect is induced by pressure leading its ground state to approach a QCP [Fig. 4.19]. Thus, as mentioned in sec. 2.9, it is possible to pass through a QCP by tuning parameters such as temperature, magnetic field, hydrostatic pressure or chemical composition. Our goal then is to be the pioneers in studying the quantum-critical behavior through $YbNiSi_{3-x}Ge_x$ alloys, a research topic that we will discuss it in sec. 8.

Part II

Research

5

Superconductivity in $YNiSi_3$ and $LuNiSi_3$

In the previous chapter we mentioned that both $YNiSi_3$ and $LuNiSi_3$ are strongly anisotropic diamagnetic compounds with metallic character in the temperature range from 2 to 300 K [sec. 4.2]. Here, we will focus on the study of their physical properties below 2 K where they have exhibited the phenomenon of superconductivity. In addition, we will discuss their electronic and phononic properties from results obtained by first-principles calculations.

5.1 Experimental results

In order to ensure that the superconductivity exhibited by $YNiSi_3$ and $LuNiSi_3$ crystals is not an extrinsic effect arising from Sn flux inclusions, which occurs at $T_c = 3.7$ K for pure Sn, elemental analysis was carried out on these samples. The results revealed a composition of $Y_{0.96(11)}Ni_{1.00(19)}Si_{3.09(18)}$ and $Lu_{1.00(1)}Ni_{0.68(2)}Si_{3.13(2)}$ with significant Ni vacancies. Moreover, no significant amount of Sn was evident in both cases.

The temperature dependence of resistivity for several magnetic fields, with $H \parallel b$ and $H \perp b$ orientations, is presented in Fig. 5.1. For $H = 0$ kOe there is an abrupt drop to zero resistivity at 1.42(2) K for $YNiSi_3$ and 1.63(2) K for $LuNiSi_3$, indicating the transition from a normal electrical resistivity state to a superconducting state [subsec. 2.8.3]. In the presence of magnetic fields, the critical temperature decreases and a small broadening appears in the transition. We observed that the superconducting behavior occur even at 10 mT and 40 mT with $H \parallel b$ and $H \perp b$ configurations, respectively for $YNiSi_3$, in contrast to 20 mT with $H \parallel b$ and 80 mT with $H \perp b$ for $LuNiSi_3$ [77]. Also, strong anisotropy is also evident on these curves which is in agreement with what was mentioned in sec. 4.2.

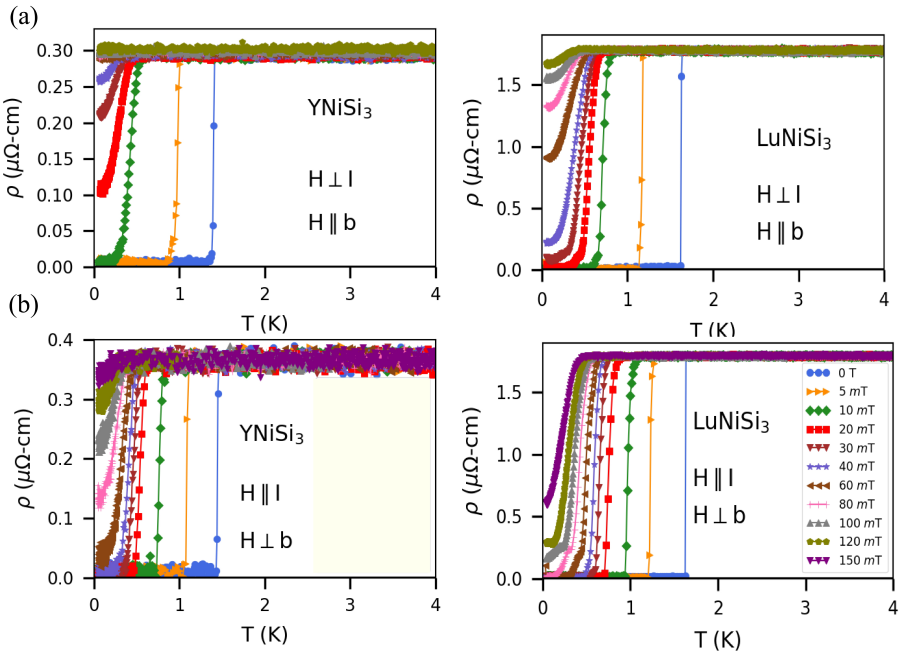

Figure 5.1: Temperature dependence for the electrical resistivity, under magnetic fields $0 < H < 150$ mT, for $YNiSi_3$ and $LuNiSi_3$ in the configurations (a) $H \parallel b$ and (b) $H \perp b$.

Susceptibility measurements as a function of temperature $\chi(T)$ at zero field cooled (ZFC) mode, with a magnetic field of $\mu_0 H = 2$ mT for $YNiSi_3$ and 1 mT for $LuNiSi_3$, are shown in Fig. 5.2(a). The susceptibility curves reach -1 at 0.5 K, indicating that at this temperature the bulk of both samples completely expels the external magnetic field and a perfect diamagnetism begins to emerge due to the Meissner effect. As the temperature rises the susceptibility also increases, until it reaches the value of 0 at $T_c = 1.31(2)$ K for $YNiSi_3$ and 1.58(2) K for $LuNiSi_3$, where the bulks have attained the normal-state diamagnetic response [77]. On the other hand, magnetic field dependent magnetization [Fig. 5.2(b)] for several temperatures below the superconducting transition displays $M = -H$ behavior at low magnetic field, followed by an abrupt jump to $M = 0$ at the critical magnetic field H_c, typical signature of a type I superconductor. However, they present an irreversible behavior, which as mentioned in subsec. 2.8.3 they are associated with some impurities or crystalline faults such as Ni vacancies inside the samples that trap the magnetic flux and generate magnetic hysteresis. Moreover, these superconductors have a simple magnetic phase diagram $H_c \times T$ [Fig. 5.2(c)] where the data points follow the empirical parabolic law of Eq. 2.54. Here we estimated that at

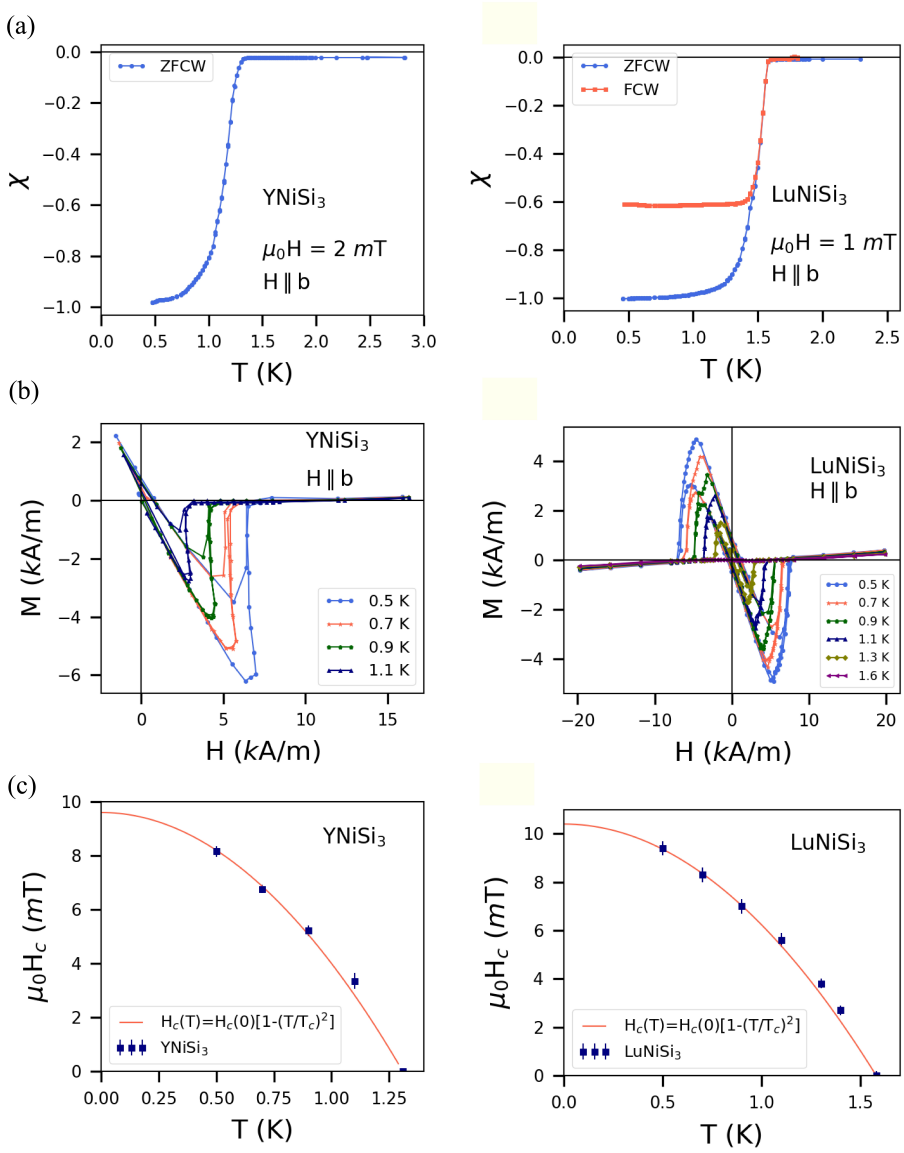

Figure 5.2: Magnetization measurements for $YNiSi_3$ and $LuNiSi_3$. (a) Temperature dependence of susceptibility at $\mu_0 H = 2$ mT using a zero-field-cooled warming (ZFCW) protocol. For $LuNiSi_3$ the field cooled warming (FCW) curve was also measured. (b) $M \times H$ curves for $0.5 < T < 1.6$ K. (c) $\mu_0 H_c \times T$ phase diagram constructed from temperatures and critical magnetic field values obtained from (b) and the empirical parabolic law curve given by Eq. 2.54.

$T = 0$ K the critical magnetic field corresponds to $\mu_0 H_c(0) = 9.6(2)$ mT for $YNiSi_3$ and 10.4(2) mT for $LuNiSi_3$ [77].

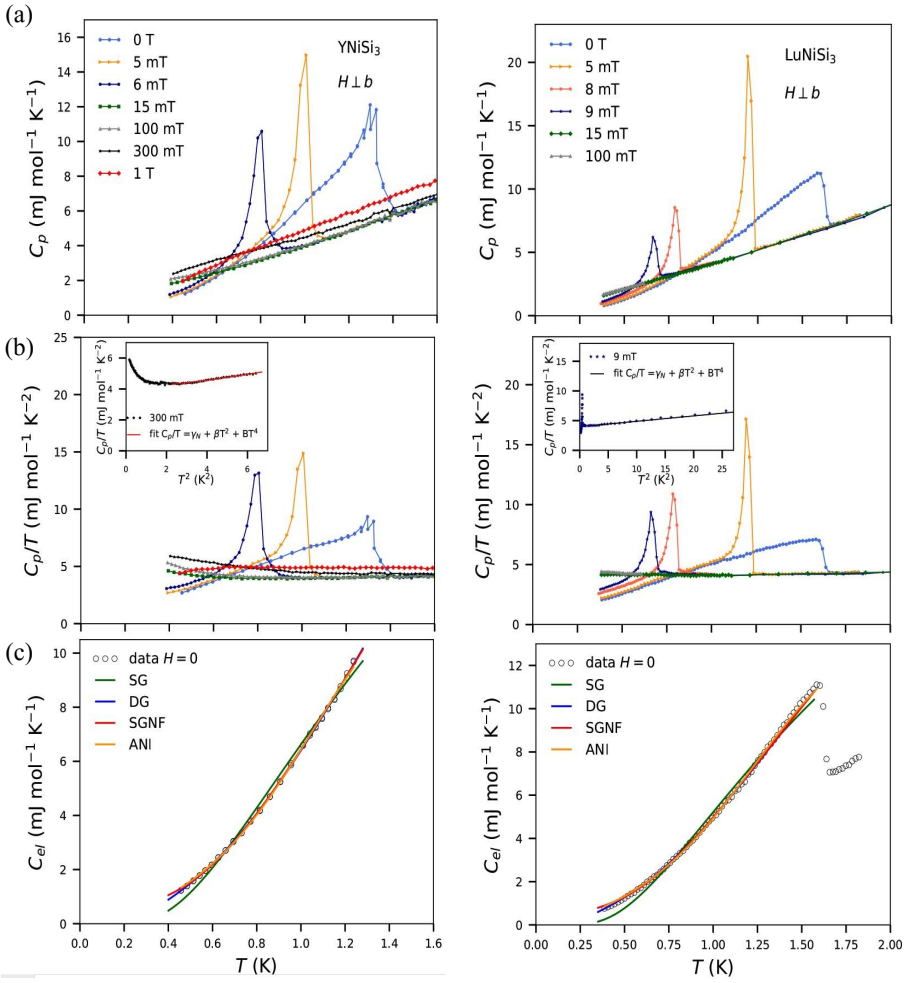

Figure 5.3: (a) Temperature dependence of specific heat and (b) $C_p/T \times T$ curve in the presence of magnetic fields $0 < H < 1$ T for $YNiSi_3$ and $LuNiSi_3$. The inset in (b) shows the Debye model fit to the $C_p/T \times T^2$ data. (c) Electronic contribution to specific heat at $H = 0$ together with the fits of different superconducting gap models, [Eq. 2.57-2.60] for both compounds.

The temperature-dependent specific heat $C_p(T)$ for different magnetic fields is presented in Fig. 5.3. We observe that at $H = 0$ there is a jump at 1.35(5) K for $YNiSi_3$ and 1.63(2) K for $LuNiSi_3$. Furthermore, for both compounds the transition temperature shifts to lower temperatures when the magnetic field increases. Note that the jumps at 5 mT are larger than at zero field,

suggesting a first-order transition for $H \neq 0$. Also, no anomaly at 15 mT is observed. In the normal state we fit the Debye model according to Eq. 2.31 including an additional phonon contribution of the form BT^4 [inset Fig. 5.3(b)]. We obtain $\gamma = 4.04(9)$ mJ mol^{-1}K^{-2}, $\beta = 0.0961(5)$ mJ mol^{-1}K^{-4} and $B = 0.0090(5)$ mJ mol^{-1}K^{-6} for $YNiSi_3$ and $\gamma = 3.97(9)$ mJ mol^{-1}K^{-2}, $\beta = 0.0910(5)$ mJ mol^{-1}K^{-4} and $B = 0.00044(9)$ mJ mol^{-1}K^{-6} for $LuNiSi_3$. These values allow us determine the Debye temperatures $\Theta_D = 466(9)$ and 474(8) K [Eq. 2.25], the densitiy of states at the Fermi level $D(E_F) = 1.71$ and 1.69 states/eV f.u. [Eq. 2.28], and therefore the electron-phonon coupling constant $\lambda_{e-ph} = 0.43(2)$ and 0.44(2) [Eq. 2.62], for $YNiSi_3$ and $LuNiSi_3$, respectively, indicating that both compounds are in the weak-coupling regime [77]. These results are summarized in Table 5.1. Since the critical temperatures measured by the three independent techniques are different, we consider the average on these, corresponding to $T_c = 1.36(3)$ K and $T_c = 1.61(2)$ K for $YNiSi_3$ and $LuNiSi_3$, respectively.

Table 5.1: The main parameters obtained from experimental measurements for $YNiSi_3$ and $LuNiSi_3$: critical temperature, Sommerfeld coefficient, density of states, Debye temperature, electron-phonon coupling, specific heat jump at the critical temperature, critical magnetic field at $T = 0$ K, London penetration depth, BCS coherence length and Ginzburg-Landau (GL) parameter.

	$YNiSi_3$	$LuNiSi_3$
T_c (K)	1.36(3)	1.61(2)
γ (mJ mol^{-1}K^{-2})	4.04(9)	3.97 (9)
$D(E_F)$ (states/eV f.u.)	1.71	1.69
Θ_D (K)	466(9)	474(8)
λ_{e-ph}	0.43 (2)	0.44(2)
$\Delta C_{el}/\gamma_N T_c$	1.14(9)	0.71(5)
$\mu_0 H_c(0)$ (mT)	9.6(2)	10.4(2)
λ_L (nm)	34 (3)	33(3)
ξ_0 (nm)	780(80)	690(70)
κ	0.113(11)	0.42(4)

For a superconductor in the weak-coupling regime, the Bardeen–Cooper–Schrieffer (BCS) theory predicts that the specific heat jump at T_c is 1.43 [subsec. 2.8.3] for a s-wave gap. However the estimated values for $YNiSi_3$ and $LuNiSi_3$ correspond to 1.14(9) and 0.71(5), respectively, lower than expected. In order to determine the type of superconducting gap in these compounds, we consider different models: a single-gap (SG) α model for BCS [Eq. 2.57], a double gap (DG) α model [Eq. 2.58], a single-gap α model with a non-superconducting contribution fraction (SGNF) [Eq. 2.59] and finally, an anisotropic gap (ANI) model [Eq. 2.60]. The parameters obtained by the

fittings are listed in Table 5.2. The SG model gave a poor fit, while the quality of the others fits is much better. Although they represent different physical hypotheses [sec. 5], the latter result in quite similar fits. As a consequence, we cannot exactly determine the superconducting gap structure in $YNiSi_3$ and $LuNiSi_3$, however we can claim that it is not simple and it must be similar in both compounds.

Table 5.2: Fit parameters of C_{el} in the superconducting region for $YNiSi_3$ and $LuNiSi_3$. A_i and α' are dimensionless, Δ_0 is measured in 10^{-23} J and γ_2 in mJ mol^{-1}K^{-2}.

C_{el} model	A_i	Δ_0	f	γ_2	α'
$YNiSi_3$					
SG	7.4	2.4	-	-	-
DG	16.2	1.3; 4.5	0.11	-	-
SGNF	10.1	3.5	-	2.42	-
ANI	-	0.9	-	-	-9.0
$LuNiSi_3$					
SG	5.5	2.6	-	-	-
DG	9.4	1.1; 4.3	0.099	-	-
SGNF	6.3	3.7	-	2.21	-
ANI	-	0.9	-	-	-9.0

As mentioned in subsec. 2.8.3 the superconducting state has a higher degree of order than the normal state, so the entropy of the superconducting state is lower than the normal state and therefore its free energy. Figure 5.4(a) shows the behavior of these curves obtained from Eq. 2.55 and 2.56 for $YNiSi_3$ and $LuNiSi_3$. We see that the shape of these is very similar for both compounds, and that for the latter they are more shifted toward higher temperature values. Now, as the application of magnetic field raises the free energy in the superconducting state [Eq. 2.55] and this is seriously affected by temperature, we can use this dependency to construct the phase diagram for both compound as shown in Figure 5.4, where comparatively we include the phase diagrams obtained from resistivity, specific heat and magnetization measurements. Table 5.3 summarizes the critical temperatures and critical magnetic fields obtained for each case. Notice that the critical field of 7.0 and 8.3 mT achieved from thermodynamic quantities is lower than 9.6(2) and 10.4(2) mT found by magnetization measurements for $YNiSi_3$ and $LuNiSi_3$, respectively. In addition, H_c values obtained from resistivity measurements with $H \perp b$ configuration, at low temperatures, is higher compared to other experimental techniques. In the literature this behavior was reported in the type-II superconductor $LaPdSi_3$ [88], and it was interpreted as arising from

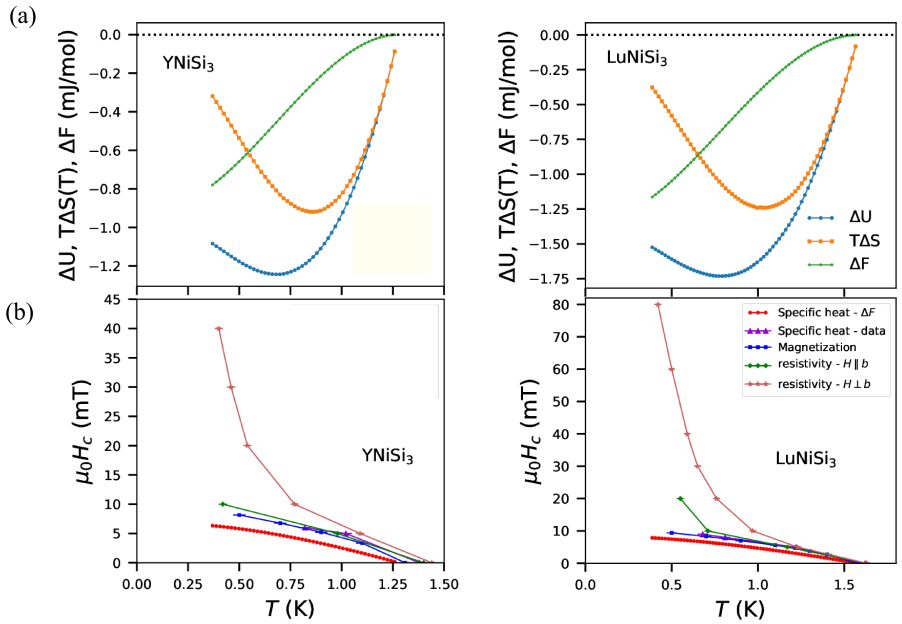

Figure 5.4: (a)Temperature dependence of the internal energy difference ΔU, latent heat $T\Delta S$ and free energy ΔF for $YNiSi_3$ and $LuNiSi_3$. (b) Temperature dependence of the critical field $H_c(T)$ obtained from free energy, specific-heat, magnetization and resistivity.

surface superconductivity.

Table 5.3: Critical temperature and critical magnetic field obtained from resistivity, specific heat and magnetization. As a reference we include the values obtained by free energy according to Eq. 2.55.

	$YNiSi_3$		$LuNiSi_3$	
	T_c (K)	$\mu_0 H_c(0)$ (mT)	T_c (K)	$\mu_0 H_c(0)$ (mT)
Specific heat -ΔF	-	7.0	-	8.3
Specific heat -data	1.35(5)	>6	1.63(2)	>9
Magnetization	1.31(2)	9.6(2)	1.58(2	10.4(2)
Resistivity $H \parallel b$	1.42(2)	>10	1.63(2)	>20
Resistivity $H \perp b$	1.42(2)	>40	1.63(2)	>80

The basic superconducting parameters for $YNiSi_3$ can be calculated considering an electron-density of $n = 12/V_{cell} = 3.70 \times 10^{28}$ m^{-3} (12 is the number of electrons in $YNiSi_3$ -three electrons for each Y^{3+} atom for four formula units of the compound (Z=4)- and V_{cell}=324.49Å^3) in which electrons have an effective

mass of $m^* = 1.54\ m_0$ [Eq. 2.29], and they move along the mean free path $l = 347$ nm [Eq. 2.46]. So the BCS coherence length, London penetration depth and the Ginzburg-Landau (GL) parameters can be estimated from Eqs. 2.51-2.53 as $\xi_0 = 780(80)$ nm, $\lambda_L = 34(3)$ nm and $\kappa = 0.113(11) < 1/\sqrt{2}$, respectively. For $LuNiSi_3$ we found $n = 3.83 \times 10^{28}$ m^{-3}, $m^* = 1.51m_0$, $l = 63$ nm, $\xi_0 = 690(70)$ nm, $\lambda_L = 33(3)$ nm and $\kappa = 0.42(4) < 1/\sqrt{2}$. Here, it is considered that all Y and Lu atoms have 3+ valence, each compound has four formula units per unit cell and their Fermi surface is spherical.

5.2 Theoretical results

The ground state crystal structure of $YNiSi_3$ and $LuNiSi_3$ was determined in the follow steps:

- We determine the converged calculations parameters [sec. 3]. In Elk code (FP-APW method) the muffin-tin radius are R^Y_{MT}=2.7777, R^{Lu}_{MT}=2.7495, R^{Ni}_{MT}=2.0563 and R^{Si}_{MT}=2.0563 for Y, Lu, Ni, Si, respectively, while the plane wave cuttof $R_{MF}|\mathbf{G}+\mathbf{k}|_{max}$ was converged to 9.5. For VASP code the cutoff energy for the plane-wave basis $E_{cut} = \frac{\hbar^2}{2m}G^2_{cut}$ where $|\mathbf{G}+\mathbf{k}| < G_{cut}$ is 550 eV. Also, in both codes, $\mathbf{k}$ grid was chosen to be a uniformly spaced: grid of $8 \times 8 \times 8$ for structural relaxation and $16 \times 16 \times 16$ for the calculation of the electronic properties ($E_n(\mathbf{k})$, DOS and Fermi surface).

- The next step was to check if Ni and Y(Lu) present some magnetic order in these compounds, knowing that the first is commonly a magnetic ion while that the last ones are not. For this purpose we consider two configurations for each atomic sublattice: parallel and antiparallel spin. As a result we obtained that both configurations converge to a non-magnetic ground state with zero local magnetic moment characteristic of diamagnetic compounds.

- The equation of state associated with each compound was then studied. Here, we simulate expansion and compression effects on $YNiSi_3$ and $LuNiSi_3$ by making volume changes of approximately 1%, while the ionic and cell shape are relaxed [Fig. 5.5]. These values were fitted by Birch-Murnaghan equation of state (3rd order) [Eq. 2.9]. The lattice parameters, volume and bulk modulus obtained are given in Table 5.4. Here we include the values found from XRD measurements previously shown in Table 4.1. Comparing experimental and theoretical values, we notice that the absolute error for the lattice constant is less than 1% for

both compounds, while the volume absolute errors are 1.71% and 1.56% for $YNiSi_3$ and $LuNiSi_3$, respectively.

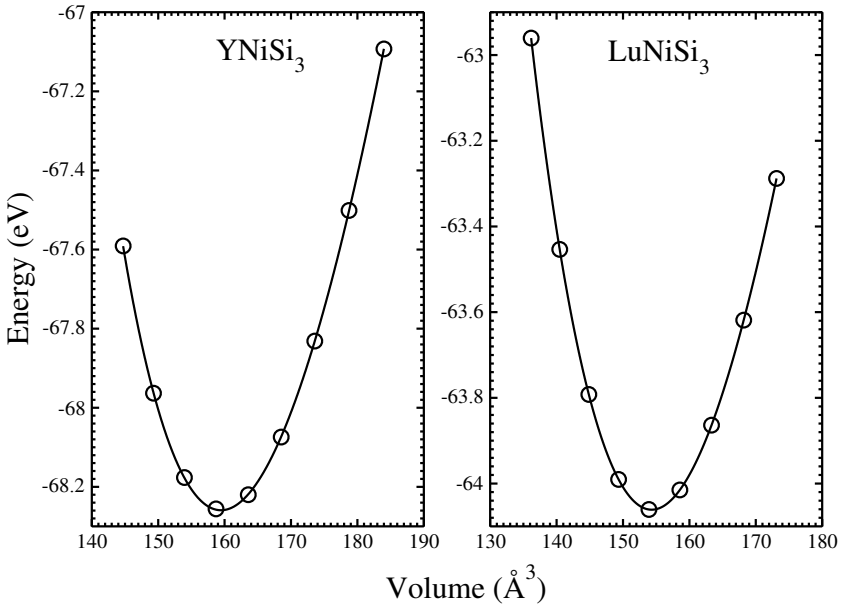

Figure 5.5: Total energy of $YNiSi_3$ and $LuNiSi_3$ as a function of the volume.

Table 5.4: Calculated lattice parameters a, b and c, volume Ω and bulk modulus B for $YNiSi_3$ and $LuNiSi_3$ compounds using PBESol exchange functional with VASP code.

Compound	a (Å)	b (Å)	c (Å)	Ω (Å^3)	B (GPa)
$YNiSi_3$					
Experimental	3.9216(1)	20.9448(6)	3.9506(1)	324.49(2)	-
Theoretical	3.8952	20.8969	3.9183	318.949	128
$LuNiSi_3$					
Experimental	3.8808(3)	20.792(1)	3.8868(3)	313.62(4)	-
Theoretical	3.8558	20.7553	3.8579	308.741	135

Having determined the ground state crystal structure for $YNiSi_3$ and $LuNiSi_3$, we proceed to calculate their bonding, electronic, elastic and phononic properties.

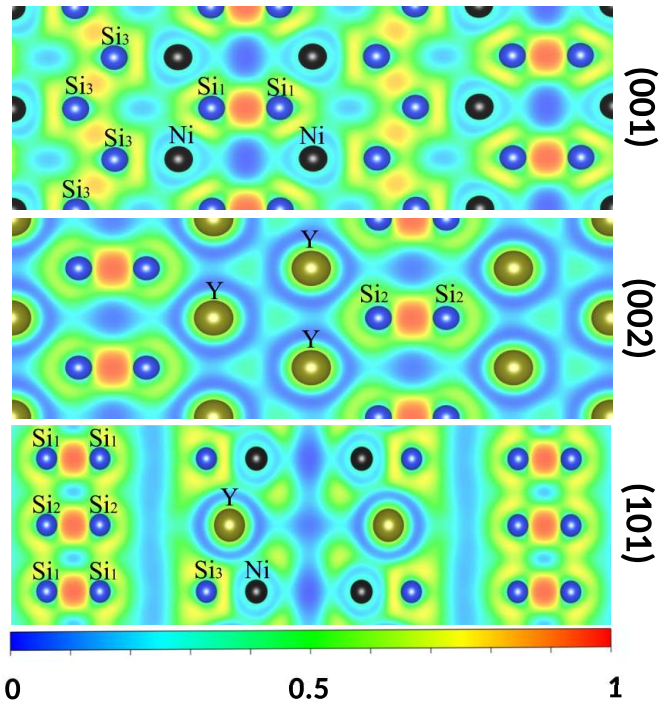

Figure 5.6: Calculated electron localization function (ELF) for $YNiSi_3$; upper, middle and bottom panels show the (001), (002) and (101) planes, respectively.

5.2.1 Bonding properties

The bonding properties of superconductors depend on how the electrons are spatially distributed in the compound. As described in subsec. 2.3.4, this can be known from the electron localization function (ELF), which we show in Figure 5.6 for $YNiSi_3$. In order to perform a comprehensive analysis of this function we will consider three different planes in the crystallographic structure: (001), (002) and (101) planes that are associated with $NiSi_2$, YSi and YNiSi layers according to Figure 4.3. We observe that between Si_1 atoms (dimers in the (001) plane and linear chains along [010] direction) and between Si_3 atoms (zigzag chain along [100] direction) the ELF presents a maximum value of 0.95 and 0.82, respectively. According to ELF definition [Eq. 2.12] these values indicate covalent bonds in both cases, while Ni-Si atoms reveal the metallic character of these bonds (maximum value of 0.48). On the other hand, on the (002) plane while Si_2 atoms (dimers) exhibit covalent bonds, Y-Si_2 has a

metallic bond (maximum value 0.51) and Y-Y has an ionic nature (maximum value 0.21). Finally, the calculated ELF on (101) shows a weakly metallic behavior of the Y–Ni bond (maximum value 0.32). In summary, $YNiSi_3$ displays all kind of chemical bonds: ionic (between Y atoms), metallic (between Ni–Si, Y–Si, and Ni–Y) and covalent (within the Si dimers and zigzag chains). The same properties were observed in $LuNiSi_3$ compound which is not presented here due to similarity with calculated ELF for $YNiSi_3$.

5.2.2 Electronic properties

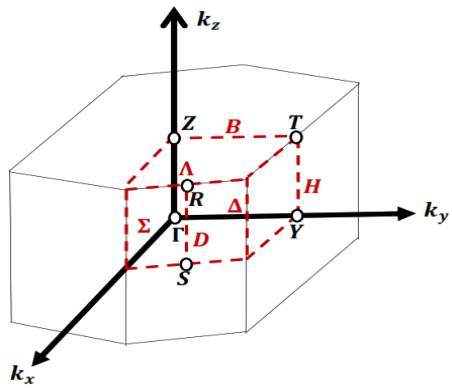

Figure 5.7: First Brillouin zone (FBZ) of the space group *Cmmm* with high symmetry points (Γ, *Y*, *T*, *Z*, *R* and *S*) and high symmetry directions (Δ, *H*, *B*, Λ, *D* and Σ).

The electronic properties of these superconductors can be accessed from a detail study of the band structure, total and partial density of states and the Fermi surface [subsec. 2.3.1-2.3.3]. In Figure 5.8 we show the calculated band structure along the high symmetry directions of the first Brillouin zone (FBZ) [Fig. 5.7] without and with SOC interaction for both superconductors. For the last one, was plotted the total and projected DOS for one spin direction. Comparing the band structure we observe that both compounds present a similar band topology in the conduction region and in the vicinity of Fermi level, regions that are not affected by SOC interaction. The conduction bands are the result of the hybridization of *d* states coming from the metallic atoms with Si *p*-states, and for energies larger than 1 eV with Si *s*-states. On the other hand, there are three partially occupied bands crossing the Fermi level. They are denoted by magenta, violet and green color and labeled as first, second

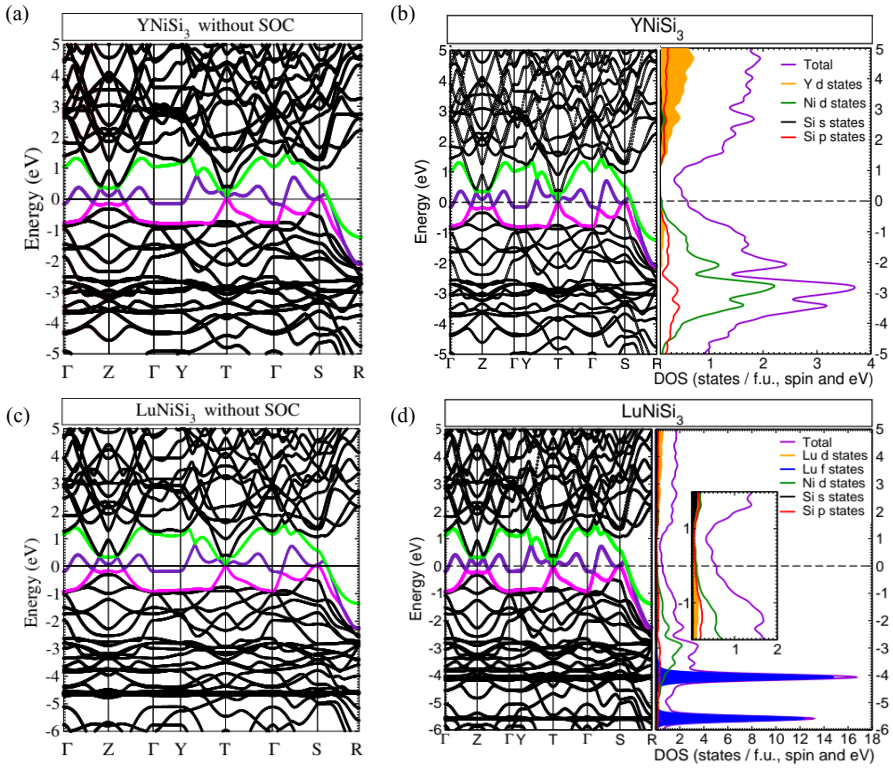

Figure 5.8: Dispersion relation for $YNiSi_3$ and $LuNiSi_3$ neglecting the spin orbit coupling (SOC) interaction (a) and (c), respectively. Electronic structure: band structure, total and projected DOS including SOC effects for (b) $YNiSi_3$ and (d) $LuNiSi_3$. Highlighted in color are the three conduction bands crossing the Fermi level; band 1 (magenta), band 2 (violet) and band 3 (green). The eigenvalues are shifted to the Fermi level defined at $E_F = 0$ eV. The inset at panel (d) is a zoom in the projected DOS contribution at the Fermi level.

and third bands, respectively. The first band crosses the Fermi level in the vicinity of the high symmetry point T with a hole-like character. It is formed by Ni d and Si p-states. The second band intersects the Fermi level in all high symmetry directions except in Δ direction (k_y), showing a hole-like character in Δ, H, $T - \Gamma$ and $\Gamma - S$. It is constructed with Y (Lu) d, Ni d and Si p-states. In addition, the hole-like character also occurs in D direction, but in this case there is only contribution of Ni d and Si p-states. Finally, the third band traverses only the D direction with an electron-like character due to Ni d and Si p-states, too. Valence bands of $YNiSi_3$ are composed by Ni d, Si p and Y d-states while $LuNiSi_3$ exhibits Ni d, Si p, Lu d and Lu f-state. The large difference between the two compounds is due to presence of dispersionless

bands associated with Lu f-states around 4.6 eV [Fig. 5.8 (a) and (c)] which are split by 1.5 eV due to SOC interaction showing two well-defined peaks around 4.1 and 5.6 eV in the total and projected DOS.

At the Fermi level, $YNiSi_3$ has a total density of states of $D(E_F) = 0.6875$ states/f.u., spin and eV with contributions of Y d (0.2131), Ni d (0.2544), Si p (0.1719); while $LuNiSi_3$ presents a $D(E_F) = 0.7433$ with contributions of Lu d (0.223), Ni d (0.2676) and Si p (0.1858). Comparing theoretical and experimental $D(E_F)$ [Table 5.1] we find a relative errors of 19.6% for $YNiSi_3$ and 12% for $LuNiSi_3$. Now, we can calculate the bare specific heat coefficient and the electron phonon coupling from Eqs. 2.28 and 2.30 which values obtained are $\gamma_{bare} = 3.24$ mJ mol^{-1}K^{-2} and λ_{e-ph}=0.247 for $YNiSi_3$ and $\gamma_{bare} = 3.50$ mJ mol^{-1}K^{-2} and λ_{e-ph}=0.134 for $LuNiSi_3$ which confirm that these compounds are in the weak-coupling regime. These values are included in Table 5.6 at the end of the next subsection.

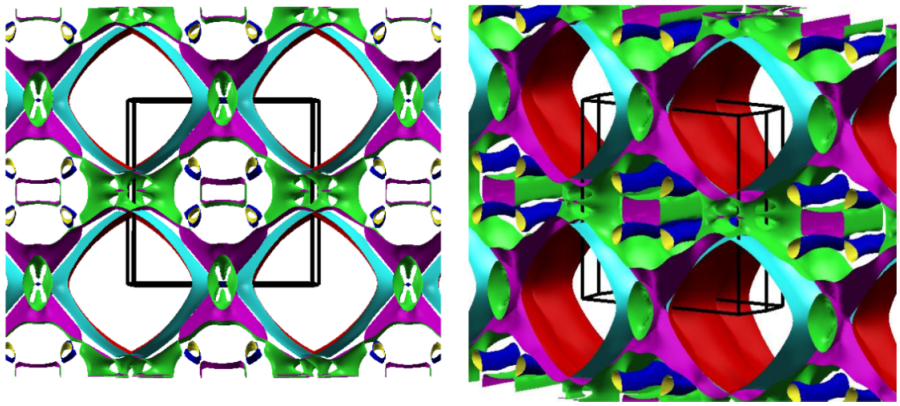

Figure 5.9: On the left the extended Fermi surface of $YNiSi_3$ oriented along the Δ direction (k_y). On the right the extended Fermi surface of $LuNiSi_3$. In both cases, the first Brillouin zone (FBZ) is shown by black lines.

Figure 5.9 shows the calculated Fermi surface for $YNiSi_3$ and $LuNiSi_3$. We can see that these surfaces consist of three branches, each one associated with a partially occupied band. The first hole branch is formed by four pipes (blue/yellow surfaces) centered around Γ and parallel to the Δ direction. The second branch has two main features, a hole-like rectangular cylinder (green/violet colors) also centered around Γ and with its axis oriented along the Δ direction, and a set of large hole-like cylinders running along the FBZ boundary, parallel to the Δ direction and intricately connected around the FBZ boundaries. The third branch is built by four large electron-like disconnected cylinders (cyan/red colors) centered around the edge of the FBZ and also running parallel to the Δ direction. The first hole and the electron branches result

from the hybridization of Ni d with Si p-states, whereas the second hole branch also has the contribution of Y (Lu) d-orbitals. We expected the two large cylindrical branches which connect the FBZ boundaries are most likely responsible for the observed superconductivity in these systems.

5.2.3 Elastic properties

Table 5.5: Calculated elastic constants (in GPa) for $YNiSi_3$ and $LuNiSi_3$.

Compound	$YNiSi_3$	$LuNiSi_3$
C_{11}	324.85	330.36
C_{12}	82.04	90.94
C_{13}	68.54	70.40
C_{22}	260.49	263.15
C_{23}	55.75	60.43
C_{33}	224.44	227.01
C_{44}	98.33	95.59
C_{55}	84.45	81.95
C_{66}	87.06	78.54

Table 5.6: The main parameters obtained from DFT calculations for $YNiSi_3$ and $LuNiSi_3$: $D(E_F)$ density of states (states/eV.f.u and spin) , γ_{bare} Sommerfeld coefficient (mJ $mol^{-1}K^{-2}$) , λ_{e-ph} electron-phonon coupling, B Bulk modulus (GPa), G shear modulus (GPa), V_m average sound velocity (Km/s) and Θ_D (K) Debye temperature (K)

	$YNiSi_3$	$LuNiSi_3$
$D(E_F)$	0.69	0.74
γ_{bare}	3.24	3.50
λ_{e-ph}	0.25	0.13
B	165.90	171.4
G	94.20	90.90
V_m	4.91	4.13
Θ_D	497	464

The elastic properties were obtained by relaxing the structure of each compound with respect to degrees-of-freedom such as cell shape and cell volume, which will allow the determination of the Hessian matrix (matrix of the second derivatives

of the energy with respect to the atomic positions [Eq. 2.38]). The values obtained are shown in Table 5.5. From these we estimated the Bulk modulus (B) and shear modulus (G), average sound velocity(v_m) and Debye temperature (Θ_D) according to Eqs. 2.40, 2.41 and 2.42, respectively, obtaining that $B = 165.90$ GPa, $G = 94.20$ GPa, V_m=4.91 Km/s and $\Theta_D = 497$ K for $YNiSi_3$ and $B = 171.4$ GPa, $G = 90.90$ GPa, V_m4.13 Km/s and $\Theta_D = 464$ K for $LuNiSi_3$.

The main parameters of $YNiSi_3$ and $LuNiSi_3$ obtained from electronic and elastic properties are summarized in Table 5.6. Comparing the experimental and theoretical Debye temperature [Tables 5.1 and 5.6] we find an absolute relative error of 6.7% for $YNiSi_3$ and 2.1% for $LuNiSi_3$. Moreover, the calculated bulk modulus from the elastic constant differs from that obtained by Birch Murnaghan fit by about 38 GPa, compare Table 5.4 and 5.6. The latter may occur due to the sensitivity of B to energy differences in the equation of state.

5.2.4 Phononic properties

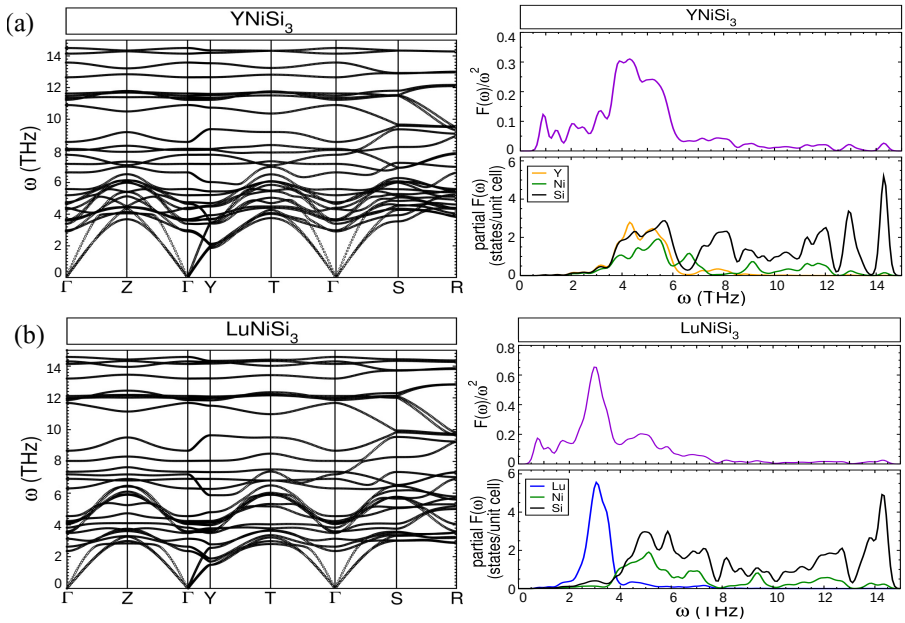

Figure 5.10: Calculated phonon dispersion relation, $F(\omega)/\omega^2$ spectral function and partial $F(\omega)$ for (a) $YNiSi_3$ and (b) $LuNiSi_3$.

Finally, the phononic properties of $YNiSi_3$ and $LuNiSi_3$ compounds can be determined from a detailed study of the phonon dispersion relation and the total and partial density of state [sec. 2.4].

In order to determine the vibrational spectrum of these compounds we use the Phonopy package [89] to create supercells large enough to avoid the self-interaction of the displaced atom with itself. Next, for each supercell we calculate the ground state energy and the total-force on each atom whose set of forces and displacements allow us determine the force constant and the dynamic matrix [Eq. 2.15] associated with the superconductors. Finally, using a $\mathbf{q}$-point grid in the first Brillouin zone, we can calculate the phonon frequencies and eigenvectors by interpolation.

The phononic band structure $\omega(\mathbf{q})$ for $YNiSi_3$ and $LuNiSi_3$ are presented in Fig. 5.10. Here we have not included the SOC because as mentioned above the crystal structure and the FS are not affected by this interaction. We observe that their corresponding branches are very similar, even the maximal phonon frequency existing in the crystal for both compounds is around of 15 THz. Moreover, none of them have imaginary frequency which ensures that these structures are dynamically stable. Now, since $RNiSi_3$ contains 10 atoms in the primitive unit cell, they have 3 acoustic and 27 optical modes [subsec. 2.6.1]. For $YNiSi_3$ the acoustic branches are determined approximately below 4 THz while for $LuNiSi_3$ below 3.2 THz.

Since the distribution of modes is almost continuous over the entire frequency range, to analyze the phonon spectrum we will consider three frequency regions: 0-4.0 and 0-3.2 THz (acoustic), 4.0–12.2 and 2.6–12.8 THz (intermediate), 12.2–14.5 THz and 12.8–14.6 THz (high) for $YNiSi_3$ and $LuNiSi_3$, respectively. In $YNiSi_3$ all atoms contribute almost uniformly to acoustic branches, in contrast to $LuNiSi_3$ where there is an appreciable contribution due to Lu atoms (heavy mass). The intermediate-frequency range has 23 branches, where 12 form the low lying optical branches (up to approximately 6.7 THz) which contributions states coming from Y(Lu), Si and Ni vibrational modes, and the 11 remaining are mainly made up by Si and Ni states. The high-frequency region has 4 branches and they are formed almost exclusively by Si contributions.

From partial density of states $F(\omega)$ we calculate the spectrum function $\omega^{-2}F(\omega)$, [righ panel in Fig. 5.10] which is a crude alternative to the Eliasberg function $\alpha^2F(\omega)$ as was mentioned in subsec. 2.8.3. Here, we can observed that both compounds exhibit the highest spectral weight between the acoustical and low lying optical branches with their most prominent peaks located in the latter. This indicates that there must be coupling among Y(Lu) and Ni d-electrons with Si-p to form Cooper pairs, and thus they are responsible for the superconductivity observed in these compounds.

5.3 Discussion

Experimental measurements allow us to categorize the superconductivity of these compounds as type-I with weak electron-phonon coupling and a Ginzburg-Landau (GL) parameter $\kappa < 1/\sqrt{2}$, as presented in Table 5.1. However, these superconductors are unconventional because the jump of the specific heat at the transition is lower than the value expected by BCS theory ($\Delta C_{el}/\gamma T_c = 1.43$). These features are also observed in other non-f-electron orthorhombic Ni-Ge systems such as $YNiGe_3$ [90, 91] and $La_3Ni_4Ge_4$ [92] where the low specific heat jump can be connected with an anisotropy of the SC gap. $YNiGe_3$ is an isoelectronic-isostructural of $YNiSi_3$ whose similarity is observed in both the density of estates at the Fermi Level and the Fermi surface. The first one is about $D(E_F) = 0.69$ states/eV f.u and spin with contributions coming from Ni $3d$, Y $4d$ and Ge $4p$ electrons. The second originates from three bands, two of them are hole-like and electron-like sheets. This has led to the suggestion that such system is a multiband-superconductor with two gaps, one for each sheets mentioned. The above seem to be also valid for the compounds we have studied through this chapter, where the models used to determine the type of superconducting gap in $YNiSi_3$ and $LuNiSi_3$ have correctly described the jump in the specific heat evidencing the existence of a large anisotropy in the superconducting gap.

5.4 Conclusions

In this chapter we presented the physical properties of $YNiSi_3$ and $LuNiSi_3$ superconductors. These have been characterized by magnetization, heat capacity and resistivity experiments, and we have given theoretical support from DFT electronic-structure calculations. We find that these compounds are anisotropic nonmagnetic type-I superconductors below T_c=1.36(3) K for $YNiSi_3$ and T_c=1.61(2) K for $LuNiSi_3$, with a complex superconducting gap. The Cooper pairs appear to be formed by weak-coupling between the d electrons from Y(Lu) and Ni to Si p electrons, which come from $3d$, $3p$, and $4d$ orbitals for $YNiSi_3$ and $3d$, $3p$, and $5d$ orbitals for $LuNiSi_3$ and determine the two large cylindrical branches that are connected around the FBZ boundaries in the Fermi surface and show continuity throughout the entire reciprocal space.

On the other hand, it is important to note that low-temperature supercon-

ductors have a wide range of applications. They are utilized as electrical components in cables, sensors, motors, generators, among others, to create nuclear magnetic resonance images (commonly employed in medicine), electrical energy storage and transmission, in the construction of particle accelerators (high energy physics), etc. It is here where $YNiSi_3$ and $LuNiSi_3$ compounds may show their usefulness.

6

$GD_{1-x}Y_xNiSi_3$

In gadolinium based compounds the crystal electric field (CEF) effect is negligible so their magnetic properties must originate mainly from exchange interaction. $GdNiSi_3$ is quite interesting because of its phase diagram where the metamagnetic transition evolves towards high fields when the temperature increases [subsec. 4.2.2]. In order to understand the role of exchange interaction in such system, in this chapter we will investigate the effect of non-magnetic Y ion doping on the magnetic properties of $Gd_{1-x}Y_xNiSi_3$ compounds. We will analyze the interactions between magnetic moments, the resultant magnetic ordering and the changes presented by the exchange interaction in these alloys. To do this, we grow single crystals of $Gd_{1-x}Y_xNiSi_3$ (x=0.25, 0.50, 0.65, 0.80) and characterized them using susceptibility, magnetization and heat capacity measurements. Also, we will include the non-magnetic $YNiSi_3$ compound in our study to evaluate the contribution of phonons and conduction electrons of Y-doped compounds. Finally, we will use first-principles calculations to determine the electronic properties of $GdNiSi_3$.

6.1 Experimental results

As a starting point, we performed a structural characterization on the obtained single crystals and we found that they grew in the desired phase. Next, we performed the magnetic characterization. Temperature dependent susceptibility curves at 1 kOe along the a crystallographic axis for $Gd_{1-x}Y_xNiSi_3$ compounds are shown in Fig. 6.1. At low temperature [Fig. 6.1(a)] these curves exhibit a peak associated with antiferromagnetic transition for all samples. Their respective Néel temperatures are calculated as the peak in $d(\chi T)/dT \times T$ curve [Fig. 6.1(b)] and they are indicated in Table 6.1. Notice that as Y-doping increases, the Néel temperature moves to lower temperatures while the peak associated to the transition and the magnetic susceptibility χ(2K) increases to higher values. This behavior can be associated with some paramagnetic

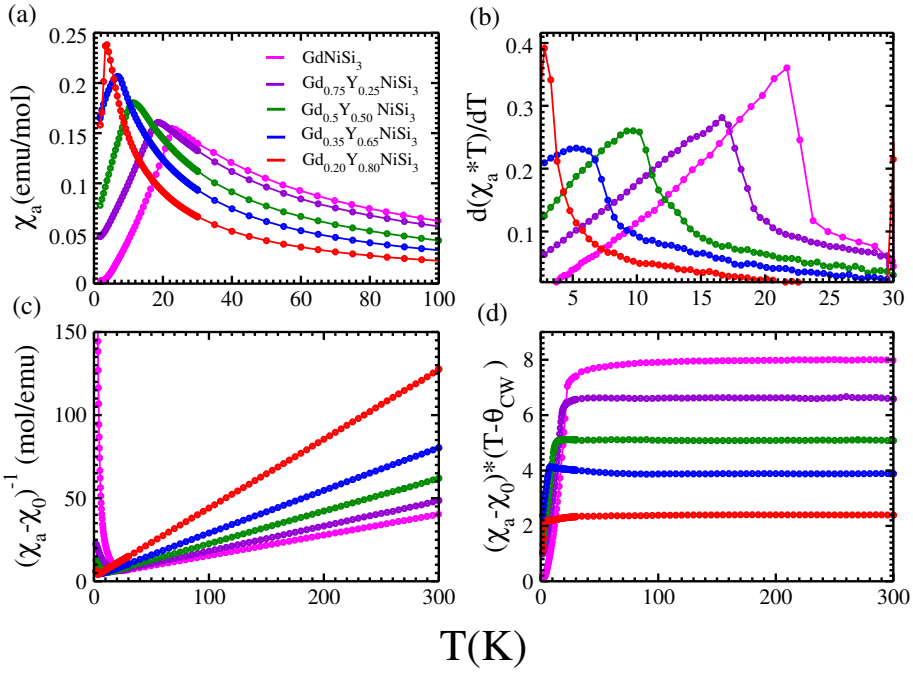

Figure 6.1: Magnetic susceptibility measurements at $H = 1$ kOe with $H \parallel a$ orientation for $Gd_{1-x}Y_xNiSi_3$ crystals ($x = 0.25, 0.50, 0.65$ and 0.80). (a) Low temperature magnetic susceptibility. (b) Temperature derivative of the product between magnetic susceptibility and temperature. (c) Inverse susceptibility as a function of temperature, subtracting the Pauli paramagnetic contribution χ_0. (d) Temperature dependence of the Curie-Weiss law $(\chi_a - \chi_0) * (T - \theta^a_{cw})$.

contribution originated by unpaired Gd^{3+} ions, spin reorientation with some ferromagnetic component [93,94] and/or by clustering effect that could introduce some parasitic ferromagnetism [95]. At high temperatures, χ decreases as T increases following Curie-Weiss behavior [Eq. 2.17]. To test this, we plot the inverse susceptibility by subtracting the Pauli paramagnetic contribution χ_0 and fitting the Curie-Weiss law for each Y concentration. The fitting parameters are given in Table 6.1. The slope of $(\chi_a - \chi_0)^{-1}$ rises gradually with Y-doping level, implying that the effective magnetic moment [Eq. 2.19] is reduced. However, except for pristine $GdNiSi_3$, the effective moment is higher than the expected values $(1-x)\mu_{Gd^{3+}}$. In addition, all compounds considered exhibit negative Curie-Weiss temperature, indicating that the interaction between Gd^{3+} ions is antiferromagnetic. Finally, we check the ranges where the found parameters correctly quantify the Curie-Weiss constant at high temperatures [Fig. 6.1(d)].

We are interested in understanding the changes in the magnetic response of

Table 6.1: Temperature dependent susceptibility parameters of $Gd_{1-x}Y_xNiSi_3$ crystals for the $H \parallel a$ orientation: Pauli paramagnetic susceptibility χ_0 (10^{-3} emu/mol), Néel temperature T_N (K), Curie-Weiss temperature θ^a_{cw} (K) , frustration parameter f and effective magnetic moments μ_{eff} (μ_B) . Additionally, we indicate magnetic field dependence magnetization parameters as highest field magnetic moment observed at 2 K μ_{HF} (μ_B). For comparison we include the expected magnetic moment for Gd^{3+} as a concentration function $(1-x)\mu_{Gd}$ (μ_B) .

x	χ^a_0	T^a_N	θ^a_{cw}	f	μ_{eff}	$(1-x)\mu_{Gd}$	μ_{HF}
0	-2.25(2)	21.7(1)	-24.2(2)	1.11	8.02(4)	7.94	-
0.25	2.10(4)	16.6(7)	-20.3(2)	1.22	7.28(4)	5.96	2.08(2)
0.50	-1.28(4)	9.7(5)	-15.0(2)	1.55	6.38(2)	3.97	2.31(2)
0.65	-1.16 (5)	5.3(5)	-12.4(1)	2.34	5.57(1)	2.78	2.13(3)
0.80	0.09 (6)	2.7(3)	-5.3(2)	1.96	4.37(2)	1.59	1.84(1)

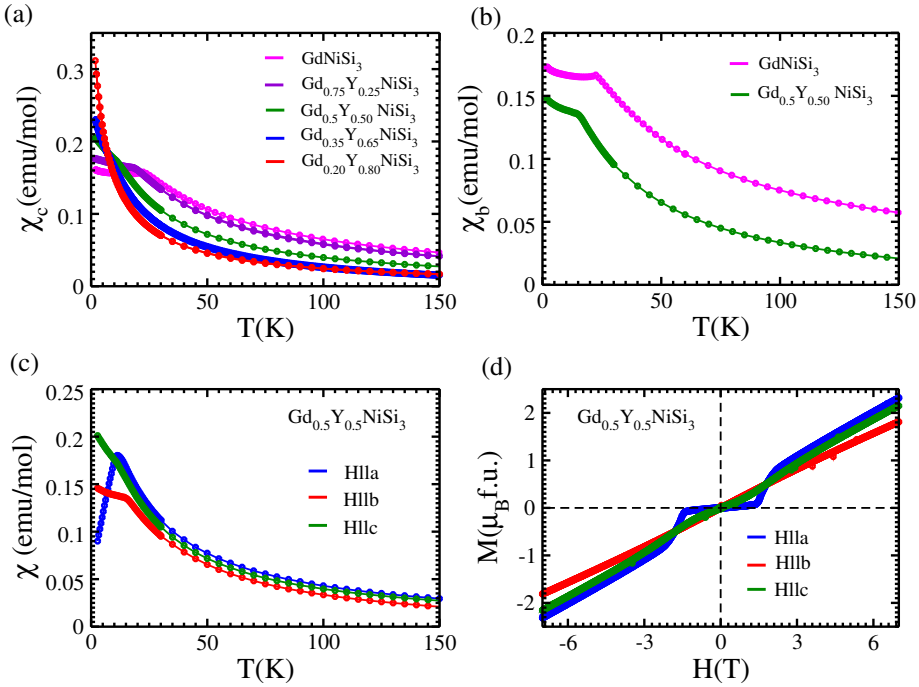

Figure 6.2: Temperature dependent susceptibility along (a) c-axis for $Gd_{1-x}Y_xNiSi_3$ ($x = 0, 0.25, 0.50, 0.65$ and 0.80) and (b) b-axis for $x = 0$ and 0.5. (c) Magnetic susceptibility and (d) magnetization measurements for $Gd_{0.5}Y_{0.5}NiSi_3$ along a, b and c crystallographic axis.

$Gd_{1-x}Y_xNiSi_3$ when including non-magnetic Y ions only along the antiferromagnetic a-axis. However, for the sake of completeness, in Fig. 6.2 we include the susceptibility for these compounds along the b and c-axis, and for $Gd_{0.5}Y_{0.5}NiSi_3$ we present the susceptibility and magnetization response along the three crystallographic axis. Notice that Y-doping causes the a and c components of magnetic moments to increase and therefore the susceptibility rises at low temperature, while that of the b-component decreases. In any case, the a-axis still holds as the antiferromagnetic easy axis.

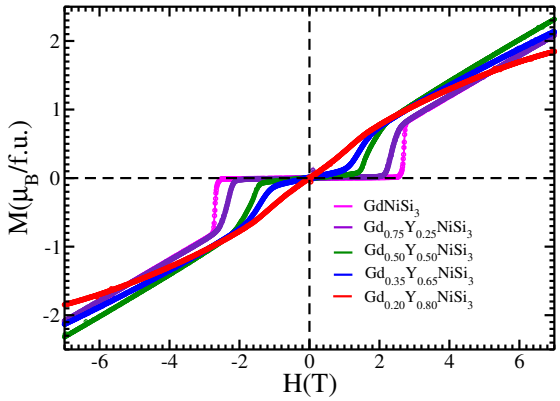

Figure 6.3: Magnetic field dependent magnetization for $Gd_{1-x}Y_xNiSi_3$ ($x = 0.25, 0.50, 0.65$ and 0.80) at $T = 2$ K with $H \parallel a$ orientation.

On the other hand, magnetization measurements as a function of magnetic field along the a-axis at $T = 2$ K in the range -7 T$\leq H \leq 7$ T has been plotted in Fig. 6.3 for diluted magnetic $Gd_{1-x}Y_xNiSi_3$. It is remarkable that even at 7 T none of the investigated compounds reaches the saturation value. $GdNiSi_3$ exhibits a spin flip-type metamagnetic transition at a critical field of 27 kOe, as was mentioned in subsec. 4.2.2. As Y-doping increases, this transition moves to lower magnetic fields, changing its form to spin-flop-type for $Gd_{0.75}Y_{0.25}NiSi_3$ and S-type for $Gd_{0.20}Y_{0.80}NiSi_3$. We calculated these transitions by inflection points in $M \times H$ curves and found values of 2.3(1), 1.5(2) and 1.4(3) T for $x = 0.25, 0.50$ and 0.65, respectively.

Figure 6.3 shows a zoom of the interval -0.25 T$\leq H \leq 0.25$ T [Fig. 6.4 (a)] evidencing that all samples exhibit a small hysteresis. However, $Gd_{0.5}Y_{0.5}NiSi_3$ and $Gd_{0.35}Y_{0.65}NiSi_3$ present a shift of the magnetic hysteresis loop from its centered position at $H = 0$. In order to determine whether this behavior is associated with intrinsic exchange bias (EB) effect in the single crystals, we verified the conditions mentioned in subsec. 2.5.5 using zero field cooling (ZFC) and field cooling (FC) protocols at $H = 0.5$ T and 5 T [Figs. 6.4 (b) and (c)]. The results are summarized in Table 6.2. Even in ZFC, both

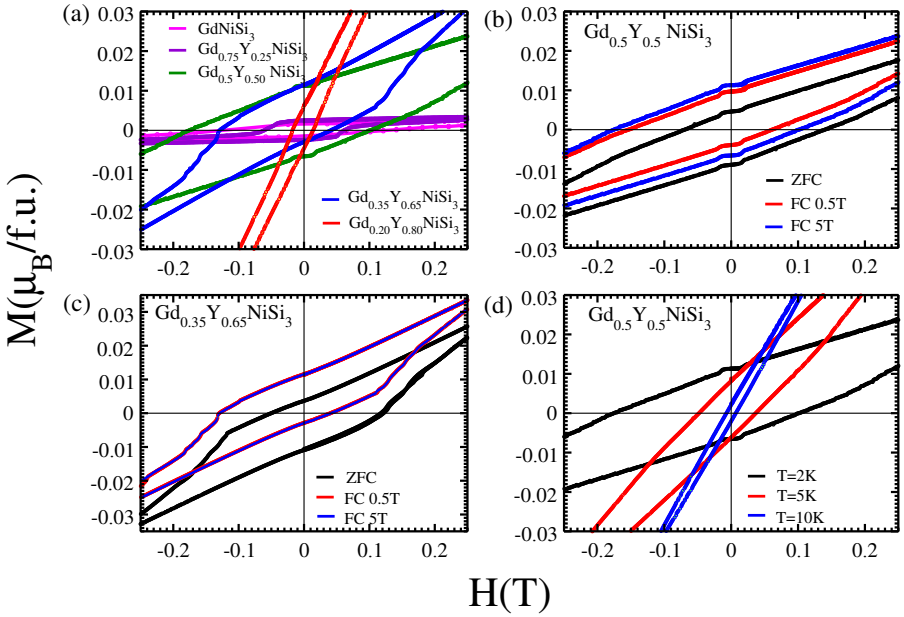

Figure 6.4: Magnetic field dependence of magnetization at $T = 2$ K with $H \parallel a$ orientation within the range -0.25 T$\leq H \leq 0.25$ T for (a) $Gd_{1-x}Y_xNiSi_3$ (x=0.25, 0.50, 0.65 and 0.8), (b) $Gd_{0.5}Y_{0.5}NiSi_3$ and (c) $Gd_{0.35}Y_{0.65}NiSi_3$ compounds. The latter were considered in zero field cooling (ZFC), 0.5 T and 5 T field cooling (FC) protocols. (c) Magnetization as a function of magnetic field and temperature at $T = 2$ K, 5 K and 10 K for $Gd_{0.5}Y_{0.5}NiSi_3$ in 5 T field cooling (FC) protocol.

compounds show a shifted hysteresis to the right of field axis and downward in the magnetization axis by $H_{EB} = +363$ Oe, $M_{EB} = -2.2\times10^{-3}\mu_B$ for $x = 0.5$, and $H_{EB} = +333$ Oe, $M_{EB} = -3.5 \times 10^{-3}\mu_B$ for $x = 0.65$, respectively. Under field cooling (FC) of 0.5 T, the hysteresis loop shifts to left of the field axis and upward in the magnetization axis by $H_{EB} = -464, -445$ Oe and $M_{EB} = +2.9, +4.3 \times 10^{-3}\mu_B$ for 50% and 65% Y-doped compounds, respectively. Finally, under FC of 5 T, the shifts for $Gd_{0.5}Y_{0.5}NiSi_3$ reach -362 Oe and $+2.3 \times 10^{-3}\mu_B$, whereas for $Gd_{0.35}Y_{0.65}NiSi_3$ the hysteresis is unaffected. In addition, both systems show an increase in the coercive field with higher field cooling. Finally, we verified that these effects vanish with increasing temperatures [Fig. 6.4].

Specific heat measurements of $Gd_{1-x}Y_xNiSi_3$ crystals from $T = 2 - 40$ K at $H = 0$ are presented in Fig. 6.5(a). Due to the presence of Gd $4f$ electrons, the specific heat of Y-doped samples is much higher than that of $YNiSi_3$. In addition, they exhibit anomalies at 22.2(5), 17.2(3), 10.8(5), 6.6(7) and 3.5(9) for $x = 0, 0.25, 0.5, 0.65$ and 0.80, respectively, signaling the onset of long-range

Table 6.2: Magnetic field dependence magnetization parameters for $Gd_{0.5}Y_{0.5}NiSi_3$ at $T = 2$ K in zero field cooling (ZFC) and field cooling (FC) protocols: coercive fields, exchange bias magnetic fields and magnetization shifts.

x	protocol	H_{coe}(Oe)	H_{EB}(Oe)	$M_{EB}(10^{-3}\mu_B)$
0.5				
	ZFC	1053	+363	-2.2
	FC 0.5 T	1072	-464	+2.9
	FC 5T	1376	-362	+2.3
0.65				
	ZFC	838	+333	-3.5
	FC 0.5T	852	-445	+4.3
	FC 5T	853	-445	+4.3

magnetic order in agreement with those determined by magnetic susceptibility. Thus, T_N moves toward lower temperatures as the Y-concentration increases. The forms of these anomalies are of well-defined λ-type for $x = 0$ and 0.25, as expected within the mean-field model, and no sharp peak for the other cases. At T_N, the samples with $x = 0.25, 0.50, 0.65$ and 0.80 reach $C_p = 15.28, 7.92, 3.79$ and 2.13 J $mol^{-1}K^{-1}$, respectively, corresponding to 77%, 49%, 30% and 18% less than 27.38 J $mol^{-1}K^{-1}$ for $GdNiSi_3$. These values are summarized in Table 6.3. Below T_N, all doped samples feature a similar broad hump. It cannot be associated to spin reorientation, since susceptibility measurements do not evidence additional magnetic transitions below the ordering temperature. This type of hump has been observed in other Gd-based compounds such as $GdCu_2Si_2$, $GdNi_2Si_2$, $GdGa_2$, $GdCu_5$ [37, 96] and has been assigned to a Schottky-like anomaly, involving the lifting of the $(2J + 1)$-fold degenerate multiplet of Gd magnetic ions due to internal magnetic field, as mentioned in subsec. 2.6.4, which is possibly generated by long-range AFM correlation between Gd atoms. On the other hand, above T_N the specific heat curve is strongly affected by increasing the doping level of the non-magnetic ion. For $x = 0.25$ an anomaly in the local minimum region appears at around 20 K. The anomaly moves to low temperatures for $x = 0.5$ and $x = 0.65$ in a hump form, and finally broadens over the antiferromagnetic transition peak at x =0.8.

With the presence of such Schottky anomalies and magnetic peaks in the specific heat at low temperatures for Y-doped compounds, it is unreliable to use $C_p/T \times T^2$ curves to determine the electronic and phononic contribution to specific heat, because in general the Debye model applies most successfully for temperatures below $\Theta_D/50$ [sec. 2.6.1]. However, to get an idea of these contributions we plot the curves [Fig. 6.5 (b)] and consider the linear region between 26-30 K above the magnetic region. From Eq. 2.31, the extrapolation

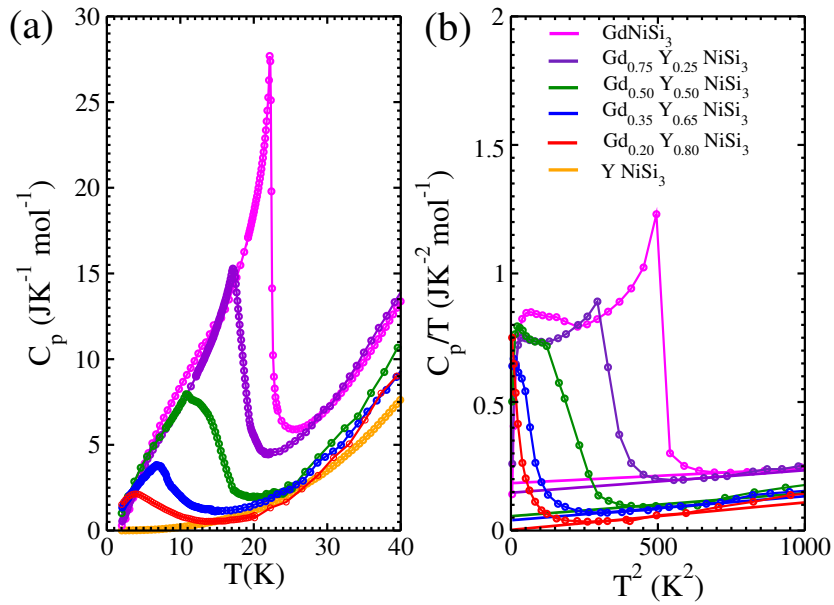

Figure 6.5: (a) Temperature dependent total specific heat and (b) $C_p/T \times T^2$ for $Gd_{1-x}Y_xNiSi_3$ ($x = 0.25, 0.50, 0.65$ and 0.80) compounds.

to $T = 0$ K determines the Sommerfeld coefficient γ and its slope the phononic coefficient β. Also, the latter allows us to calculate the Debye temperature from Eq. 2.25. These results are listed in Table 6.3. Notice that by this procedure $GdNiSi_3$ exhibits $\gamma \approx 184.25(2)$ mJ mol^{-1}K^{-2}, comparable to $YbNiSi_3$ [sec. 4.3] which is classified as a moderately heavy-electron system. This is already an indication that the procedure is not applicable here, since there are no known cases of Gd-based compounds showing $4f$ hybridization with conduction electrons and heavy-electron behavior. Moreover, due to difference between atomic mass of Gd (157.25 g/mol) and Y (88.91 g/mol) we expect that $GdNiSi_3$ and $YNiSi_3$ present the maximum and minimum Debye temperature, respectively. Furthermore, we hope that with increasing Y-doping this temperature will gradually decrease. However, it is underestimated for $Gd_{0.20}Y_{0.80}NiSi_3$ with respect to the non-magnetic compound, while $GdNiSi_3$, $Gd_{0.75}Y_{0.25}NiSi_3$ and $Gd_{0.5}Y_{0.5}NiSi_3$ overestimate it with respect to $LuNiSi_3$ [$\Theta_D = 474(8)$ K, sec. 5]. Lu has an atomic mass of 174.967 g/mol, greater than Gd and Y.

Another method commonly used to calculate the electronic and phononic contribution to specific heat for the $Gd_{1-x}Y_xNiSi_3$ series is to consider the isomorphic non-magnetic compound $YNiSi_3$ with a renormalization factor in temperature in $C \times T$ curves due to the difference in molar masses between

Table 6.3: Temperature dependent specific heat parameters for $Gd_{1-x}Y_xNiSi_3$ crystals at $H = 0$ T: Néel temperature T_N^{sp} (K), specific heat at Néel temperature $C_p(T_N)$ (J mol^{-1}K^{-1}), Sommerfeld coefficient γ (mJ mol^{-1}K^{-2}), phononic coefficient β (mJ mol^{-1}K^{-4}) and Debye temperature Θ_D (K). The values indicated for $YNiSi_3$ were taken from Ref. [77]

x	T_N^{sp}	$C_p(T_N)$	γ	β	Θ_D
0	22.2(5)	27.38	184.25(2)	0.056(1)	555(3)
0.25	17.2(3)	15.28	147.09(3)	0.087(5)	481(8)
0.50	10.8(5)	7.92	55.74(2)	0.090(4)	476(6)
0.65	6.6(7)	3.79	40.07(4)	0.093(7)	470(4)
0.80	3.5(9)	2.13	2.51(1)	0.107(2)	449(2)
1	-	-	4.04(9)	0.096(5)	466(9)

Table 6.4: Temperature dependent specific heat parameters for $Gd_{1-x}Y_xNiSi_3$ crystals at $H = 0$ T, after renormalization in temperature in $C \times T$ for the nonmagnetic compound: renormalization parameter [Eq. 2.34], Debye temperature, magnetic entropy and ratio of magnetic entropy with doping level (where R is the gas constant).

x	ρ_{norm}	Θ_D (K)	S_{mag} (J mol^{-1}K^{-1})	S_m/(1-x)R
0	0.846	550.82	16.2	1.94
0.25	0.875	532.57	12.9	2.07
0.50	0.910	512.08	8.9	2.14
0.65	0.934	498.93	4.4	1.51
0.80	0.960	485.42	2.5	1.50

Gd and Y, according to Eq. 2.34. In Table 6.4 we indicate the renormalization parameter for each compound and the Debye temperature obtained by this method [Eq. 2.35].

Having determined the electronic and phononic contributions, we calculate the magnetic contribution to specific heat for these compounds using Eq. 2.32. In Fig. 6.6(a) we plot $C_m/T \times T$ for all samples. Here, the magnetic anomalies at T_N and the broad humps at low and high T_N are again evident, as discussed in total specific heat. Below T_N, we observe that the Schottky anomaly is very broad for $GdNiSi_3$, whereas it is reduced and shifted towards lower temperatures for $Gd_{1-x}Y_xNiSi_3$. In addition, the presence of a hump for $x = 0.50$ and $x = 0.65$ above T_N indicates that these are a magnetic origin and they may be associated with short-range magnetic correlation. On the other hand, all compounds show that the magnetic contribution persists over a

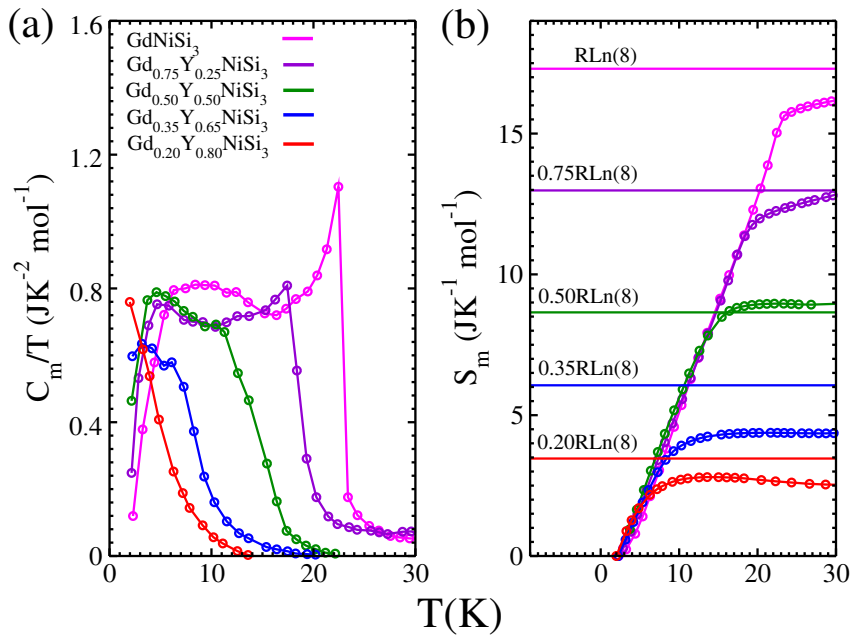

Figure 6.6: Temperature dependence of (a) magnetic specific heat divided by temperature (C_m/T) and (b) magnetic entropy S_{mag} for $Gd_{1-x}Y_xNiSi_3$ crystals. The dotted lines indicate $(1-x)R\ln(8)$ limits.

wide temperature range above the ordering temperature. Even for 50, 65 and 80% Y-doping, C_m/T vanishes at 21.22, 19.20, 15.16 K, respectively, which is beyond $2T_N$ and mimics the behavior of many magnetically ordering heavy fermions [97, 98].

The temperature dependent magnetic entropy $S_{mag}(T)$ calculated by numerical integration of C_{mag}/T is displayed in Fig. 6.6 (b). Note that magnetic entropy first increases with rise in temperature and then saturates. At $T = 30$ K, S_m reaches the values of 16.2, 12.9, 8.9, 4.4 and 2.5 J mol^{-1}K^{-1} for $x = 0, 0.25, 0.50, 0.65$ and 0.80 concentrations, respectively. In order to determine some tendency of magnetic entropy we calculate the ratio $S_m/(1-x)R$ where R is the molar gas constant (8.315 J mol^{-1}K^{-1}). These values are summarized in Table 6.4. For all compounds these ratios are around 2, an indicative that S_m is proportional to the number of Gd^{3+} atoms, $S_{mag} = (1-x)R\ln(8)$. Here $Gd_{0.35}Y_{0.65}NiSi_3$ and $Gd_{0.20}Y_{0.80}NiSi_3$ show a low entropy saturation value compared to the expected value, due to overestimation of electron and phonon contribution to specific heat.

6.2 Theoretical results

As a first step to understand the experimentally observed behaviors in $Gd_{1-x}Y_xNiSi_3$, we study in detail the structural and electronic properties of $GdNiSi_3$. Here we consider an exchange correlation functional in the generalized gradient approximation (GGA) with Perdew-Burke-Ernzerhof (PBE) parametrization [17]. In Elk code (FP-APW method) the muffin-tin radius are R_{MT}^{Gd}=2.8, R_{MT}^{Ni}=R_{MT}^{Si}=2.1327 for Gd, Ni, Si, respectively, while the plane wave cutoff $R_{MF}|\mathbf{G}+\mathbf{k}|_{max}$ converged to 9.0. The Brillouin zone is sampled with 6×2×6 uniform grid for structural relaxation and a 10×2×10 k-point grid to calculate the electronic properties.

6.2.1 Magnetic structure

We check the magnetic structure of $GdNiSi_3$ from three different collinear configurations (a), (b) and (c) [Fig. 6.7] considering an uniformly spaced **k**-grid 20×6×20. The results are given in Table 6.5. Taking into account energy differences of meV-order, we find that the configuration (b) exhibits the lowest energy which is in agreement with resonant X-ray magnetic diffraction experiments [79].

Table 6.5: Ground state volume (Å^3) and energy (eV) for $GdNiSi_3$ in the configurations presented in Fig. 6.7 for uniformly spaced k-grid 20×6×20.

	Configuration (a)	Configuration (b)	Configuration (c)
Volume	332.16	332.10	332.10
Energy	-158.255	-158.274	-158.271

6.2.2 Electronic properties

For the ground state configuration we have calculated the electronic structure with GGA [Fig. 6.8(a)]. We note that Gd f-states define large peaks located at -5.5 eV and 1.4 eV. The former is a deep state in the valence band while the

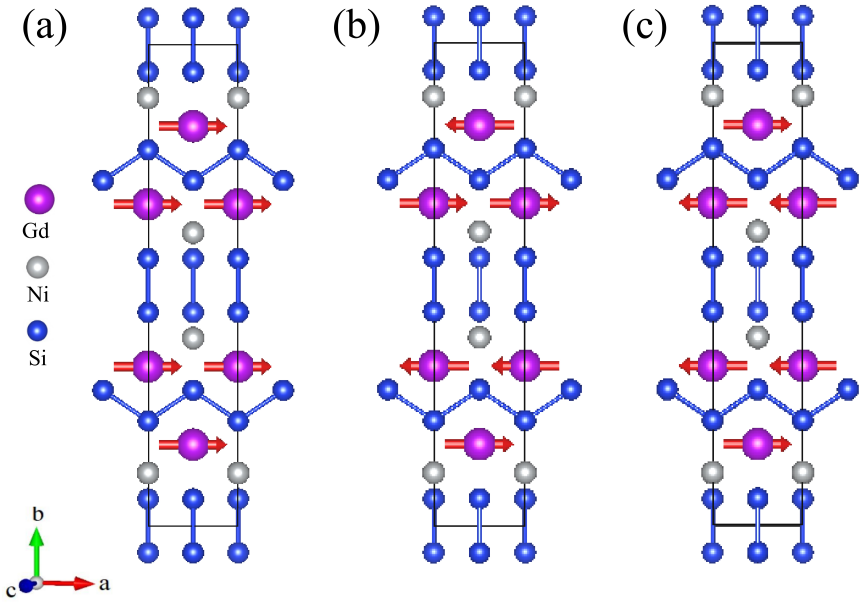

Figure 6.7: Collinear magnetic structure for $GdNiSi_3$ along *a*-axis in the configurations (a) ferromagnetic, (b) antiferromagnetic and (c) mixture of antiferromagnetism and ferromagnetism along *b*-axis. The latter configuration is formed by blocks whose magnetic interaction between neighboring magnetic moments is antiferromagnetic while between blocks is ferromagnetic.

latter belongs to conduction bands. Since, in general, Gd-based compounds are strongly correlated systems it is necessary to determine whether or not these states contribute to Fermi level and therefore play a fundamental role in the conductivity of $GdNiSi_3$. For this purpose, we introduce an intra-atomic electron interaction by means of the DFT+U approach [subsec. 2.1.3] for different forms of the double-counting term [Eq. 2.6]. Initially, we include an interpolation between fully localized limit (FLL) and around mean field (AFM) with Yukawa screening length parameter λ=1.5 [Eq. 2.8]. We even varied this parameter for λ = 1.6, 1.7, 1.8 and 1.9, to see if there is any modification to DOS. However, in all cases we observed that DOS profile remains intact [Fig. 6.8(b)], the magnetic moment of Gd (7.26 μ_B) and the density of states at the Fermi level (1.91 states/f.u., spin and eV). Next, we consider only FLL [20] with the Hubbard parameter U = 6.7 eV and exchange-correlation interaction energy J=0.7 eV [99]. Here we note that the peaks shift about 3 eV away from the Fermi level [Fig. 6.8(c)] decreasing $D(E_F)$ at 1.15 states/f.u., spin and eV. In addition, the peak in the valence band becomes sharper and increases slightly, while the peak in the conduction band is weakly reduced. Finally, we

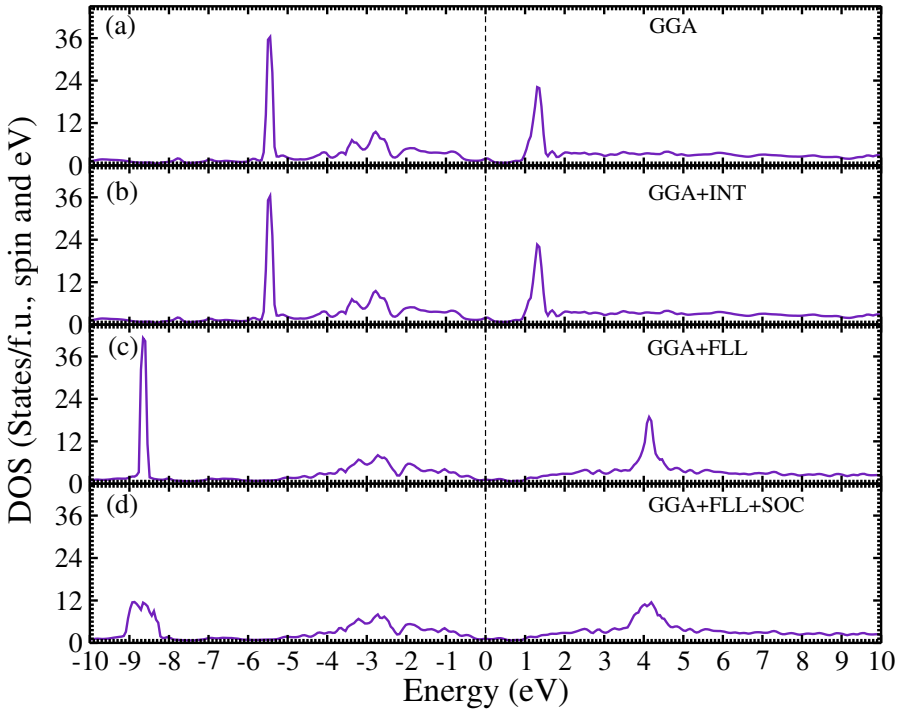

Figure 6.8: Calculated total DOS for $GdNiSi_3$ with (a) GGA. Additionally we incorporate an intra-atomic electron interaction [Eq. 2.6] which double-counting term are (b) an interpolation between fully localized limit (FLL) and around mean field (AFM) with Yukawa screening length parameter λ =1.5 and (c) only FLL with U = 6.7 eV and J=0.7 eV. (d) The last one includes spin-orbit coupling (SOC) interaction.

include the SOC interaction and we find that it only affects the Gd f-states partially breaking the degeneracy of this orbitals levels.

Knowing the type of intra-atomic interaction occurring in Gd atoms, we obtain the dispersion relations along the high symmetry directions in the first Brillouin zone (FBZ) [Fig. 5.7] and the projected DOS for $GdNiSi_3$ compound. These results are shown in Fig. 6.9. The projected DOS exhibits Gd f-states as two large peaks quite far from Fermi level but distributed in both valence and conduction bands indicating the localized character of $4f$ orbitals. Valence bands are mainly formed by Ni d-states, Si p and s-states with a weak hybridization between Gd d-states and Ni p-states. Moreover, conduction bands are determined primarily by Gd d-states, Si p, Ni d and to lesser extent by Ni p and Si s-states. Also, we have the presence of dispersionless bands associated with Gd f-states at -8.5 and 4.5 eV. At the Fermi level we have contributions from Ni d, Si p and Gd d-state. The hybridization of these states

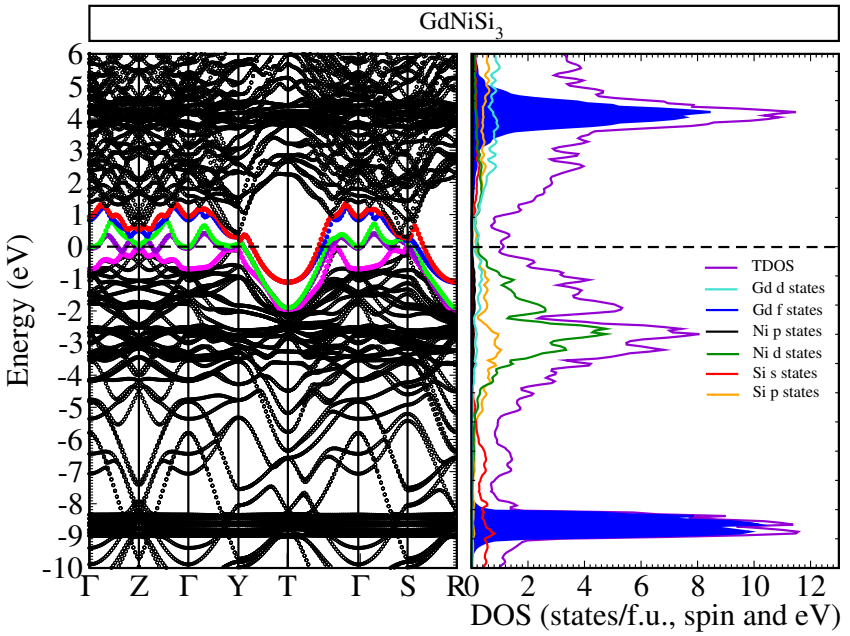

Figure 6.9: Calculated electronic structure: dispersion relation, total and projected DOS for $GdNiSi_3$ in GGA+FLL approximation. Highlighted in color denote the six conduction bands crossing the Fermi level (dashed line).

determines six partially occupied bands crossing the Fermi level with spin up polarization, and they are equivalent when considering spin down. These have the characteristic parabola-shaped bands at T high symmetry point indicating a similarity to the free electron bands and therefore suggesting an electron like-character as was mentioned in subsec. 2.3.1.

A visual representation of calculated Fermi surface (FS) can be observed in Fig. 6.10. It exhibits six branches. Four of them are similar to the ones shown by $YNiSi_3$ [Fig. 5.9], two branches are built by four large electron-like disconnected cylinders (cyan/red and green/violet colors), while the other two branches are thin cylinders (yellow/blue and cyan/red colors) centered around Γ and included within a set of large hole-like cylinders running along the FBZ boundary. The fifth branch includes four pipes (green/violet surfaces) centered around Γ with two cigars and small pieces on H and B high symmetry directions distributed in the surrounding BZ one in front of the other. Finally, the sixth branch is formed by pairs of small pieces situated on the sides of FBZ along Δ

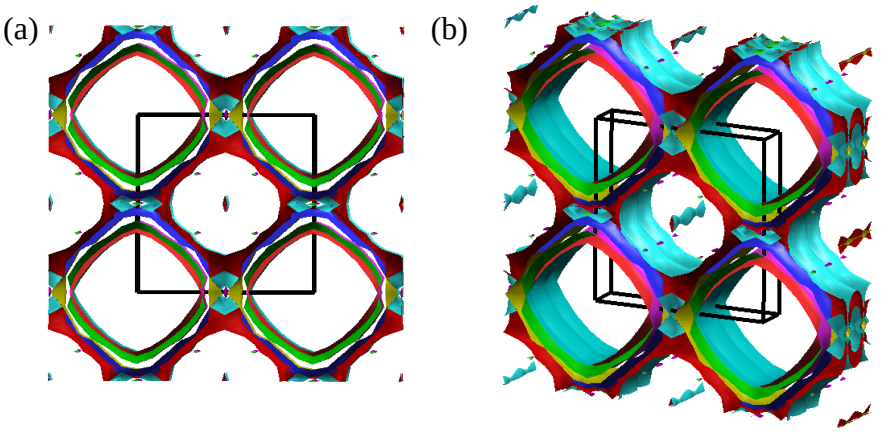

Figure 6.10: Extended Fermi surface of $GdNiSi_3$. The FBZ is shown by black lines.

direction.

6.3 Analysis and discussion

Due to similarity in the ionic radius of Y^{3+} and Gd^{3+} the bond distances and lattice parameters of $Gd_{1-x}Y_xNiSi_3$ compounds are essentially the same. However, their magnetic properties change as the doping level increases as a result of the different local environments between Gd atoms. Fig. 6.11 shows the concentration dependent effective magnetic moment determined from susceptibility measurements, as well as the highest magnetic moment observed at 2 K in magnetization curves. Additionally, we include the theoretical magnetic moment by Gd concentrations. The value obtained for $GdNiSi_3$ is in agreement with that published in Ref. [2], where Ni seems to be non-magnetic. However, for doped compounds μ_{eff} are above of concentration dependence theoretical values for gadolinium μ=7.94 $(1-x)$ μ_B/Gd^{3+}, and follow a decreasing behavior with rising x [Table 6.1]. As this excess of magnetic moment reaches 2.8 μ_B at x=0.80, we assume that the origin of this may be associated with a partially filled Ni-3*d*, whose magnetic moment gradually rises with increasing doping level, as was observed in heavy rare-earth containing RNi [100], $Gd_{1-x}Y_xNi$ [98] compounds and other Gd-Y alloys [101]. Thus, $Gd_{1-x}Y_xNiSi_3$ should exhibit a coexistence of localized magnetic moment of Gd and induced itinerant ferromagnetism of Ni. Further experiments will be

required to test this hypothesis.

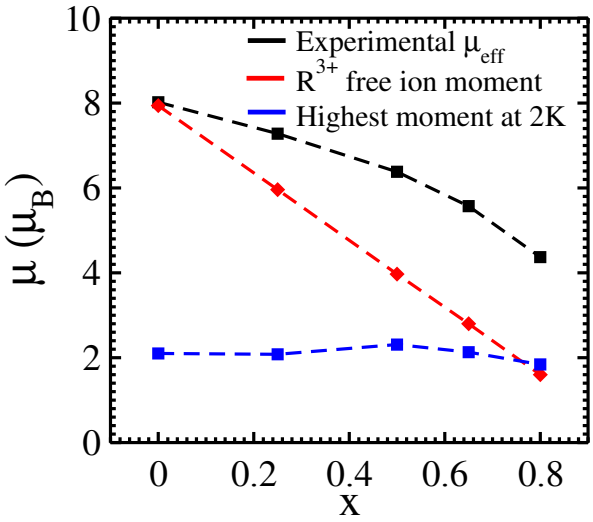

Figure 6.11: Concentration dependence experimental effective magnetic moment (black dashed) and highest observed moment at 2 K (blue dashed) for $Gd_{1-x}Y_xNiSi_3$ alloys. For comparison we include the theoretical value of the free rare earth ions (red dashed).

In the $GdNiSi_3$ unit cell, the magnetic moments associated with Gd atoms are aligned antiferromagnetically along the a axis without canting [Fig. 4.11]. At T_N, C_m reaches 27.38 J $mol^{-1}K^{-1}$ value commonly obtained for magnetically ordered systems with equal magnetic (EM) moment [96, 102]. For $Gd_{1-x}Y_xNiSi_3$, due to addition of nonmagnetic Y atoms and the rise of Ni magnetic moment, Gd moments are canted resulting in a weak ferromagnetic moment along the c axis but keeping the a crystallographic direction as antiferromagnetic easy axis, as shown in Fig. 6.2. In these cases, it is possible that the magnetic structure becomes amplitude modulated (AM) [subsec. 2.5.3] because at T_N the values of C_m are reduced while the hump is broadened to compensate the loss of entropy, as was exhibited at x=0.50, 0.65 and 0.80 doping levels, and the magnetic fluctuations persist even beyond $2T_N$. For comparison, these behaviors were observed in $GdCu_2Si_2$ as a commensurate simple antiferromagnetic structure with EM moment, $GdNi_2Si_2$ is an incommensurate AM antiferromagnetic structure [103] and $DyNi_2Ge_2$ which shows two distinct magnetic transitions with decreasing temperature: one is from the paramagnetic phase to an AM antiferromagnetic and the other from this phase to an EM antiferromagnetic structure [104].

In a pictorial scheme the substitution of Y by Gd causes that within the unit cell appears spatially inhomogeneous magnetic state and therefore microscopic interfaces. These define antiferromagnetically coupled subdomains whose interaction is long-range, and ferromagnetically correlated subdomains whose interaction is short-range. Competition between these interactions could explain the anomalous magnetic properties of $Gd_{0.50}Y_{0.50}NiSi_3$ and $Gd_{0.35}Y_{0.65}NiSi_3$, such as the presence of broadening in C_m above T_N and exchange bias effect. Note that hysteresis loops are an intrinsic property of these alloys, however at x=0.5 and 0.65 concentrations the exchange coupling between the coexisting magnetic phase are very strong to generate unidirectional anisotropy and therefore a shift in the magnetization hysteresis loop. This behavior was also observed in Al-Fe [105] $R_{1-x}Gd_xAl_2$ [106], $SmFeO_3$ [107] alloys, while the broadening associated with short-range magnetic correlation was also exhibited in $Gd_{1-x}Y_xNi_2Si_2$ compounds [97].

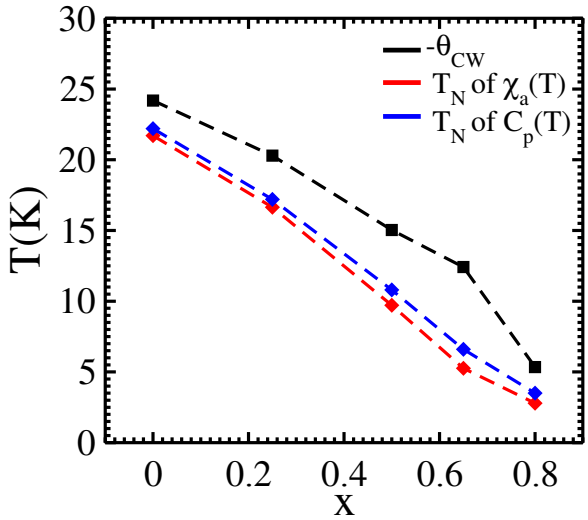

Figure 6.12: Concentration dependence negative Curie-Weiss (black dashed) and Néel temperature obtained from magnetic susceptibility (red dashed) and specific heat (blue dashed) measurements for $Gd_{1-x}Y_xNiSi_3$ compounds.

Figure 6.12 shows the dependence of negative Curie-Weiss temperature ($-\theta^a_{cw}$) and Néel temperature (T_N) on yttrium concentration. The latter was obtained from susceptibility and specific heat measurements with excellent agreement between both techniques. Substitution of Y by Gd in $Gd_{1-x}Y_xNiSi_3$ solid solutions leads to scaling of magnetic ordering temperature with concentration which is consistent with indirect exchange interaction. Additionally, Curie Weiss temperatures exhibit a monotonic decrease with negative values as sign

of strong antiferromagnetic ordering. The frustration parameters $f = \theta^a_{cw}/T_N$ for these compound are approximately constant [Table 6.1] as an indicative that the antiferromagnetic coupling between Gd ions was relieved by Ni atoms due to Y doping.

On the other hand, the metallic and antiferromagnetic behavior shown by $GdNiSi_3$ allows us to assume a RKKY type exchange interaction between Gd magnetic moments. As observed from magnetic measurements, the doping effect causes the antiferromagnetic interplane coupling to be higher than intra-plane (see *bc* plane in Fig. 4.3 and compare Figs. 6.1 and 6.2) leading to a change of exchange interaction and to a weakening of it, which is also evidenced by the reduction of critical magnetic field in magnetization measurements.

The electronic structure of $GdNiSi_3$ and $YNiSi_3$ compounds are similar due to isomorphisms in crystal structure and localization of Gd $4f$ states. At the Fermi level the total DOS of $GdNiSi_3$ is $D(E_F) = 1.15$ states/f.u., spin and eV, and its more important contributions are 0.44, 0.32 and 0.27 states/f.u., spin and eV of Ni d, Si p and Gd d-states, respectively, while for $YNiSi_3$ $D(E_F) = 0.6875$ states/f.u., spin and eV due to 0.2131, 0.2544 and 0.1719 for Y d, Ni d and Si p-states [77], respectively. We expected that in $Gd_{1-x}Y_xNiSi_3$ alloys Y atoms compensate Gd d-states and Ni-d states are gradually reduced while the ferromagnetic exchange interaction between Ni atoms is large at x=0.5 and 0.65. However this situation will be analyzed in more detail.

6.4 Conclusions

We observe that $Gd_{1-x}Y_xNiSi_3$ (x=0, 0.25, 0.50, 0.75, 0.80) compounds have an AFM ground state. Substitution of Y by Gd causes an increase in the magnetic moment above the Gd expected value, a reduction of critical magnetic field and anomalies in the specific heat in both below and above the Néel temperature. We propose that these effects can be explained by the gradual rise of Ni magnetic moment with Y-doping level. As a consequence in the alloys would coexist a localized magnetism (due to Gd) and an induced itinerant ferromagnetism (presumably from Ni $3d$ band) whose Gd-Gd and Gd-Ni interactions are antiferromagnetic while Ni-Ni is ferromagnetic, the latter two being short range. This would allow us to explain the exchange bias effect as an intrinsic property of $Gd_{0.50}Y_{0.50}NiSi_3$ and $Gd_{0.35}Y_{0.65}NiSi_3$, with potential applicability in the field of spintronics for magnetic recording and in the design of spin valves.

7

$Tb_{1-x}Y_xNiSi_3$ systems

Following the same research strategy used for $Gd_{1-x}Y_xNiSi_3$, in this Chapter we will make a detailed study from an experimental approach of nonmagnetic Y-dilution effects on localized Tb-4f moment in $Tb_{1-x}Y_xNiSi_3$, in order to clarify the intrinsic character of the metamagnetic transitions, magnetic hysteresis and complex magnetic phase exhibited by $TbNiSi_3$ [subsec. 4.2.2].

7.1 Experimental results

7.1.1 Structural characterization

Similar to $TbNiSi_3$, the flux method allows us to grow single crystals of $Tb_{1-x}Y_xNiSi_3$ in thin platelike morphology with well defined edges and shiny surfaces. Structural characterization through X-ray diffraction confirms that the crystal structure corresponds to an $SmNiGe_3$-type orthorhombic lattice with $Cmmm$ space group, as expected for such compound. However, the patterns obtained for $x = 0.25, 0.50$ and 0.65 show the presence of peaks that have not been indexed, suggesting the presence of other phases that could not be identified. The XRD patterns of $Tb_{1-x}Y_xNiSi_3$ together with their calculated Rietveld refinement are summarized in Fig. 7.2, while the lattice parameters and volume are included in Table 7.1. Notice that the difference in volume between different samples is less than 1 $Å^3$ and the lattice parameters remain almost constant [Fig. 7.2]. This is expected due to Y atoms having similar ionic radius to those of Gd and Tb.

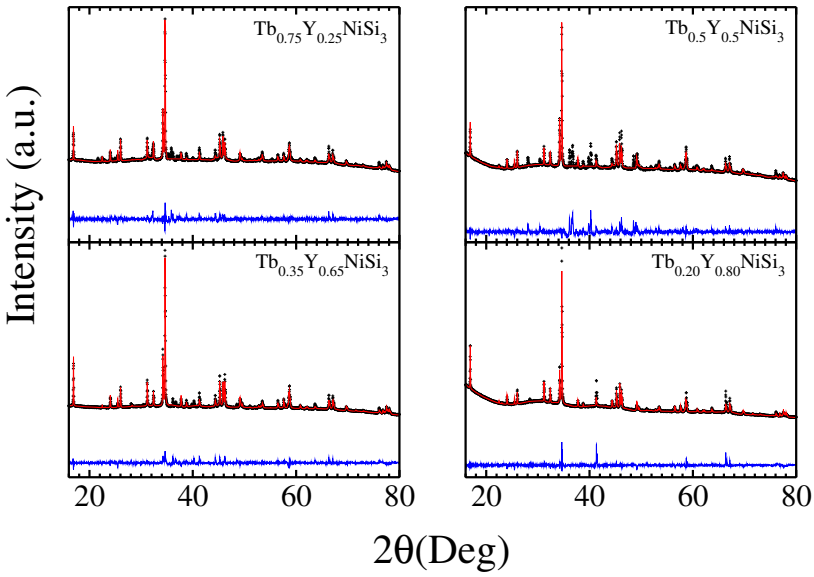

Figure 7.1: Rietveld plot for $Tb_{1-x}Y_xNiSi_3$ (x=0.25, 0.50, 0.65 and 0.80). The black crosses represent the observed data, the red line indicates the calculated pattern, and the blue line depicts the difference between the observed and calculated patterns.

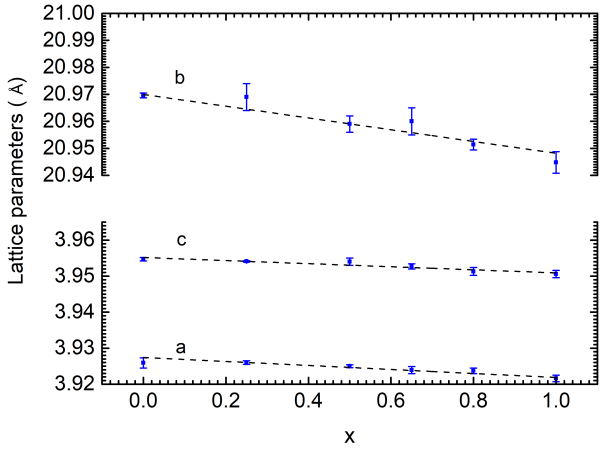

Figure 7.2: Concentration dependent lattice parameters of $Tb_{1-x}Y_xNiSi_3$.

Table 7.1: Lattice parameters of $Tb_{1-x}Y_xNiSi_3$. The values shown for $x = 0$ and $x = 1$ are taken from Ref. [2].

x	a (Å)	b (Å)	c (Å)	V (Å^3)
0	3.9259(1)	20.9696(5)	3.9547(1)	325.57(1)
0.25	3.9260(5)	20.9692(5)	3.9541(2)	325.52(1)
0.5	3.9252(4)	20.9590(3)	3.9540(1)	325.29(2)
0.65	3.9239(1)	20.9514(5)	3.9527(7)	325.00(2)
0.8	3.9237(8)	20.9514(2)	3.9513(1)	324.82(2)
1	3.9216(1)	20.9448(6)	3.9506(1)	324.49(2)

7.1.2 Magnetic susceptibility

The temperature dependence of magnetic susceptibility and inverse susceptibility of $Tb_{1-x}Y_xNiSi_3$ compounds at 1 kOe along the a, b and c-axis and the polycrystalline average are shown in Fig. 7.3 (a) and (b), respectively. All samples exhibit a large peak along the a-axis associated with the antiferromagnetic transition, indicating that the AFM ordered moments remain aligned along the a axis in these crystals. In contrast, χ_b and χ_c show weak temperature dependence, as was observed in $TbNiSi_3$ [Fig. 4.8]. All curves have a broad peak around 50 K along the c-axis [Fig. 7.4], that is preserved upon reducing the Tb concentration. This was also found in $TbCu_2Ge_2$ and it was associated with the existence of some magnetic correlation [3]. In addition, the magnetic response is strongly anisotropic at both high and low temperature, consistent with other Tb-based compounds such as $TbNiGe_3$ [83]. These features were confirmed in magnetization measurements as a function of magnetic field [Fig. 7.3(c)]. Here, depending on the orientation of the single crystal, external magnetic fields can cause a drastic effect on its magnetic properties. The magnetization along the hard direction (b, c-axis) increases almost linearly with the magnetic field. Conversely, the response along the a-axis for all samples except $Tb_{0.2}Y_{0.8}NiSi_3$ is more complex due to the occurrence of metamagnetic transitions accompanied by hysteresis.

In order to make comparisons and understand the effect of non-magnetic Y inclusions on the magnetic properties of $TbNiSi_3$, we plot in Fig. 7.5(a) and (c) the temperature dependence of the average magnetic susceptibility and inverse average susceptibility by subtracting the temperature-independent contribution χ_0, respectively. At low temperature, these samples show an anomaly marking their Néel temperatures, which were estimated by the maximum in the $d(\chi T)/dT \times T$ curves [Fig. 7.5(b)] and are given in Table 7.2.

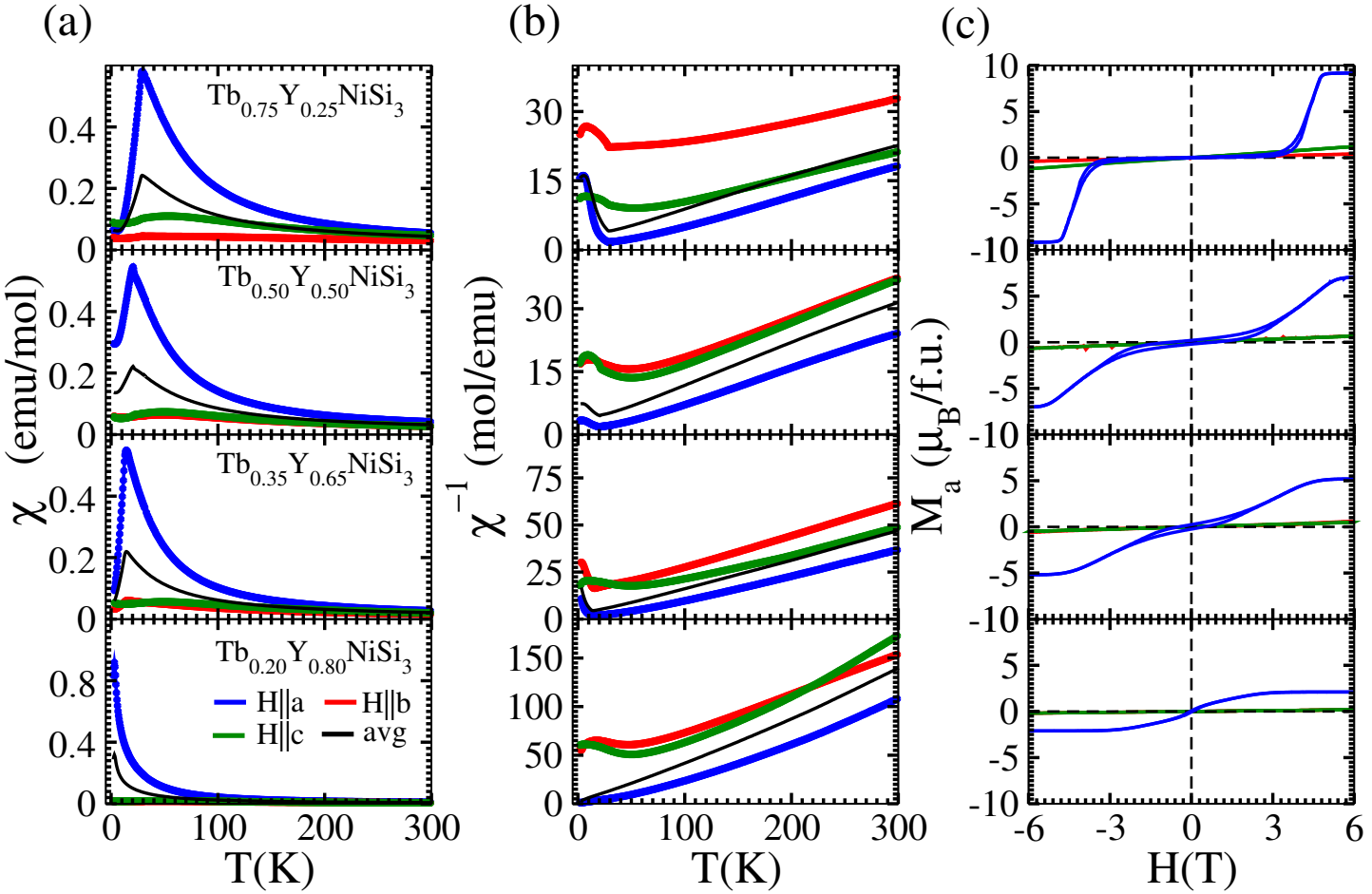

Figure 7.3: Magnetic properties of $Tb_{1-x}Y_xNiSi_3$ with x=0.25, 0.50, 0.65 and 0.80. Temperature dependence of (a) susceptibility and (b) inverse susceptibility at H=1 kOe along a, b and c orientations. Here we include the polycrystalline average for each compound. (c) Magnetic field dependence of magnetization at T=2 K with $H \parallel a$ orientation.

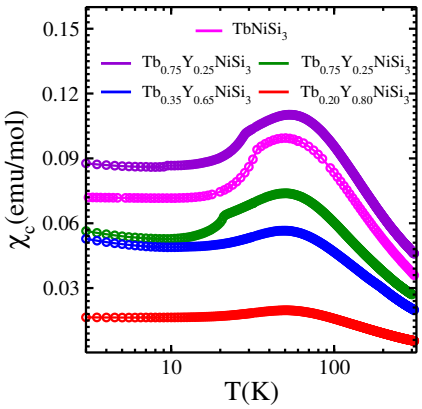

Figure 7.4: Temperature dependence of the magnetic susceptibility along c orientation at $H = 1$ kOe for $Tb_{1-x}Y_xNiSi_3$ ($x = 0.25, 0.50, 0.65$ and 0.80).

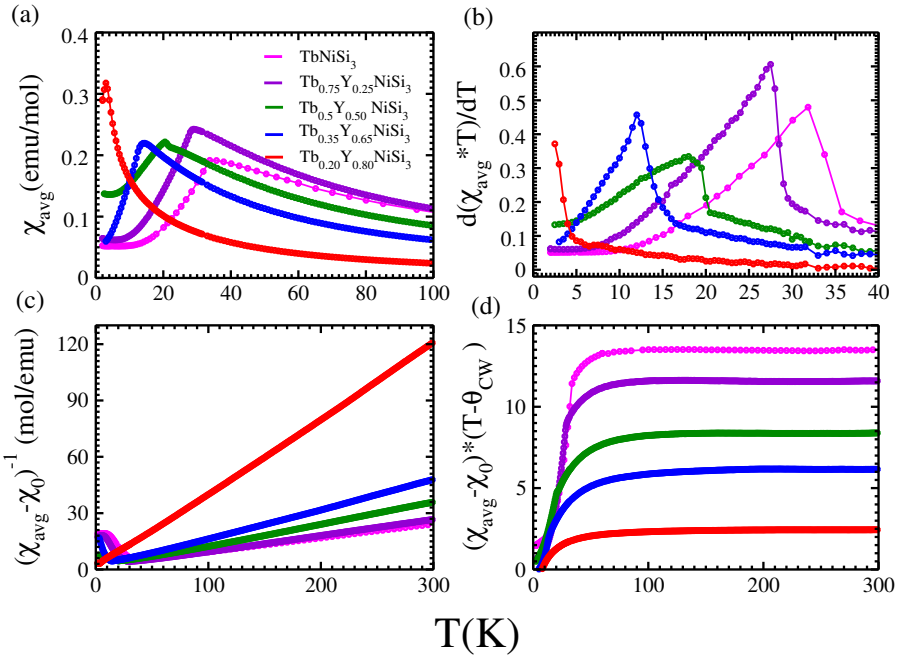

Figure 7.5: Temperature dependence of the average magnetic susceptibility at $H = 1$ kOe for $Tb_{1-x}Y_xNiSi_3$ ($x = 0.25, 0.50, 0.65$ and 0.80). (a) Low temperature magnetic susceptibility. (b) Temperature derivative of the product between magnetic susceptibility and temperature. (c) Inverse susceptibility as a function of temperature, subtracting the Pauli paramagnetic contribution χ_0. (d) Temperature dependence of the Curie-Weiss law $(\chi_{avg} - \chi_0) * (T - \theta_{cw})$.

As expected, T_N is reduced with increasing Y-doping level. For $Tb_{0.5}Y_{0.5}NiSi_3$

Table 7.2: Temperature dependent susceptibility parameters for $Tb_{1-x}Y_xNiSi_3$: Pauli paramagnetic susceptibility χ_0, Néel temperature T_N, Curie-Weiss temperature along a, b and c-axis θ^a_{cw} θ^b_{cw} and θ^c_{cw}, respectively, polycrystalline average θ^p_{cw}, frustration parameter f and effective magnetic moments μ_{eff}. For comparison we include the expected magnetic moment for Tb^{3+} as a concentration function ($(1-x)\mu_{Tb}$) and the excess magnetic moment ($\mu^1_{exc} = \mu_{eff} - (1-x)\mu_{Tb}$).

Parameters	Y-doping level				
	0	0.25	0.50	0.65	0.80
χ_0 (10^{-3} emu/mol)	-0.14(2)	6.59(7)	3.88(6)	0.46(4)	-1.10(2)
T^χ_N(K)	31.8(4)	27.5(2)	18.0(5)	12.0(5)	-
θ^a_{cw}(K)	24.69	30.07	31.86	20.53	24.65
θ^b_{cw}(K)	-103.76	-216.7	-96.99	-64.02	50.94
θ^c_{cw}(K)	-86.4	-64.1	-58.7	-127.8	-43.83
θ^p_{cw}(K)	-25.8(5)	-9 01(2)	-1.3(7)	4.6(2)	7.7(2)
$f = \theta^p_{cw}/T_N$	0.81	0.33	0.07	-0.38	
$\mu_{eff}(\mu_B)$	10.3(8)	9.6(3)	8.2(2)	7.02(2)	4.39(3)
$(1-x)\mu_{Tb}(\mu_B)$	9.72	7.29	4.86	3.40	1.94
$\mu^1_{exc}(\mu_B)$	-	2.31	3.34	3.62	2.45

there is an additional anomaly in the jump shape, above but very close to T_N, which may be related to competition between different magnetic interactions. We will return to this point in the analysis and discussion section. At high temperature (above 150 K), the reciprocal susceptibilities obey the linear Curie-Weiss law $(\chi(T) - \chi_0)^{-1} = (T - \theta_{cw})/C$ [Eq. 2.17]. The fitting parameters are also included in Table 7.2. Note that $TbNiSi_3$ has an effective moment $\mu_{eff} = 10.3(8)\ \mu_B$, which is not far from 9.72 μ_B expected by Hund's rule for the ground state of the free Tb^{3+} ion [Table 2.1], while diluted systems effective moments are higher than the expected $(1-x)\mu_{Tb^{3+}}$ values. On the other hand, the paramagnetic Curie temperatures θ^a_{cw}, θ^b_{cw} and θ^c_{cw} display a large difference as a consequence of the strong magnetic anisotropy in this system. As in the case of $TbNi_2Si_2$ [108, 109], it may be mainly due to crystalline field effects. Here an analysis of the paramagnetic susceptibilities using the CEF Hamiltonian would be very difficult due to the orthorhombic symmetry of the crystal. Moreover, the average paramagnetic Curie temperature θ^p_{cw} increases with raising doping level, evidencing a sign change at $x = 0.65$ maybe due to the presence of ferromagnetic correlations in the material. Finally, we check that these parameters correctly quantify the Curie-Weiss constant at high temperatures [Fig. 7.5(d)].

7.1.3 Magnetization

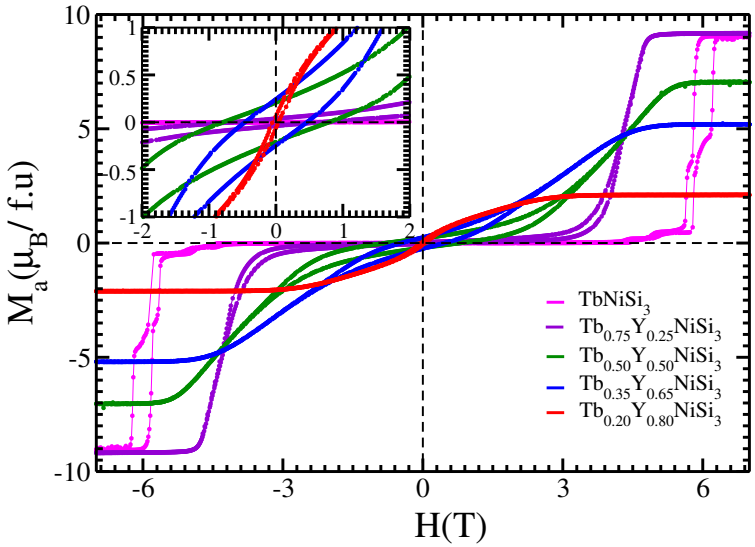

Figure 7.6: Magnetic field dependence of magnetization for $Tb_{1-x}Y_xNiSi_3$ ($x = 0.25, 0.50, 0.65$ and 0.80) at $T = 2$ K with $H \parallel a$ orientation. The inset is a zoom in the range $-2 \leq H \leq 2$ T.

The magnetic isotherms of $Tb_{1-x}Y_xNiSi_3$ at 2 K along the AFM easy axis a are displayed in Fig. 7.6. Its inset shows the behavior at low magnetic field. As reported in Ref. [2], $TbNiSi_3$ exhibits four well-defined steps, in which the metamagnetic transitions occur by flipping of different sublattices that are stable for a specific range of the applied magnetic field. It displays a relatively small magnetization response for applied fields up to 3 T, followed by multiple-step like features. The magnetization suddenly jumps through four well-defined plateaus before saturating at 9.05(3) μ_B where the moments come into a field-induced ferromagnetic state. The hysteresis is asymmetric, with a maximum width of 0.4 T. The magnetization of $Tb_{0.75}Y_{0.25}NiSi_3$ demonstrates a change in slope at around 3 T followed by a gradual increase up to 4.8 T, and again change in slope until saturation is reached at 9.17(5) μ_B. Here the multiple steps observed in $TbNiSi_3$ have vanished and the metamagnetic transition is not as sharp, possibly due to thermal effects and a reduction in magnetic interaction caused by Y atoms. The hysteresis is symmetrically centered around $H = 0$ with a coercive field of 0.68 T [inset Fig. 7.6]. Increasing the Y-doping to $x = 0.50$ causes the coercive field to reach 0.80 T, while the

critical magnetic field and saturation moments decrease. $Tb_{0.2}Y_{0.8}NiSi_3$ shows S-type metamagnetic behavior with no hysteresis nor remanence. However, all samples attain the saturation state, contrary to the Gd system in the previous chapter. These results are summarized in Table 7.3. Here, we include the critical magnetic field estimated by using local maxima in dM/dH, and the magnetic saturation (μ_{HF_a}) obtained by extrapolating of the measured magnetization to infinite field.

Table 7.3: Magnetic field dependence of magnetization parameters along the a-direction for $Tb_{1-x}Y_xNiSi_3$: highest field magnetic moment, saturation magnetic moment ($\mu_{sat} = (1-x)g_J J\mu_B$), excess magnetic moment ($\mu^2_{exc} = \mu^a_{HF} - \mu_{sat}$), critical field and coercive field.

Parameters	Y-doping level				
	0	0.25	0.50	0.65	0.80
μ^a_{HF} (μ_B)	9.05(3)	9.17(5)	7.06 (2)	5.17(2)	2.1(1)
μ_{sat} (μ_B)	9	6.75	4.5	3.15	1.8
μ^2_{exc} (μ_B)	-	2.42	2.56	2.02	0.3
H_c (T)	5.8(6)	4.2(5)	3.8(7)	3.3(9)	-
H_{coe} (T)	0.40(5)	0.68(2)	0.80(5)	0.46(3)	0.05(3)

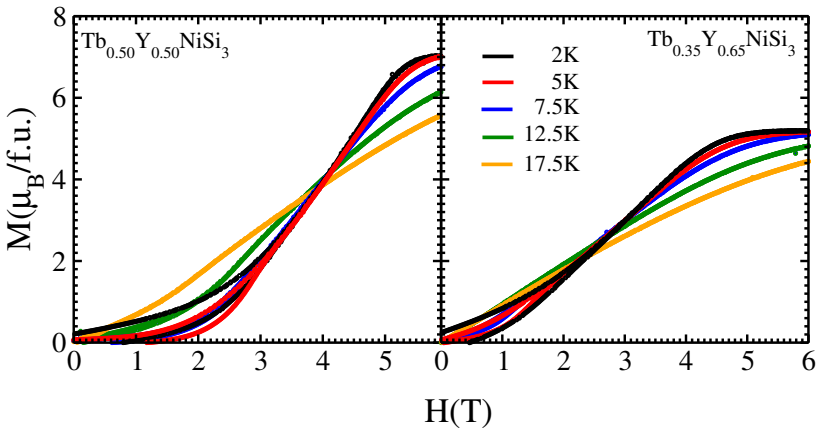

Figure 7.7: Magnetic field dependence of magnetization for $Tb_{0.50}Y_{0.50}NiSi_3$ and $Tb_{0.35}Y_{0.65}NiSi_3$ at $T = 2, 5, 7.5, 12.5$ and 17.5 K with $H \parallel a$ orientation.

Finally, we study the influence of thermal fluctuation on the magnetization measurements presented in Fig. 7.7 for $Tb_{0.50}Y_{0.50}NiSi_3$ and $Tb_{0.35}Y_{0.65}NiSi_3$. We find that all compounds present a reduction in the hysteresis, critical magnetic field, coercive field and saturation moment as the temperature arises, except in the 50% Y-doping where at $T = 5$ K the curve exhibits the maximum coercive field $H_{coe} = 1.17$ T and then gradually decreases due to reduction of

the molecular field.

7.1.4 Normalized Resistance

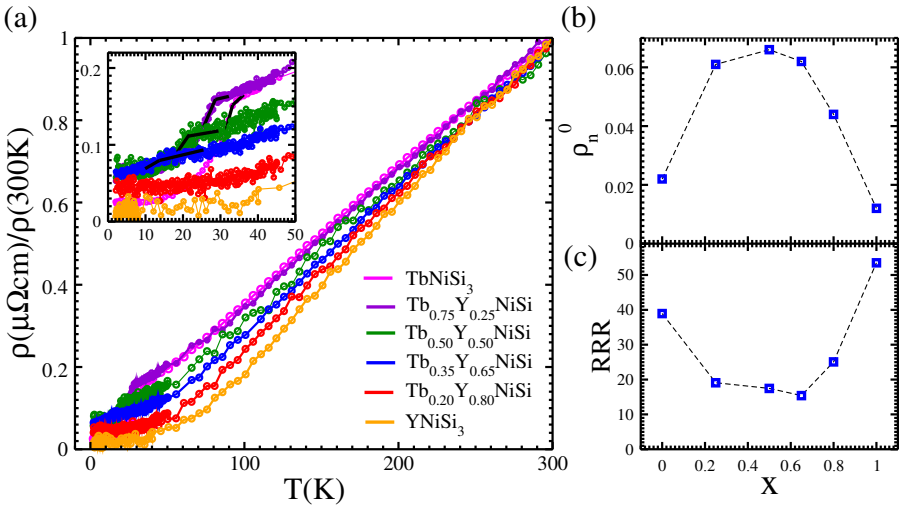

Figure 7.8: (a) Normalized resistance measurements for $Tb_{1-x}Y_xNiSi_3$ under zero field in the configuration $I \perp b$. The inset shows a zoom in the range $2 \leq T \leq 50$ K, where the AFM transition takes place. (b) Concentration dependence of normalized residual resistivity obtained from the extrapolation of $\rho(T)/\rho(300\text{ K}) = \rho_n^0 + A_n T^2$. (c) Residual resistivity ratio RRR as a function of concentration x.

Table 7.4: Normalized resistance measurement parameters for $Tb_{1-x}Y_xNiSi_3$: Néel temperature T_N^ρ (K), normalized residual resistivity ρ_n^0 ($\mu\Omega$cm) and normalized Fermi-liquid constant A ($\mu\Omega\text{cmK}^2$) obtained from the extrapolation of $\rho(T)/\rho(300\text{ K}) = \rho_n^0 + A_n T^2$, and the residual resistivity ratio RRR calculated with Eq. 2.44.

Parameters	Y-doping level					
	0	0.25	0.50	0.65	0.80	1
T_N^ρ	32.3(7)	25.7(9)	17.6(2)	11.9(1)	-	-
ρ_n^0	0.022(4)	0.061(7)	0.066(2)	0.062(7)	0.044(1)	0.012(2)
$A_n(10^{-5})$	5.1(3)	6.4(3)	2(2)	1.1(2)	2(2)	6(3)
RRR	38.93	19.09	17.46	15.40	25.06	53.5

Figure 7.8 shows the resistance, normalized to the value at 300 K, as a function of temperature for $Tb_{1-x}Y_xNiSi_3$ at $H = 0$ and $I \perp b$. At high temperature ρ

increases monotonically with rising temperature, exhibiting a T-linear behavior characteristic of metals. Moreover, the value of ρ for the pure compound is slightly higher than for the alloys, where there is a systematic reduction in the slope of linear resistivity with decreasing Tb concentration compared to the non-magnetic reference compound $YNiSi_3$, which can be attributed to crystal electric field effects. At low temperature [inset Fig. 7.8], except for $x = 0.8$ all samples exhibit a sharp cusp that marks the cooperative magnetic transition and defines the ordering temperature of the Tb sublattice which shifts to lower temperatures with ascending Y-doping level. To extract sufficiently accurate values of T_N, we use the segmented linear regression model of Eq. 2.47. We find that at $x = 0, 0.25, 0.50$ and 0.65 concentrations, the Néel temperatures are 32.3(7), 25.7(9), 17.6(2) and 11.9(1) K, respectively, which are in very good agreement with those obtained from magnetic measurements (compare with Table 7.2) Below the Néel temperature, the slope of resistivity curves becomes more convex with decreasing temperature and therefore follow Fermi liquid behavior [Eq. 2.48] due to loss of magnetic scattering. We determine the normalized residual resistivity ρ_n^0 as a parabolic extrapolation at $T = 0$ K of the $\rho(T)/\rho(300\text{ K})$ curves, and the residual resistivity ratio RRR as $\rho(300\text{ K})/\rho(2\text{ K})$ whose values are illustrated in Fig. 7.8(b) and (c), respectively, and they are listed in Table 7.4. These indicate few impurities in the compounds and thus a high quality of single crystals. ρ_n^0 exhibits a negative concavity curve-type and RRR a positive concavity curve-type with Y-doping, displaying a slope change in the region $0.50 < x < 0.65$ where the long-range order changes, which confirms the fact that Tb concentration level is strongly correlated with RRR and therefore the substitution of Tb by Y strongly affects the electrical resistivity of these compounds.

7.2 Analysis and discussion

Figure 7.9 displays the magnetic moment as a function of concentration. We note that for $Tb_{1-x}Y_xNiSi_3$ the observed effective moment is larger than that of the free ion moment. Moreover, the values of the highest field magnetic moment μ_{HF}^a are above the expected saturation moment μ_{sat} for an assembly of Tb^{3+} ions. Therefore, the additional contribution appears to be an induced moment and may be associated with Ni $3d$-electrons, as for $Gd_{1-x}Y_xNiSi_3$ compounds mentioned in the previous Chapter 6.

Curie-Weiss temperature along a, b, c -axis evidenced the large magnetic anisotropy in these compounds due to the strong dependence of θ_{cw} with the direction of applied magnetic field, Table 7.2. Since they give an indication of

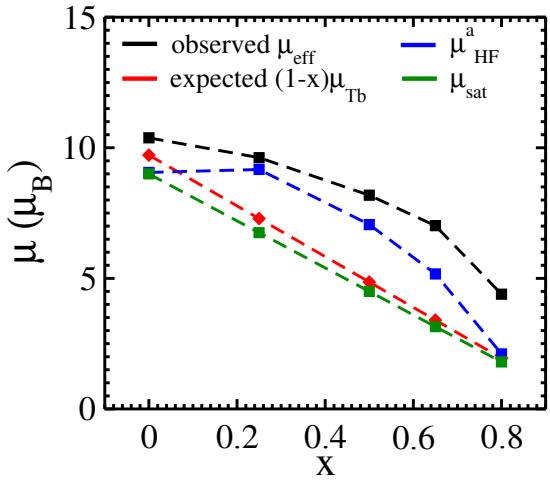

Figure 7.9: Concentration dependent experimental effective magnetic moment μ_{eff} (black dashed) and the highest observed moment at 2 K μ^a_{HF} (blue dashed) for $Tb_{1-x}Y_xNiSi_3$ alloys. For comparison we include the theoretical value of free rare earth ions $(1-x)\mu_{Tb}$ (red dashed) and the saturation expected value μ_{sat} (green dashed).

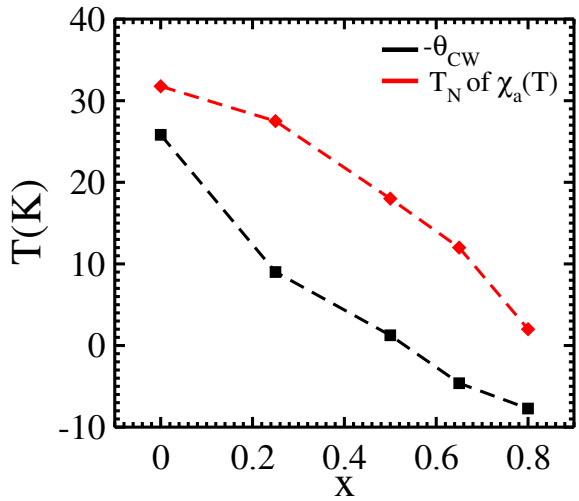

Figure 7.10: Concentration dependent negative Curie-Weiss (black dashed) and Néel temperature (red dashed) obtained from magnetic susceptibility (red dashed) and specific heat (blue dashed) measurements for $Tb_{1-x}Y_xNiSi_3$ compounds.

the strength of magnetic interactions, the positive value of θ^a_{cw} corresponds to a dominant ferromagnetic interaction between *cb*-planes while the negative value of θ^b_{cw} and θ^c_{cw} alludes to an antiferromagnetic interaction between *ca*-planes.

Similar behaviors are observed in $Tb(Ni_{1-x}Co_x)_2Ge_2$ [110] and $TbCu_2$ [111]. Conversely, as seen in Fig. 7.10, θ^p_{cw} is negative for the pure compound but as the concentration of Y increases, it becomes positive in the region $x > 0.50$ where ferromagnetic interactions predominate differently from those found for $Gd_{1-x}Y_xNiSi_3$ where θ^p_{cw} is always negative [Fig. 6.12]. Notice that this effect is observed despite the fact that all samples exhibit antiferromagnetic order in the susceptibility curve [Fig. 7.5]. On the other hand, Néel temperature shifts toward lower temperatures in a nearly linear form as Y atoms are diluted in $TbNiSi_3$. This behavior is observed in other Y-Tb solid solutions [112], where the RKKY interaction is mainly responsible for the magnetic ordering, indicating a gradual weakening of the antiferromagnetic interaction. The ratio between Curie-Weiss and Néel temperature, that determining the frustation parameter $f = \theta^p_{cw}/T_N$, is very small due to the system not being frustrated, however it moves away from 1 with increasing Y concentration due to possible existence of a significant short-range magnetic order beyond the magnetic transition as exhibited by the hump-shape in the susceptibility curve [Fig. 7.5].

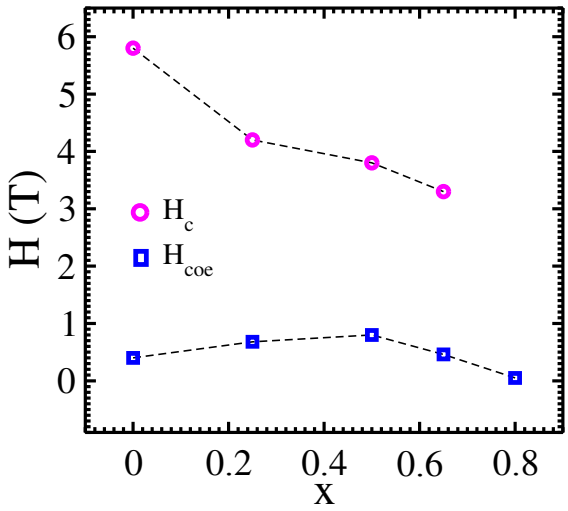

Figure 7.11: Concentration dependent magnetic coercive field (blue square) and critical field (magenta circle) obtained of $M \times H$ measurements at T=2 K for $Tb_{1-x}Y_xNiSi_3$ compounds.

The critical field and coercivity as a function of Y-concentration are shown in Fig. 7.11. We observe that with increasing Y doping, the coercive field increases up to 0.80(5) T at 50%-Y and above it decreases monotonically, while the critical fields decrease for all concentrations considered. Moreover, both decrease exponentially with increasing temperature. Therefore, the metamagnetic transition and the hysteresis around the critical field are very sensitive to

the compound composition and thermal fluctuations [Fig. 7.7].

The magnetic properties of $Tb_{1-x}Y_xNiSi_3$ discussed above are consequence of competition between several magnetic interactions. $TbNiSi_3$ is a commensurate structure with collinear Tb-moments along a-axis [Fig. 4.11], whose Tb-Tb interaction is determined by long-range antiferromagnetic indirect exchange and CEF effects. Its complex magnetic behavior is similar to $TbNi_2Si_2$ [113] and $TbNi_2Ge_2$ [114], which are considered as Ising systems with competing interaction [115, 116]. When Y is replaced by Tb the magnetically ordered structure is destabilized, the molecular field is locally reduced altering the bilinear exchange interactions but the magnetocrystalline anisotropy apparently is not decreased and it is present still in $YNiSi_3$ [subsec. 4.2.1]. Notice that each compound correspond to different magnetic structures where the magnetic moments follow the same a-axis collinearity as the pure compound at low magnetic fields, and formed a non-collinear configuration above a critical field [Figs. 7.3-7.6 and subsec. 2.5.3]. Also, the susceptibility measurement indicates the existence of magnetic order with weak ferromagnetism from $x > 0.5$ which was attributed to arising of Ni magnetic moments, however it is not seen in the electrical resistivity. In spite of this, we expected that the considerable magnetic contribution to resistivity causes a scattering of conduction electrons by localized $4f$-electrons of Tb and weakly by $3d$-electrons of Ni.

7.3 Conclusions

All $Tb_{1-x}Y_xNiSi_3$ compounds exhibit an AFM ground state with strong magnetic anisotropic and crystalline field effects. The presence of Y atoms do not strongly alter the lattice parameters, the metallic behavior nor the a-easy axis observed in $TbNiSi_3$. However, it causes a reduction of Néel temperature and therefore a drop in the strength of antiferromagnetic long-range interaction between Tb-Tb atoms. In addition, it modifies the sign of Curie-Weiss temperature from negative to positive at 65% Y-doping indicating the presence of ferromagnetic short-range interaction, which is also visible as a jump shape in the susceptibility measurements for $Tb_{0.5}Y_{0.5}NiSi_3$. Finally, we observe that the dilutes compounds have both effective and saturation magnetic moments above the expected value, suggesting the gradual emergence of Ni magnetic moment, whose Ni-Ni interaction is ferromagnetic. Thus, the physical properties of Tb-alloys will be determined by the competition between these interactions.

Part III

Work in progress

8

$YbNiSi_{3-x}Ge_x$

The competition between Kondo effect and RKKY interaction can lead to new stable states of matter near a quantum critical point (QCP). These are controlled by some parameter tuning such as magnetic field, hydrostatic pressure or chemical composition. As mentioned in subsec. 4.3-4.4 magnetic field suppresses the magnetic order of the antiferromagnetic-Kondo lattice $YbNiSi_3$, while the pressure induces the Kondo effect in the non-magnetic structure $YbNiGe_3$. In this chapter we are interested in studying from an experimental approach how the RKKY indirect exchange coupling changes and how the hybridization between magnetic moments and conduction electrons increases through chemical substitution of Si by Ge in $YbNiSi_{3-x}Ge_x$ and the application of the magnetic field on each of these compounds. This will allow to change the magnetic ground state continuously and moving towards a non-magnetic state by passing through a QCP. For this purpose we perform several attempts to grow single crystals, which will be characterized by means of magnetization and resistivity measurements.

8.1 Single crystal growth

A bibliographic review on $YbNiSi_3$ indicates that these grow from Sn flux using a starting proportion of Yb:Ni:Si:Sn 1:1:3:20 and a temperature ramp such that the sample is heated to 1150 °C and slowly cooled to 500 °C [10]. Thus, to grow $YbNiSi_{3-x}Ge_x$ single crystals, we consider an initial proportion Yb:Ni:Si:Ge:Sn 1:1:3-x:x:20 for x=0, 0.003, 0.03, 0.05, 0.1, 0.2, 2.7, 2.85 and 3 with the same temperature ramp mentioned in subsec. 3.1.2. Now, in order to determine whether these growths are sensitive to small changes in composition, we performed some test with the initial proportion Yb:Ni:Si:Ge:Sn 1:1:3-x:x:45 for x=0.15 and 2.85 used to successfully grow $RNiSi_3$ (R=Y, Gd-Tm, Lu) [sec. 4.1]. In Fig. 8.1 we include some images of the obtained single crystals,

where we observed that they have the platelike morphology expected with well-defined shapes and shiny surfaces.

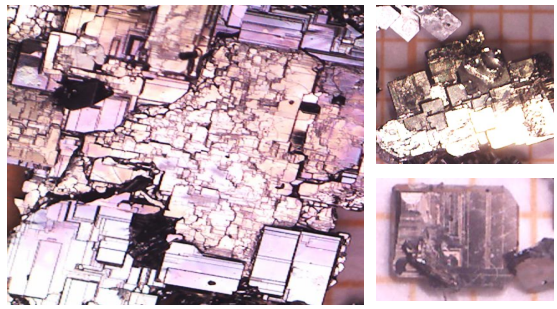

Figure 8.1: Single crystals obtained of initial proportion Yb:Ni:Si:Ge:Sn 1:1:3-x:x:20.

For each compound we chose clusters of single crystals and on them we performed X-ray powder diffraction measurements, whose patterns are shown in Fig. 8.2. Rietveld refinements allow us to distinguish at least three different phases: (i) $YbNiSi_3$ [Fig. 4.3] is a $SmNiGe_3$-type orthorhombic structure with space group $Cmmm$ (No. 65), (ii) $YbNi_2Si_3$ [Fig. 8.3] is a $ScNi_2Si_3$-type tetragonal structure with space group $I4/mmm$ (No.139) and (iii) $YbNiGe_3$ [Fig. 4.17] is a tetragonal crystal class with space group $I4_1/amd$ (No.141). Figure 8.2 (a) presents the indexing of (i) and (ii) phases, (b) and (d) the indexing of (ii) and (iii) phases, respectively, while the pattern in (c) corresponds to an unknown phase. In Table 8.1 we include the initial proportion of growth, parameters and volume resulting from Rietveld refinement. The weak reduction in the volume of the crystalline structure evidences a weak shift of the central peak of the #1, #2, #3 and #4 patterns towards high angles, although this is imperceptible on the scale used. Therefore, by Bragg law [Eq. 3.1] they demonstrate a weak reduction in their volume. However, #5 and #6 exhibit a gradual expansion in the unit cell volume due to possible valence change of Yb as it goes from $YbNiSi_3$ with Yb^{3+} to $YbNiGe_3$ with a fluctuating valence state between +2 and +3. These behaviors were also observed in $YbCu_{5-x}Al_x$ and $Ce(Cu_{1-x}Co_x)_2Ge_2$ systems [24, 117]. Due to some difficulties generated by COVID-19 pandemic, it was not possible to use other experimental techniques to determine the exact composition of the samples. We then decided to organize the samples according to the increment in the coherence temperature observed in resistivity measurements, this will be detailed in the next section, and to label them by sample number corresponding to the sequence considered.

$YbNi_2Si_3$ has a layered crystal structure similar to that of $YbNiSi_3$ and

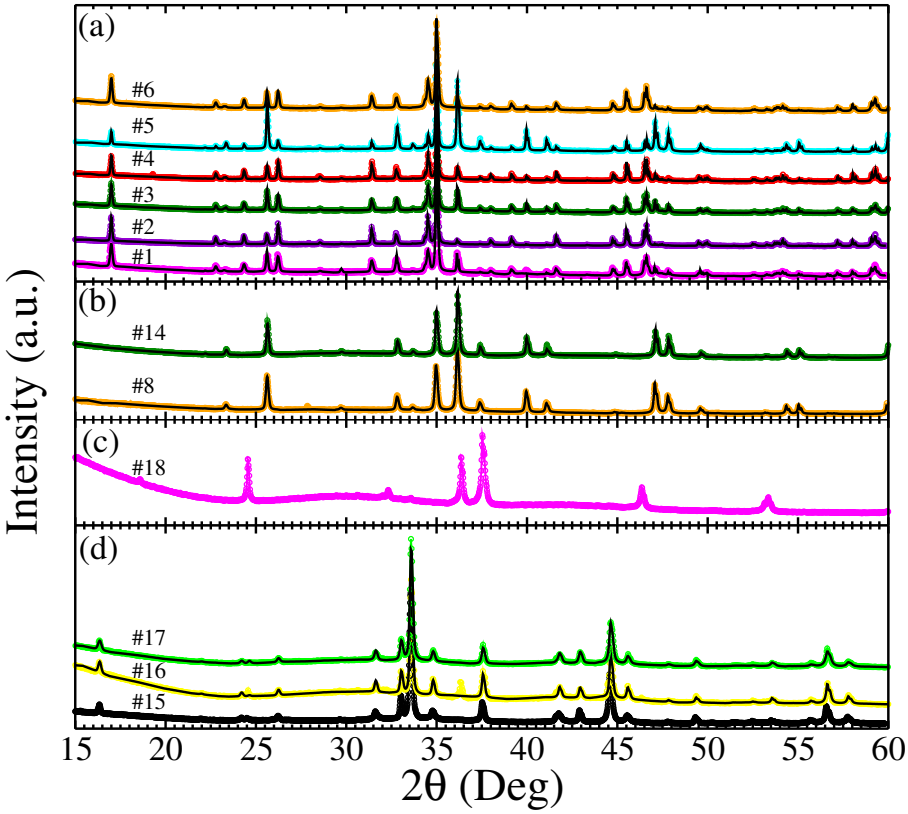

Figure 8.2: The XRD Rietveld refinement for (a) $SmNiGe_3$-type orthorhombic structure with space group $Cmmm$, (b) $ScNi_2Si_3$-type tetragonal structure with space group $I4/mmm$, (c) unknown phases and (d) tetragonal crystal class with space group $I4_1/amd$.

$YbNiGe_3$, whose layer sequences is Si-Ni-Yb-Si-M-Si-Yb-Ni-Si, Si-Ni-Yb-Si-Si-Yb-Ni-Si and Ge-Yb-Ni-X-[X-Ni-Yb-Ge-Ge-Yb-Ni-X]-X-Ni-Yb-Ge while accommodating 20, 24 and 40 atoms in the unit cell, respectively, with simultaneous occupation of M(Ni/Si) and X(Ni/Ge). In all cases, Yb has a single crystallographic site, however its $2mm$ local inversion symmetry is broken at $4mm$ for 123-system [Tables 4.2, 4.8 and 8.2], where Ni atoms have two Wyckoff positions $4e$ and $4d$. Additionally, the magnetic properties of $YbNi_2Si_3$ are similar to those of $YbNiSi_3$. This is treated as an antiferromagnetic Kondo lattice with c-AFM easy axis, Néel temperature T_N=0.35 K and Kondo temperature T_K=2 K, whose magnetism comes from Yb^{3+} ions. [118].

On the other hand, the $YbNiSi_3$ structure has three different sites for Si [Table 4.2]. The incorporation of Ge atom can randomly go to one of these or

Table 8.1: Compounds that crystallize in $SmNiGe_3$-type orthorhombic structure (space group $Cmmm$), in $ScNi_2Si_3$-type tetragonal structure (space group $I4/mmm$) and a tetragonal crystal class (space group $I4_1/amd$). Initial proportion considered in the growth, and the lattice parameters and volume obtained from Rietveld refinement also are included.

Sample	Intial prop.			Lattice parameters			Volume
Number	Si :	Ge:	Sn	a (Å)	b (Å)	c (Å)	V (Å^3)
$SmNiGe_3$-type (Cmmm)							
#1	2.95	0.05	20	3.8933	20.8714	3.9034	317.187
#2	3	0	20	3.8930	20.8682	3.9033	317.106
#3	2.8	0.2	20	3.8923	20.8662	3.9026	316.956
#4	2.97	0.03	20	3.8919	20.8592	3.9022	316.790
#5	2.997	0.003	20	3.8917	20.8624	3.9022	316.824
#6	2.9	0.1	20	3.8930	20.8647	3.9026	316.994
$ScNi_2Si_3$-type (I4/mmm)							
#7	2.95	0.05	20	3.8590	3.8590	24.0249	357.776
#8	3	0	20	3.8580	3.8580	24.0346	357.733
#9	3	0	20	3.8580	3.8580	24.0272	357.620
#10	2.9	0.1	20	3.8574	3.8574	20.0309	357.573
#11	2.8	0.2	20	3.8572	3.8572	24.0273	357.483
#12	2.997	0.003	20	3.8568	3.8568	24.0236	357.354
#13	2.97	0.03	20	3.8565	3.8565	24.0178	357.203
#14	2.85	0.15	45	3.8551	3.8551	24.0171	356.928
$YbNiGe_3$-Tetragonal class ($I4_1$/amd)							
#15	0	3	20	4.0618	4.0618	43.3833	715.738
#16	0.15	2.85	20	4.0578	4.0578	43.3524	713.822
#17	0.3	2.7	20	4.0579	4.0579	43.3416	713.846
Unknown phase							
#18	0.15	2.85	45	-	-	-	-

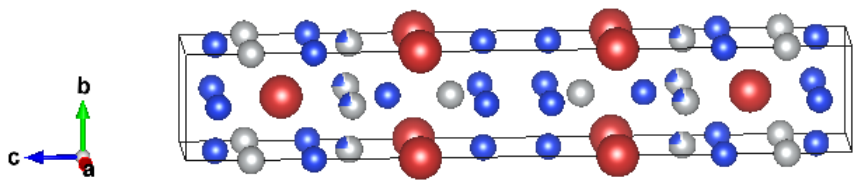

Figure 8.3: Unit cell of $YbNi_2Si_3$ tetragonal structure in space group $I4/mmm$. Dark red, gray and blue spheres denote the Yb, Ni and Si atoms, respectively.

Table 8.2: Atom coordinates for $YbNi_2Si_3$ compound [118].

Site	Wyckoff position	Site symmetry	x	y	z	Occ.
Yb	4*e*	4*mm*	0	0	0.351936(16)	1
Ni	4*e*	4*mm*	0	0	0.09782(5)	1
Si1	8*g*	2*mm*	0	0.5	0.04880(7)	1
Si2	4*e*	4*mm*	0	0	0.19220(12)	1
M(Ni/Si)	4*d*	$\bar{4}m2$	0	0.5	0.25	0.74/0.21

even occupy all sites. We check the latter possibility in the Rietveld refinements and we include these results in Table 8.3. Here we observed that Si_2 and Si_3 sites are more probable to be occupied by the Ge atom, since the maximum occupancy corresponds to 0.2 according to ratio multiplicity atoms/ multiplicity group=4/20. However, the results obtained do not allow to determine the Si/Ge concentration, nor the vacancies in the Yb and Ni sites. For this, it will be necessary to perform an energy dispersive X-Ray (EDX) analysis, which we will leave for future work.

Table 8.3: Yb, Ni, Si and Ge occupancies obtained from Rietveld refinement when considering that the three silicon crystallographic sites can be occupied by Ge atoms. Here we include the χ^2 parameter to indicate the refinement quality.

# Sample	Yb	Ni	Si1	Ge1	Si2	Ge2	Si3	Ge3	χ^2
#1	0.197	0.200	0.198	0.008	0.161	0.029	0.186	0.003	10.3
#2	0.199	0.199	0.200	0.000	0.204	0.000	0.199	0.000	4.59
#3	0.206	0.203	0.106	0.047	0.190	0.016	0.049	0.071	5.75
#4	0.203	0.201	0.195	0.002	0.203	0.002	0.199	0.002	8.14
#5	0.205	0.204	0.203	0.000	0.198	0.000	0.204	0.002	7.82
#6	0.199	0.200	0.193	0.000	0.106	0.041	0.114	0.037	4.72

8.2 Resistivity

Temperature-dependent resistivity $\rho(T)$ curves normalized with respect to room-temperature resistivity $\rho(300\ K)$ for $YbNiSi_{3-x}Ge_x$ at H=0 T are shown in Fig. 8.4. As expected, all compounds exhibit a large drop at low temperatures which is attributed to the combined effect of the reduction of spin-disorder

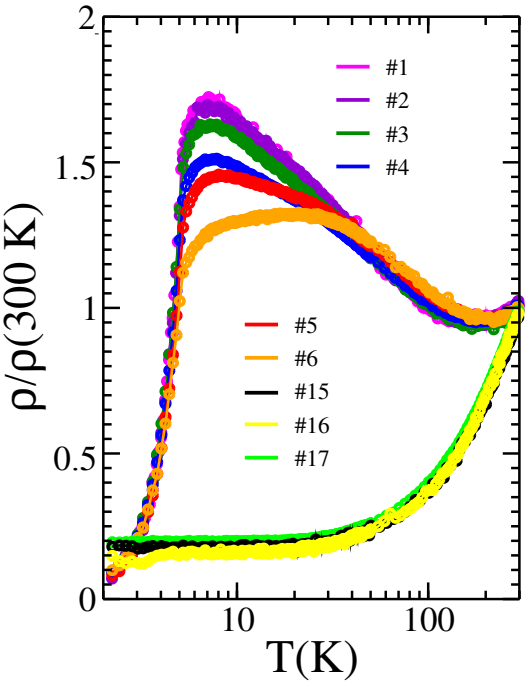

Figure 8.4: Temperature dependent normalized resistance measurements for $YbNiSi_{3-x}Ge_x$ under zero field in the configuration $I \perp b$. The notation used for the compounds correspond to those given in Table 8.1.

scattering and the occurrence of coherent scattering of electrons by Yb ions sublattice. In order to quantify the changes generated by the presence of Ge-atoms, we fit Eqs. 2.48 and 2.50 in the low (2-4.5 K) and high (55-100 K) temperature regions, respectively. In Table 8.4 we indicate the results given for residual resistivity ρ_0, prefactor A, exponent n, a and b parameters, as well as the Néel temperature obtained by $d\rho/dT$, the coherence temperature and the minimal temperature [subsec. 2.8.2]. All these are plotted in Fig. 8.5. The values of n allude to the electron scattering by acoustic phonons [subsec. 2.8.1]. Therefore, the 2-4.5 K region is very high to observe Fermi-liquid behavior. As reference, the results reported for $YbNiSi_3$ indicate that this occurs below 1 K [10]. Despite this, the sequence of compounds considered along this chapter is quite special. Samples with high Si-concentration show a Kondo-like upturn that decreases and broadens becoming flattened at #5 and #6 while T_{coh} and T_{min} shift to high temperatures similar to the effect observed in $YbNiGe_3$ when reducing the hydrostatic pressure from 6.5 GPa to 0 GPa [Fig. 4.19], with the strong Kondo hybridization intensity happening for #3 and #4 due to the maximum values attained for b parameter [Eq. 2.50].

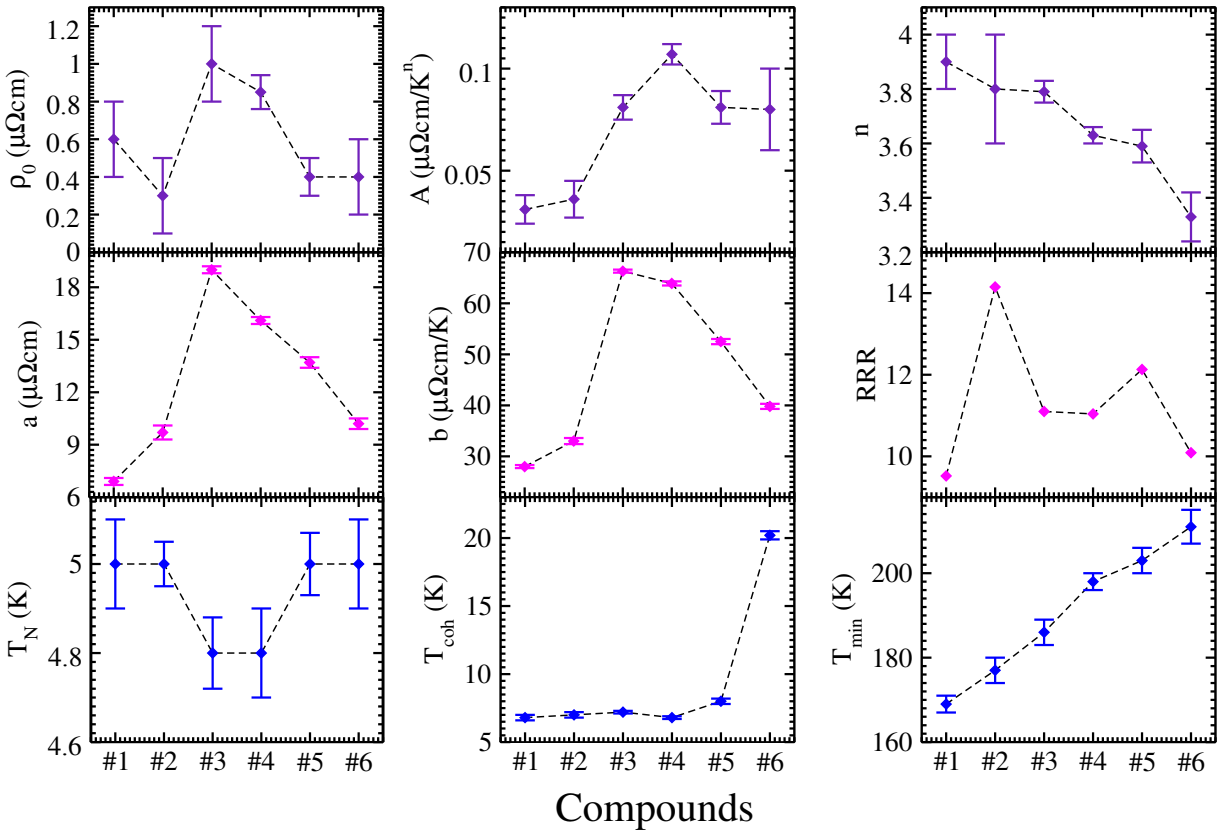

Figure 8.5: Graphical evolution of some parameters describing the physics of $YbNiSi_{3-x}Ge_x$ in relation to the sequence of compounds considered in Table 8.1. These parameters are the residual resistivity ρ_0, resistivity coefficient A and resistivity exponent n of Eq. 2.48, a and b-parameter of Eq. 2.50, residual resistivity ratios RRR, Néel temperature T_N, coherence temperature T_{coh} and minimal temperature T_{min}.

Table 8.4: Main resistivity parameters for $YbNiSi_{3-x}Ge_3$ as a function of magnetic field applied H for the sequence of compounds considered in Table 8.1 These are the residual resistivity ρ_0 ($\mu\Omega$cm), resistivity coefficient A ($\mu\Omega$cm/K^n) and resistivity exponent n of Eq. 2.48, a and b-parameter of Eq. 2.50, residual resistivity ratios RRR, Néel temperature T_N^ρ (K), coherence temperature T_{coh} (K) and minimal temperature T_{min} (K).

H	ρ_0	A	n	a	b	T_N^ρ	T_{coe}	T_{min}	RRR
					#1				
0	0.6(2)	0.031(7)	3.9(1)	6.9(2)	28.0(3)	5.0(1)	6.8(2)	169(2)	9.52
1	0.5(1)	0.048(7)	3.7(1)	7.7(2)	29.2(2)	4.8(2)	7.0(1)	169(2)	9.83
					#2				
0	0.3(2)	0.036(9)	3.8(2)	9.7(4)	33.0(6)	5.0(1)	7.0(2)	177(3)	14.15
1	0.3(2)	0.040(9)	3.8(1)	9.5(2)	32.9(4)	4.8(1)	8.0(1)	177(3)	12.45
3	0.4(2)	0.060(9)	3.57(9)	8.9(3)	31.8(4)	4.6(1)	10.2(1)	177(3)	10.11
					#3				
0	1.0(2)	0.081(6)	3.79(4)	19.0(2)	66.3(3)	4.8(1)	7.2(1)	186(3)	11.10
1	0.7(2)	0.093(8)	3.75(5)	18.5(2)	65.5(3)	4.82(9)	7.6(2)	186(3)	11.29
3	0.9(1)	0.21(1)	3.23(4)	17.3(2)	63.2(3)	4.6(1)	9.4(2)	186(3)	7.62
5	2.1(4)	0.12(3)	3.6(2)	14.9(3)	58.7(5)	4.02	12.8(2)	186(3)	6.22
7	-9.5(2)	7(1)	0.86(8)	13.1(4)	54.9(7)	2.4(1)	19.8(2)	186(3)	6.28
					#4				
0	0.85(9)	0.107(5)	3.63(3)	16.1(2)	63.9(4)	4.8(1)	6.8(1)	198(2)	11.04
1	0.9(1)	0.102(5)	3.68(3)	15.1(4)	62.0(7)	4.8(1)	8.2(1)	198(2)	10.07
3	0.6(1)	0.26(1)	3.11(3)	16.2(2)	63.9(4)	4.6(1)	9.8(1)	198(2)	8.15
5	1.1(2)	0.24(2)	3.15(5)	14.2(2)	60.1(3)	4.0(1)	13.2(1)	198(2)	7.65
7	-12(2)	9(1)	0.78(6)	12.5(3)	56.7(6)	2.8(1)	25.2(2)	198(2)	6.74
					#5				
0	0.4(1)	0.081(8)	3.59(6)	13.7(3)	52.5(5)	5.0(1)	8.0(2)	203(3)	12.13
1	0.55(7)	0.091(4)	3.54(3)	13.4(2)	51.9(3)	4.8(1)	8.6(3)	203(3)	11.13
3	0.1(2)	0.21(2)	3.02(4)	12.5(2)	50.1(3)	4.6(1)	15.8(2)	203(3)	9.32
5	0.3(2)	0.22(2)	3.00(7)	12.4(3)	49.9(6)	4.0	24.8(2)	203(3)	8.65
7	-7(1)	5(1)	0.87(9)	10.9(2)	46.7(4)	2.8	31.8(2)	203(3)	6.94
					#6				
0	0.4(2)	0.08(2)	3.33(9)	10.2(3)	39.8(5)	5.0(1)	20.2(3)	211(4)	10.09
1	0.5(2)	0.09(2)	3.4(1)	10.8(4)	41.3(8)	4.8(1)	24.4(2)	211(4)	9.08
3	-0.6(3)	0.38(5)	2.44(8)	10.3(2)	40.1(5)	4.6(1)	26.6(2)	211(4)	8.17
5	-1.1(7)	0.5(2)	2.1(2)	9.6(2)	38.7(4)	3.8(1)	29.6(3)	211(4)	7.94
7	-5(1)	4(1)	0.8(1)	8.7(2)	36.9(4)	2.8(1)	35.8(2)	211(4)	6.99

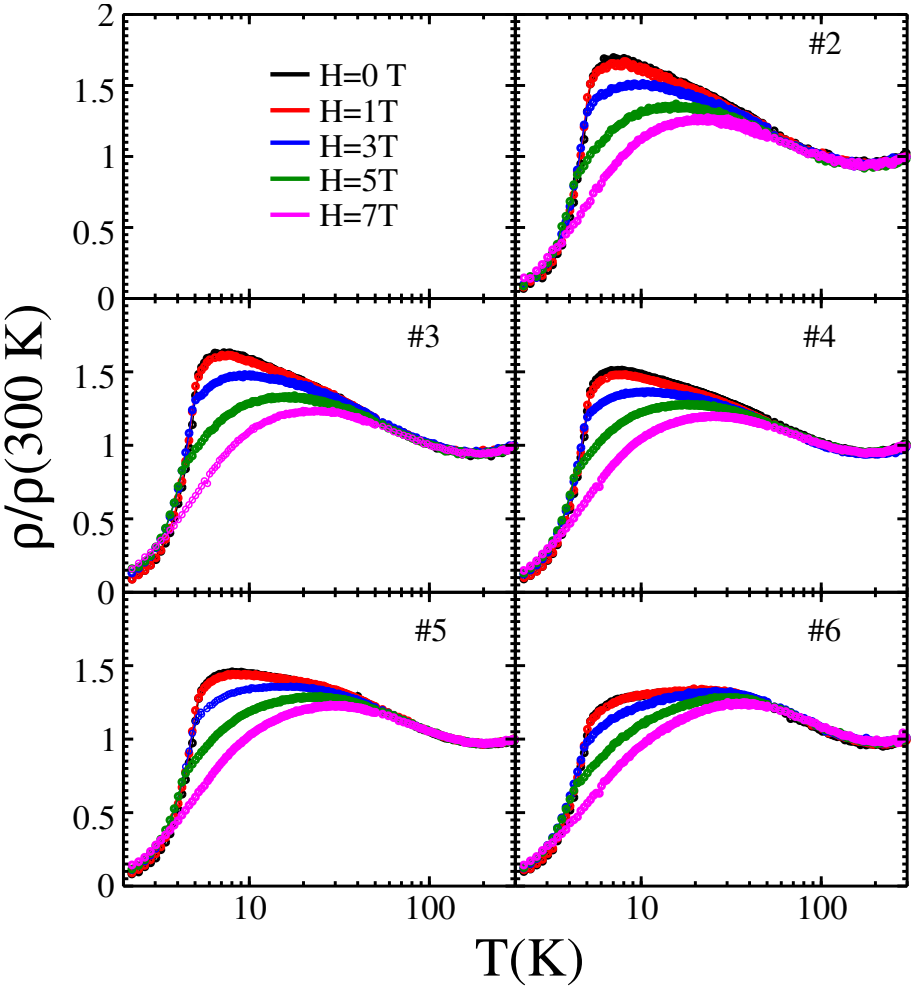

Figure 8.6: Temperature dependent normalized resistance measurements for $YbNiSi_{3-x}Ge_x$ under an applied magnetic field of H=0, 1, 3, 5 and 7 T in the configuration $I \perp b$. The notation used for the compounds correspond to those given in Table 8.1.

In addition, we see that A [Eq. 2.48] increases, while n decreases suggesting a valence change in the compound while following the expected behavior when approaching a QCP [8]. On the other hand, the variation of ρ_0 in the range 0.3-1.2 $\mu\Omega cm$ and the residual resistivity ratio $RRR \leq 15$ [Eq. 2.44] is an indication that Ge-doping introduces only a small amount of disorder in this sample showing the high crystallographic quality of the sample. Finally, Néel temperature is weakly reduced to 4.8 K for #3 and #4 compounds. For compounds with higher Ge-concentrations have the behavior typical for a

valence fluctuating $YbNiGe_3$ system [Figs. 4.18 and 4.19]. However, #16 shows a weak anomaly around 3 K possibly due to the inclusion of Si atoms, which can alter the neighborhood of some Yb ions and possibly their valence causing them to act as magnetic impurities in the system.

Another way to approach a QCP was through the magnetotransport properties in $YbNiSi_{3-x}Ge_3$. For this purpose, in Fig. 8.6 we plot temperature-dependent normalized resistivity $\rho(T)$ curves at different magnetic fields H=0, 1, 3, 5 and 7 T. Here we perceive that the magnetoresistance in all compounds is positive in the magnetically ordered state consistent with the antiferromagnetic nature of the magnetic ordering, and it is negative in the paramagnetic state due to the freezing out of spin-flip scattering in a Kondo compound by the magnetic field. Moreover, Néel temperature decreases with the arising of the field while the coherence temperature increases showing that as soon as the antiferromagnetic ordering is disappearing the Kondo effect increases gradually overcoming it even though the intensity of the hybridization between the magnetic moment of Yb and conduction electrons is weakening in accordance with the reduction of the b-parameter [Eq. 2.50]. For its part, A and ρ_0 parameters show a tendency towards divergence with increasing field, while the latter shifts to negative values between 5 and 7 T for all compounds except for #6 where it occurs around of 3 T. This is an expected signature of a QCP [119], where the inclusion of Ge allows us to investigate the neighborhood of the QCP at low magnetic field.

8.3 Magnetic properties

We study the magnetic properties of $YbNiSi_{3-x}Ge_x$ from $\chi \times T$ at H=1 kOe and $M \times H$ at T=2 K measurements along a, b and c-direction. The obtained curves are plotted in Fig. 8.7 for each compound. We observed that the sample labeled as #1 (Yb:Ni:Si:Ge 1:1:2.95:0.05) follows the expected magnetic response for $YbNiSi_3$ as reported in the literature [10] [sec. 4.3]. This is an anisotropic antiferromagnetic compound, whose Yb moments are aligned along b-AFM easy axis. In the inverse susceptibility, we observed that at high temperatures the three orientations have a linear behavior and they are parallel to each other as observed for paramagnetic local moments with CEF effects [Fig. 4.14(a)]. Also, isothermal magnetization measurement along b the lower-field metamagnetic transition is observed around 1.52 T, however due to the range of the applied magnetic field (0 to 7 T), it is not possible to observe the second metamagnetic transition expected to 8 T [10].

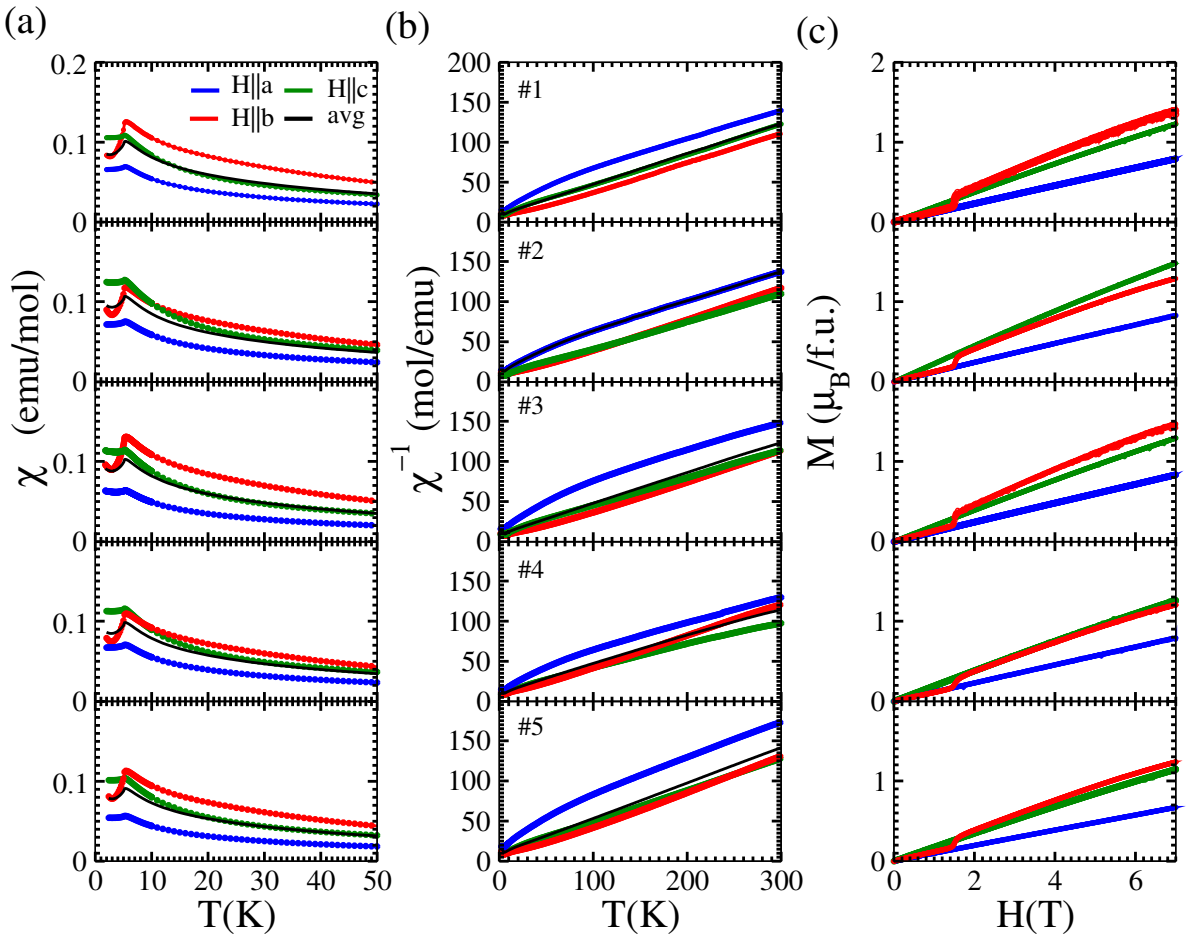

Figure 8.7: Magnetic properties of $YbNiSi_{(3-x)}Ge_x$ along a, b and c orientations. Temperature dependence of (a) susceptibility and (b) inverse susceptibility at H=1 kOe. Here we include the polycrystalline average for each compound. (c) Magnetic field dependence of magnetization at T=2 K. The notation used for the compounds correspond to those given in Table 8.1

The other orientations are linear and reversible up to 7 T, which is consistent with the antiferromagnetic nature of the magnetic ordering. The above leads us to believe that in #1 there is not inclusion of Ge atoms and their respective atomic positions are vacant. For other compounds, except for #2, where we expected Ge-doping these behaviors were approximately maintained implying weak changes in the planar measurements due to a possible competition between CEF and magnetocrystalline anisotropy.

Since the exact Yb, Ni, Si and Ge concentration is unknown for us, in order to make comparisons and understand the effect of Ge atoms on magnetic properties of $YbNiSi_3$, we analyze the susceptibility measurements as follows: we initially plot $\chi \times T$ (in emu/g) and fit the equation $\chi = \frac{1}{M_{at}} \left(\chi_0 + \frac{C}{T-\theta_{cw}}\right)$ with the atomic mass M_{at} as a parameter. With this, we calculate the magnetic susceptibility in emu/mol and trace it to fit the Curie-Weiss law to determine the Pauli paramagnetic contribution χ_0. Then, temperature dependence of inverse average susceptibility by subtracting χ_0 is drawn $\chi - \chi_0 \times T$ and a linear fit is generated to calculate the magnetic moment of compounds [Eq. 2.19]. The results obtained are included in Table 8.5.

Table 8.5: Main magnetic parameters for $YbNiSi_{3-x}Ge_x$: effective magnetic moment μ_{eff} calculated of χT at high temperatures, high field moment μ_{HF} observed at 2 K and H = 70 kOe in $M \times T$, atomic mass M_{at} (g/mol), Pauli paramagnetic susceptibility χ_0 (10^{-3} emu/mol), Curie-Weiss temperature θ^a_{cw} , θ^b_{cw} and θ^c_{cw} (K) along a, b and c directions, correspondly, and on polycrystalline average θ^p_{cw} (K). Néel temperature T^{χ}_N (K), Kondo temperature T_K (K) and critical field H_c (T) are calculated from $\frac{d(T\chi_{avg})}{dT}$, $\frac{|\theta^p_{cw}|}{2}$ and $\frac{dM}{dH}$, respectively. The notation used for the compounds correspond to those given in Table 8.1

# Sample	M_{at}	θ^a_{cw}	θ^b_{cw}	θ^c_{cw}	θ^p_{cw}
#1	271.12	-85.5(6)	15.1(5)	-25.7(2)	-18.15(8)
#2	266.55	-77.3(2)	-5.1(2)	-16.3(2)	-19.90(7)
#3	284.85	-66.3(4)	2.72(1)	-26.1(7)	-23.89(1)
#4	196.35	-105.0(9)	9.9(4)	0.5(5)	-20.48(1)
#5	255.52	-72.7(4)	5.8(2)	-24.05(9)	-23.91(6)

# Sample	T^{χ}_N	T_K	χ_0	μ_{eff}	H_c	μ^b_{HF}
#1	5.0(2)	4.54	0.42(8)	4.42(3)	1.48(3)	1.39
#2	5.0(2)	4.98	0.14(4)	4.57(2)	1.52(2)	1.33
#3	5.2(1)	5.97	0.17(3)	4.52(1)	1.52(1)	1.46
#4	5.0(2)	5.12	1.28(3)	4.36(1)	1.52(2)	1.20
#5	5.0(2)	5.98	-0.21(1)	4.33(2)	1.52(3)	1.24

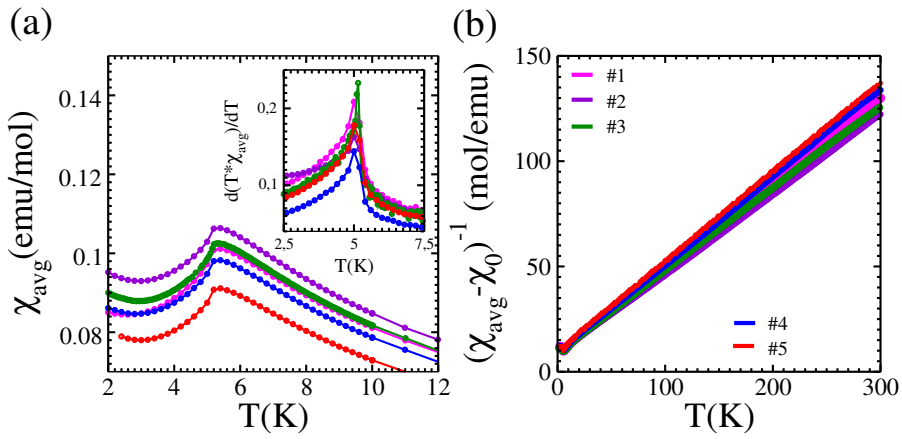

Figure 8.8: Temperature dependence of (a) susceptibility and (b) inverse susceptibility on polycrystalline average at H=1 kOe for $YbNiSi_{(3-x)}Ge_x$. The inset in (a) correspond to $\frac{d(T\chi_{avg})}{dT}$. The notation used for the compounds correspond to those given in Table 8.1

The average magnetic susceptibility and inverse susceptibility subtracting the Pauli paramagnetic contribution χ_0 as a function of temperature are shown in Fig. 8.8 for the sequence of compounds considered in Table 8.1 At low temperatures, we note that all compounds exhibit the antiferromagnetic anomaly at T=5 K, except #3 which shifts to 5.2(1) K, according to the maximum peak exhibiting $d(T\chi)/dT$ [inset Fig. 8.8 (a)]. At high temperature, the susceptibility curves retains a T-Curie-Weiss dependence that is nearly identical for all compounds. The slope of the curves increases weakly to include Ge-doping and thus the effective magnetic moment decreases slowly. Notice that #1, #2 and #3 compounds have an effective paramagnetic moment close to the expected value for Yb^{3+} moment (4.5 μ_B), and it weakly reduces to 4.3 μ_B for #5. In addition, χ_0 varies from -0.21×10^{-4} to 1.28×10^{-4}, which is negligible compared to the measured value of the overall $\chi(T)$. On the other hand, the estimated Curie-Weiss temperatures θ^a_{cw}, θ^b_{cw} and θ^c_{cw} change from -85.5, 15.1, -25.7 K to -72.7, 5.8 and -24.1 K, respectively, as one progresses through the sequence of compounds, indicating weak anisotropy that can be attributed to the CEF effect. Even the polycrystalline Curie-Weiss temperature goes towards increasingly negative values from -18.15 K in #1 to -23.9 K in #5 suggesting that antiferromagnetic exchange interactions increase due to hybridization between the Yb magnetic moment and conduction electrons leading to an enhancement of the Kondo effect in these compounds [Fig. 8.5]. Thus, in Kondo antiferromagnetic systems, θ^p_{cw} is a measure of both Kondo and RKKY interaction. So, it can be used to calculate the Kondo temperature as $T_K = \frac{|\theta^p_{cw}|}{4}$ [24] whose estimated values are included in Table 8.5. Notice

that these are lower than $T_K = 30$ K reported in the literature for $YbNiSi_3$ [10] [sec. 4.3].

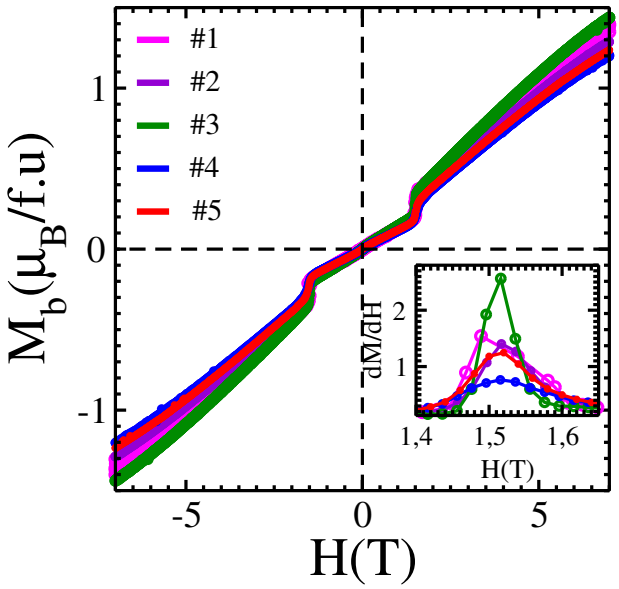

Figure 8.9: Magnetic field dependence of magnetization at T=2 K in $H \parallel b$ orientation for $YbNiSi_{3-x}Ge_3$. The notation used for the compounds correspond to those given in Table 8.1.

Magnetization measurements along the b easy axis at T=2 K for $YbNiSi_{3-x}Ge_x$ are shown in Fig. 8.9. Here we observe that there is a shift of metamagnetic transition toward high magnetic fields from 1.48 T in #1 to 1.52 T in #2, and it is maintained for other compounds. These behavior was verified in dM/dH curves [inset Fig. 8.9] and their values are included in Table 8.5, as well as the high magnetic moment at H=7 T which are very lower that the expected for Yb^{3+}. On the other hand, the magnetization at T=2, 3, 4, 6 K for each compound is presented in Fig. 8.10. In all case we perceive that the metamagnetic transition moves to low fields with increasing temperature and disappears above the Néel temperature. Even, the curves at T=4 K exhibit a noticeable curvature change around of 6 T which apparently is displaced weakly to 5 T for these sequence of compounds. This anomaly can be associated with high-field metamagnetic transition observed in $YbNiSi_3$ at T=2 K above to 8 T [Fig. 4.14 (d)].

Additionally, we perform susceptibility and magnetization measurements on compounds with high Ge concentration along $H \perp c$ and $H \parallel c$. Since they are weakly anisotropic, in Fig. 8.9 we plot the curves in the latter orientation. We

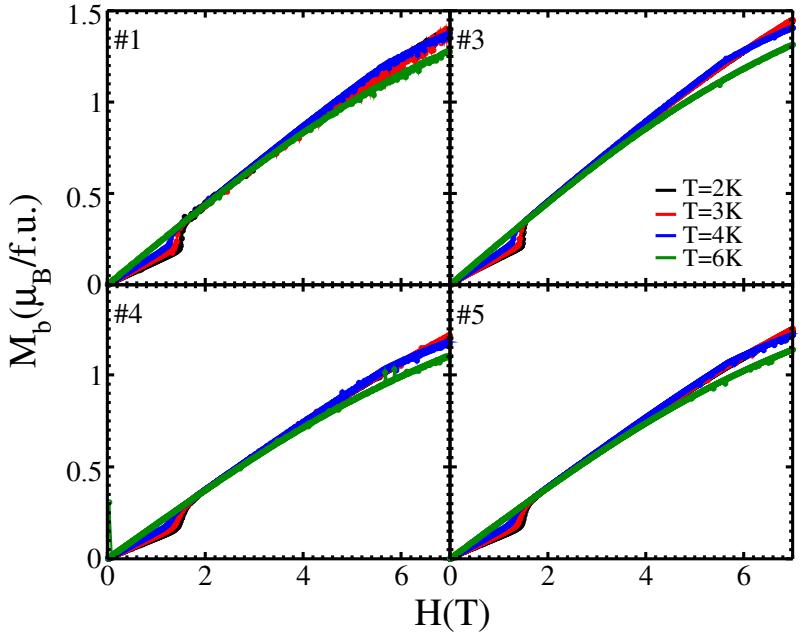

Figure 8.10: Magnetization as a function of magnetic field for $YbNiSi_{3-x}Ge_x$ at different temperatures T=2, 3, 4 and 6 K. The notation used for the compounds correspond to those given in Table 8.1.

observed that in $\chi(T)$ with decreasing temperature, the pure germanium compound exhibits a broad follow by a minimum around 50 K due to the presence of mixed-valence Yb ions [83] [sec. 4.4]. However, the inclusion of Si atoms allows that this minimum be gradually broadened and shifted to high temperatures. Remark that at low temperatures #16 exhibit a weak anomaly around of 2.3 K which suggests the occurrence of some exchange magnetic interaction in this compound. This fact is confirmed by plotting $M \times H$ where the magnetization exhibits a S-like behavior compared to other compounds. Moreover, these are agree with those found in resistivity measurements [Fig. 8.4].

8.4 Some remarks

The results obtained in this chapter are preliminary and require to be revised again, after performing Energy-Dispersive X-Ray Spectroscopy (EDS) measurements in order to determine the exact composition of each element in the samples. With it we will calculate their respective atomic mass and then check

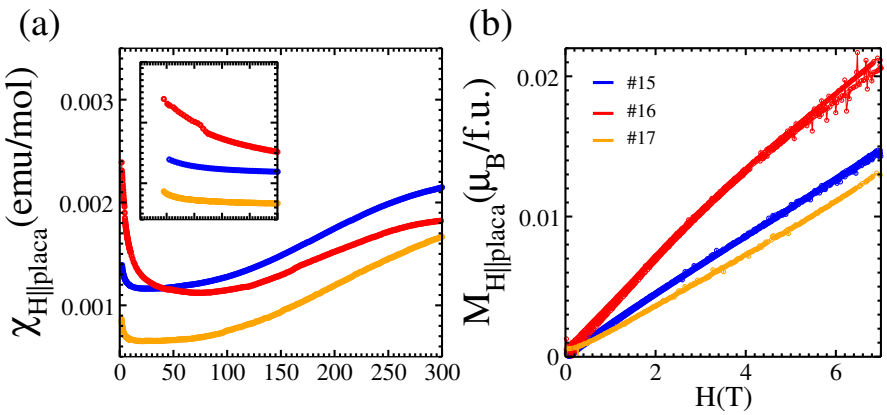

Figure 8.11: Magnetic properties of $YbNiSi_{3-x}Ge_x$ along c orientation. (a)Temperature dependence of susceptibility at H=1 kOe and (b) Magnetic field dependence of magnetization at T=2 K. The notation used for the compounds correspond to those given in Table 8.1.

the sequence of compounds according to Ge concentration increases.

In our attempt to change the distance between ions by introducing Ge-atoms into $YbNiSi_{3-x}Ge_x$ we are playing with several factors: (i) we try to gradually change the crystal structure of orthorhombic $YbNiSi_3$ ($Cmmm$) toward a tetragonal $YbNiGe_3$ ($I4_1/amd$) and simultaneous occupation of Ni and Si/Ge at some crystallographic position [Tables 4.2 and 4.8]. (ii) We create a chemical pressure on the Yb atoms (since replacing the ionic radius of Si 0.41 Å with that of Ge 0.53 Å), which alters the magnetic properties of the compounds. From all our growth experiments we perceive that the inclusion of Si atoms in $YbNiGe_3$ or Ge atoms in $YbNiSi_3$ compounds is quite difficult due to the instability of these dilutes. For example, keeping the growth conditions and the same initial proportion of Yb:Ni:Si:Sn 1:1:3:20 [such as #8 and #2], do not guarantee the same phase. This occurs due to the magnetic and structural similarity that $YbNiSi_3$ exhibits with $YbNi_2Si_3$. Even, increasing the Sn proportion to 45 [#14] stabilizes the latter phase and on the contrary further destabilizes the formation of phases with high Ge-concentrations [#18] with respect to the desired phase.

On the other hand, we expect that the characteristics exhibited by $YbNiSi_{3-x}Ge_x$ in resistivity and magnetization measurements are due to the presence of Ge atoms in the samples. These exert a chemical pressure on some Yb atoms, causing them to increase their local volume through hybridization between the conduction and f-states of ytterbium. Thus, the valence of Yb changes from its trivalent to fluctuating valence state (Yb^{3+}=0.86 Å,

Yb^{2+}=1.13 Å). This is consistent with the fact that the lattice expansion enhances the Kondo effect, where we saw it by the shift of T_{coh} toward high temperature with the pressure rise. Also, notice that the magnetic moment of #4 is weakly reduced to 4.36(1) μ_B with respect to 4.5 μ_B expected for Yb^{3+}, due to the local moment having a low Kondo screening.

It is natural to expect that the pressure effect leads to a reduction of T_N. However, our results demonstrate that for the sequence of compound considered, the increase of Kondo screening is accompanied by a minimal weakening in the RKKY interaction which always overcomes the former at low temperatures. This is verified by averaging the values obtained by resistivity and magnetization measurements, where a possible shift towards 4.9 K is observed for #4, however specific heat measurements should be performed to confirm this statemet. Thus, the strong competition between Kondo and RKKY interaction in $YbNiSi_{1-x}Ge_x$ and the existence of CEF make it difficult to change the magnetic properties of these systems.

The compounds considered and the measurement performed above 2 K are not conclusive. We do not observe power-law T dependence at low temperature in resistivity measurements, nor other anomalous behavior in the susceptibility measurements. However these show that we are well on our way to finding the quantum critical point.

8.5 Perspectives

In future work we will attempt to grow single crystals of $YbNiSi_{3-x}Ge_x$ for intermediate Si concentration levels from $YbNiGe_3$ using a Ni–Ge rich self-flux with a starting molar proportion of 1:1.6:9-x x (Yb : Ni : Ge: Si) similar to that used by Mun in Ref. [83] in order to avoid the growth of second phases. Structural and magnetic characterization will require the use of techniques such as Energy-dispersive X-ray spectroscopy (EDS) and X-ray absorption/emission (PFY-XAS, RXES or HAXPES) to determine the exact composition of the compounds and the magnetic state of Yb-systems. In addition, specific heat and resistivity measurements below 2 K should be performed to determine possible NFL behavior near the QCP. On the other hand, it will be interesting to study in detail the importance of CEF in these systems and its role in the competition between RKKY and Kondo interaction to stabilize the magnetic ground state of these systems. Finally, we could consider carrying ac-susceptibility measurements in order to evaluate whether chemical

disorder produces magnetic clustering that may impact its low-temperature behavior.

9

Summary

High-quality single crystals of ternary intermetallics $YNiSi_3$, $LuNiSi_3$, doped systems $Gd_{1-x}Y_xNiSi_3$, $Tb_{1-x}Y_xNiSi_3$ (x=0, 0.25, 0.50, 0.65. 0.80) and $YbNiSi_{3-x}Ge_x$ (x= 0, 0.003, 0.03, 0.05, 0.1, 0.2, 2.7 2.85, 3 still to be verified) were grown via the Sn-flux method and studied by X-ray diffraction, magnetization, specific-heat and resistivity measurements. All single crystals grew in thin plate geometry with well-defined shapes and shiny surfaces. They assume a layered orthorhombic $SmNiGe_3$ structure belonging to $Cmmm$ space group, except to $YbNiGe_3$ which is a tetragonal crystal class with space group $I4_1/amd$. $YNiSi_3$ and $LuNiSi_3$ are found to be type-I superconductors bulks with critical temperatures $T_c = 1.36(3)$ and 1.61(2) K, critical fields $\mu_0 H_c(0) \approx 0.05$ and 0.08 T, and a jump in specific heat at T_c of $\Delta C_{el}/\gamma T_c = 1.14(9)$ and 0.71(5), respectively, values lower than those expected from BCS theory (1.43). Its electronic structure calculated from first-principles density functional theory exhibits highly anisotropic and complex Fermi surfaces with one electronic and two hole-like branches, where one hole and the electron branches have a large cylindrical topology connecting the first Brillouin-zone boundaries. The former is built up by the hybridization of Y(Lu) d, Ni d, and Si p states, and the latter is built up by Ni d and Si p states. Meanwhile, the phononic structures indicate that the coupling of the Y(Lu), Ni d with Si p electrons in the low-lying optical phonon branches are responsible for the formation of Cooper pairs. So, these can be categorized as anisotropic three-dimensional metals with multiband superconducting ground states in the weak-coupling regime. On the other hand, Gd-based systems reveal the gradual emergence of Ni magnetic moment when the Y-doping level increases, and the coexistence of ferromagnetic (due to Ni 3d) and antiferromagnetic (due to Gd) interactions which generate that $Gd_{0.50}Y_{0.50}NiSi_3$ and $Gd_{0.35}Y_{0.65}NiSi_3$ present the exchange bias phenomena with potential for applications in magnetic memory and spintronics. Similarly, Y-doping in Tb compounds has remarkable influence on the magnetic properties. These changes include a decrease in the antiferromagnetic Tb-Tb exchange and the presence of short-range ferromagnetism due to the presumed magnetism of Ni atoms which dominates for concentrations $x > 0.50$. Finally, preliminary results on $YbNiSi_{3-x}Ge_x$ demonstrate that Ge induces a change in the valence

state of Yb (3+ to 2+), giving rise to the lattice expansion and an enhancement in the Kondo effect despite not overcoming the RKKY interaction.

Bibliography

[1] D Aristizábal and MA Avila. Crescimento e caracterização de monocristais da série $RNiSi_3$ (R=terra rara). Master's thesis, Universidade Federal do ABC, 2015.

[2] FR Arantes, D Aristizábal, SH Masunaga, FN Costa, FF Ferreira, T Takabatake, L Mendonça, RA Ribeiro, and MA Avila. Structure, magnetism, and transport of single-crystalline $RNiSi_3$ (R=Y,Gd-Tm,Lu). *Physical Review Materials*, 2(4):044402, 2018.

[3] T Shigeoka, M Shiraishi, Y Uwatoko, T Fujiwara, T Goto, and H Mitamura. Anomalous metamagnetic behavior of $TbCu_2Ge_2$ single crystal. *Physica B: Condensed Matter*, 346:112–116, 2004.

[4] T Shigeoka, N Iwata, A Garnier, D Gignoux, D Schmitt, and FY Zhang. Multi-step metamagnetism of $TbRu_2Si_2$ single crystal. *Journal of Magnetism and Magnetic Materials*, 140:901–902, 1995.

[5] P Gegenwart, Q Si, and F Steglich. Quantum criticality in heavy-fermion metals. *Nature Physics*, 4(3):186–197, 2008.

[6] K Grube, T Wolf, P Adelmann, C Meingast, and H Löhneysen. $YbNiSi_3$ and $YbNiGe_3$: Magnetic order vs. nonmagnetic groundstate. *Physica B: Condensed Matter*, 378:750–751, 2006.

[7] S Alexander, JS Helman, and I Balberg. Critical behavior of the electrical resistivity in magnetic systems. *Physical Review B*, 13(1):304, 1976.

[8] K Umeo, N Hosogi, MA Avila, and T Takabatake. Pressure-induced quantum critical phenomena in $YbNiGe_3$. *Physica Status Solidi (B)*, 247(3):751–753, 2010.

[9] D Aristizábal, FR Arantes, FN Costa, FF Ferreira, RA Ribeiro, and MA Avila. Single crystal growth and magnetic characterization of $RNiSi_3$ (R=Dy, Ho). *Physics Procedia*, 75:545–551, 2015.

[10] MA Avila, M Sera, and T Takabatake. $YbNiSi_3$: An antiferromagnetic Kondo lattice with strong exchange interaction. *Physical Review B*, 70(10):100409, 2004.

[11] RM Martin. *Electronic structure: basic theory and practical methods*. Cambridge university press, 2004.

[12] RM Dreizler and E Engel. *Density Functional Theory: An Advanced Course*. Springer, 2011.

[13] EK Gross and RM Dreizler. *Density functional theory*, volume 337. Springer Science & Business Media, 2013.

[14] DM Ceperley and BJ Alder. Ground state of the electron gas by a stochastic method. *Physical Review Letters*, 45(7):566, 1980.

[15] JP Perdew and A Zunger. Self-interaction correction to density-functional approximations for many-electron systems. *Physical Review B*, 23(10):5048, 1981.

[16] JM Wills, M Alouani, P Andersson, A Delin, O Eriksson, and O Grechnyev. *Full-Potential Electronic Structure Method: energy and force calculations with density functional and dynamical mean field theory*, volume 167. Springer Science & Business Media, 2010.

[17] JP Perdew, K Burke, and M Ernzerhof. Generalized gradient approximation made simple. *Physical Review Letters*, 77(18):3865, 1996.

[18] JP Perdew, A Ruzsinszky, GI Csonka, OA Vydrov, GE Scuseria, LA Constantin, X Zhou, and K Burker. Restoring the density-gradient expansion for exchange in solids and surfaces. *Physical Review Letters*, 100(13):136406, 2008.

[19] GI Csonka, JP Perdew, A Ruzsinszky, Pier PH Philipsen, S Lebègue, J Paier, OA Vydrov, and JG Ángyán. Assessing the performance of recent density functionals for bulk solids. *Physical Review B*, 79(15):155107, 2009.

[20] AI Liechtenstein, VI Anisimov, and J Zaanen. Density-functional theory and strong interactions: Orbital ordering in Mott-Hubbard insulators. *Physical Review B*, 52(8):R5467, 1995.

[21] MT Czyżyk and GA Sawatzky. Local-density functional and on-site correlations: The electronic structure of La_2CuO_4 and $LaCuO_3$. *Physical Review B*, 49(20):14211, 1994.

[22] F Bultmark, F Cricchio, O Grånäs, and L Nordström. Multipole decomposition of LDA+U energy and its application to actinide compounds. *Physical Review B*, 80(3):035121, 2009.

[23] A Otero-de-la Roza and V Luaña. Gibbs2: A new version of the quasi-harmonic model code. I. robust treatment of the static data. *Computer Physics Communications*, 182(8):1708–1720, 2011.

[24] R Tripathi, D Das, C Geibel, SK Dhar, and Z Hossain. Non-Fermi-liquid behavior at the antiferromagnetic quantum critical point in the heavy-fermion system $Ce(Cu_{1-x}Co_x)_2Ge_2$. *Physical Review B*, 98(16):165136, 2018.

[25] C Kittel. *Introduction to solid state physics*, volume 8. Wiley New York, 1996.

[26] AP Kracknell and KC Wang. The Fermi surface: Its concept, determination and use in the physics of metals, 1973.

[27] NW Ashcroft and ND Mermin. *Solid State Physics*. Saunders College, 1976.

[28] AD Becke and KE Edgecombe. A simple measure of electron localization in atomic and molecular systems. *The Journal of Chemical Physics*, 92(9):5397–5403, 1990.

[29] B Silvi and A Savin. Classification of chemical bonds based on topological analysis of electron localization functions. *Nature*, 371(6499):683, 1994.

[30] S Blundell. Magnetism in condensed matter, 2003.

[31] R Skomski. *Simple models of magnetism*. Oxford University Press on Demand, 2008.

[32] J Coey. *Magnetism and magnetic materials*. Cambridge university press, 2010.

[33] WE Wallace. *Rare earth intermetallics*. Elsevier, 2012.

[34] J Jensen and AR Mackintosh. *Rare earth magnetism*. Clarendon Press Oxford, 1991.

[35] B Lüthi. Crystal field effects in rare earth systems. *Journal of Magnetism and Magnetic Materials*, 15:1–8, 1980.

[36] MA Avila, SL Bud'ko, and PC Canfield. Anisotropic magnetization, specific heat and resistivity of RFe_2Ge_2 single crystals. *Journal of magnetism and magnetic materials*, 270(1-2):51–76, 2004.

[37] M Bouvier, P Lethuillier, and D Schmitt. Specific heat in some gadolinium compounds. I. Experimental. *Physical Review B*, 43(16):13137, 1991.

[38] A Tari. *The specific heat of matter at low temperatures*. Imperial Coll., 2003.

[39] RE Newnham. *Properties of materials: anisotropy, symmetry, structure*. Oxford University Press on Demand, 2005.

[40] NX Miao, CY Pu, CZ He, FW Zhang, C Lu, ZW Lu, and DW Zhou. Mechanical and thermodynamic properties of the monoclinic and orthorhombic phases of SiC_2N_4 under high pressure from first principles. *Chinese Physics B*, 23(12):127101, 2014.

[41] W Voigt. *Lehrbuch der kristallphysik*, volume 962. Teubner Leipzig, 1928.

[42] A Reuss. Z. angew. math. mech. *ZAMM*, 9:49, 1929.

[43] J. Bass. Conductivity, electrical. In F Bassani, GL Liedl, and P Wyder, editors, *Encyclopedia of Condensed Matter Physics*, pages 219–225. Elsevier, Oxford, 2005.

[44] K Kadowaki and SB Woods. Universal relationship of the resistivity and specific heat in heavy-fermion compounds. *Solid State Communications*, 58(8):507–509, 1986.

[45] J Bardeen, LN Cooper, and JR Schrieffer. Theory of superconductivity. *Physical Review*, 108(5):1175, 1957.

[46] AC Rose-Innes and EH Rhoderick. Introduction to superconductivity;. 1996.

[47] F Marsiglio and JP Carbotte. Superconductivity: Conventional and unconventional superconductors, 2008.

[48] T Dahm. Superconductivity of magnesium diboride: theoretical aspects. In *Frontiers in Superconducting Materials*, pages 983–1009. Springer, 2005.

[49] A Junod, D Bichsel, and J Muller. Modification of the acoustic phonon spectrum in A_{15}-type superconductors as a function of the electronic density of states. *Helvetica Physica Acta*, 52(5):580–596, 1979.

[50] A Junod, T Jarlborg, and J Muller. Heat-capacity analysis of a large number of A_{15}-type compounds. *Physical Review B*, 27(3):1568, 1983.

[51] WL McMillan. Transition temperature of strong-coupled superconductors. *Physical Review*, 167(2):331, 1968.

[52] P Coleman and AJ Schofield. Quantum criticality. *Nature*, 433(7023):226–229, 2005.

[53] Y Chen, Z Weng, S Michael, X Lu, and H Yuan. High-pressure studies on heavy fermion systems. *Chinese Physics B*, 25(7):077401, 2016.

[54] S Jang, BD White, PC Ho, N Kanchanavatee, M Janoschek, JJ Hamlin, and MB Maple. Crossover between Fermi liquid and non-Fermi liquid behavior in the non-centrosymmetric compound $Yb_2Ni_{12}P_7$. *Journal of Physics: Condensed Matter*, 26(42):425601, 2014.

[55] ED Mun, SL Bud'ko, C Martin, H Kim, MA Tanatar, JH Park, T Murphy, GM Schmiedeshoff, N Dilley, R Prozorov, et al. Magnetic-field-tuned quantum criticality of the heavy-fermion system YbPtBi. *Physical Review B*, 87(7):075120, 2013.

[56] Y Lai, SE Bone, S Minasian, MG Ferrier, J Lezama-Pacheco, V Mocko, AS Ditter, SA Kozimor, GT Seidler, WL Nelson, et al. Ferromagnetic quantum critical point in $CePd_2P_2$ with Pd$\rightarrow$ Ni substitution. *Physical Review B*, 97(22):224406, 2018.

[57] S Doniach. The Kondo lattice and weak antiferromagnetism. *Physica B+ C*, 91:231–234, 1977.

[58] Z Fisk and JP Remeika. Growth of single crystals from molten metal fluxes. *Handbook on the Physics and Chemistry of Rare Earths*, 12:53–70, 1989.

[59] PC Canfield and IR Fisher. High-temperature solution growth of intermetallic single crystals and quasicrystals. *Journal of Crystal Growth*, 225(2-4):155–161, 2001.

[60] M Tachibana. *Beginner's Guide to Flux Crystal Growth*. Springer, 2017.

[61] PC Canfield and Z Fisk. Growth of single crystals from metallic fluxes. *Philosophical Magazine B*, 65(6):1117–1123, 1992.

[62] PC Canfield. Solution growth of intermetallic single crystals: A beginner's guide. In *Properties and Applications of Complex Intermetallics*, pages 93–111. World Scientific, 2010.

[63] ST Hartmann and GH Cie. Stoe stadi p, 2013.

[64] RA Young. *The Rietveld method*, volume 5. International union of crystallography, 1993.

[65] Inc QuantumDesign. PPMS physical property measurement system.

[66] Inc QuantumDesign. Physical property measurement system hardware manual.

[67] Inc QuantumDesign. Physical property measurement system evercoolii option user's manual.

[68] Inc QuantumDesign. Physical property measurement system, heat capacity option user's manual.

[69] Inc QuantumDesign. Magnetic propertymeasurement system, mpms3 user's manual.

[70] JK Dewhurst and S Sharma. Development of the Elk LAPW Code.

[71] A Gulans, S Kontur, C Meisenbichler, D Nabok, P Pavone, S Rigamonti, S Sagmeister, U Werner, and C Draxl. Exciting: a full-potential all-electron package implementing density-functional theory and many-body perturbation theory. *Journal of Physics: Condensed Matter*, 26(36):363202, 2014.

[72] PE Blöchl. Projector augmented-wave method. *Physical Review B*, 50(24):17953, 1994.

[73] M Martijn. VASP: Plane waves, the paw method, and the selfconsistency cycle, 2011.

[74] NAW Holzwarth, AR Tackett, and GE Matthews. A Projector Augmented Wave (PAW) code for electronic structure calculations, Part I: atompaw for generating atom-centered functions. *Computer Physics Communications*, 135(3):329–347, 2001.

[75] G Kresse and J Furthmüller. Efficient iterative schemes for ab initio total-energy calculations using a plane-wave basis set. *Physical Review B*, 54(16):11169, 1996.

[76] B Belan, Y Tokaychuk, M Manyako, and R Gladyshevskii. New ternary phases in the Lu–Ni–Si system. *Chemistry of Metals and Alloys*, (6,N 3-4):209–213, 2013.

[77] FR Arantes, D Aristizábal, DA Mayoh, Y Yamane, C Yang, MR Lees, JM Osorio, T Takabatake, and MA Avila. Superconductivity in monocrystalline $YNiSi_3$ and $LuNiSi_3$. *Physical Review B*, 99(22):224505, 2019.

[78] T Shigeoka, T Fujiwara, K Munakata, K Matsubayashi, and Y Uwatoko. Component-separated magnetic transition in $HoRh_2Si_2$ single crystal. In *Journal of Physics: Conference Series*, volume 273, page 012127. IOP Publishing, 2011.

[79] R Tartaglia, FR Arantes, CW Galdino, D Rigitano, UF Kaneko, MA Avila, and E Granado. Magnetic structure and magnetoelastic coupling of $GdNiSi_3$ and $TbNiSi_3$. *Physical Review B*, 99(9):094428, 2019.

[80] SL Bud'ko, PC Canfield, MA Avila, and T Takabatake. Magnetic-field tuning of the low-temperature state of $YbNiSi_3$. *Physical Review B*, 75(9):094433, 2007.

[81] K Grube, W Knafo, S Drobnik, P Adelmann, Th Wolf, C Meingast, and H Löhneysen. Suppression of magnetic order in $YbNiSi_3$ by magnetic fields. *Journal of Magnetism and Magnetic Materials*, 310(2):354–356, 2007.

[82] Y Kobayashi, T Onimaru, MA Avila, K Sasai, M Soda, K Hirota, and T Takabatake. Neutron scattering study of Kondo lattice antiferromagnet $YbNiSi_3$. *Journal of the Physical Society of Japan*, 77(12):124701, 2008.

[83] ED Mun, SL Bud'ko, H Ko, GJ Miller, and PC Canfield. Physical properties and anisotropies of the $RNiGe_3$ series (R=Y, Ce–Nd, Sm, Gd–Lu). *Journal of Magnetism and Magnetic Materials*, 322(21):3527–3543, 2010.

[84] H Sato, H Yamaoka, Y Utsumi, H Nagata, MA Avila, RA Ribeiro, K Umeo, T Takabatake, Y Zekko, and JF Lin. Pressure-induced valence change of $YbNiGe_3$ investigated by resonant X-ray emission spectroscopy at the YbL_3 edge. *Physical Review B*, 89(4):045112, 2014.

[85] H Sato, Y Utsumi, J Kodama, H Nagata, MA Avila, RA Ribeiro, K Umeo, T Takabatake, K Mimura, and S Motonami. Electronic structure of $YbNiX_3$ (X= Si, Ge) studied by hard X-ray photoemission spectroscopy. *Physica Status Solidi (C)*, 12(6):620–623, 2015.

[86] T Moriya and T Takimoto. Anomalous properties around magnetic instability in heavy electron systems. *Journal of the Physical Society of Japan*, 64(3):960–969, 1995.

[87] AV Morozkin, VO Yapaskurt, J Yao, R Nirmala, S Quezado, and SK Malik. Magnetic entropy change and magnetocaloric effect of $DyNiSi_3$, $Dy_2Ni_3Si_5$, $DyNiSi_2$ and $HoNiSi_{0.33}Ga_{67}$ antiferromagnets. *Intermetallics*, 107:81–92, 2019.

[88] M Smidman, AD Hillier, DT Adroja, MR Lees, VK Anand, RP Singh, RI Smith, DM Paul, and G Balakrishnan. Investigations of the superconducting states of noncentrosymmetric $LaPdSi_3$ and $LaPtSi_3$. *Physical Review B*, 89(9):094509, 2014.

[89] A Togo and I Tanaka. First principles phonon calculations in materials science. *Scripta Materialia*, 108:1–5, 2015.

[90] AP Pikul and D Gnida. Superconducting phase transition in $YNiGe_3$, a non-f-electron reference to the unconventional superconductor $CeNiGe_3$. *Solid State Communications*, 151(10):778–780, 2011.

[91] MJ Winiarski and M Samsel-Czekała. The electronic structure of $CeNiGe_3$ and $YNiGe_3$ superconductors by *ab initio* calculations. *Solid State Communications*, 179:6–10, 2014.

[92] MJ Winiarski and M Samsel-Czekała. Electronic structure of the 344-type superconductors $La_3(Ni;Pd)_4(Si;Ge)_4$ by ab initio calculations. *Journal of Alloys and Compounds*, 546:124–128, 2013.

[93] DA Joshi, F Wrubl, P Manfrinetti, and SK Dhar. Magnetic properties of $RMgSi_2$ (R=La, Ce, Pr, and Nd) compounds. *Physical Review B*, 80(21):214412, 2009.

[94] DA Joshi, CV Tomy, and SK Malik. Magnetic, transport and thermal properties of ternary indides R_2CoIn_8 (R= rare earths and Y). *Journal of Physics: Condensed Matter*, 19(13):136216, 2007.

[95] J Souletie and R Tournier. Specific heat and magnetization in dilute magnetic alloys. *Journal of Low Temperature Physics*, 1(2):95–108, 1969.

[96] JA Blanco, D Gignoux, and D Schmitt. Specific heat in some gadolinium compounds. II. Theoretical model. *Physical Review B*, 43(16):13145, 1991.

[97] EV Sampathkumaran and I Das. Enhancement of heat capacity above the Néel temperature in $Gd_{1-x}Y_xNi_2Si_2$ alloys, and its implications. *Physical Review B*, 51(13):8178, 1995.

[98] R Mallik, PL Paulose, EV Sampathkumaran, S Patil, and V Nagarajan. Coexistence of localized and (induced) itinerant magnetism and heat-capacity anomalies in $Gd_{1-x}Y_xNi$ alloys. *Physical Review B*, 55(13):8369, 1997.

[99] BN Harmon, VP Antropov, AI Liechtenstein, IV Solovyev, and VI Anisimov. Calculation of magneto-optical properties for 4f systems: LSDA+ Hubbard U results. *Journal of Physics and Chemistry of Solids*, 56(11):1521–1524, 1995.

[100] CW Chuang, FMF de Groot, YF Liao, YY Chin, KD Tsuei, R Nirmala, D Malterre, and A Chainani. Hard X-ray photoemission spectroscopy of GdNi and HoNi. *Physical Review B*, 102(16):165127, 2020.

[101] WC Thoburn, S Legvold, and FH Spedding. Magnetic properties of the Gd-La and Gd-Y alloys. *Physical Review*, 110(6):1298, 1958.

[102] JA Blanco, D Gignoux, P Morin, and D Schmitt. Thermodynamical properties of incommensurate magnetic systems. *EPL (Europhysics Letters)*, 15(6):671, 1991.

[103] JM Barandiaran, D Gignoux, D Schmitt, JC Gomez-Sal, JR Fernandez, P Chieux, and J Schweizer. Magnetic properties and magnetic structure of $GdNi_2Si_2$ and $GdCu_2Si_2$ compounds. *Journal of Magnetism and Magnetic Materials*, 73(2):233–239, 1988.

[104] Z Islam, C Detlefs, AI Goldman, SL Bud'Ko, PC Canfield, and A Zheludev. The magnetic structures of $DyNi_2Ge_2$. *Solid State Communications*, 108(6):371–376, 1998.

[105] JS Kouvel. Exchange anisotropy in an iron-aluminum alloy. *Journal of Applied Physics*, 30(4):S313–S314, 1959.

[106] PD Kulkarni, S Venkatesh, A Thamizhavel, VC Rakhecha, S Ramakrishnan, and AK Grover. Exchange bias and its phase reversal in zero magnetization admixed rare-earth intermetallics. *IEEE Transactions on Magnetics*, 45(7):2902–2906, 2009.

[107] X Wang, X Cheng, S Gao, J Song, K Ruan, and X Li. Room temperature exchange bias in $SmFeO_3$ single crystal. *Journal of Magnetism and Magnetic Materials*, 399:170–174, 2016.

[108] JA Blanco, D Gignoux, and D Schmitt. Crystal field and magnetic properties of the tetragonal $TbNi_2Si_2$ compound. *Zeitschrift für Physik B Condensed Matter*, 89(3):343–350, 1992.

[109] JM Barandiaran, D Gignoux, D Schmitt, JG Sal, and JR Fernandez. Magnetic properties of RNi_2Si_2 compounds (R=rare earth). *Journal of Magnetism and Magnetic Materials*, 69(1):61–70, 1987.

[110] TA Wiener, IR Fisher, and PC Canfield. The magnetic characteristics of the $Tb(Ni_{1-x}Co_x)_2Ge_2$ system. *Journal of Alloys and Compounds*, 303:289–292, 2000.

[111] CA Poldy and E Gratz. Electrical resistivity and magnetic investigations of the orthorhombic $Tb(Ni,Cu)_2$ system. *Journal of Magnetism and Magnetic Materials*, 8(3):223–231, 1978.

[112] S Weinstein, RS Craig, and WE Wallace. Magnetic characteristics of Tb–Y and Ho–Y solid solutions. *The Journal of Chemical Physics*, 39(6):1449–1454, 1963.

[113] T Shigeoka, H Fujii, M Nishi, Y Uwatoko, T Takabatake, I Oguro, K Motoya, N Iwata, and Y Ito. Metamagnetism in $TbNi_2Si_2$ single crystal. *Journal of the Physical Society of Japan*, 61(12):4559–4565, 1992.

[114] SL Bud'ko, Z Islam, TA Wiener, IR Fisher, AH Lacerda, and PC Canfield. Anisotropy and metamagnetism in the RNi_2Ge_2 (R=Y, La–Nd, Sm–Lu) series. *Journal of Magnetism and Magnetic Materials*, 205(1):53–78, 1999.

[115] JR Banavar, D Jasnow, and DP Landau. Fluctuation-induced first-order transition in a bcc Ising model with competing interactions. *Physical Review B*, 20(9):3820, 1979.

[116] AK Murtazaev, MK Ramazanov, DR Kurbanova, MK Badiev, and Ya K Abuev. A study of the critical properties of the Ising model on body-centered cubic lattice taking into account the interaction of next behind nearest neighbors. *Physics of the Solid State*, 59(6):1103–1109, 2017.

[117] J He and Z Ling, Gand Ye. Magnetic properties of hexagonal $YbCu_{5-x}Al_x$: Crossover from intermediate valence to trivalence of Yb ion. *Journal of Alloys and Compounds*, 325(1-2):54–58, 2001.

[118] S Nakamura, K Hyodo, Y Matsumoto, Y Haga, H Sato, S Ueda, K Mimura, K Saiki, K Iso, and M Yamashita. Heavy fermion state of $YbNi_2Si_3$ without local inversion symmetry. *Journal of the Physical Society of Japan*, 89(2):024705, 2020.

[119] SA Grigera, RS Perry, AJ Schofield, M Chiao, SR Julian, GG Lonzarich, SI Ikeda, Y Maeno, AJ Millis, and AP Mackenzie. Magnetic field-tuned quantum criticality in the metallic ruthenate $Sr_3Ru_2O_7$. *Science*, 294(5541):329–332, 2001.